UNIVERSITÉ DE GRENOBLE

THÈSE

Pour obtenir le grade de

DOCTEUR DE L'UNIVERSITÉ DE GRENOBLE

Spécialité : **Automatique-Productique**

Arrêté ministériel :

Présentée par

Maria Adelina Rivas Caicedo

Thèse dirigée par **M. Olivier Sename et M. Pascal Higelin**

préparée au sein **Gipsa Lab, PRISME et Renault**
et de **Électronique, Électrotechnique, Automatique, Traitement du Signal**

Modélisation et contrôle du moteur à allumage commandé pour Euro 6

Thèse soutenue publiquement le **10 Octobre 2012**,
devant le jury composé de :

M. Thierry-Marie Guerra
Professeur Université de Valenciennes, Rapporteur

M. Gianfranco Rizzo
Professeur Université de Salerno, Rapporteur

M. Stéphane Richard
Docteur Ingénieur IFP, Examinateur

M. Christian Caillol
Maître de Conférences Université d'Orléans, Encadrant

M. Emmanuel Witrant
Maître de Conférences UJF, Encadrant

M. Olivier Sename
Professeur Grenoble INP, Directeur de thèse

M. Pascal Higelin
Professeur Université d'Orléans, Directeur de thèse

M. Vincent Talon
Ingénieur de recherche Renault, Invité

Acknowledges

This thesis is the result of several exchanges: technical, scientific and personal.
First, I am deeply grateful with my industrial advisor Vincent Talon, your orientation and support were fundamental for my research. I admire your ability to balance the industry interests with the personal goals of the people you work with. Above all, you made me feel as a friend, which I value.
My sincere gratitude to my thesis supervisor Prof. Olivier Sename, you oriented and supported me with promptness and care, thanks for always being patient and encouraging me to pursuit new ideas and recover from difficulties.
I am also very grateful to my thesis advisor Emmanuel Witrant, your technical advice and attention to details have been fundamental for my research. Thanks for all the pertinent comments in this thesis and for your support.
Thanks to my thesis supervisor Prof. Pascal Higelin and to my advisor Christian Caillol, your engine understanding is tremendous, and your scientific work oriented me on my academic research. Thanks for many motivating discussions that helped me to success on my thesis.
I also feel grateful for the privilege of knowing and collaborating with many other people in Gipsa Lab and Renault, who became friends over the last three years.
Thanks to Gipsa Lab and Renault for helping me to carry out my doctoral research and for their financial support.
Finally, I thank the members of my close family: my husband, my parents and my sisters for their love and support.

To my beloved family.

Table of contents

Chapter 1

Contexte et enjeux de la thèse

Cette thèse a été développé grâce à une *Conventions Industrielles de Formation par la Recherche* (CIFRE). Cette convention fait partie d'un programme de l'Association nationale de la recherche et de la technologie (ANRT), coordonné par le Centre nationale de la recherche scientifique (CNRS). L'accord CIFRE subventionne les entreprises françaises qui engagent un thésard pour conduire un projet scientifique dans l'entreprise, en partenariat avec un laboratoire publique de recherche. Pour cette thèse, l'accord CIFRE a été signé par Renault et les laboratoires GIPSA Lab de Grenoble et PRISME d'Orléans.

- Le Groupe Renault, qui est présent dans 118 pays, design, construit et vend des voitures des marques Renault, Dacia et Renault Samsung Motors.

- Gipsa-lab est un laboratoire multidisciplinaire de recherche, créé en group avec l'Institut nationale Polytechnique de Grenoble (INP), le CNRS, l'université Joseph Fourier et l'université Stendhal. Gipsa Lab a aussi des collaborations avec l'Institut de recherche en informatique et en automatique (INRIA), l'Observatoire de Grenoble et l'université Pierre Mendès. La recherche au Gipsa-lab est centrée dans les domaines de l'automatique, contrôle, les signaux, l'image et la voix.

- PRISME est un laboratoire de recherche qui appartient à l'université d'Orléans en France. Les activités de recherche de ce laboratoire sont lieés aux systèmes de fluides et aérodynamique, énergétique, combustion, moteurs, mécanique des matériaux, génie civil, nano matériaux, robotique, traitement des signaux et automatique.

1.1 Contexte de l'étude: modélisation, observation et contrôle pour un moteur à allumage commandé

Le transport a un rôle fondamental dans la société et les individus: les relations entre les personnes, leurs travails, leur loisirs, la façon comme ils s'organisent la production, le développent des villes et leurs manières d'accéder aux services, aux biens et à la nourriture. Tous ces éléments sont liés au développement de la mobilité. Le transport privé propulsé par de moteurs à combustion interne a augmenté de façon drastique dans les dernières décennies; il est accepté de tous que les voitures soient accessibles à tout le monde, qu'elles soient plus sures et plus performantes, avec une utilisation extrêmement fréquente. Malgré ces avantages, il y a plusieurs conséquences du développement des véhicules qui ne sont pas toujours pris en compte: l'augmentation de la consommation de carburant, la quantité d'émissions polluants et l'exposition des gens à la pollution, laquelle peut causer des maladies très graves [Krzyzanowski et al., 2005]. En Europe, plusieurs études ont reporté que la pollution de l'air est directement lié à l'utilisation des voitures [Adams et al., 2009], [International Energy Agency, 2011].

La persistance des problèmes par rapport à la qualité de l'air et les problèmes de santé liés aux transports ont déclenché des réponses au niveau politique qui cherchent à réguler les émissions des véhicules légers [Weiss et al., 2011]. Ces politiques deviennent de plus en plus contraignantes au niveau mondial:

- l'introduction des limites plus contraignantes pour les véhicules légers avec les normatives Euro 5b en 2011 et Euro 6 en 2014 [Summaries of EU legislation, 2009],
- le remplacement de l'actuel Nouvelle Cycle Européen de Conduit (New European Driving Cycle (NEDC)) par un cycle de conduite harmonisé au niveau mondial pour 2014 [Weiss et al., 2011],
- et potentiellement, l'implémentation des mesures supplémentaires pour vérifier les émissions des véhicules en dehors d'un seul cycle de conduite standardisé en 2014.

Le Tableau 1.1 présent un résumé des principales régulations et de l'évolution de la législation sur les émissions polluants pour la Communauté Européen depuis sa première apparition.

Un autre élément très contraignent pour le développement des véhicules est la limitation du carburant fossile. Etant donné que la consommation du pétrole représente 35% de l'énergie utilisé dans la planète, avec le gaz naturel et le charbon qui font jusqu'à 24% et 28% respectivement, il est logique de dire que l'économie mondial dépend de façon critique de ces ressources non renouvelables. En sachant que le gaz naturel, le charbon et le pétrole sont des ressources finîtes, il est clair qu'il y aura un moment où la production arrivera à un maximum pour commencer à décliner. [Brecha, 2008].

Stage	Date	CO	HC	HC+NOx	NOx	PM	PN
Euro 1	1992.07	2.72 (3.16)	-	0.97 (1.13)	-	-	-
Euro 2	1996.01	2.2	-	0.5	-	-	-
Euro 3	2000.01	2.30	0.20	-	0.15	-	-
Euro 4	2005.01	1	0.10	-	0.08	-	-
Euro 5	2011.09[b]	1	0.10[a]	-	0.06	0.005[b,fc]	-
Euro 6	2014.09	1	0.10[d]	-	0.06	0.005[e,f]	6.0×10^{11}[e,g]

* Véhicules désignés et construits pour le transport de passagers et ne comprenant pas plus de huit sièges en plus de la siège du conducteur. Dans les stages Euro 1-4, véhicules de passagers $> 2500\ kg$ ont été approuves dans la catégorie $N1$.
Catégorie $N1$: véhicules désignés et construits pour le transport de biens et ayant maximum une masse que n'excède pas les 3.5 tons.
a. jusqu'à 1999.09.30 (après ce date, les moteurs DI doivent accomplir les limitations des moteurs IDI.)
b. 2011.01 pour tous les modèles
c. 2013.01 pour tous les modèles
d. et NMHC = 0.068 g/km
e. applicable seulement aux véhicules qu'utilisent des moteurs DI
f. 0.0045 g/km en utilisant la procédure PMP pour mesurer
g. $6.0 \times 10^{12}, \quad 1/km$ entre les premières trois années des que d'Euro 6 soit effective

Table 1.1: Normative Européen pour les voitures des passagers (Catégorie M1*).

Les questions énergétiques, la limitation du carburant, les problèmes de santé, d'environnement, avec en plus les normes sur les émissions polluants sont des thématiques très importantes au niveau international, spécialement dans l'industrie de l'automobile et le transport. Ces éléments poussent les constructeurs a développer des nouvelles technologies pour économiser le carburant et diminuer les émissions polluants, tout en maintenant ou améliorant le performance des moteurs. Plusieurs technologies et l'ajout des nouveaux dispositifs sont une solution pour atteindre ces objectives.

A cause de la complexité des nouveaux dispositifs et technologies développés dans les véhicules, et en vue d'attendre les normes pour émissions polluants, il y a une forte demande d'explorer de nouvelles stratégies de contrôle. Ceci permet d'attendre les standards d'émissions, toujours en respectant la performance des moteurs. Une stratégie très répandue pour s'affranchir ces considérations est le contrôle basé sur les modèles. Dans ce schéma, des modèles phénoménologiques basés sur la physique des éléments qui constituent la voiture sont développés, pour représenter le comportement physique du moteur. Ces approximations permettent de tester des nouveaux concepts et de simuler des processus physiques, les interactions et le comportement des diffèrents composants du

véhicule, sans avoir besoin d'une validation expérimental, laquelle est utilisé uniquement dans des stages finales du design.

Aujourd'hui, la recherche et le développement du moteur basés sur des modèles est typiquement fait avec des modèles 0 dimension ou un (0D-1D). Dans un modèle $0D$, seul les variations au niveau temporal des variables sont considérés, sans tenir compte des références au niveau spatial. Dans la modélisation $1D$, les variations temporales sont considérés avec une dimension spatial (i.e la variation de vitesse dans un tuyau par rapport au temps et à la longueur du tube). Ces types de modèles permettent de développer et de valider des lois de contrôle pour le moteur. Adapter des stratégies de contrôle basées sur des modèles 0D-1D a beaucoup d'avantages, ça permet de s'affranchir des problèmes trouvés quand on utilise des contrôleurs basés sur les data-maps, lesquels sont valables que dans les conditions d'opération pour lesquels ils ont été développés, en plus, ils introduisent des erreurs pendant les transitoires. Développer des modèles physiques en prenant en compte comme objectif les normes d'émissions de polluants et le respect de la performance du véhicule a un impact direct sur la performance des contrôleurs du véhicule, et aussi dans les coûts de recherche et développement. Cela aidé à diminuer le nombre de tests expérimentaux, lesquels sont alors utilisés comme un outil de validation finale.

1.2 Objectif de l'etude

Le développement du control moteur est crucial pour réduire les émissions polluantes et la consommation de carburant. Dans le cas du processus de la combustion, la plus part des stratégies de modélisation utilisées dans l'industrie aujourd'hui sont faites avec des modèles empiriques, ou les processus physiques sont considérés comme des " boites noires", cela veut dire qu'ils ne sont pas décrit de façon explicite : une relation entre les entrées et les sorties est obtenue à partir des mesures. Les data-maps sont des exemples de ce type de modélisation. Même si ces modèles représentent le comportement du moteur, ils ne peuvent pas être utilisés en dehors du régime d'opération pour lequel ils ont été définis. Il est un fait que la plus part des problèmes des modèles de combustion sont à l'origine dues à la manque de fondement physique. À cause de cette situation, il est très important de construire des modèles plus physiques et prédictifs pour la combustion, lesquels peuvent être utilisés comme référence pour synthétiser des lois de contrôle et des stratégies d'estimation pour des autres paramètres comme le remplissage et l'estimation des masses dans la chambre de combustion, entre autres.

Dans le cas spécifique de la modélisation du moteur, les ingénieurs font face à un système très complexe. Le comportement du moteur inclut des phénomènes liés à la thermodynamique, la chimie, la mécanique, la mécanique des fluides et l'électrique. D'un autre coté, les modèles 3D du moteur sont trop complexes pour être utilisés dans la synthèse des

lois de contrôle, ils sont mieux adaptés à la conception et au processus d'apprentissage de la physique des moteurs. Pour cette raison, il est préférable de développer des modèles dynamiques en 0D pour les applications liées au contrôle.

Le développement des modèles moteur 0D a beaucoup amélioré ces dernières années, aujourd'hui, la modélisation physique 0D est utilisée dans tous les étapes du développement du moteur : depuis le concept et le design, jusqu'à la propulsion, la calibration, le contrôle et la mise au point. Dans le cas des modèles thermodynamiques du moteur, la plus part des modèles existant sont basés sur des relations empiriques, lesquelles dans certains cas ne sont pas assez prédictives, spécialement pour les phénomènes de remplissage et combustion. En plus de ces difficultés, l'absence des capteurs représente aussi un obstacle concret pour le contrôle moteur. En raison de la viabilité et du coût, le moteur ne peut pas être équipé avec tous les capteurs pour le contrôle et la supervision. Etant donné que la fonctionnalité du moteur doit être quand même garantie, les approches basées sur la modélisation et l'utilisation des observateurs ont prouvé leur qualité pour être des solutions possibles pour affranchir le manque de capteurs.

Cette thèse se focalise sur la modélisation 0D, en particulier sur une description plus détaillé du processus de la combustion et l'estimation des masses enfermées dans la chambre de combustion d'un moteur à allumage commandé (Spark Ignited (SI) engine). Les principaux développements comportent des points suivants :

- L'impact flamme parois pendant la combustion : un nouveau modèle pour prendre en compte ce phénomène dans le cadre d'un modèle de combustion 0D à deux zones a été développé. Ce modèle permet de prendre en compte la géométrie de la chambre de combustion et la proportion de flamme que brûle proche des parois du cylindre. Plusieurs études ont montré qu'une grand proportion $(20 - 30\%)$ du mélange frais brûle dans ce mode de combustion [Poinsot & Veynante, 2001], [Bozza et al., 2005], ce qui montre l'importance de prendre en compte ce phénomène.

- L'estimation de la mass totale enfermée dans la chambre de combustion après la fermeture des soupapes est un phénomène très intéressant qui présente un challenge pour les chercheurs motoristes. Une estimation plus précise de la mass enfermée dans la chambre de combustion permet d'avoir un meilleur contrôle de l'injection du carburant et une amélioration dans le traitement des polluants.

- Le dernier point à traiter dans cette thèse est la commande d'un système d'injection "common rail". Ce point a pour but de compléter la modélisation de la combustion en ajoutant une thématique liée à l'injection, lequel est un paramètre crucial dans le processus de la combustion. L'objectif d'un système d'injection common rail est de contrôler l'avance de l'injection, la durée et la pression, de façon indépendent dans chaque cylindre, pour avoir un meilleur contrôle de la combustion, en dépendant des conditions d'opération. Cette injection permet de réguler le carburant en quantités

très petites, ce qu'aide à réduire la consommation, les émissions polluants, et aussi à améliorer la performance du moteur.

Remark 1.2.1. Les développements pour la commande common rail ont été faites pour des moteurs diesel Renault. Cependant même, il est possible d'appliquer les stratégies proposées pour les moteurs à allumage commande car l'architecture du système common rail dans le deux cas est très similaire.

1.3 Index du manuscrit

Ce manuscrit a été organisé de la façon suivante :

1.3.1 Chapitre 3: Modélisation moteur

Dans ce chapitre, une description détaillé d'un model thermodynamique 0D à deux zones et du phénomène de l'interaction de la flamme avec les parois sont présentées. Dans le modèle deux zones, le processus de combustion est représenté par un modèle de propagation de flamme : l'approche fractale. Le modèle d'interaction flamme-parois proposé dans cette thèse est développé comme un complément du model 0D deux zones et peut être inclus dans d'autres modèles de propagation de flamme, du fait qu'il est conçu comme une fonction adimensionnelle que multiplie le taux de combustion.

Cette étape de modélisation aide à mieux appréhende les bases de la modélisation 0D thermodynamique, ce qui permet de construire un modèle plus simple pour faire des estimateurs de mases enfermées qui sont présentés dans le Chapitre 4.

1.3.2 Chapitre 4: Observateurs pour l'estimation des masses enfermées dans la chambre de combustion d'un moteur à allumage commandé

Ce chapitre est focalisé sur la synthèse de trois observateurs : un observateur pour l'estimation des pertes aux parois et deux autres observateurs pour l'estimation des masses enfermées dans la chambre de combustion d'un moteur à allumage commandé.

Des lois empiriques très complexes ont été proposées pour l'estimation des pertes aux parois. Dans le but de proposer un alternative pour modéliser ce phénomène, un observateur "sliding mode" à été synthétisé pour estimer l'enthalpie des pertes aux parois pendant les phases de compression et combustion du cycle moteur.

Pour l'estimation des masses dans la chambre de combustion, deux observateurs non-linéaires ont été synthétisés : un observateur à grand gain classique et un observateur à grand gain étendu aux systèmes à paramètres variantes (LPV). Les observateurs utilisent la pression cylindre mesurée pendant la compression et la combustion pour estimer les masses. Pour construire les observateurs, un modèle 0D à une zone est utilisé. Ce modèle est basé sur le modèle en deux zones présenté dans le chapitre 3, où le schéma de combustion à été remplacé par un modèle de combustion paramétrique.

1.3.3 Chapitre 5: Commande du système d'injection common rail en utilisant la transformation input-state linéarisation et une stratégie de contrôle optimal avec action intégral.

Ce chapitre est focalisé sur le développement d'un contrôleur pour le système d'injection common rail. Le but est de synthétiser un contrôleur pour un moteur à allumage commandé, lequel est basé sur les mêmes principes physiques qu'un système d'injection common rail pour un moteur diesel. En première lieu, une transformation input state linéarisation du model du système common rail est réalisée, dans le but de s'affranchir des fortes non-linéarités du modèle et de construire un modèle linéaire virtuel. En utilisant ce modèle virtuel, deux stratégies de contrôle linéaire ont été implémentées pour réguler la pression du rail : un régulateur linéaire quadratique optimale LQR avec action intégrale et un régulateur optimal quadratique LQR optimale avec tracking (feedforward) et action intégral. Les deux stratégies sont basées sur la méthode du contrôle basé sur le modèle et sont développées pour l'architecture des moteurs diesel K9 utilisés chez Renault.

Le schéma synoptique dans la Figure 1.1 présente un résumé des principaux thématiques traitées dans cette thèse, et la liaison entre eux. Sur le schéma, le titre des développements principaux sont présentés. Ce diagramme sert de plan et guide des chapitres du manuscrit, pour faciliter la compréhension et le suivi de ce projet de thèse.

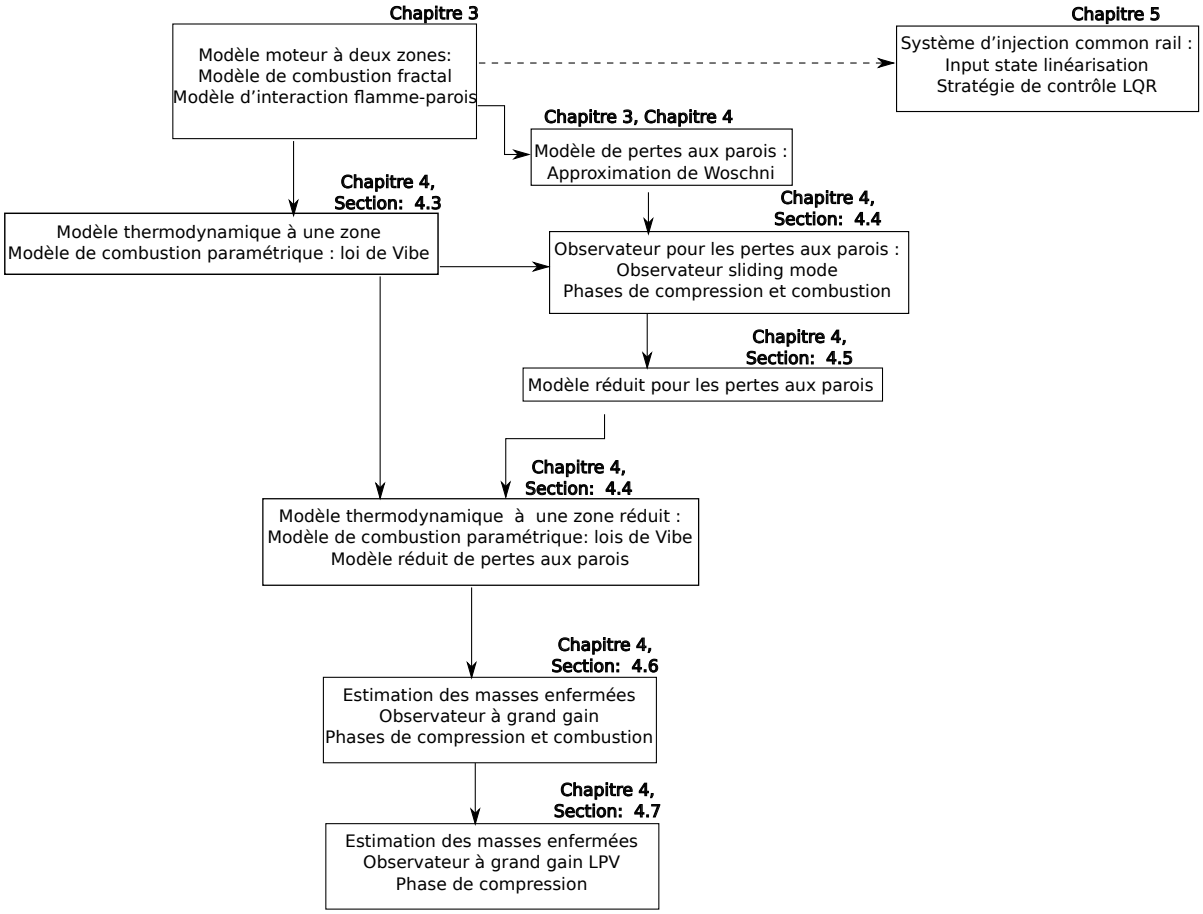

Figure 1.1: Diagramme: résumé des développements de ce projet de thèse.

1.4 Publications

Les contributions principales de cette thèse ont fait l'objet des publications suivantes:

- M. Rivas, P. Higelin, C. Caillol, O. Sename, E.Witrant and V.Talon. Validation and Application of a New 0D Flame/Wall Interaction Sub Model for SI Engines. SAE 2011-01-1893. 2011. SAE Technical Paper included in SAE International Journal of Engines - Electronic Version, Power trains and fuels proceedings, JSAE Kyoto Conference.

- M. Rivas, O. Sename, E. Witrant, P. Higelin and C. Caillol. Model Based High Gain Non Linear Observer for Enclosed Mass Estimation in a Spark Ignited Engine. IEEE 2012. IEEE American control conference, Montreal.

- M. Rivas, O. Sename, E. Witrant, P. Higelin and C. Caillol. Model Based High Gain Non Linear Observer for Enclosed Mass Estimation in a Spark Ignited Engine. IFAC ECOSM 2012, Rueil Malmaison.

- M. Rivas, O. Sename, E. Witrant, P. Higelin and C. Caillol. Energy Wall Losses Estimation of a Gasoline Engine Using a Sliding Mode Observer. SAE 2012-01-0674. 2012. SAE Technical Paper included in Modeling of SI and Diesel Engines, 2012.

Chapter 2

Context and stakes of the study

This thesis has been developed thanks to a *Conventions Industrielles de Formation par la Recherche* (CIFRE)[1] agreement, that is a program of the french agency *Association nationale de la recherche et de la technologie* (ANRT)[2], coordinated by the *Centre nationale de la recherche scientifique* (CNRS) [3]. The CIFRE program grants the french companies who engage a PhD student to carry out a research project of the company within a public research lab. For this thesis, a CIFRE agreement has been accorded between the automobile company Renault France and the scientific laboratories Gipsa Lab in Grenoble and PRISME in Orléans.

- The Renault Group, which is represented in over 118 countries, designs, manufactures and sells vehicles under three brands: Renault, Dacia and Renault Samsung Motors.
- Gipsa-lab is a multidisciplinary research lab created as a group between the CNRS, the *Institute Polytechnique de Grenoble* (INP) [4], the Joseph Fourier university and the Stendhal University. It also collaborates with the *Institut nationale de recherche en informatique et en automatique* (INRIA)[5], the Grenoble Observatory and Pierre Mendès University. Gipsa-lab developments are merged especially on the automating control, signal, images, voice and cognition fields.
- PRISME is a research lab that belongs to the Orléans University in France. The research activities of this lab are focused on fluids and aerodynamics systems, energy, combustion, engines, material mechanics, civil engineering, nano materials, robotics, signals treatment and automation.

[1] Industrial Agreement for the Research and the Education
[2] Education and Research French Agency
[3] French National Center of Scientific Research
[4] Grenoble Polytechnic Institute
[5] National Institute for Research in Computer Science and Control

2.1 Context of the study : modeling, observation and control development of the Spark Ignited Engine

Transport plays a fundamental role in the lives of societies and individuals: how people interact, work, play, organize production, develop cities, and get access to services, amenities and goods, are inextricably linked with the development of mobility. The private transport powered by internal combustion engines has increased dramatically in the last decades; vehicles are expected to become accessible to everybody, safer and more performing, besides the fact that they have to be driven more frequently. However these expectations, many of the ensuing consequences of the vehicles developments are not taken into account: increased fuel consumption, greater emissions of air pollutants and greater exposure of people to hazardous pollution that causes serious health problems [Krzyzanowski et al., 2005]. Within Europe, a significant amount of studies have reported air emissions data directly linked to the vehicles use [Adams et al., 2009], [International Energy Agency, 2011].

The persistence of air quality problems and health problems related to transporting have triggered several policy responses which are targeted to the emissions of light-duty vehicles [Weiss et al., 2011]. Such policies are becoming more and more stringent worldwide:

- the introduction of more stringent emission limits for light-duty vehicles with Euro 5b normative in 2011 and Euro 6 normative in 2014 [Summaries of EU legislation, 2009],
- the replacement of the currently applied New European Driving Cycle (NEDC) by a world-wide harmonized driving cycle in 2014 [Weiss et al., 2011],
- and potentially, the implementation of supplementary measures for verifying vehicles emissions outside with a single standardized driving cycle in 2014.

Table 2.1 shows a summary of the main regulations and the evolution of the emissions legislation in the European community from its apparition.

Another stringent issue on the vehicle development is the limitation of fossil fuel. Given that the consumption of petroleum represents 35% of world primary energy use, with natural gas and coal making up 24% and 28% respectively, it is an understatement to say that the world economy depends critically on these non-renewable resources. Since oil, natural gas and coal are finite natural resources, it is clear that at some point in time, production will reach a maximum and begin to decline [Brecha, 2008].

The energetic issues, the limitation of fuel, the health, the environment together with the pollutant emissions normative are main issues at international level, especially in the

Stage	Date	CO	HC	HC+NOx	NOx	PM	PN
Euro 1	1992.07	2.72 (3.16)	-	0.97 (1.13)	-	-	-
Euro 2	1996.01	2.2	-	0.5	-	-	-
Euro 3	2000.01	2.30	0.20	-	0.15	-	-
Euro 4	2005.01	1	0.10	-	0.08	-	-
Euro 5	2011.09[b]	1	0.10[a]	-	0.06	0.005[b,fc]	-
Euro 6	2014.09	1	0.10[d]	-	0.06	0.005[e,f]	6.0×10^{11}[e,g]

* Vehicles designed and constructed for the carriage of passengers and comprising no more than eight seats in addition to the driver's seat. At the Euro 1-4 stages, passenger vehicles $> 2500\ kg$ were type approved as Category $N1$ vehicles.
Category $N1$: Vehicles designed and constructed for the carriage of goods and having a maximum mass not exceeding 3.5 tons.
a. until 1999.09.30 (after that date DI engines must meet the IDI limits)
b. 2011.01 for all models
c. 2013.01 for all models
d. and NMHC = 0.068 g/km
e. applicable only to vehicles using DI engines
f. 0.0045 g/km using the PMP measurement procedure
g. $6.0 \times 10^{12}, \quad 1/km$ within first three years from Euro 6 effective dates

Table 2.1: EU Emission Standards for Passenger Cars (Category M1*).

automobile and the transportation field. Those facts push the car makers to develop new technologies to increase the fuel economy and decrease the emissions, while maintaining or improving the engine's performance. Several new technologies and the inclusion of new devices in the vehicles, have resulted as the solutions to accomplish these goals, showing that increasing the internal combustion engine performance helps to enhance the engine efficiency.

Because of the complexity of the new devices and technologies developed in the vehicle to overcome the current requirements on pollutant emissions, there is a strong demand to explore new modeling and control concepts capable of meeting the stringent emission standards, maintaining the engine performance. A very spread strategy adopted to overcome these considerations is the referred to as engine model based control. In such scheme, phenomenological models based on the physics of the different elements that constitutes the vehicle are developed to represent the physical behavior of the vehicle. This approach allows the test of new concepts and the simulation of the physical processes, the interactions and the behavior of the elements composing the vehicle, through simulation tests only. The experimental validation is used at the final stages of the design procedures.

Today, the research and development of the engine model based control is established in zero dimensional-one dimensional (0D-1D) engine models. In a $0D$ model only the variations in time of the variables involved in the model are taking into account, without spatial references. In the $1D$ model, the element of time is taken into account together with a spatial dimension (i.e the flow speed in a pipe variation with respect to the time and the pipe length). Such models allow the development and validation of the engine control laws. Adopting 0D-1D model based control strategies has many advantages, it overcomes the problems found when using data-maps based control, which are only valid on the engine operating points for which they were developed, and then introduce errors under transient conditions. Developing physical models, taking into account the goals of pollution and emissions standards and the engine performance, has a direct impact on the engine control performance and on the research and development costs. Besides, it reduces the development time allowing the use of experimental tests only as a final validation tool.

2.2 Objective of the study

The development of the engine control is crucial in order to reduce the pollutant emission and the fuel consumption. In the case of the combustion process, most of the current modeling strategies in the automobile industry are carried through empirical models, where the physical processes are considered as "black boxes" and are not explicitly described: a direct relation between the inputs and outputs is obtained from measurement data. Correlations and look-up tables are examples of empirical models. These models are very spread in the industry because they are very simple to implement, however, they cannot be used outside of the operating range described by the reference measurement data. It is a fact that many of the problems of current control combustion models originate from the lack of a physical basis. This situation pushes the researchers to look for more physical and predictable combustion modeling schemes, which can be used as reference to synthesize control and estimation strategies for further issues as the fill-in modeling and the enclosed mass estimation, among others.

For the specific case of the internal combustion engine modeling, it is a fact that the designers face a complex system. The engine behavior includes phenomena related to thermodynamics, chemistry, mechanics, fluid mechanics and electrical fields. On the other hand, 3D engine models are too complex to be used in control law design, they are better adapted to the conceptualization and learning process of the engine physics. For this reason it is better to develop 0D dynamical models for control purposes.

The development of 0D engine models has been improved over the years and today, physical 0D models can be used at all stages of the engine development: from concept design to powertrain control development and calibration. In the case of the thermody-

namical engine model, most of the existent modeling approaches are generally based on empirical models which in many cases are not predictable enough, especially in the in-cylinder and combustion phenomena. Besides to these modeling difficulties, the absence of sensors also represents a concrete obstacle related to the engine control. Because of the viability and the cost, the engine cannot be equipped with all the needed sensors for control and supervision. As the functionality of the engine must be guaranteed, the modeling approaches and the use of observation and estimation strategies have proved to be a suitable solution to overcome the lack of sensors.

This thesis is focused on the modeling of a more detailed description of the 0D combustion process and the estimation of the enclosed mass in the combustion chamber for a Spark Ignited (SI) engine. The main developments will involve the improvement of the following points:

- The combustion process is frequently modeled as a growing flame inside of the combustion chamber. Many 0D thermodynamical engine models mostly focus on the laminar characteristics of such a free developing flame, but they lack of a suitable approximation of the combustion when the flame reaches the cylinder walls. Such a flame-wall interaction is an essential issue in accurately modeling the combustion process. Some studies have shown that a great portion $(20 - 30\%)$ of the unburned mixture actually burns in this particular combustion mode [Poinsot & Veynante, 2001], [Bozza et al., 2005].

- The model based observation and control strategies allow the estimation of the air and fuel introduced into the cylinder to be improved. The estimation of the total mass enclosed in the combustion chamber, which corresponds to the air plus the fuel and the recycled gases in the combustion chamber, after the inlet valve closure (IVC), is an interesting and challenging task for the engine control community. An accurate estimation of the cylinder enclosed mass allows a better control of the associated fuel injection and a better treatment of the pollutants residuals. The estimation of this parameter is crucial for the good progress of the combustion, which helps for an effective reduction of the pollutant emissions.

- A last point considered in this thesis is related to the control of the common rail injection system. This issue intends to complete the combustion modeling introducing a synthesis for the injection control, which is a crucial parameter in the combustion process. The goal of a common rail injection system is to control the injection advance, duration and pressure, individually cylinder by cylinder, in order to manage accurately the combustion depending on the engine operating conditions. This injection control allows the injection to be regulated in small quantities, helping to decrease the pollutant emissions and also increasing the engine performance.

Remark 2.2.1. The common rail developments have been designed for a Renault diesel engine. However, it is possible to apply them to the SI engine because the common rail architecture on both cases is very similar.

2.3 Manuscript outline

This manuscript has been organized as follows:

2.3.1 Chapter 3: Engine modeling

In this chapter, a deep description of a 0D two zones thermodynamical model and the flame-wall interaction phenomena are presented. In the two zones engine model, the combustion process is represented with the flame propagation model: a fractal approach. The flame-wall interaction model proposed in this thesis is developed as a complement of the 0D two zones thermodynamical model and can be included in several flame propagation combustion modeling schemes since it is conceived as a dimensionless function multiplying the burning rate equation.

This modeling stage helps to apprehend the basis of the 0D thermodynamical engine modeling in order to build a simpler modeling scheme for the enclosed mass observer synthesis presented in Chapter 4.

2.3.2 Chapter 4: Observers for enclosed mass estimation in the combustion chamber for a SI engine

This chapter is focused on the synthesis of three observers: one for the heat wall losses estimation and two observers to estimate the enclosed mass in the combustion chamber of a Spark Ignited (SI) engine.

Very complex empirical laws have been proposed to model the heat wall losses. In order to propose an alternative to model such phenomenon, a sliding mode observer is designed to estimate the heat wall losses enthalpy during the compression and combustion strokes.

For the enclosed mass estimation, two nonlinear observers are synthesized: a classical nonlinear high gain observer and an extended linear parameter varying (LPV) high gain observer are proposed. The observers use the cylinder pressure measurement during the compression and combustion strokes to estimate the enclosed mass. In order to build the observers, a 0D one zone engine model is used. Such model is based on the two zones engine model presented in Chapter 3, where the combustion scheme has been changed

for a simpler parametric combustion model.

2.3.3 Chapter 5: Common rail injection system controller using input-state linearization and optimal control strategy with integral action

This chapter is focused on the development of a common rail controller. The aim is to synthesize a common rail control scheme for gasoline engines, which is based on the same physical principles of a diesel engine common rail system. First, an input state linearization of the common rail model is performed, in order to overcome the strong nonlinearities and build a virtual linear model. Using the virtual model, two linear control strategies are implemented to regulate the common rail pressure: an optimal linear quadratic regulator LQR with integral action and an optimal LQR tracking (feed-forward) with integral action strategy. Both strategies are merged in the model based control method and are based in the architecture of the current K9 diesel engine used in Renault.

The flow chart in Figure 2.1 presents a summary of the main issues treated in this thesis and the link between them. In the chart, the title of the main developments presented in this manuscript are found. This chart serves as a map of the manuscript chapters, to facilitate the understanding and the following of this thesis project.

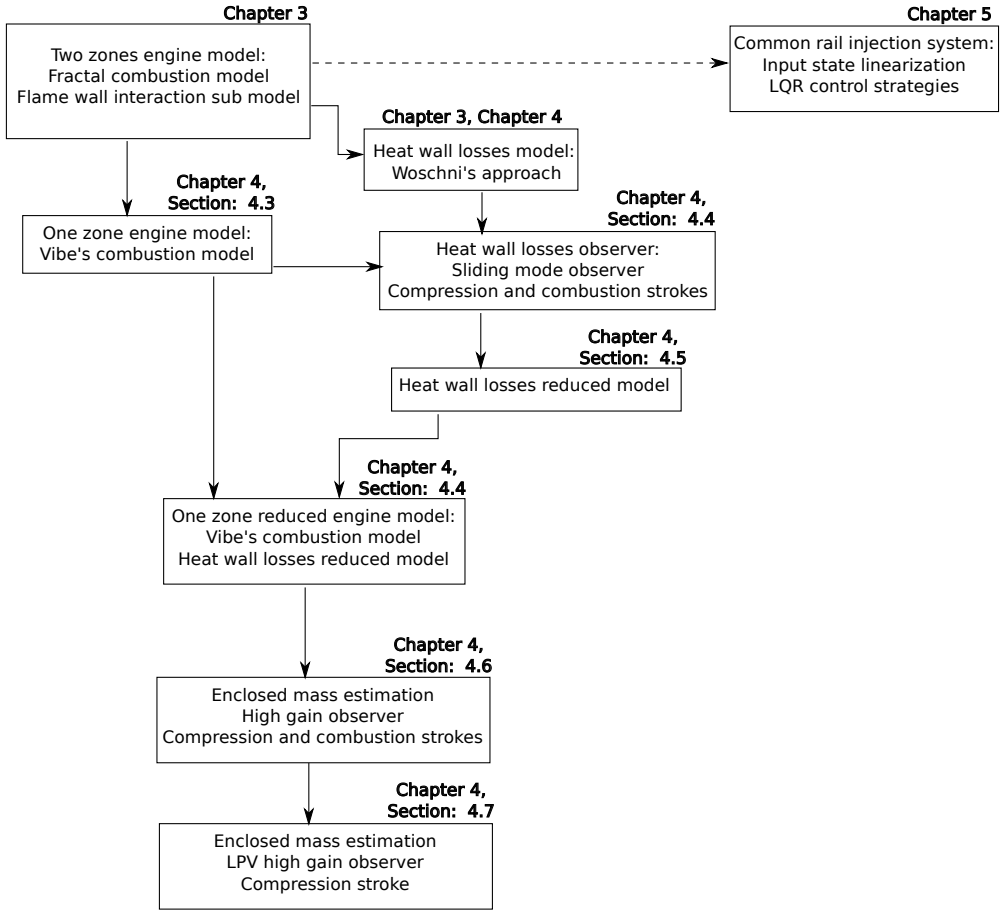

Figure 2.1: Flow chart: summary of the developments of this thesis project.

2.4 Publications

The main contributions of this thesis are the principal subject of the following publications:

- M. Rivas, P. Higelin, C. Caillol, O. Sename, E.Witrant and V.Talon. Validation and Application of a New 0D Flame/Wall Interaction Sub Model for SI Engines. SAE 2011-01-1893. 2011. SAE Technical Paper included in SAE International Journal of Engines - Electronic Version, Power trains and fuels proceedings, JSAE Kyoto Conference.
- M. Rivas, O. Sename, E. Witrant, P. Higelin and C. Caillol. Model Based High Gain Non Linear Observer for Enclosed Mass Estimation in a Spark Ignited Engine. IEEE 2012. IEEE American control conference, Montreal.
- M. Rivas, O. Sename, E. Witrant, P. Higelin and C. Caillol. Model Based High Gain Non Linear Observer for Enclosed Mass Estimation in a Spark Ignited Engine. IFAC ECOSM 2012, Rueil Malmaison.

- M. Rivas, O. Sename, E. Witrant, P. Higelin and C. Caillol. Energy Wall Losses Estimation of a Gasoline Engine Using a Sliding Mode Observer. SAE 2012-01-0674. 2012. SAE Technical Paper included in Modeling of SI and Diesel Engines, 2012.

Chapter 3

Engine modeling

The research and the technological development of modern car engines have been focused on the design of new modes of combustion and/or the inclusion of controlled mechanical devices such as turbochargers, variable valve timing (VVT) and exhaust gas recirculation (EGR). These new developments improve dramatically the engines performance, but it also results in a less predictable combustion, which might alter the proper functionality of the exhaust treatment systems. In order to maintain the performance of the engine, a more accurate engine modeling is essential.

The engine modeling is a multidisciplinary subject that involves thermodynamics, fluid mechanics, chemical reactions, mathematical analysis, turbulence, heat transfer, combustion and numerical methods. Different levels of modeling have been used to represent the behavior of the engine. Such models go from basic air standard engine cycles to more complex 3D models including turbulence, chemical reactions, spray dynamics, mass transport delay, engine geometry, etc. The engine modeling is frequently classified into categories: 0D/1D one zone/two zones model (phenomenological thermodynamical models), quasi-dimensional multizone models and multidimensional models (3D models).

In 0D/1D models, the engine is usually represented as a network of volumes (the intake and the exhaust manifolds), which are interconnected among them with elements that represent different parts of the engine: the valves, the cylinders, the turbocharger, etc. Depending on the application field, the elements in the engine are detailed differently. For instance, in air path models, it is common to give more details to the engine valves, the turbocharger (for turbocharged engines) and pipes than to other elements. Contrary, in combustion models, the phenomena in the combustion chamber, more specifically related to the combustion process are detailed. These models have a high computational efficiency and a good degree of predictability of the engine performance, and are then very useful for control applications and parametric studies.

On the other hand, 3D computational fluid dynamics (CFD) codes are a very useful to

explore and better understand the physical processes occurring inside the engine in order to design new engine concepts. The principal idea of these models consist on describing locally the parameters as fuel/air (F/A) equivalence ratio in fresh gases, composition (including residual gases) and temperature, transport delay in air path models, among others. Besides, this type of modeling helps to relate the global engine parameters to different engine geometrical data. This deep modeling scheme helps to improve the learning of the engine physical processes, which allows a better description of the physical phenomena to then build more simpler modeling schemes. The computational resources required for the 3D modeling is evidently high. These models are therefore not applicable for the engine controller development process.

Remark 3.0.1. As the developments proposed in this thesis are related to the control and observation of different phenomena in the combustion chamber, the modeling scheme used for this purpose is merged in the framework of the 0D SI engine modeling.

0D engine modeling The 0D combustion modeling relies on a basic understanding of the physics involved in the combustion, trying to capture the main features of the process. By including the description of the most important aspects, the 0D thermodynamical combustion models achieve a good performance and are capable of predicting engine performance and fuel economy accurately with few computational resources.

In the 0D engine combustion modeling, the combustion process is frequently modeled depending on the application field and different levels of complexity are found (in Section 3.4, a review of some combustion modeling schemes is presented):

- *Parametric* combustion models, which intend to describe the rate of heat release of the fuel using several input parameters, are very spread in applications related to control, indirect identification and optimization processes. These methods have the advantage of consuming very few computational resources and its complexity is low when compared to other 0D combustion models. However, the predictability of these models is very low, as they depend on several input parameters which sometimes are unknown and also because these models are usually calibrated exclusively to a specific engine under certain operating conditions.
- Semi-empirical models, which allows an extrapolation outside of the operating range for which they are originally developed, through a parametric calibration. These models are very useful to represent some phenomena related to the combustion process which are hard to define through more simple physical approaches: the heat wall losses, the turbulence phenomena, the thermodynamical constants, among others. Usually, these models are built using the information acquired form more complex 3D computations or experimental tests. These models have some predictive capabilities, regarding the heat release rate and emissions formation, but

need a rigorous process of calibration and experimental test to define the range of validity.

- 0D thermodynamical models, which describe the physical phenomena occurring during the combustion using the physical thermodynamical principles. In these models, the combustion chamber might be divided in zones, where the thermodynamical characteristics of the gases, the heat release and the emissions formation are predicted for each zone. The number of considered zones depends on the chosen approach and can range between one or two and as many as several hundreds. The computational effort increases with the applied number of zones. This kind of models are based on the thermodynamical principles and are composed by some dynamical equations usually related to the heat exchanges, and several submodels representing the multiple phenomena related to the combustion process like the turbulence, the injection and the flame-wall interaction among others. These models have the advantage to consume few computational resources (one zone up to three zones schemes), thus are useful for parametric studies and some control applications.

- 0D models based on chemical reactions are mainly used to predict pollutants formations, models of CO and NO creation based on chemical reaction approaches are suitable to predict these phenomena. Similarly, phenomena as the *knock* and the cyclic variation might be explained from chemical approaches.

The choice of an engine combustion model in the framework of the 0D approach, is faced to unavoidable trade-offs: computational effort, predictability, physical phenomenon representation, application field and robustness, among others.

There are many issues and phenomena that are still not well represented in the current combustion models: the knock, the cyclic irregularities, the initiation phases, the injection, the ignition and the flame-wall interaction are some of a non-exhaustive list of issues that need a modeling improvement. In this thesis, the aim is to contribute to the development of a 0D gasoline engine model that leads to the design of control and estimation strategies based on more physical and predictive schemes, in order to achieve the restraining current normative with respect to pollution and emissions from vehicles. Taking into account these goals, it has been chosen to focus the modeling stage of this project to a 0D two zones thermodynamical representation of the combustion process. This modeling scheme is used to obtain valuable information with respect to the pressure, temperature and evolution of the gases in the combustion chamber, which helps to have a better control of the combustion process in the engine which allows for a better treatment of the pollutant residuals and a diminution of the gasses emissions.

In the 0D two zones thermodynamical model, the combustion process is modeled as a growing flame of burning gases propagating inside the combustion chamber. Many of

this type of combustion models mostly focus on the laminar characteristics of such a free developing flame, but they lack of a suitable approximation of the combustion when the flame reaches the cylinder walls. As said before, there are studies that have shown that a great portion (20% - 30%) of the unburned mixture in the combustion chamber actually burns close to the cylinder wall [Poinsot & Veynante, 2001], [Bozza et al., 2005], thus the flame-wall interaction is a very important issue that cannot be neglected in order to obtain realistic engine cycle simulations. With the aim to contribute to the engine modeling development, a new flame-wall interaction model is proposed in this thesis and is the principal contribution presented in this chapter.

Chapter structure This chapter is introduced with a basic explanation of the functionality of a four strokes Spark Ignited (SI) engine, where the main aspects as the geometry and operating mode are presented. Later, a 0D thermodynamical two zones model is detailed, where main topics as the combustion, the turbulence model and the flame-wall interaction phenomena are treated. The proposal of a new model that takes into account the flame-wall interaction is also described. Such model is named *local approach* by the author. The flame-wall interaction model is included in the 0D two zones model and can be included in several combustion schemes, since it is conceived as a dimensionless function multiplying the burning rate equation. The *local approach* that takes into account the impact of the cylinder walls constitutes the main result presented in this chapter. Comparison with experimental data are presented in order to validate the proposed model. Further validations for changes in the spark plug position are also presented.

The main contributions presented in this chapter are the principal subjects of the following publication:

- SAE Technical Paper included in SAE International Journal of Engines - Electronic Version, Power trains and fuels proceedings, JSAE Kyoto Conference. M. Rivas, P. Higelin, C. Caillol, O. Sename, E.Witrant and V.Talon. Validation and Application of a New 0D Flame/Wall Interaction Sub Model for SI Engines. SAE 2011-01-1893. 2011.

3.1 Chapter nomenclature

Unless it is specified, all variables are in SI Metric Units.

Variables

Two zones engine model variables: the sub index u means unburned gases, the sub index b means burned gases:

A_f	Laminar flame surface
$A_{w_{u,b}}$	Heat transfer wall area
$c_{p_{u,b}}$	Specific heat at constant pressure
$c_{v_{u,b}}$	Specific heat at constant volume
F_{ext}	Extinction function
$h_{u,b}$	Enthalpy flow
$h_{c_{u,b}}$	Heat transfer coefficient for wall losses
H_p	Piston height
m	Total mass in the combustion chamber
m_b	Burned mass
m_f	Fuel mass
m_u	Fresh or unburned mass
p	Pressure
$\delta Q_{th_{u,b}}$	Heat wall losses
$r_{u,b}$	Specific gases constant
R_f	Flame radius
S_t	Turbulent flame speed
S_l	Laminar flame speed
$T_{u,b}$	Temperature
$u_{u,b}$	Internal energy
$U_{u,b}$	Energy
V	Cylinder volume covered by the piston
$V_{u,b}$	Gas volume

$Y_{u,b}$	Gases mass fraction
Ψ	Flame/wall interaction model
$\rho_{u,b}$	Gas density
Ξ	Wrinkling coefficient
$\gamma_{u,b}$	Specific heat ratio
θ	Crank angle in rad

Turbulence model variables:

l_i	Integral scale, (the sub index i means integral)
l_k	Kolmogorov scale, (the sub index k means Kolmogorov)
u'	Turbulence intensity

Constant parameters

H_{cyl}	Cylinder geometric height
C_l	Calibration constant
N	Engine speed (rpm)
R_{cyl}	Cylinder geometric radius
r_v	Volumetric ratio
V_{cyl}	Cylinder geometric volume
X_{egr}	Exhaust gas recirculation fraction
ϕ	equivalence ratio
ω	engine speed (rad/s)

Acronyms

CAD	Crank angle degree
IMEP	Mean effective pressure
EVC	Exhaust valve closure
EVO	Exhaust valve opening
EVO_d	Exhaust valve opening delay
IVC	Inlet valve closure
IVC_d	Inlet valve closure delay

IVO	Inlet valve opening
IT	Ignition timing
rpm	Revolutions per minute
SI	Spark ignited engine

3.2 Four strokes SI engine: operating cycle

The purpose of Internal Combustion (IC) engines is to produce mechanical power from the heat generated during the chemical reaction between a fuel (i.e coil, gasoline) and an oxydant (i.e oxygen). The use of internal combustion engines was commercially spread by the late 19th century. Today, the automotive industry mainly proposes two types of IC engines: the Spark Ignited SI engines or also referred to as gasoline engine and the Compression Ignited CI engine, also referred as diesel engine. Among them, the four-strokes engine is probably the most common one. The developments of this thesis are focused on the four-strokes SI engine type.

The four stroke engine is characterized by four reciprocating movements of a piston in a cylinder or combustion chamber. Those reciprocating linear movements of the piston are transmitted through the crankshaft into rotation, which is characterized by the crank angle position degree θ and goes from $0 - 720$ deg for an engine cycle. Each stroke takes 180 deg. Those movements or phases are the intake stroke (From 0 deg to 180 deg), the compression stroke (From 0 deg to 360 deg), the combustion or power stroke (From 360 deg to 540 deg) and the exhaust stroke (From 540 deg to 720 deg). Besides, the Top Dead Center (TDC) position is defined, that is the position of the piston in which it is farthest from the crankshaft, this parameter usually is defined at 0 deg and 360 deg. Even though this convention, it is a fact that when including Variable Valve Timing (VVT) and advanced Ignition Timing (IT) in the engine, the piston position and the actual position of the valves and the IT event do not coincide exactly with the four strokes of 180 deg, at the positions mentioned before: i.e the intake valve does not close at 180 deg but at 210 deg. For this reason, it is also common to characterize the engine strokes by the valves positions and the IT event as presented in Table 3.1.

Remark 3.2.1. The convention presented in Table 3.1 is preferred in this thesis because it describes better the physical meaning of each of the engine strokes, thus in this manuscript, the engine strokes are established according to this rule.

Remark 3.2.2. As the VVT and the advanced IT techniques are used, the opening and closure of the valves is advanced or delayed from a reference position depending on the engine operation conditions, similarly, the IT is advanced or delayed. The reference position for the VVT or the IT usually coincides with the piston reference position (each

Engine stroke	Crank angle position [deg]
Intake	From Inlet Valve Opening (IVO) angle to Inlet Valve Closure (IVC) angle ($\theta_{IVO} - \theta_{IVC}$)
Compression	From IVC to IT ($\theta_{IVC} - \theta_{IT}$)
Combustion or power	From IT to Exhaust Valve Opening (EVO) ($\theta_{IT} - \theta_{EVO}$)
Exhaust	From EVO to Exhaust Valve Closure (EVC) ($\theta_{EVO} - \theta_{EVC}$)

Table 3.1: Valves position and TI with respect to the crank angle degree.

180 degrees) but it might be different depending on the convention used for the engine design. Refer to Appendix A.1 for a summary of the VVT technique.

Remark 3.2.3. Notice that the IT makes reference to both, the ignition event and to the crank angle degrees that are advanced or delayed from the TDC to start the ignition: the ignition starts at $\theta_{IT} = 360 - IT\ CAD$.

The combustion chamber is assumed to have an intake port that is the intake valve and an exhaust port that is the exhaust valve. Upstream the combustion chamber is located the intake manifold. This element of the engine supplies the fuel/air mixture through the intake valve to the cylinders. Downstream the combustion chamber is located the exhaust manifold. This is the part of the engine that evacuates the burned gases from the combustion chamber to the exhaust path through the exhaust valve. In this thesis, the combustion chamber and the piston are assumed to be cylindrical bodies. The combustion chamber or cylinder is characterized geometrically by its radius R_{cyl} and height H_{cyl}. The piston head is assumed to have a disc shape, of the same radius of the combustion chamber. The spark plug is centered in the combustion chamber head unless a different location is pointed. Figure 3.1 shows a scheme of the combustion chamber geometry.

There are two important variables related to the cylinder geometry: The piston height $H_p(t)$ and the cylinder volume $V(t)$. Both variables depend on the combustion chamber geometry, piston kinematics and crank angle. $H_p(t)$ represents the dynamic length swept by the piston movement, it varies from 0 up to the cylinder geometrical height H_{cyl}. The cylinder volume $V(t)$ is the space available in the combustion chamber with respect to the piston movement, it varies from 0 up to the cylinder geometrical volume $2\pi R_{cyl} H_{cyl}$. Other important parameter in the cylinder is the dead volume V_{dead}, that is the volume that is left in the combustion chamber when the piston is at TDC. Indifferently, $V(t)$ is referred to as the cylinder volume or the combustion chamber volume.

Figure 3.2 shows a scheme of the four strokes operation (for an engine without VVT or variable IT). During the intake stroke, the piston starts at the top, the intake valve opens, and the piston moves down to let the engine take in a mixture of air and fuel,

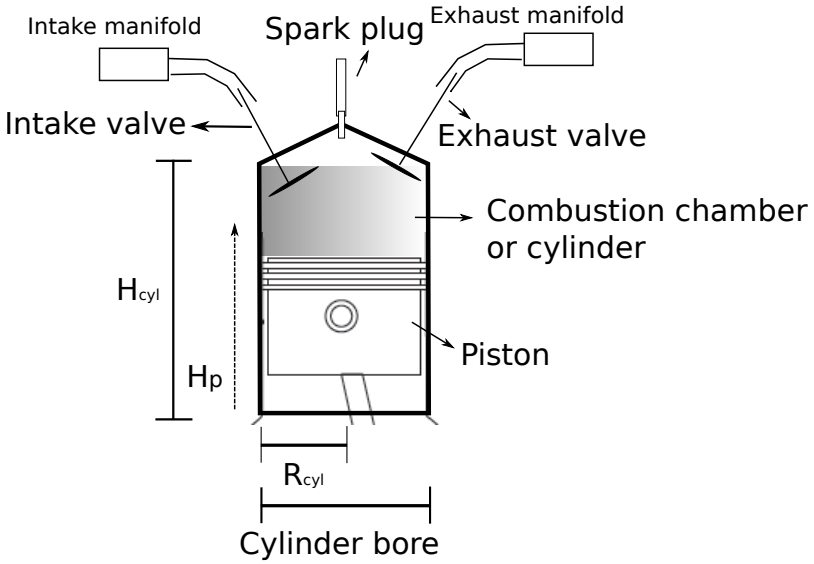

Figure 3.1: SI engine: Four strokes operation

or only air in direct injection engines. In the compression stroke, the piston moves back up to compress the air/fuel mixture. When the piston is at the top dead center (TDC), the spark plug emits a spark to ignite the air/fuel mixture allowing the combustion to start. The power generated by the combustion drives the piston down. The exhaust valve opens and the piston is moved up to exhaust the burned gases from the cylinder to the exhaust pipe. Modeling each of these processes gives a simulation of the complete engine cycle. In an engine with VVT or variable IT, the piston movements are exactly as it has been explained in the figure, but the valves opening and closure and the ignition is delayed with respect to the piston position.

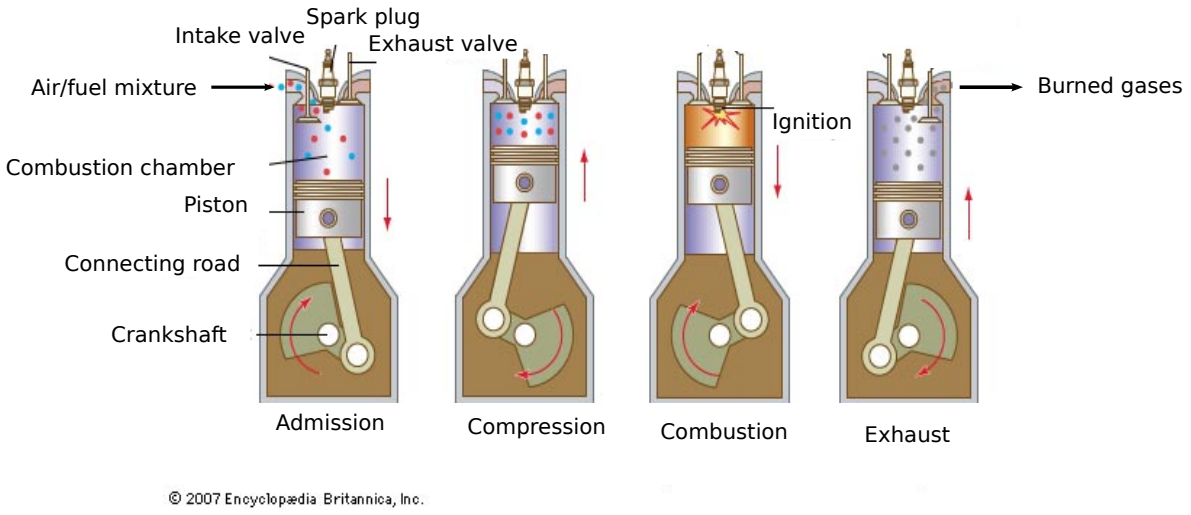

Figure 3.2: SI engine: Four strokes operation

In the next section, a 0D two zones thermodynamical engine model is presented, where the different processes during the engine cycle are presented. As it was mentioned in the thesis objectives in Section 2.2, the modeling part of this study is focused in the flame-wall interaction during the combustion process, thus in the next sections, the compression and combustion strokes are modeled in more detail than the intake and the exhaust processes.

3.3 Two zones 0D thermodynamical engine modeling

The modeling of SI engines has progressed significantly since the thermodynamic analysis of the air standard Otto cycle and several combustion models have been proposed. A spread strategy to model the SI engine is the so called thermodynamical or phenomenological 0D modeling. In this strategy, the combustion chamber is chosen as the control volume and an energy balance during the engine cycle is performed, using the thermodynamical physical principles. Most of the thermodynamical properties of the process (i.e cylinder pressure, gases temperature) are averaged and there are no spatial references with respect to the cylinder geometry.

The phenomenological models might be described as multizone models. A common approach of this type of models is to consider one control volume that is the combustion chamber and two gases zones. During the combustion, the load in the control volume is divided into two zones with burned and unburned gases respectively and the heat release is described by the classical turbulent premixed flame propagation. Some of the first works published on this area are detailed in [Blumberg et al., 1980], [Mattavi et al., 1980] and [Heywood, 1980] among others. In those works the basic physical principles to model the engine are stated. More recent proposals are based on those works and have added new features concerning the thermodynamics properties, the pollutant treatment, the *knock* and the flame-wall interaction among a non-exhaustive list of subjects. Besides the thermodynamical model, a fill-in model that describes the composition and amount of the gases getting into the combustion chamber might be also included to complete the engine model. The fill-in model used in this thesis is described in the Appendix A.2, where a brief summary of the fill-in modeling is presented.

The main assumptions in the SI engine that permits a representation of the combustion process with a two zones approximation [Heywood, 1988] are:

- The pressure is assumed to be uniform throughout the cylinder load;
- the volume occupied by the reaction is small in comparison with the clearance volume, thus the flame is a thin reaction layer that becomes wrinkled as it develops.

Under these assumptions, the combustion chamber is generally divided into the burned and unburned zones separated by a flame front. Figure 3.3 presents a brief scheme of the combustion chamber and the two zones.

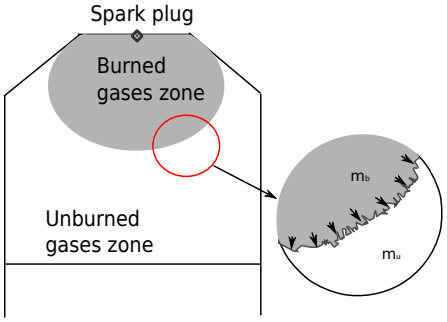

Figure 3.3: Two zones model scheme: the burned gases and the unburned gases zones separated by the reaction layer. $m_b = burned\ gases,\ m_u = \ unburned\ gases$

In this section, a two zone thermodynamical model based on the work of [Lavoie et al., 1970] that has been improved by [Bordet et al., 2010] is described. This model has been considered for the further developments presented in this chapter.

In the two zones combustion model, the first law of thermodynamics, equation of state and conservation of mass and volume are applied to the burned and unburned zones. Each zone is defined by its mean thermodynamic properties and the specific heat and specific enthalpy of each gas component change according to the JANAF thermodynamic properties table [Chase Jr et al., 1986]. Both zones are assumed to have the same uniform in-cylinder pressure. Each zone is considered as a separate open system. The mass flow rate into each zone is deduced from a balance equation corresponding to the mass transfer through the intake and the exhaust valves. The energy equation for each zone is written as:

$$dU_i(t) = \delta Q_{th_i}(t) - p(t)dV_i(t) + \left(\sum_j h_j(t)dm_j(t)\right)_i, \quad i = b, u \qquad (3.3.1)$$
$$j = int, \quad exh, \quad comb$$

where the subscript i denotes the zone: $i = b$ for burned gases or $i = u$ for unburned gases. The sub index j indicates intake ($j = int$), exhaust ($j = exh$) and combustion ($j = comb$), denoting the enthalpy flow source (int for the enthalpy of the gases passing through the intake port, exh for enthalpy of the gases passing through the exhaust port and $comb$ for enthalpy from the gases issued from the combustion process). $U_i(t)$ is the internal energy of the gas mixture in the zone i, $p(t)$ is the cylinder pressure, $V_i(t)$ is the gases volume of the zone i, $\delta Q_{th_i}(t)$ expresses the heat transfer of the cylinder contents to the cylinder walls, $p(t)dV_i(t)$ corresponds to the work delivered by the piston.

$dm_j(t)$ is the mass flow of each gas (admitted, exhausted, combustion) and $h_j(t)$ is the specific enthalpy. Thus the last term in the right side of (3.3.1) represents the enthalpy flowing into or out of the zone i.

The internal energy variation in Equation (3.3.1) can be written as:

$$dU_i(t) = u_i(t)dm_i(t) + m_i(t)\sum_j u_{i,j}(t)dY_{i,j}(t) + m_i(t)c_{v_i}(t)dT_i(t) \tag{3.3.2}$$

where $u_{i,j}(t)$ is the internal energy of the gas j in the zone i and $u_{i,j}(t)$ corresponds to the internal energy of the whole mixture j in the zone i, $Y_{i,j}(t)$ corresponds to the mass fraction of the gases j in the zone i. The cylinder charge is supposed to be premixed and homogeneous, which implies that $dY_{i_{int,exh}}(t) = 0$. $T_i(t)$ corresponds to the temperature of the mixture in the zone i.

The term $\delta Q_{th_i}(t)$ is replaced by $-\delta Q_{th_i}(t)$ because the heat transfers to the surroundings are considered as heat losses in the cylinder walls. Using (3.3.1) and (3.3.2) and following the procedure presented in the Appendix A.3, two ordinary differential equations are implemented as governing equations for the system temperatures dynamics $dT_i(t)$:

$$dT_u(t) = \frac{1}{m_u(t)c_{p_u}(t)}\left(V_u(t)dp(t) - \delta Q_{th_u}(t) - h_u(t)dm_u(t) + \left(\sum_j h_j(t)dm_j(t)\right)_u\right) \tag{3.3.3}$$

$$dT_b(t) = \frac{1}{m_b(t)c_{p_b}(t)}\left(V_b(t)dp(t) - \delta Q_{th_b}(t) - h_b(t)dm_b(t) + \left(\sum_j h_j(t)dm_j(t)\right)_b\right) \tag{3.3.4}$$

where $V_u(t)$ is the unburned gases volume, $V_b(t)$ is the burned gases volume.

The heat losses from the gases in the combustion chamber to the cylinder walls are given by:

$$\delta Q_{th_i}(t) = h_{c_i}(t)A_{w_i}(t)(T_i(t) - T_w), \quad i = b, u \tag{3.3.5}$$

where T_w is the cylinder walls temperature which is considered as a constant. $A_{w_i}(t)$ is the wall transfer area for each zone:

$$A_{w_i}(t) = \frac{\pi}{2}d^2 + 4\frac{V_i(t)}{d}, \quad i = b, u \tag{3.3.6}$$

where d is the constant cylinder bore. $h_{c_i}(t)$ is the heat transfer coefficient computed from Woschni's equation [Woschni, 1967]:

$$h_{c_i}(t) = \alpha_{th} d^{-0.2} p(t)^{0.8} T_i^{-0.53} \Big(C_1 V_p + C_2 \frac{V_{cyl} T_1}{p_1 V_1} (p(t) - p_0(t)) \Big) \tag{3.3.7}$$

where V_{cyl} is the engine volume, α_{th} and C_1 are calibration constants fixed by Woschni to 130 and 2.28 respectively and C_2 is a tuning parameter, p_1 and T_1 represent the known state of the working gas related to the instantaneous cylinder volume V_1, (e.g. at inlet valve closure IVC), and $p_0(t)$ is the pressure reference in the absence of combustion. (In this equation the pressures are in *bar*). The Woschni's law was initially proposed for diesel engines but it has been also used in gasoline engine applications.

The volume V_i in each zone is defined by the algebraic relation:

$$V_b(t) = \frac{m_b(t) r_b(t) T_b(t)}{m_b(t) r_b(t) T_b(t) + m_u(t) r_u(t) T_u(t)} V(t) \tag{3.3.8}$$

$$V_u(t) = V(t) - V_b(t) \tag{3.3.9}$$

where $r_{u,b}(t)$ is the mixture specific gas constant in the unburned or burned zones and $V(t)$ is the cylinder volume. The cylinder pressure dynamics is obtained from equations (3.3.3) and (3.3.4) following the procedure presented in the Appendix A.3. Thus the in-cylinder pressure dynamics $dp(t)$ is modeled as:

$$\begin{aligned} dp(t) = \frac{1}{\frac{V_u(t)}{\gamma_u(t)} + \frac{V_b(t)}{\gamma_b}} \Bigg\{ & \left(1 - \tfrac{1}{\gamma_u(t)}\right) \delta Q_{th_u}(t) + \left(1 - \tfrac{1}{\gamma_b(t)}\right) \delta Q_{th_b}(t) - p(t) dV(t) \\ & - \left(\tfrac{1}{\gamma_u(t)} - 1\right) \left(\textstyle\sum_j h_j(t) dm_j(t)\right)_u - \left(\tfrac{1}{\gamma_b(t)} - 1\right) \left(\textstyle\sum_j h_j(t) dm_j(t)\right)_b \\ & + dm_u(t) \left(\tfrac{1}{\gamma_u(t)} h_u(t) - u_u(t)\right) + dm_b(t) \left(\tfrac{1}{\gamma_b} h_b(t) - u_b(t)\right) \Bigg\} \end{aligned} \tag{3.3.10}$$

In the thermodynamical model, a system of ordinary differential equations has been obtained for the pressure (Equation (3.3.10)) and temperature (equations (3.3.3) and (3.3.4)) and different statical relations for the heat transfer between the unburned and burned zones, the heat transfers to the cylinder wall, the enthalpies and the zones volume. The only remaining variable to define is the mass dynamic. For a control volume enclosing the fuel/air mixture, the rate of change of the total mass $m(t)$ is equal to the balance of the mass flow going into and out of the system:

$$\begin{aligned} dm(t) = &\quad \textstyle\sum_j dm_{i,j}(t) \quad i = u, b \\ j = &\quad int, \quad exh, \quad comb \end{aligned} \tag{3.3.11}$$

where $dm_{i,j}(t)$ depends on the intake and exhaust mass flow and also on the combustion process as:

$$\begin{aligned} dm_u(t) &= dm_{u,int}(t) - dm_{u,exh}(t) - dm_{u,comb}(t) \\ dm_b(t) &= dm_{b,int}(t) - dm_{b,exh}(t) + dm_{u,comb}(t) \end{aligned} \tag{3.3.12}$$

When the cylinder valves are open, the rate of change of the mass is due to the mass flow coming into or out the cylinder: $dm_{b,int,exh}(t)$ and $dm_{u,int,exh}(t)$. These variables are modeled as the mass flow of a compressible fluid through a nozzle as presented in the appendix A.3 in Figure A.2 and Table A.1.

However, when the valves are closed, the total rate of change of the mass depends only on the combustion process: $dm_{u,comb}(t)$. Thus, during the valves closure $dm_{u,int,exh}(t) = 0$ and $dm_{b,int,exh}(t) = 0$ and it is verified that:

$$dm_b(t) = -dm_u(t) = dm_{u,comb}(t) \tag{3.3.13}$$

During the valves closure the mass enclosed in the combustion chamber remains constant and there is only a mass transfer of the gases which get burned in the zone u to the zone b. During the valves closure, $dm_b(t)$ is referenced as *the burning rate*, and a combustion model is considered to define its dynamics. In the next section, some of the most common combustion models based in the two zones hypothesis are detailed.

To finish this section, a summary of the model main variables and parameters is presented in Table 3.2.

The crank angle $\theta(t)$ is an independent state which only depends on N:

State space variables	$p(t)$, $m_u(t)$, $m_b(t)$, $T_u(t)$, $T_b(t)$, $\theta(t)$
Parameters	$N[rpm]$
Inputs	IVC_d, EVO_d, IT and the injected fuel m_{fuel}
Valves opening (Intake, exhaust)	$dm_{u,b_{int,exh}}(t) \neq 0$, $dm_{b,u,_{comb}}(t) = 0$
Valves closure (Compression)	$dm_{u,b_{int,exh}}(t) = 0$, $dm_{b,u,_{comb}}(t) = 0$
Valves closure (Combustion)	$dm_{u,b_{int,exh}}(t) = 0$, $dm_{b,u,_{comb}}(t) \neq 0$

Table 3.2: Two zones model summary

$$d\theta(t) = \frac{2\pi}{60}N \tag{3.3.14}$$

Remark 3.3.1. The inputs IVC_d, EVC_d, IT and m_{fuel} are considered as parameters since no control is performed with these inputs. These inputs defines the inlet and exhaust valves opening and closing profiles, the ignition timing and the injected fuel respectively.

In an engine model it is usual to use as temporal reference the crank angle $\theta(t)$ instead of the time, thus assuming as initial state $\theta(t) = IVC$, the initial conditions for the engine model might be approximated to the gases characteristics at IVC as: $p_0 = p_{IVC}$, $T_{u_0,b_0} = T_{IVC}$ where $T_{IVC} = \frac{p_{IVC}V_{IVC}}{r_{IVC}m_{ivc}}$ is the temperature of the inlet mass m_{IVC} at IVC. The initial conditions detail for $m_{b,u}$ are given by the fill in model, which is detailed in the Appendix A.2 in equation A.2.2.

3.4 0D phenomenological combustion modeling

The combustion is a crucial process in the engine cycle. It determines the heat release and influences other phenomena that occur outside of the combustion chamber. The proper prediction of the combustion is essential in the engine modeling.

The rate of combustion is strongly influenced by the flow field in the engine, which is mostly turbulent under normal operating conditions. However, a sophisticated theory of turbulence, including fluctuating quantities and conservation equations is necessary to detail the engine flow field. Such characteristics can be obtained through detailed 3D mechanisms, but this method is too complex to be included in the phenomenological models that represent the dynamical behavior as the two zones model presented previously. Therefore some simpler strategies have also been proposed, where the parametric combustion models and the 0D combustion models mentioned in the introduction of this chapter are the most spread strategies.

As it was mentioned in the introduction of this chapter, in the 0D engine combustion modeling, the combustion process is frequently modeled depending on the application field and different types of strategies in different levels of complexity are found: parametric combustion models, semi-empirical combustion models, 0D combustion models based on chemistry and 0D thermodynamical combustion models. In this thesis, the 0D two zones thermodynamical scheme has been chosen for the engine modeling. In the last section, the burning rate $dm_b(t)$ was introduced in Equation (3.3.13) to represent combustion process. In this thesis, the models that represent the combustion process as a growing flame of burning gases propagating inside the combustion chamber are considered as the most adapted choice for modeling the burning rate, regarding the main goal of building a flame-wall interaction model.

In the next paragraphs, some of the most common parametric models and 0D combustion models are detailed. It is important to remark, that only some of the 0D combustion models are mentioned in this summary. Those models have been chosen because they are very representative among the existent combustion modeling schemes, and because these models can be adapted to be used in the 0D two zones thermodynamical modeling framework.

The combustion model survey starts with a simple parametric approximation for the combustion process referred to as Vibe's law. This strategy is simple, but is too dependent on the calibration parameters and it is not closely related to the physics, thus it is only valid for the calibration parameters and the engine conditions specified during the calibration process. In order to take into account some physical knowledge like the turbulent behavior in the combustion modeling to obtain more predictive models, the flamelet approximations have been proposed.

In the flamelet models, two zones are distinguished: fresh and burned gases which are separated by a flame front, which propagates from the burned gases towards the fresh mixture. The chemical reactions of fuel oxidation that produces the combustion occurs in a very thin layer compared to all scales of the turbulent flow. The combustion reaction is assumed to be fast enough so that the dominant effect of turbulence on the flame is to wrinkle the flame surface while the inner flame structure is not significantly altered by the turbulent flow field [Zhao et al., 1994]. In these approximations, the large and small eddy length scales effects of the turbulent behavior are considered.

In this review three flamelet approximations are compiled. The first model is the entrainment combustion model proposed by [Keck, 1982], which separates the combustion process into two phases. Later, three models merged in the flamelet model type are presented, where the conversion of fuel is introduced directly: the flame propagation combustion model from [Bougrine et al., 2009] is presented, this model results from the reduction of the 3D coherent flame model (CFM) proposed in [Colin et al., 2003]. Finally, in the works [Yoshiyama et al., 2001], [Bozza et al., 2005] and [Baratta et al., 2005],

different fractal combustion models are proposed and the most relevant elements to characterize the fractal representation of the burning rate are developed.

3.4.1 Vibe's law combustion model

A common way to model the combustion process with a parametric approximation is the referred to as Vibe's law [Vibe, 1956]. In this model, the burning rate is modeled empirically as a function of the crank angle position:

$$\left.\frac{dm_b(t,u)}{dt}\right|_{wiebe} = m_o a e^{-a\left(\frac{\theta(t)-\theta_0(u)}{\Delta_\theta}\right)^{(m_w+1)}} (m_w+1)\left(\frac{\theta(t)-\theta_0(u)}{\Delta_\theta}\right)^{m_w} \frac{2N\pi}{60\Delta_\theta} \qquad (3.4.1)$$

where N is the engine speed in rpm, $u = IT$ is the ignition timing, $\theta_0 = 360 - IT$ is the crank angle where the combustion begins, m_o is the unburned mass mixture at the IVC, and a, m_w and Δ_θ are calibration parameters. The variable Δ_θ is included to calibrate the duration of the burn. a and m_w are usually between 3 and 6 and Δ_θ varies from 60 to 110 degrees, being smaller for a retarded ignition timing and bigger for an advanced ignition timing.

3.4.2 Entrainment combustion model

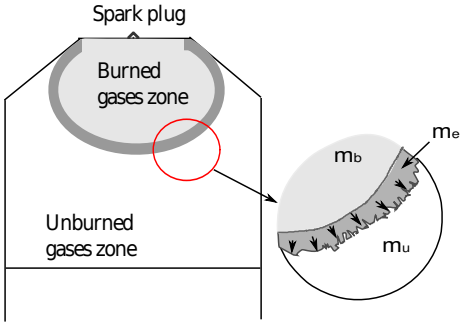

Figure 3.4: Two zones model scheme: the burned gases and the unburned gases zones separated by the reaction layer. $m_b = burned\ gases$, $m_u = unburned\ gases$, $m_e = entrainment\ gases$.

The entrainment model was developed by [Keck, 1982]. In the entrainment combustion model an intermediate zone in the middle of the burned and unburned gas zones is added (Figure 3.4). In the intermediate zone the gases are burned during a characteristic time τ_b. The gases in the middle zone are called entrainment gases m_e. In the entrainment model, it is considered that the fuel passes directly from the unburned zone to the burned zone following a turbulent behavior, the middle zone is considered as *virtual* because it does not have any contribution in the energetic exchange.

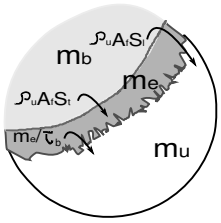

Figure 3.5: Three zones model mass transfer scheme.

The entrainment combustion model is based on the Eddy Burning equations, where the following equations for the mass burning rate and the entrainment gases are proposed:

$$\frac{dm_{b(t)}}{dt} = \rho_u(t) A_f(t) S_l(t) + \frac{m_e(t)}{\tau_b(t)} \tag{3.4.2}$$

$$\frac{dm_u(t)}{dt} = -\rho_u(t) A_f(t) (S_l(t) + S_t(t)) \tag{3.4.3}$$

$$\frac{dm_e(t)}{dt} = \rho_u(t) A_f(t) S_t(t) - \frac{m_e(t)}{\tau_b(t)} \tag{3.4.4}$$

where $\rho_u(t)$ is the unburned gases density, $\tau_b(t) = l_i(t)/S_l(t)$. $S_l(t)$ is the gases laminar speed of the flame, derived from experimental measurements in [Metghalchi & Keck, 1982] as:

$$S_l(t) = S_{L0} \left(\frac{T_u(t)}{T_0} \right)^{\alpha} \left(\frac{p(t)}{p_0} \right)^{\beta} (1 - 2.21 X_{egr}^{0.773}) \tag{3.4.5}$$

where $p(t)$ is the cylinder pressure, $T_u(t)$ is the unburned gases temperature, p_o and T_0 are the atmospheric pressure and temperature respectively. The parameters S_{L0}, α and β are characteristics of the fuel. In [Gulder, 1984], specific data to characterize these parameters are given. For the study considered here:

$$\alpha = 2.4 - 0.271\phi^{3.51}, \quad \beta = -0.357 + 0.14\phi^{2.77}, \quad S_{L0} = \beta_m + \beta_\phi (\phi - \phi_m)^2 \tag{3.4.6}$$

where $\beta_m = 30.5\ cm/s$, $\phi_m = -54.9\ cm/s$ and ϕ is the equivalence fuel ratio of the mixture. $l_i(t)$ (the sub index i refers to integral) is the eddy integral scale which is defined later in Section 3.5.

$A_f(t)$ is the laminar burning area, which may be approximated by a spherical surface of radius $R_f(t)$ with its center located at the same radial and angular position as the *best fit* circle and at the same height as the spark (a design method for $A_f(t)$ is presented in Section 3.4.5 and in Appendix A.4).

$S_t(t)$ is modeled empirically as:

$$S_t(t) = 0.08 r_v \frac{A_p}{A_{iv}} 2NH_p(t) \tag{3.4.7}$$

where r_v is the engine volumetric ratio, A_p is the piston area, A_{iv} is the maximum open area of the inlet valve, N is the engine speed and $H_p(t)$ is the piston height.

Equations (3.4.2), (3.4.3) and (3.4.4) verify that the mass balance in the combustion chamber equals 0, which is expected because as the chamber valves are closed, there are no mass transfer or energy exchanges from the cylinder ports.

3.4.3 Flame propagation combustion model

This model is taken from the works presented in [Lafossas et al., 2005], [Richard et al., 2007] and [Bougrine et al., 2009]. This model is also based in the two zones hypothesis, thus the mass burning rate is proportional to the density of the unburned mixture $\rho_u(t)$, to the turbulent flame speed $S_t(t)$ and to the laminar flame area $A_f(t)$, considered as a spherical surface centered in the spark plug location (The laminar flame area is detailed in Section 3.4.5 and in the Appendix A.4). Thus, the mass burning rate is modeled as:

$$dm_b(t) = \rho_u(t) A_f(t) S_t(t) \tag{3.4.8}$$

The turbulent flame speed $S_t(t)$ is defined as $S_t(t) = S_l(t)\Xi(t)$, where $\Xi(t)$ is the turbulent wrinkling coefficient and $S_l(t)$ is defined as (3.4.5). After ignition, the fresh gases reach the flame front at the laminar flame speed $S_l(t)$ and they get burned into the thin front layer. The wrinkling phenomenon is due to the turbulent behavior of the flame surface because of the *tumble* [Heywood, 1988] flow movement. This phenomenon is detailed in Section 3.5. The wrinkling factor $\Xi(t)$ represents the increase in the flame surface, $\Xi(t) = A_t(t)/A_f(t)$, where $A_t(t)$ means the wrinkled turbulent flame surface (Note that $\Xi(t) = 1$ means laminar combustion). Thus, the burning rate of the fuel is expressed as:

$$dm_b(t) = \rho_u(t) A_f(t) S_l(t) \Xi(t) \tag{3.4.9}$$

At the beginning of the combustion the flame surface is not wrinkled by the turbulence. Before the flame surface reaches a characteristic length of the flame radius r_0, it is

supposed to be laminar: $\Xi(t) = 1$. Once the transition radius is reached, the wrinkles in the upper layer of the surface are significant and this phenomenon is taken into account by the wrinkling factor that multiplies the burning rate: $\Xi(t) > 1$. According to [Lafossas et al., 2005], in this model the wrinkling factor $\Xi(t)$ variations are defined as:

$$\begin{aligned}\frac{1}{\Xi(t)}\frac{d\Xi(t)}{dt} &= \Gamma\left(\frac{u'(t)}{S_l(t)}, \frac{l_i(t)}{\delta_l(t)}\right)\frac{u'(t)}{l_i(t)}\left(\frac{\Xi_{eq}(t)-\Xi(t)}{\Xi_{eq}(t)-1}\right) \\ &\quad -\frac{2}{r_{bg}(t)}(1+\tau_\Xi(t))(\Xi(t)-1)S_l(t)\end{aligned} \tag{3.4.10}$$

where Γ is the efficiency function of the turbulent flow on the flame strain [Charlette et al., 2010]. The turbulent intensity $u'(t)$ and the integral scale $l_i(t)$ depend on the turbulent flow field and are defined next in section 3.5. $\delta_l(t)$ is the laminar flame thickness estimated using Blint's correlation [Blint, 1986]. $\tau_\Xi(t) = \frac{\rho_u(t)}{\rho_b(t)}$ is the thermal expansion rate and $r_{bg}(t) = \sqrt[3]{\frac{3}{4\pi}V_b(t)}$ is the current burned gases mean radius. The weighting term $\Xi_{eq}(t)$ is defined as:

$$\Xi_{eq}(t) = 1 + \frac{S_t(t)}{S_l(t)} = 1 + 2\frac{\sqrt{Ev_T(t)}}{S_l(t)} \tag{3.4.11}$$

where $\nu_t(t)$ is the turbulent viscosity and $E(t) = \alpha_\Xi \frac{u'(t)}{l_i(t)}$, with α_Ξ a positive constant.

This model was considered in this thesis and the obtained simulation results were satisfactory. However, the strategy was not retained because it was found that the fractal approach that is presented next gives also very satisfactory results and has a simpler implementation structure as it does not add any additional space variable, differently from this strategy where the variable $\frac{d\Xi(t)}{dt}$ must be defined. Besides, the main contribution with respect to the flame-wall interaction presented in this thesis is based on the work developed by [Foucher et al., 2002] and [Foucher & Mounaim-Rousselle, 2005], where a fractal approach is used to evaluate the burning rate in the vicinity of the piston. For these reasons, the fractal approach representation for the wrinkling coefficient which is presented next is retained to model the combustion model in this thesis.

3.4.4 Fractal theory based wrinkling coefficient

In this thesis, the fractal theory based wrinkling coefficient developed in [Bozza et al., 2005] is used. Applying fractal geometry concepts to the modeling of the wrinkled flame front surfaces has shown to give suitable estimations of the turbulent speed [Gulder et al., 2000]. Similarly to the previous flame propagation model, in the fractal theory

the burning rate is expressed as in Equation (3.4.9) changing only the way to define the wrinkling coefficient $\Xi(t)$.

In the fractal model, it is assumed that the wrinkling phenomenon can be represented by a fractal dimension $D_3(t)$ for a range of turbulence length scales L_{min} and L_{max}. The Kolmogorov's scale $l_k(t)$ is chosen as the minimum wrinkling scale L_{min} [Bozza et al., 2005]. The maximum wrinkling scale is a function of the flame spherical surface radius $R_f(t)$ and the calibration constant c_r. Thus the wrinkling coefficient $\Xi(t)$ in Equation (3.4.9) is expressed as:

$$\Xi(t) = \left(\frac{L_{max}}{L_{min}}\right)^{D_3(t)-2}, \quad L_{max} = c_r R_f(t), \quad L_{min} = l_k(t) \tag{3.4.12}$$

The fractal dimension $D_3(t)$ depends on the turbulence intensity $u'(t)$ and the laminar flame speed $S_l(t)$ as:

$$D_3(t) = \frac{2.35u'(t) + 2.05S_l(t)}{u'(t) + S_l(t)} \tag{3.4.13}$$

The fractal dimension $D_3(t)$ and the Kolmogorov's scale $l_k(t)$ are functions of the turbulent flow behavior inside the chamber, which is presented in Section 3.5.

3.4.5 Flame surface: laminar flame area geometric model

In order to implement the combustion model a well-defined representation of the flame surface is necessary. The flame surface model is the basis in order to model the combustion close to the walls. In this section a brief summary of the flame surface geometric model is presented, a more detailed explanation is presented en the Appendix A.4.

To model the combustion chamber and the flame surface evolution inside it, the following parameters are taken into account:

- cylinder geometry (Bore, spark position, cylinder height);
- piston height $H_p(t)$;
- burned gases volume during combustion $V_b(t)$.

Using these parameters, a simplified geometric model of the combustion chamber is obtained. A geometric spherical surface of the flame progressing inside the combustion

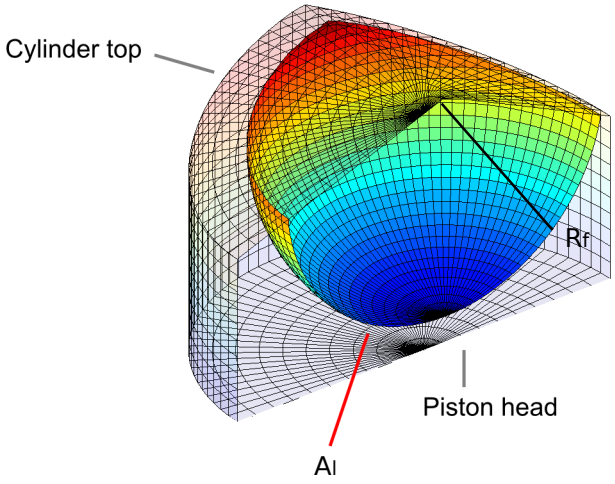

Figure 3.6: Scheme of the flame surface $A_l(t)$ developing inside the combustion chamber, with radius $R_f(t)$.

chamber is designed as presented in Figure 3.6. A normalized data map for the sphere volume $V_b(t)/V(t)$ and a data map of the sphere surface $A_l(t)$ are designed. Both data maps are functions of the flame radius $R_f(t)$ and the piston height $H_p(t)$ as:

$$V_b(t)/V(t) = f_v(R_f(t), H_p(t)), \quad A_l(t) = f_A(R_f(t), H_p(t)) \tag{3.4.14}$$

$V_b(t)$ is the sphere volume that represents the burned gases volume. As $V_b(t)/V(t)$ is the ratio between the burned gases volume and the combustion chamber volume, its magnitude varies between 0 up to 1. The data map of $V_b(t)/V(t)$ is inverted to obtain a map of the flame surface radius:

$$R_f(t) = f_v^{-1}(V_b(t)/V(t), H_p(t)) \tag{3.4.15}$$

Thus the data maps of the flame surface and the flame radius are used in the combustion model. The input parameters of these functions are $H_p(t)$ and $V_b(t)/V(t)$, the data maps are interpolated during the two zones model simulation in order to obtain $R_f(t)$ and $A_l(t)$ as depicted in Figure 3.7.

When the combustion takes place, the burned gases increase and the gases volume expands, occupying the available space in the combustion chamber. In the flame surface model, the ratio between the volume of the burned gases and the available cylinder volume V_b/V is taken into account as an input parameter. The volumes ratio increases in time as a function of the piston height and the burned gases volume: it starts at zero

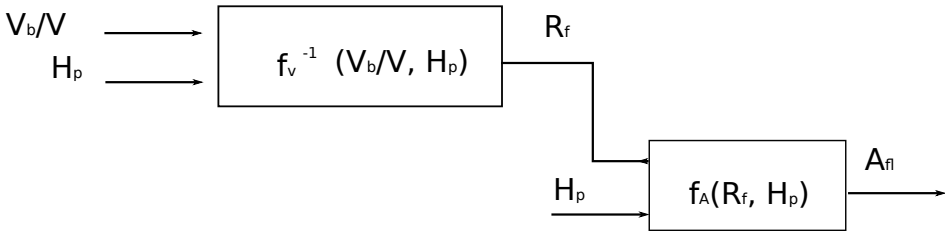

Figure 3.7: Diagram of the interpolation of the look up tables of the flame surface and flame radius. During the simulation, $V_b(t)$ is computed according to (3.3.8)

at the beginning of the combustion and increases towards one, when the burned gases volume equals the cylinder volume.

3.5 0D phenomenological turbulence model

The combustion resulting in a turbulent flame is the most used for industrial application. The main effect of the turbulence is to accelerate the burning rate, which promotes the oxidation of fuel and air in the SI engine. A vaporized fuel/air mixture actually burns quite slowly, when compared to the engine speed. Without turbulence, a flame starting at a central spark plug would take too long to reach the edge of the combustion chamber yielding on deficient engine performances. The burning rate needs to occur within about a tenth of a revolution to achieve reasonable efficiency. If the gases in the combustion chamber are moving rapidly, it will "stir up" the flame and help it to propagate much faster. The turbulence effect in the burning rate is represented by the wrinkling phenomenon presented in Sections 3.4.3 and 3.4.4. For these reasons, the turbulence constitutes a main component in the combustion process.

From the turbulence model, the turbulence intensity $u'(t)$ and the length scales as the integral scale $l_i(t)$ and the Kolmogorov's scale $l_k(t)$ are defined. These variables have an important impact in the SI model and in the flame-wall interaction modeling.

The combustion turbulent flow field is mainly characterized by the kinetic energy per unit volume $k(t)$, and several energetic sources referred to as terms (production terms, dissipative terms, convective terms) are considered as main components of $k(t)$. These terms represent the energy produced from the gases movement in the combustion chamber which is represented as kinetic energy. Such energy is produced from the gases movement during the intake and compression strokes and is transferred during the combustion stroke. This transfer is usually referred to as a transfer from a mean flow field (intake and compression) towards a turbulent flow field (combustion).

In this thesis, two turbulence models are considered: a phenomenological $k-\epsilon$ 0D turbulence model from [Lafossas et al., 2005], and as part of this thesis contribution, a turbulence model based on the classical phenomenological $K-k$ turbulence model is also developed. Such modeling schemes are taken into account because they are based in the definition of the Reynolds-stress tensor which describes the random fluctuations of the various flow properties. Such a scheme has shown to constitute an accurate representation of the combustion turbulent flow field.

3.5.1 0D phenomenological $k-\epsilon$ turbulence model

The engine turbulence modeling arise from the fluid dynamics theory. The most common turbulence models are based on the *Reynolds stress tensor* τ, where the kinetic energy per unit volume of the turbulence fluctuations is assumed to be proportional to the trace of the *Reynolds stress tensor* equation [Wilcox, 1993], which is presented the Appendix

A.5. The Reynolds-stress tensor describes the random fluctuations of the various flow properties. According to Reynolds, all the quantities are expressed as sums of mean fluctuating terms. The so called $k-\epsilon$ turbulence model results of the 0D reduction of the *Reynolds stress tensor* for turbulence kinetic energy.

Reynolds stress tensor equation 0D reduction The $k-\epsilon$ model reduction is based on the work developed in [Alizon, 2005] and [Wilcox, 1993]. (Unless it is specified, all the variables in this section are variable with the time. The time dependency of the equations in this section has been omitted for simplicity).

According to Prandlt, for an incompressible flow the kinetic energy per unit mass k can be defined as:

$$k = \frac{1}{2}\overline{u_i u_i} \tag{3.5.1}$$

where the sub index i is a spatial coordinate (i, j, k) and u_i is the flow speed. Based on the Reynolds stress tensor, it is possible to derive the corresponding dynamics for k and the following transport equation for the turbulent kinetic energy is obtained [Tennekes & Lumley, 1985]:

$$\frac{\partial k}{\partial t} + \overline{\mathbf{U}}_j \frac{\partial k}{\partial x_j} = -\overline{u_i u_j}\frac{\partial \overline{\mathbf{U}}_i}{\partial x_j} - \frac{\partial}{\partial x_j}\overline{\left(\left(\frac{p u_j}{\rho} + \frac{1}{2}u_i u_i u_j\right)\right)} + \frac{\partial}{x_j}\mu\frac{\partial k}{\partial x_j} - \nu\overline{\frac{\partial u_i}{\partial x_j}\frac{\partial u_i}{\partial x_j}} \tag{3.5.2}$$

where ∂x indicates spatial derivative (i.e $\frac{\partial u_i}{\partial x_j}$ is the spatial derivative of u_i with respect to the spatial coordinate j), $\mathbf{U}$ is the mean fluid velocity, μ is the molecular viscosity, ν is the kinematic viscosity and p is the instantaneous static flow pressure.

On the right hand of the equation, the first term is known as the energy production term and represents the rate at which kinetic energy is transferred from the mean flow to the turbulence, the second term is referred to as the turbulent transport and represents the rate at which turbulence energy is transported through the fluid by turbulent fluctuations, the term involving $\mu\frac{\partial k}{\partial x_j}$ is called molecular diffusion and represents the diffusion of turbulence energy caused by the fluid natural molecular transport process. The last term is the dissipation per unit mass.

The fluid speed $\mathbf{U}_i$ in the direction i is defined as the sum of the mean speed $\overline{\mathbf{U}}_i$ and a fluctuation u_i:

$$\mathbf{U}_i = \overline{\mathbf{U}}_i + u_i \tag{3.5.3}$$

The turbulent diffusion term can be modeled as:

$$\overline{\left(\frac{pu_j}{\rho} + \frac{1}{2}u_i u_i u_j\right)} = -\frac{v_{Turb}}{\sigma_k}\frac{\partial k}{\partial x_j} \tag{3.5.4}$$

where ν_{Turb} is the turbulent viscosity and σ_k is an empirical constant. The dissipation rate ϵ is modeled according to the Prandtl-Kolmogorov hypothesis as:

$$\epsilon = \nu\overline{\frac{\partial u_i}{\partial x_j}\frac{\partial u_i}{\partial x_j}} = C_{diss}\frac{k^{3/2}}{l_i} \tag{3.5.5}$$

where C_{diss} is an empirical calibration constant. Including equations (3.5.4) and (3.5.5) in Equation (3.5.2), follows that:

$$\frac{\partial k}{\partial t} + \overline{\mathbf{U}}_j\frac{\partial k}{\partial x_j} = -\overline{u_i u_j}\frac{\partial \overline{\mathbf{U}}_i}{\partial x_j} + \frac{\partial}{\partial x_j}\left(\frac{\nu_{Turb}}{\sigma_k}\frac{\partial k}{\partial x_j}\right) + \nu\frac{\partial^2 k}{\partial x_j x_j} - C_{diss}\frac{k^{3/2}}{l_i} \tag{3.5.6}$$

According to [Barba & Burkhardt, 2000], the turbulent kinetic energy k is supposed to be homogeneous in the combustion chamber, it implies that k is constant with respect to the spatial coordinates. Under this assumption $\frac{\partial k}{\partial x_j} = 0$ and (3.5.6) is reduced to:

$$\frac{\partial k}{\partial t} = -\overline{u_i u_j}\frac{\partial \overline{\mathbf{U}}_i}{\partial x_j} - C_{diss}\frac{k^{3/2}}{l_i} \tag{3.5.7}$$

In order to obtain a 0D expression, the production term $-\overline{u_i u_j}\frac{\partial \overline{\mathbf{U}}_i}{\partial x_j}$ can be defined as a function of the spatial speed taking apart the isentropic $(i = j)$ and non-isentropic $(i \neq j)$ parts. Taking as spatial coordinates the Cartesian plane (x, y, x), the isentropic part of (3.5.7) yields to:

$$\overline{u_i u_j}\frac{\partial \overline{\mathbf{U}}_i}{\partial x_j}_{\,i=j} = \overline{u_x u_x}\frac{\partial \overline{\mathbf{U}}_x}{\partial x} + \overline{u_y u_y}\frac{\partial \overline{\mathbf{U}}_y}{\partial y} + \overline{u_z u_z}\frac{\partial \overline{\mathbf{U}}_z}{\partial z} \tag{3.5.8}$$

For the isentropic case $\overline{u_x u_x} = \overline{u_y u_y} = \overline{u_z u_z} = u'^2$, where u' is the turbulent speed or turbulent intensity in the flow direction. Thus from Equation (3.5.1) the relation between the turbulent kinetic energy k and the turbulent intensity u' is:

$$k = \frac{3}{2}u'^2 \tag{3.5.9}$$

Including this equality in Equation (3.5.8) the final expression for the production term is obtained as:

$$\overline{u_i u_j}\frac{\partial \overline{\mathbf{U}}_i}{\partial x_j} = \frac{3}{2}k\nabla\mathbf{U} + \overline{u_i u_j}\frac{\partial \overline{\mathbf{U}}_i}{\partial x_j}_{non-isentropic} \tag{3.5.10}$$

where $\mathbf{U}$ is $(\overline{\mathbf{U}}_x, \overline{\mathbf{U}}_y, \overline{\mathbf{U}}_z)$.

Taking the continuity equation for fluids and assuming that the density ρ is constant over the space:

$$\frac{\partial \rho}{\partial t} + \rho\nabla\mathbf{U} = 0 \tag{3.5.11}$$

It is also assumed that the density is constant (incompressible gas), then the speed $\mathbf{U}$ divergence is also 0. Including this result in Equation (3.5.7), the production term is only related to the non-isentropic speed as:

$$\frac{\partial k}{\partial t} = -\overline{u_i u_j}\frac{\partial \overline{\mathbf{U}}_i}{\partial x_j}_{non-isentropic} - C_{diss}\frac{k^{3/2}}{l_i} \tag{3.5.12}$$

The non-isentropic production term represents the turbulent kinetic energy produced by the different turbulent sources: the swirl, the squish, the spray and the tumble. For a SI engine, the effects of swirl, squish and spray on turbulence can be neglected [Lafossas et al., 2005]. The tumble energy is then the only turbulence source for the production term:

$$-\overline{u_i u_j}\frac{\partial \overline{\mathbf{U}}_i}{\partial x_j}_{non-isentropic} = \frac{\partial k}{\partial t}_{tumble} \tag{3.5.13}$$

The turbulent kinetic energy due to the tumble can be obtained assuming a linear decrease of the tumble motion from the intake valve closure (IVC) to the top dead center (TDC) as it is suggested in [Richard et al., 2009] (Note that there exists several approaches for the tumble motion modeling), (The temporal dependency on the variables is introduced from here):

$$\frac{\partial k(t)}{\partial t}_{tumble} = \frac{1}{8} m \omega_e^2 \left(H_p(t)^2 \frac{dN_{tumble}(t)}{dt} + 2 N_{tumble}(t) H_p(t) \frac{dH_p(t)}{dt} \right) \tag{3.5.14}$$

where $H_p(t)$ is the piston height, $m(t)$ is the gases mass in the combustion chamber, ω_e is the engine speed in rad/s and $N_{tumble}(t)$ is the tumble number.

The computation of the tumble number $N_{tumble}(t)$ can be complex, however, some simple approximations have been proposed. In the work of [Richard et al., 2009], the tumble number is modeled as:

$$N_{tumble}(t) = \frac{N_{tumble_{IVC}}(\theta(t) - 360)}{\theta_{IVC} - 360} \tag{3.5.15}$$

where θ_{IVC} is the inlet valve closure crank angle. A data map for the tumble number at IVC $N_{tumble_{IVC}}$ is normally used.

Finally, including (3.5.13) in Equation (3.5.12), the turbulent kinetic energy $k(t)$ dynamics for the $k - \epsilon$ turbulence model is obtained as:

$$\frac{\partial k(t)}{\partial t} = \frac{1}{8} m \omega_{eng}^2 \left(H_p(t)^2 \frac{dN_{tumble}(t)}{dt} + 2 N_{tumble}(t) H_p(t) \frac{dH_p(t)}{dt} \right) - C_{diss} \frac{k(t)^{3/2}}{l_i(t)} \tag{3.5.16}$$

where C_{diss} is a calibration constant.

Further parameters from the turbulence model. Further parameters are defined from the turbulent model, among them the large turbulent length scales characterized by the Kolmogorov's length scale $l_k(t)$ and the integral scale $l_i(t)$:

$$l_k(t) = \frac{l_i(t)}{Re_t(t)^{\frac{3}{4}}} \tag{3.5.17}$$

where $Re_t(t)$ is the turbulence Reynolds number $Re_t(t) = \frac{u'(t) l_i(t)}{\nu_u(t)}$, where $\nu_u(t)$ is the kinematic viscosity of the unburned gases mixture.

The integral scale $l_i(t)$ can be defined with a simple geometrical relation as:

$$l_i(t) = C_l \sqrt[3]{V(t)} \tag{3.5.18}$$

where C_l is a calibration constant.

The turbulence intensity $u'(t)$ is defined thanks to the isentropic condition (3.5.9) as:

$$u'(t) = \sqrt{\frac{2}{3}k(t)} \tag{3.5.19}$$

This model was considered in this thesis, the validations shown later in Section 3.6.3.1 correspond to the two zones model simulated using this turbulence scheme and the obtained results were satisfactory. This strategy was replaced for a K-k approach for the further validations presented in Section 3.6.3.2. The aim of this change was to analyze the simulations results when changing the turbulence model. Besides, when using the $k-\epsilon$ model as described in this section, it is needed to define a function for the tumble number $N_{tumble}(t)$ and its derivative and such information might not always be available. Thus, in order to avoid the definition of a function for the tumble number, the K-k turbulence model presented next in Sections 3.5.2 is proposed.

3.5.2 K-k turbulence model

Another spread model for the 0D turbulence phenomenon in the SI engine is the so called classical K-k model [Poulos & Heywood, 1983]. In this model, the turbulence energy is transferred from a mean flow field (intake, exhaust) during the breathing process to a turbulent flow field during the combustion. The parameters as the eddy length scales and the turbulent intensity $u'(t)$ remain like the $k-\epsilon$ model presented before and the changes are in the method to define the turbulent kinetic energy $k(t)$.

In this method, two dynamical equations are defined for the mean energy $K(t)$ and for the turbulent kinetic energy $k(t)$. Both equations are linked by a production and dissipation term. Five terms compose the mean kinetic energy $K(t)$:

$$\begin{aligned}\frac{dK(t)}{dt} = & \underbrace{\frac{1}{2}dm_{int}(t)v_{int}(t)^2 + \frac{1}{2}dm_{exh}(t)v_{exh}(t)^2}_{1} + \underbrace{dK_t(t)}_{2} - \underbrace{P(t)}_{3} \\ & + \underbrace{\frac{\dot{\rho}_u(t)}{\rho_u(t)}K(t)}_{4} - \underbrace{\frac{dm_{exh}(t)}{m(t)}K(t)}_{5}\end{aligned} \tag{3.5.20}$$

The first term is the energy due to the intake and exhaust flows where $dm_{int}(t)$ and $dm_{exh}(t)$ are the intake and exhaust mass flow and $v_{int}(t)$ and $v_{exh}(t)$ are the intake and exhaust mass flow speeds. $\rho_u(t)$ is the density of the unburned gases mixture and $m(t)$ is the total enclosed mass in the combustion chamber. The second term is the dissipated energy due to the tumble motion, which is presented later.

The mean kinetic energy $K(t)$ is transferred to the turbulent flow field during the combustion through the third term in Equation (3.5.20) that is the production term:

$$P(t) = C_p \frac{K(t)}{l_i(t)/u'(t)} \tag{3.5.21}$$

where C_p is a calibration constant fixed at 0.25. $u'(t)$ is the turbulence intensity defined in Equation (3.5.19) and the integral scale $l_i(t)$ and the Kolmogorov's scale $l_k(t)$ are defined as in the previous turbulence model.

The fourth term in Equation (3.5.20) corresponds to the turbulence produced by the compression and the fifth term represent a diminution of the turbulence at the end of the cycle.

The turbulent kinetic energy $k(t)$ is given by:

$$\frac{dk(t)}{dt} = \underbrace{P(t)}_{1} - \underbrace{D(t)}_{2} + \underbrace{\frac{\dot{\rho}_u(t)}{\rho_u(t)} k(t)}_{3} - \underbrace{dm_{exh}(t) \frac{k(t)}{m(t)}}_{4} \tag{3.5.22}$$

where the first term corresponds to the production term, the second term represents the dissipation:

$$D(t) = C_d \frac{2}{3} \frac{k(t)^{3/2}}{l_i(t)} \tag{3.5.23}$$

with C_d a constant fixed at 0.25. The third term represents the impact of the compression and the relaxation and the fourth term represents the extinction of the turbulence at the end of the cycle.

Remark 3.5.1. Notice that the dissipation term D in the $K-k$ model is similar to the dissipation term ϵ in the $k-\epsilon$ model. The difference remains in the constant parameter multiplying the term $k(t)^{3/2}$. This resemblance is due to the fact that both models are based in the hypothesis of an energy transfer between a mean field to a turbulent field, which are the main assumptions from the Reynolds equation for turbulent fluids.

3.5.3 Tumble motion

The new turbulence model developed in this thesis is based on the classical $K-k$ turbulence model presented previously and a new scheme for the dissipation energy due to the tumble motion is proposed.

The tumble phenomenon is produced because of the gases mass rotation around the cylinder diameter. Figure 3.8 shows a scheme of the tumble movement. This movement generates kinetic energy, which is dissipated to produce turbulence in the combustion chamber. The assumptions to build the tumble model are:

- the gases mass is considered as a cylindrical body,
- the maximum length for the translation of the rotation axis is the piston height,
- the tumble energy has its maximum at Inlet Valve Closure (IVC) and decays linearly from IVC up to Top Dead Center (TDC),
- the tumble is destroyed at TDC [Kang & Baek, 1998].

The kinetic energy due to the tumble motion is considered as a linear decay from its initial value at IVC up to TDC, where the kinetic energy is destroyed because of the piston movement. The maximum tumble displacement axis is the piston height: at TDC there is no space for the mass to move, then the kinetic energy is set to 0. The tumble energy is dissipated in the turbulence phenomenon.

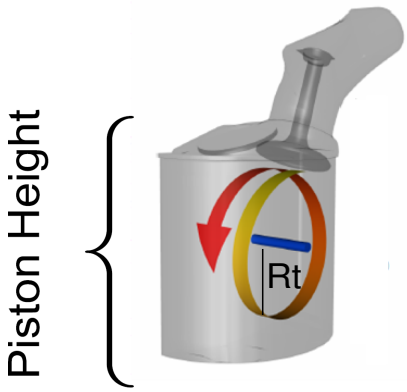

Figure 3.8: Tumble movement scheme

$$K_t(t) = \frac{1}{2} N^2_{tumble_0} \omega_t^2 J(t) F(\theta) \tag{3.5.24}$$

where $F(\theta)$ is a function dependent on the crank angle that models the tumble motion linear decay, ω_t is the tumble speed, N_{tumble_0} is the tumble number at IVC and J is the inertia of the mass:

$$J(t) = \frac{1}{2} m(t) R_t^2 \tag{3.5.25}$$

where R_t is the body radius, which is equal to the piston height at IVC $R_t = H_p(\theta_{IVC})$. The angular mass of the system is assumed as a rigid cylindrical body rotating with respect to its axis, as depicted in Figure 3.8. The rotational tumble speed is defined as $\omega_t = \sqrt{\frac{2K_t(t)}{J(t)}}$.

Summarizing the K-k proposed model it yields to:

$$\begin{cases} \frac{dK(t)}{dt} = & \frac{1}{2}dm_{int}(t)v_{int}(t)^2 + \frac{1}{2}dm_{exh}(t)v_{exh}(t)^2 + dK_t(t) - P(t) + \frac{\dot{\rho}_u(t)}{\rho_u(t)}K(t) \\ & -\frac{dm_{exh}(t)}{m(t)}K(t) \\ \frac{dk}{dt} = & P(t) - D(t) + \frac{\dot{\rho}_u(t)}{\rho_u(t)}k(t) - dm_{exh}(t)\frac{k(t)}{m(t)} \\ dK_t(t) & = \frac{1}{2}N^2_{tumble_0}\omega^2 J_0 F(\theta(t)) \end{cases} \tag{3.5.26}$$

The validation of the $K-k$ turbulence model is exposed in this section. The validations and the results related to the direct application of the submodel for the flame-wall interaction are presented next in a different section.

The $K-k$ based turbulence model was tested taking as reference 3D computations of the turbulence intensity $u'(t)$ in a SI engine. Table 3.3 summarizes the main characteristics of the test engine. The data used to the test the model is the turbulence intensity $u'(t)$. The test was performed at $N = 1200\ rpm$, $N = 2000\ rpm$ and $N = 3000\ rpm$.

Bore x Stroke: 72.2x73.1 mm
Piston rod: 132.5 mm
Volumetric ratio: 9.5:1
Engine speed: 1200, 2000 and 3000 rpm

Table 3.3: $K-k$ turbulence model validation: Engine Test Characteristics.

Figure 3.9 shows the turbulence intensity $u'(t)$. The figure shows a comparison between $u'(t)$ computed from 3D data and the proposed model for three different engine speeds. Satisfactory results are obtained. The simulation starts at IVC, where the tumble motion produces a mean kinetic energy $K(t)$. As it was expected, $u'(t)$ reaches its maximum before the top dead center TDC and starts to decay. A dependency on the engine speed is observed.

The results depicted in Figure 3.9 are very satisfactory, the proposed tumble motion represents adequately the dissipation energy in the turbulence model and the turbulence intensity $u'(t)$ prediction is accurate with respect to the 3D data references.

Remark 3.5.2. The $k-\epsilon$ model and the K-k model with the new proposed tumble modeling have been used and validated in this thesis, in the framework of the 0D two

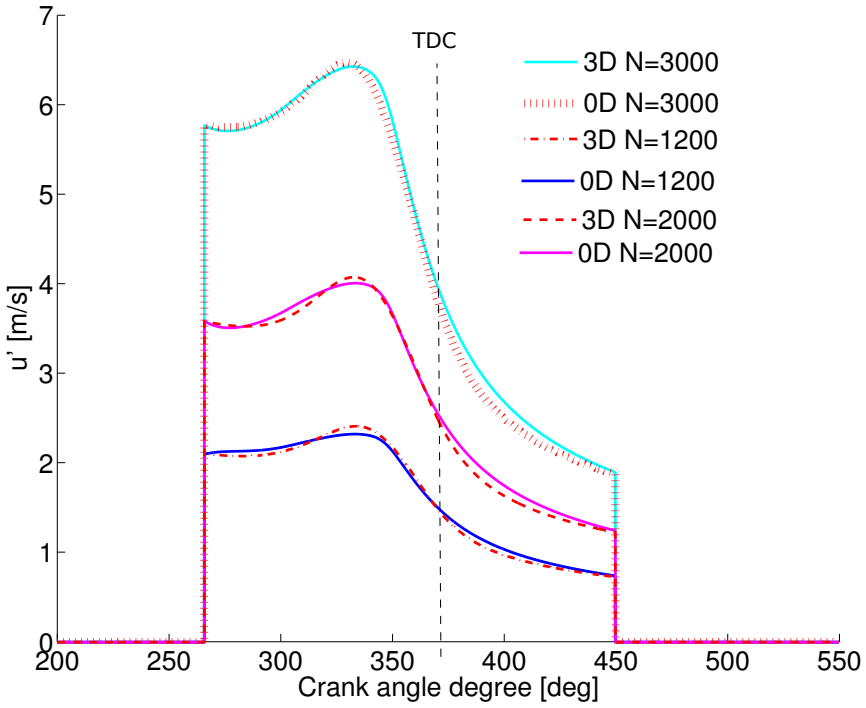

Figure 3.9: Turbulence intensity u'(t)

zones engine combustion modeling. The results were satisfactory in both cases. In this thesis have been chosen to privilege the K-k model with the tumble motion proposed scheme. The reason of this choice is the fact that for the $k-\epsilon$ model it is necessary a detailed definition of the tumble number and such information is not available for this project. This is not the case for the K-k model under the tumble motion scheme proposed in this thesis. Besides, the validations of the turbulence intensity $u'(t)$ using the modified K-k turbulence model have shown to give a good approximation of the turbulence phenomena.

3.6 Validation and application of a new 0D flame-wall interaction model for SI engines

The flame-wall interaction is accurately explained by 3D computations, direct numerical simulations, computational fluid dynamics and experimental observations. Such studies allow to understand how this flame-wall interaction occurs. Thanks to those works, it has been shown that when the flame front approaches the cylinder wall, there is a deceleration of the burning rate because the boundary layer of the walls surface acts as a barrier that extinguishes the gases expansion. Besides, the relatively low temperature of the walls colds the gases. A considerable fraction of the unburned mixture actually

burns in this combustion mode [Poinsot & Veynante, 2001].

The 0D models mentioned in Section 3.4 mostly focus on the laminar characteristics and on the wrinkling phenomena of a free developing flame, but they lack a suitable approximation of the wrinkling phenomenon when the flame reaches the cylinder walls. Consequently, the wrinkling coefficient $\Xi(t)$ as presented in 3.4.4 is valid when the flame surface propagates freely across the combustion chamber, but the combustion close to the cylinder walls is not well represented. A more accurate modeling of the flame-wall interaction allows obtaining more realistic combustion curves in the engine cycle simulation.

The near-wall velocity tends to be characterized by a very-thin layer of low momentum fluid, with direct interaction of the wall and turbulent structures. Many works usually use $1D$ and $2D$ methodologies to study the near-wall velocity characteristics through gas velocity measurements in the cylinder. Those works do not necessarily provide a model of the flame-wall interaction but explain the behavior of the flame approaching the quenching region. In the work of [Pierce et al., 1992], the near-wall flow characteristics are observed in different two-stroke geometries. The results of these studies show that the behavior of the fluid near the wall depends on the engine intake geometry, combustion chamber geometry and operating conditions. In more recent works, it has been possible to obtain more detailed representations of the flow characteristics near to the walls. For instance in the work of [Alharbi & Sick, 2010], elements such as the crank angle position dependency and a precise vortex structure near to the cylinder walls can be appreciated. With such information the velocity, temperature, and turbulence profiles are computed. Those turbulence profiles and velocity characteristics of the flame near the cylinder wall confirm that there is a deceleration in the burning rate in the quenching region. Such deceleration is due to the natural barrier that the cylinder wall represents for the fuel mobility, but also because the wall temperature is colder when compared to the gases temperature, which also decreases the gases expansion. Such a flame-wall interaction is an essential issue in accurately modeling the combustion process.

For the 0D flame-wall interaction modeling, to make the problem feasible, some arbitrariness and empiricism must be used. A number of assumptions will have to be invoked and the justifications of all hypothesis may not be done here. This is due to the breach that the 0D modeling imposes with respect to the spatial considerations. In this thesis, the flame-wall interaction phenomenon is modeled as a dimensionless function multiplying the burning rate equation. The model considers the cylinder shape, including the spark plug position and the flame surface that spreads inside the combustion chamber.

To introduce the thesis contribution presented in this chapter, a review of some flame-wall interaction models is presented first.

3.6.1 Flame-wall interaction models review

As it has been remarked in several parts of this manuscript, in the 0D two zones thermodynamical model, the combustion process is usually modeled as a growing flame of burning gases propagating inside the combustion chamber. However, most of the modeling schemes focus on the laminar characteristics of such a free developing flame, but they lack of a model of the combustion when the flame reaches the cylinder walls, which is a very important issue that cannot be neglected in order to obtain realistic engine cycle simulations.

It is clear that when using complex modeling schemes as the 3D models, the flame-wall interaction is an issue that can be treated locally on each studied cell of the combustion chamber. However, when lowering the modeling complexity to a 0D description, the most common strategy is to look for a model that introduces a loss of energy in the combustion process. Two main strategies of 0D flame-wall interaction modeling are compiled in this review, since they represent modeling approaches that can be easily included in the framework of the two zones combustion modeling:

- the flame-wall interaction might be treated as a heat flux lost at the walls, thus the method to characterize this phenomenon focuses on finding a heat flow model for the quenching region, or,

- the flame-wall interaction might be treated as a function that introduces a deceleration directly in the burning rate equation, this approach will be called extinction coefficient.

Remark 3.6.1. The flame-wall interaction model proposed in this thesis is lined up to the extinction coefficient approach.

The flame-wall interaction in a SI engine is closely related to the turbulent flow field and the different variables related to the turbulent flow field as the turbulent intensity $u'(t)$, the eddy length scales (the integral scale $l_i(t)$ and the Kolmogorov scale $l_k(t)$) and the flow thickness. One of the first works that has treated the phenomenon of a flow in a boundary is the *law of the wall*, which was first published by Theodore von Kármán, in 1930 [von Kármán, 1930]. In this work the concept of a less turbulent condition of the flow near a wall was introduced. This law however is valid for stationary fluid only, which is not the case of the gases flow during the combustion in a SI engine, thus the *law of the wall* might not be applied directly to the engines. For this reason, a modified *law of the wall* and other empirical models for the flame-wall interaction to be used in engine modeling have been proposed. Notice that those models keep a close relation to the turbulent flow field variables.

3.6.1.1 Flame-wall interaction modeling: heat flux approaches

From a simplified analysis of the flame-wall interaction in laminar combustion, in the work of [Ferguson & Keck, 1977] an equation that relates the heat flow in the quenching region $\delta Q_{wall}(t)$ to the flow thickness $\delta_q(t)$ is proposed as:

$$\frac{\delta Q_{wall}(t)}{Q_l(t)} = \frac{\lambda(t)}{\rho_u(t) c_p(t) S_l(t) \delta_q(t)} \tag{3.6.1}$$

where $Q_l(t)$ is the laminar combustion flow and $\lambda(t)$ is the flow conductivity. ($Q_l(t)/\delta Q_{wall}(t)$ is refer to as the Peclet number). Even if this model is simple, it allows estimating approximately some parameters related to the flame-wall interaction.

The approach of [Han & R.Reitz, 1997] is frequently used. This model takes into account the incompressible behavior of the flow. The released heat $Q'''(t)$ is averaged over the volume, to avoid using spatial characteristics near to the wall:

$$\delta Q_{wall}(t) = \frac{-\rho(t) c_p(t) u'(t) T(t) ln\left(\frac{T(t)}{T_{wall}(t)}\right) - (2.1 y(t)^+ + 33.4) < Q'''(t) > \nu(t)/u'(t)}{2.1 ln(y(t)^+) + 2.5} \tag{3.6.2}$$

where $\rho(t)$ is the gas density, $T_{wall}(t)$ is the wall temperature, $\nu(t)$ is the kinematic viscosity and $y(t)^+$ is the dimensionless distance to the wall. $< Q'''(t) >$ means the average of $Q'''(t)$ over the volume.

A similar model is presented by [Angelberger et al., 1997], who considers the same approach neglecting the heat release $Q'''(t)$ and assuming a quasi-isothermal boundary layer. Besides, the constant 2.5 is replaced by 3.9 taking into account experimental observations:

$$\delta Q_{wall}(t) = \frac{-\rho(t) c_p(t) u'(t) T_{wall}(t) ln \frac{T(t)}{T_{wall}(t)}}{2.1 ln(y(t)^+) + 3.9} \tag{3.6.3}$$

To finish this compilation of flame-wall interaction modeling using heat flux approaches, a model mentioned in [Boust et al., 2007] is presented. In this model, the heat flux lost near the wall is modeled by an approach based in the thermal conduction of the walls and the kinetic gases theory. This model is based on the heat conduction law $\delta Q_{wall}(t) = h(T(t) - T_{wall}(t))$, where the exchange coefficient $h(t)$ is defined by the empirical law:

$$h(t) = \rho(t)\sqrt{T(t)}\sqrt{\frac{2}{\pi}}\left(\frac{R}{M}\right)^{3/2}\left(\eta + \frac{\kappa}{\sqrt{T_{wall}(t)}} - \frac{\lambda(t)}{T_{wall}(t)}\right) \tag{3.6.4}$$

where R is the perfect gases constant, M is the molar mass of the gas and κ, η and λ are parametric constants defined from experimental data.

3.6.1.2 Flame-wall interaction modeling: extinction coefficient

In the work of [Steiner & Boulouchos, 1995], a model based on a spectral wall approach has been developed in order to describe the evolution of a flame in the vicinity of the combustion chamber. In this work, the turbulence in the combustion chamber is considered to have an order of magnitude higher than the one created in the boundary layer close to the wall due to local shear stress. Therefore the turbulence generated in the boundary layer itself is neglected. The influence of the wall on the approaching premixed flame front is accounted in the following way:

First, vortexes of the turbulent flow that are equal to or larger than their actual distance from the wall are not considered; therefore only the turbulent kinetic energy of the smaller vortexes is assumed to effectively act upon the flame. It is considered that the smaller vortexes approach the wall at distances smaller than the integral length scale $l_i(t)$. These considerations lead to the introduction of an additional upper cut-off scale $l_u(t)$ defined with a linear dependency with respect to the distance to the wall $x_{wall}(t)$, thus $l_u(t) = c_{l_{ie}} x_{wall}(t)$, where $c_{l_{ie}}$ is an empirical constant close to 1.

When $l_u(t) < l_i(t)$, the effective turbulence intensity in the vicinity of the wall changes when compared to the one of the free stream. The effective turbulence intensity that wrinkles the flame front near-wall is obtained as:

$$u'_{eff}(t) = u_{rms}\left(\frac{l_u(t)^{2/3} - l_k(t)^{2/3}}{l_i(t)^{2/3} - l_k(t)^{2/3}}\right)^{1/2} \tag{3.6.5}$$

where $l_k(t)$ is the Kolmogorov's scale and u_{rms} is the root mean square of the velocity fluctuations $u_i(t)$ (see Section 3.5). Thus, the mean turbulent flame front propagation speed is reduced and the flame arrival at one quenching distance from the solid surface is delayed when compared to the undisturbed free stream propagation.

Second, the flamelets exhibit the wall effect at a typical distance x_q from the surface given by $P_{eq} = x_q/\delta_f \approx 4\,to\,10$, where δ_f is the flame thickness. Besides, the wall can be seen as a sink for flame surface. Introducing a probability density function $P_{fb}(t)$, to describe

the distribution of flamelet locations relative to the mean flame position $x_{wall}(t)$, the amount of extinguished flame surface may be accounted for a wrinkling $\Xi_{eff}(t)$ factor in the following way:

$$\Xi_{eff}(t) \mid_{l_x} = \int_{-\infty}^{x_w all - x_q} P_{fb}(t)(x(t) - x_{wall}(t))\Xi(t) \mid_{l_x} dx \tag{3.6.6}$$

According to [Bruneaux, 1996], the deceleration in the burning rate due to the flame-wall interaction can be accounted for using an effective length scale for a wall cell of size Δy, where $y(t)$ is the distance from the flame to the wall, defined by:

$$l_{eff}(t) = \frac{1}{\Delta y} \int_0^{\Delta y} min\left(l_i(t), \frac{l_i(t)y(t)^+}{50}\right) dy \tag{3.6.7}$$

where $y(t)^+$ is the dimensionless distance from the flame to the wall. This effective length scale is then used in the flame stretch $\Gamma\left(\frac{u'(t)}{S_l(t)}, \frac{l_{eff}(t)}{\delta_l(t)}\right)$ to compute the wrinkling coefficient as in [Charlette et al., 2010].

In the work of [Nishaiwaki & Saijyo, 1999], a phenomenological combustion model is proposed and in order to model the flame-wall interaction, an empirical expression for the burning rate in the quenching region $\overline{w}_q(t)$ is proposed:

$$\overline{w}_q(t) = \overline{w}(t)\frac{max(\widetilde{Y}_{fu}(t) - \widetilde{Y}_{fq}(t), 0)}{\widetilde{Y}_{fu}(t)} \tag{3.6.8}$$

where $\overline{w}(t)$ is the mean burning rate and $\widetilde{Y}_{fu,fq}(t)$ is the fuel in the unburned gas and the fuel in the unburned gas in the quenching region respectively. The model depends on the typical turbulent flow field characteristics related to a combustion model.

3.6.1.3 Flame/wall interaction model: the *global approach*

To finish this review, the so called *global approach* in this thesis is presented. This approach is taken from the work developed by [Bozza et al., 2005]. The *global approach* is presented in more detail than the precedent approaches and is also validated with experimental measurements in order to compare the results obtained with the *local approach* proposed in this thesis.

When using the extinction coefficient to model the flame-wall interaction, it is common to consider this phenomenon as a global decay on the burning rate, thus:

- There is a time t_r where the combustion switches from a turbulent combustion mode to a decelerated burning rate mode,
- it is considered that from t_r until the end of the combustion, all the available fresh gases in the combustion chamber are influenced by the cylinder walls,
- the combustion chamber geometry is not considered.

Differently from the *global approach*, the aim in this thesis is to propose a model that takes into account the cylinder geometry to enhance the flame-wall interaction modeling, thus in this thesis it is proposed a model refer to as the *local approach*, which fits into the extinction coefficient approaches for the flame-wall interaction. Such model will be developed later in Section 3.6.2,

In the *global approach*, a weighting term $w(t)$ that represents the transition between the turbulent combustion mode and the walls combustion is used. In [Bozza et al., 2005], the wrinkling coefficient is modeled with the fractal combustion model presented in Section 3.4.4. The weighting term $w(t)$ increases linearly with time: it models in an affine way which one of the two combustion modes, fractal or near to walls has more influence on the process, thus the burned mass dynamics is:

$$dm_{b_{overall}}(t) = (1 - w(t))dm_b(t) + w(t)dm_{b_{walls}}(t) \tag{3.6.9}$$

where $w(t)$ is given by:

$$w(t) = 1 - \frac{m(t) - m_b(t)}{(m(t) - m_b(t))_{t_r}} \tag{3.6.10}$$

In [Bozza et al., 2005], t_r is the time when the transition between the turbulent combustion mode and the walls combustion mode occurs. It is computed at a fixed distance from the cylinder walls, called the transition length, where the combustion model shifts from a fractal burning rate to a linear deceleration as:

$$dm_{b_{walls}}(t) = \frac{m(t) - m_b(t)}{\tau_g} \tag{3.6.11}$$

The characteristic time τ_g is computed in the transition length, thus the burning rate speed during the rest of the cycle is assumed to be equal to the one computed from the fractal mode at the transition time t_r as:

$$\tau_g = \frac{(m(t) - m_b(t))_{t_r}}{dm_b(t)} \tag{3.6.12}$$

Even if this approximation gives an acceptable result for the cylinder pressure computation, various concepts are questioned from this approximation:

- the unburned mass available in the combustion chamber $m(t) - m_b(t)$ is not necessarily close to the cylinder walls at a given time t_r: the assumption of a linear decay of this mass is consequently not consistent with the model;
- τ_g suggests that when the flame gets close to the cylinder walls, the burning rate is equal to the one derived for the turbulent mode with the fractal approximation. This assumption is not accurate since in the quenching region, the burning rate tends to be more similar to a laminar flame [Foucher & Mounaim-Rousselle, 2005]. Even if $w(t)$ might supply the desired effect, it lacks a physical sense.
- the combustion chamber shape is not taken into account to consider the flame-wall interaction.

Figures 3.10a and 3.10b show the two zones combustion model simulation using Equation (3.6.9) for the burning rate. The measurement are in solid lines and the *global approach* model in dotted lines. In Figure 3.10a, it is possible to see that there is an overestimation in the heat release rate. This overestimation is reflected in the cylinder pressure, depicted in Figure 3.10b, where an error attaining 10% is obtained. The error in the heat release rate is about 15% .

In the figures, the crank angle is referenced from 0^o to 720^o for a complete cycle, starting in the intake stroke and the top dead center (TDC) is placed at 360^o. The test was performed at an engine speed of $N = 5250\,rpm$, and a brake mean effective pressure IMEP $= 11.4\,bar$.

Aiming to propose a more realistic approximation of the combustion process behavior close to the cylinder walls than the *global approach*, the cylinder shape and the flame surface distribution in the combustion chamber have to be taken into account. This allows modeling in which proportion the cylinder wall affects the flame expansion inside the combustion chamber. A *local approach* of the flame-wall interaction has been modeled. This new approach complements the fractal combustion model introducing the flame-wall interaction during all the combustion phase instead of switching to a linear deceleration from a given moment of the combustion as it is suggested in the *global approach*.

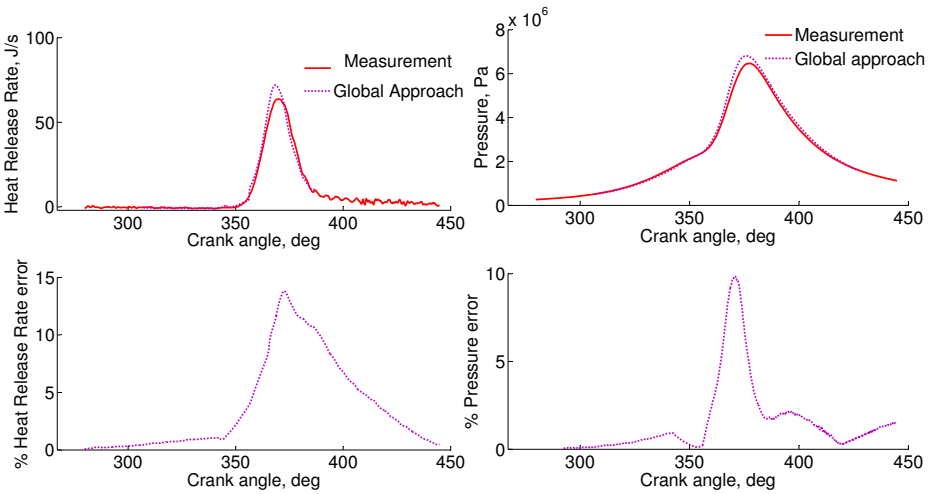

(a) Heat release rate (b) Cylinder Pressure

Figure 3.10: Heat release rate and cylinder pressure: *global approach*. IMEP=11.4 bar, N=5250rpm.

3.6.2 Flame/wall interaction model: *local approach*

A new model that takes into account the impact of the cylinder walls in the burning rate is proposed in this thesis. This approach is mainly based in the following considerations:

- the flame surface distribution with respect to the combustion chamber is taken into account,
- it is assumed a linear decay in the burning rate during the flame-wall interaction (hypothesis based on the validated work of [Foucher et al., 2002]),
- a well-defined geometric model of the combustion chamber is designed in order to have more realistic results.

The flame-wall interaction model proposed is developed as a complement of the 0D two zones thermodynamical model presented in Section 3.4 and can be included in several combustion schemes since it is conceived as a dimensionless function multiplying the burning rate equation.

In this section, the *local approach* is detailed and two validations are performed taking as reference the available experimental measurements. In the first validation the flame-wall interaction model is compared with the cited *global approach* to illustrate the improvements. In the second validation, the model is tested changing the spark plug position from centered position to lateral position. The model is included in the 0D two zones combustion model.

As mentioned before, the burning rate during the combustion exhibits a deceleration when the flame surface is getting close to the cylinder walls. In order to model this behavior, the term $\Psi(t)$ is introduced in Equation (3.4.9) as:

$$dm_b(t) = \rho_u(t) A_f(t) S_l(t) \Xi(t) \Psi(t) \tag{3.6.13}$$

Differently from the *global approach* presented in the previous section, in the *local approach* the term $\Psi(t)$ introduces a deceleration in the burning rate taking into account the cylinder geometry and the burned gases volume in the combustion chamber. Moreover, $\Psi(t)$ does not switch from a combustion mode to another, but it supplies a continuous calculation of the cylinder walls influence during the whole combustion process.

Three main aspects are taken into account to build $\Psi(t)$: the quenching distance, the distribution of the flame surface with respect to the cylinder walls and an extinction function to consider the influence of the wrinkling phenomenon depending on the distance of the flame surface to the cylinder walls.

3.6.2.1 Quenching distance

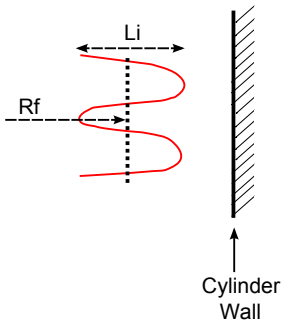

Figure 3.11: Scheme of the flame approaching to the cylinder walls and the distance to take into account the flame-wall interaction.

A main issue to understand the flame-wall interaction is the distance between the flame and the wall where the flame surface is supposed to be influenced by the cylinder walls, also known as the quenching distance. In [Poinsot & Veynante, 2001], this phenomenon has been deeply studied using a two-dimensional full Navier-Stokes solver with simple chemistry. In such work the quenching distance is related to the Peclet (P_e) number and it has been shown that for head-on quenching (flame front perpendicular to the wall) the quenching phenomena is perceived at $P_e \approx 3.4$. However, in [Foucher & Mounaim-Rousselle, 2005] a new quenching parameter Q_r to integrate the evolution of the burning rate represented by a fractal approach and the quenching distance has been proposed.

Q_r relates P_e and the total flame length inside a circle ϵ in the vicinity of the piston. In such work, the study developed in [Poinsot & Veynante, 2001] has been revised and it has been shown that even if the approximation of $P_e \approx 3.4$ to perceive the quenching phenomena is valid, it is also true that P_e does not really affect the magnitude order and evolution of the quenching parameter Q_r. Thanks to the parameter Q_r it has been shown that the fractal dimension D_3 (equation (3.5.23)) increases, until the distance between the flame and the wall is half of the integral scale length for the engine used in the experimental tests of such work. Besides, a linear decrease in the burning rate from a given distance to the cylinder walls was found.

These hypothesis have been considered in this work and the integral length scale l_i, that represents the largest turbulent eddies occurring in a given geometry is taken as reference to consider the walls influence. Thus when the flame radius reaches a value such that $R_f > R_{cyl} - l_i/2$, the walls influence is considered.

It is important to recall here that the aim of this thesis contribution is not to provide an approximation of the quenching distance length but to give a methodology to include the cylinder geometrical aspects to take into account the flame-wall interaction in a 0D modeling framework. The choice of $l_i/2$ as quenching distance has been done taking into account the work developed in [Foucher & Mounaim-Rousselle, 2005] mentioned previously. The analysis of a different quenching distance does not make part of this study and will be developed in further works. The choice of $l_i/2$ as quenching distance does not change the method proposed here for modeling the flame-wall interaction.

3.6.2.2 Flame distribution with respect to the walls

According to [Poinsot & Veynante, 2001], two typical situations can be studied with respect to the quenching phenomena: head-on quenching (flame front touching the wall perpendicularly) and side-wall quenching (flame front touching the wall in an angle smaller than 90^o). Studies have shown that most of the quenching occurs in the head-on way.

Using the flame surface model tabulation presented in Section 3.4.5 and detailed in the Appendix A.4, the normal distance from the flame surface to the cylinder walls is computed. With this information, a distribution of the flame surface with respect to the cylinder walls during the combustion is obtained. This concept is presented in Figure 3.12,where $A_l(t)$ is the total flame surface and A_{di} is the flame surface corresponding to a cell which is at a distance d_i from the cylinder walls. $A_l(t)$ and A_{di} are extracted from the surface model map.

Remark 3.6.2. Notice that $A_l(t)$ and $A_f(t)$ (equation (3.4.9)), represent both the flame surface. A_l represents the geometric flame surface mentioned in Section 3.4.5, which

is designed in order to build the flame radius and flame surface data maps for the combustion model. A_f represents the flame surface interpolated during the simulation when the actual values of the flame radius R_f and the burned gases volume V_b are used.

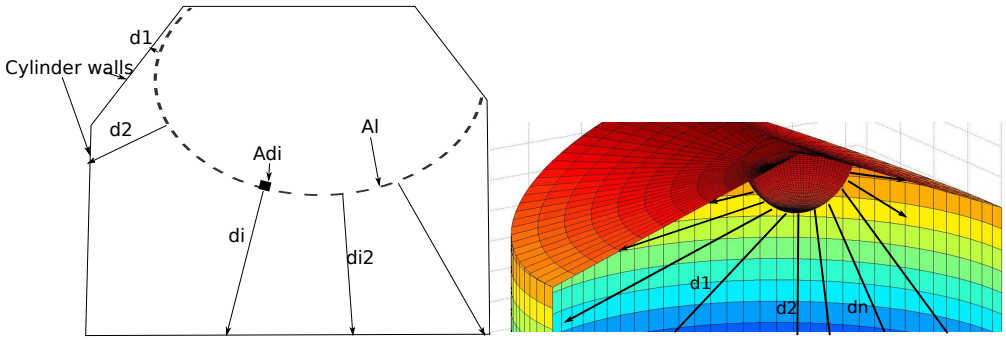

Figure 3.12: Flame surface distribution with respect to the cylinder walls distance.

Only the head-on quenching is considered, thus the surface fraction is computed as the sum of the cell areas at a normal distance d_i from the flame surface to the cylinder walls, divided by the total flame surface as:

$$A_{f_{d_i}} = \frac{\sum_j A_{d_{i,j}}}{A_l} \tag{3.6.14}$$

where $A_{d_{i,j}}$ is the surface of all the j flame surface cells at a distance d_i from the cylinder wall and A_l is the total flame surface.

To clarify the indexes: i makes reference to the number of components of a vector of distances length d_i, between the flame and the cylinder wall. d_i varies in a range of 0 up to 50 mm and is discretized in two ranges: each 0.01 mm for distances < 5 mm and each 0.5 mm for distances between 5 $mm < d_i < 50$ mm. It allows to obtain a data map for a varying quenching distance and a more detailed discretization in a range < 5 mm where most of the flame length scales are situated. Notice that during the interpolation, only the values of a magnitude $d_i < l_i/2$ are taken into account. j makes reference to the number of flame surface cells which are at a distance d_i from the cylinder wall. Notice that j and A_l vary depending on the evolution of the flame surface in the cylinder wall.

Figure 3.13 shows the obtained distribution with respect to the flame radius during simulation. In the results depicted in the figure, the ignition time is 33 CAD before TDC. When the combustion has not started the flame surface fraction is zero. Once the combustion starts, the flame wrinkles start to appear and the flame surface starts to get closer to the cylinder walls. The flame surface fraction which is close to the cylinder

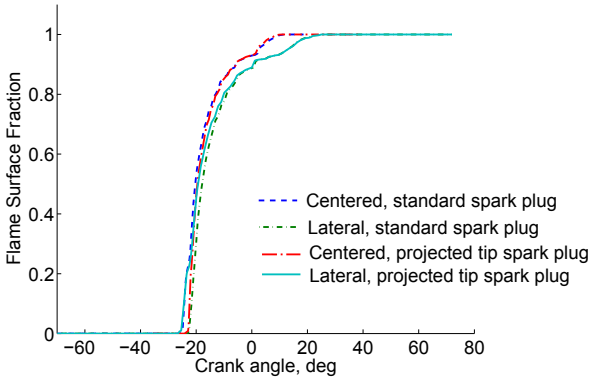

Figure 3.13: Flame surface fraction $A_{f_{d_i}}$ at a distance $d_i(t) < l_i(t)/2$

walls then increases, until the moment when the whole flame surface has spread inside the cylinder, vanishing into the walls (flame surface fraction equals to 1). Simulations with fourth combinations of spark plug positions and type are shown in the figure (see the experimental setup in Section 3.6.3.2 for a detailed description of the experience). For all cases, it can be seen that 50% of the flame surface fraction interacts with the cylinder walls only after about 7 CAD after spark timing. This remark emphasizes the importance of the flame-wall interaction combustion model in the evaluation of the burning rate. Comparison between lateral and centered positions of the spark plug shows a slower evolution of the flame surface fraction which interacts with the walls for lateral position cases, which leads to a more progressive deceleration of the burning rate in these cases. This reflects the impact of the geometrical aspects on the flame-wall interaction model that cannot be described with a *global approach*.

3.6.2.3 Extinction function

According to [Foucher & Mounaim-Rousselle, 2005], when the flame is getting close to the cylinder walls, the flame surface can be considered as decreasing linearly as a function of the distance to the wall. This hypothesis is used and an extinction function F_{ext} is introduced to consider such influence on the burning rate. F_{ext} is defined as a function of the distance from the flame surface to the cylinder walls. For distances in the quenching region: $l < l_i/2$, l being the variable representing the distance between the flame and the cylinder wall, F_{ext} must introduce an attenuation profile. For larger distances between the flame surface and the cylinder walls, the value of this function is assigned to one; it means that the flame surface is developing completely free in the combustion chamber, without attenuation in the burning rate.

Figure 3.14 shows the so called quenching parameter Q_R proposed by [Foucher & Mounaim-Rousselle, 2005]. According to this work, the quenching parameter Q_R represents the evolution of the burning rate in the quenching region. Q_R starts to decrease

linearly at a distance from the cylinder wall of 1.2 mm, that corresponds to half of the integral scale length determined for the engine where the experiences were carried out, thus it is assumed that the fractal dimension decreases when the flame front is at approximately a half of the integral scale $l_i(t)$.

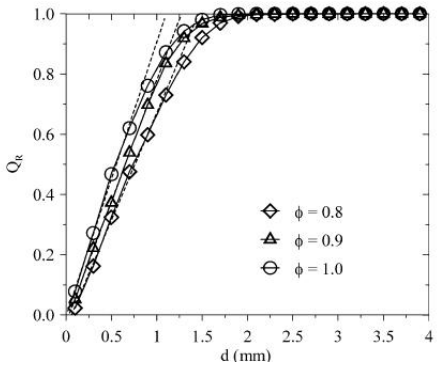

[Foucher & Mounaim-Rousselle, 2005]

Figure 3.14: Evolution of Q_R versus the distance to the cylinder wall d for three equivalence ratios ϕ

Using this hypothesis of a linear dependency between the burning rate deceleration and the distance from the cylinder wall, an extinction function is designed to build the function $\Psi(t)$ to take into account the flame-wall interaction. The extinction function $F_{ext}(t)$ is defined taking into account the distance from the flame surface to the cylinder walls $l(t)$. The walls influence in the combustion process is considered when $l(t) < l_i(t)/2$ ($l(t)$ represents all the distances d_i in Figure 3.12). For larger distances between the flame surface and the cylinder walls, the value of this function is assigned to 1; it means that the flame surface is developing completely free in the combustion chamber, without attenuation in the burning rate.

The designed extinction function is presented in Figure 3.15. It represents the flame surface behavior with respect to the wall interaction. For distances that reach $l_i(t)/2$, there is a linear decrease, represented by the $1/l_i(t)$ slope in the extinction function. Due to the definition of the mean flame radius $R_f(t)$, when the distance to the cylinder walls is $l(t) = -l_i(t)/2$ the function value is assigned to 0 (representing the flame surface which has been fully extinguished).

The extinction function is applied to the flame surface fraction in Equation (3.6.14). The result is integrated across the domain of definition of $F_{ext}(t)$ i.e. between ∞ and $-\infty$, with respect to the variable $l(t)$ that represents the distance to the cylinder wall:

$$\Psi(t) = \int_{l=-\infty}^{l=\infty} F_{ext}(t) A_{f_l}(t) \mathrm{d}d \tag{3.6.15}$$

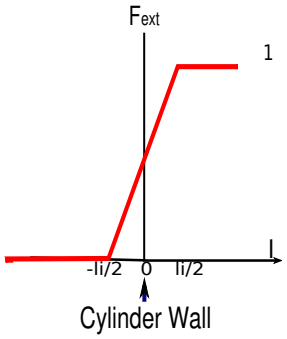

Figure 3.15: Extinction function F_{ext}

The result of this integral is stored in a data map which represents the flame-wall interaction when the flame surface approaches the cylinder walls and is denoted by $\Psi(t)$. $\Psi(t)$ is a look up table $\Psi(t) = f_\Psi(H_p(t), R_f(t), l_i(t))$ that depends on the flame radius, the piston height, and the integral scale. During the simulation, the look up table is interpolated, resulting in a function that represents the deceleration of the burning rate depending on the flame surface distribution in the combustion chamber.

Notice that $F_{ext}(t)$ has dimensions $[\frac{1}{m(t)}]$ and $A_{f_l}(t)$ is dimensionless as it was defined in (3.6.14). Thus when performing the integral $\Psi(t)$ as a dimensionless function.

3.6.2.4 Flame-wall interaction model design

Figures 3.16, 3.17 and 3.18 show a scheme of the flame surface propagating inside the combustion chamber for centered spark plug positions tests, and the cumulative flame surface fraction distribution that corresponds to each piston height and flame radius lengths multiplied by the extinction function. In the figures, $l_i(t) = 3\ mm$ to give a simple view of the process. The original flame surface fraction and the extinction function are overlapped in the figures for a better understanding. These figures represent $\Psi(t)$ before the simulation in the two zones combustion model. The geometry of the engine used for these tests is presented in Table 3.5 and two positions of the spark plug were tested. For each depicted example the obtained $\Psi(t)$ using Equation (3.6.15) is presented in the figure caption.

In Figure 3.16, a flame surface at early stage is represented. Analyzing the Figure 3.16a, it is clear that there is a part of the flame surface that is touching the cylinder top. However, the flame surface is small, and most of the surface might be considered as not that close to the cylinder wall, thus the static value of $\Psi(t)$ according to Equation (3.6.15) is $\Psi(t) = 0.882$. In Figure 3.17, the flame front has advanced with respect to the precedent figure and there is a bigger proportion of the flame surface that is influenced by the cylinder walls according to the chosen criterion, thus the value of $\Psi(t) = 0.795$. In Figure 3.18 the flame front has advanced more with respect to the precedent cases

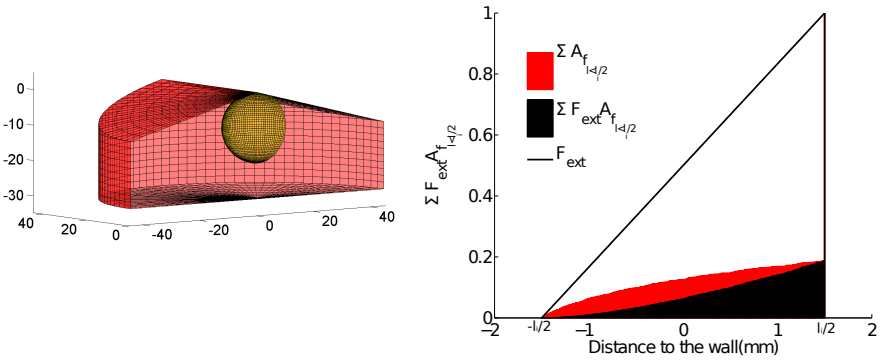

(a) Flame surface (b) Flame surface distribution

Figure 3.16: Centered spark plug position. $R_f(t) = 10\,mm$, $H_p(t) = 30\,mm$, $l_i(t) = 3\,mm$; leading to $\Psi(t) = 0.882$.

and a bigger proportion of the flame front which is influenced by the cylinder walls is obtained, thus $\Psi(t) = 0.679$.

Remark 3.6.3. Notice that the flame surface that takes part on the computation of $\Psi(t)$ is the surface that has not touched the cylinder walls but is close to it. The flame surface that has already touched the walls does not count for the total flame surface $A_l(t)$.

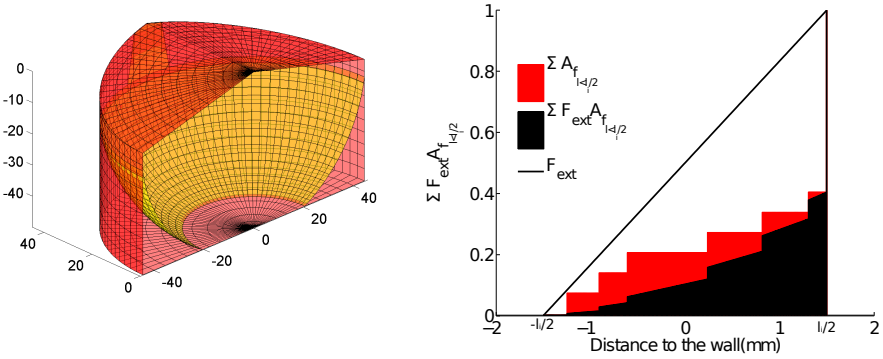

(a) Flame surface (b) Flame surface distribution

Figure 3.17: Centered spark plug position. $R_f(t) = 45\,mm$, $H_p(t) = 50\,mm$, $l_i(t) = 3\,mm$; leading to $\Psi(t) = 0.795$.

Similarly, Figures 3.19, 3.20 and 3.21 show a scheme of the flame surface propagating inside the combustion chamber and the cumulative flame surface fraction distribution

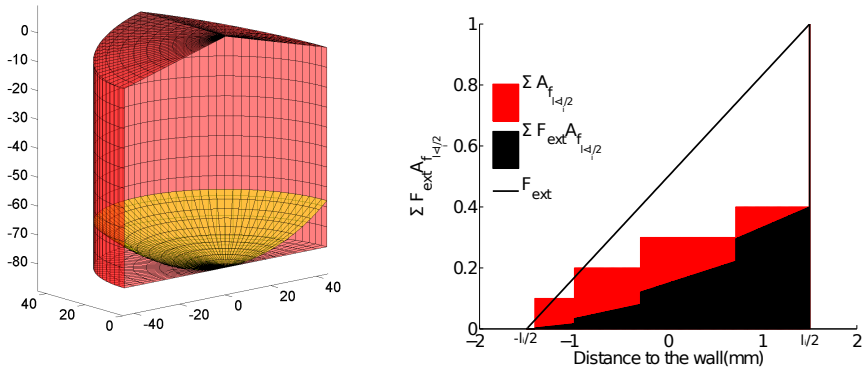

(a) Flame surface (b) Flame surface distribution

Figure 3.18: Centered spark plug position. $R_f(t) = 70\,mm$, $H_p(t) = 80\,mm$, $l_i(t) = 3\,mm$; leading to $\Psi(t) = 0.679$.

multiplied by the extinction function for the tests performed with the spark plug shifted to a lateral position. A similar analysis than the performed for the three cases presented previously can be re-created for the additional results.

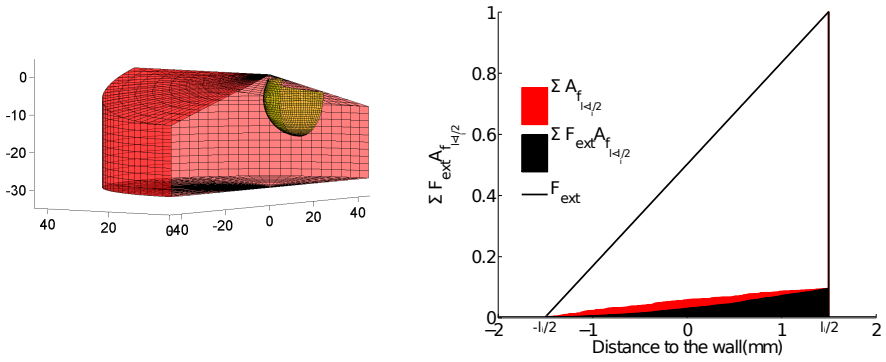

(a) Flame surface (b) Flame surface distribution

Figure 3.19: Lateral spark plug position. $R_f(t) = 10\,mm$, $H_p(t) = 30\,mm$, $l_i(t) = 3\,mm$; leading to $\Psi(t) = 0.948$.

Including the model $\Psi(t)$ in the burning rate equation, the proposed burning rate for the combustion model is represented by Equation (3.6.13). Figure 3.22 shows a plot of the data map of $\Psi(t)$ for the spark plug in a lateral position and the engine specifications presented later in Section 3.6.3.2 in Table 3.5. In order to plot the data map, a fixed integral scale of 3 mm has been chosen. In the figure $\Psi(t)$ has a maximum value of 1. Depending on the position of the piston $H_p(t)$, the flame radius $R_f(t)$ and the distance

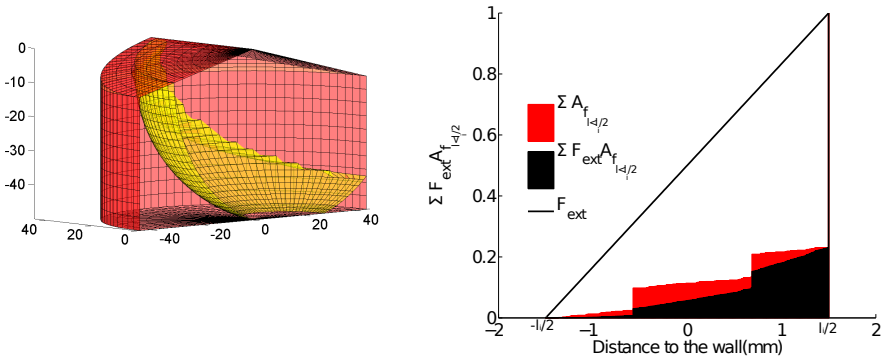

(a) Flame surface (b) Flame surface distribution

Figure 3.20: Lateral spark plug position. $R_f(t) = 45\,mm$, $H_p(t) = 50\,mm$, $l_i(t) = 3\,mm$; leading to $\Psi(t) = 0.893$.

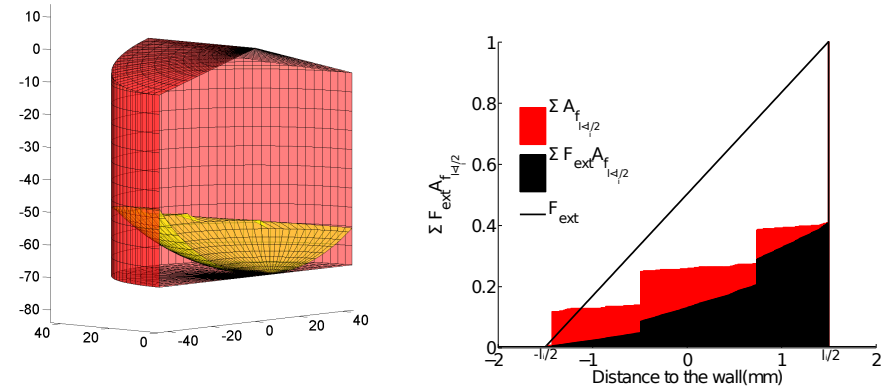

(a) Flame surface (b) Flame surface distribution

Figure 3.21: Flame surface for lateral spark plug position and $R_f(t) = 66\,mm$, $H_p(t) = 70\,mm$, $l_i(t) = 3\,mm$; leading to $\Psi(t) = 0.73$.

criterion, $\Psi(t)$ is interpolated among the values in the data map. In Figure 3.22 for instance, at the beginning of the combustion, when the $H_p(t)$ is almost at its maximum and $R_f(t)$ is still small, $\Psi(t) = 1$, which means that the flame develops freely in the combustion chamber, but later, in an early stage of the combustion, for $H_p(t) = 63\ mm$ and $R_f(t) = 7\ mm$, the burning rate is weighted by $\Psi(t) = 0.87$ (if the distance criterion is $l_i(t) = 3\ mm$), which means that there is a percentage of the flame surface that has touched the cylinder walls and $\Psi(t)$ supplies the corresponding weight.

During the actual simulation, $l_i(t)$ is time variable, thus the data map of $\Psi(t)$ has four dimensions.

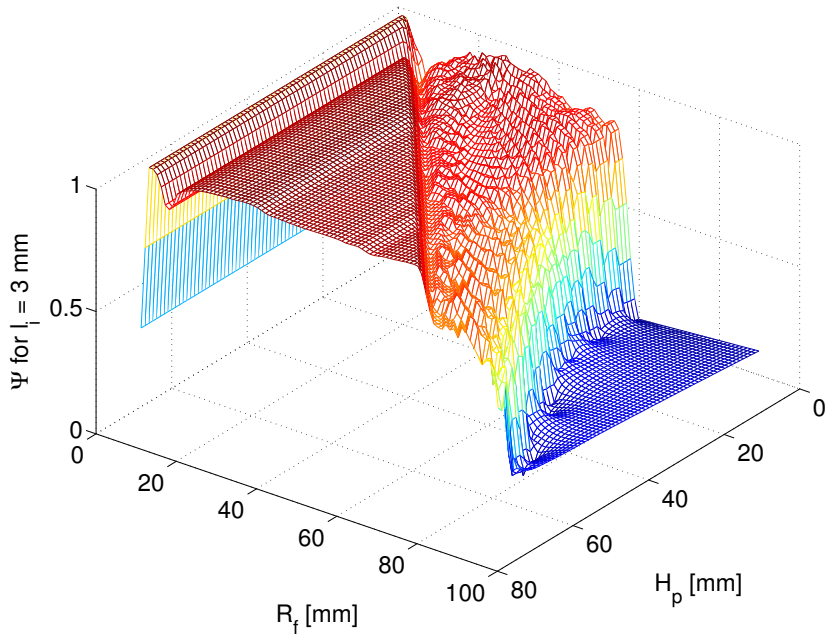

Figure 3.22: Ψ coefficient map for a fixed $l_i(t) = 3\ mm$

Model identification. To adjust the model to the experimental data, three parameters are be calibrated. Those parameters are:

- The coefficient c_r in Equation (3.4.12), which adjusts the maximum length scale of the fractal coefficient $\Xi(t)$ ($L_{max}(t) = c_r R_f(t)$),
- the second parameter is the mechanism to simulate the spark ignition that consists in a dirac of burned mass at the ignition time,
- and the third parameter to adjust is C_2 in Equation (3.3.7) that adjusts Woschni's approach for the wall losses.

Once the complete engine model is calibrated, the tuning parameters of the system are stored in look-up tables and the model can be used as virtual engine for different applications. The tuning parameters are obtained through classic identification procedures from test bench data.

In order to summarize the flame-wall interaction model proposed, a scheme of the modeling procedure is presented in Figure 3.23. In order to build $\Psi(t)$, the cylinder geometry is used together with two main hypothesis:

- the quenching distance is the integral scale $l_i(t)$,

- there is a linear decay in the burning rate when the flame surface is close to the cylinder walls.

With this assumptions, the coefficient $\Psi(t)$ is designed according to Equation (3.6.15) to take into account the flame-wall interaction during the whole combustion process. $\Psi(t)$ models the flame-wall interaction in the early flame development (i.e. when the flame approaches the cylinder top) and also at the end of the combustion when the flame is extinguished in the cylinder walls.

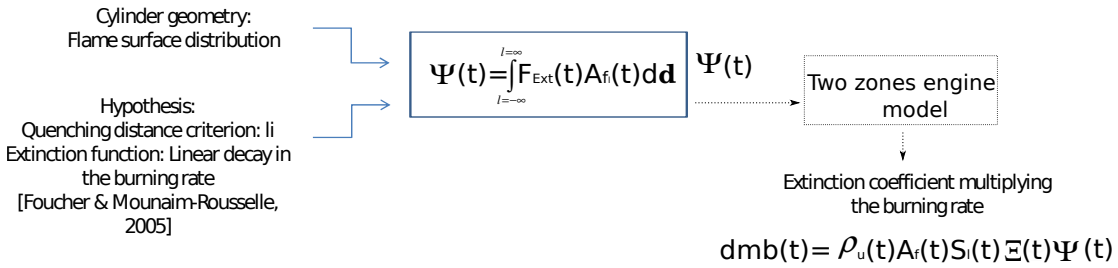

Figure 3.23: *Local approach* modeling scheme

3.6.3 Flame-wall interaction *local approach*: Model validation and results

Two validations of the engine model including the *local approach* for the flame-wall interaction are performed, the first one aims to compare the *global approach* with respect to the *local approach* proposed in this thesis. In the second validation, the efficiency and validity of the model for changes in the spark plug position is tested. The main characteristics of each validation are summarized in the following paragraphs.

Validation 1. Engine model presented in Section 3.3, fractal combustion model presented in Section 3.4.4 and $k-\epsilon$ turbulence model presented in Section 3.5.1. The references are taken from the measurements on a 2 liters engine whose main characteristics are presented in Table 3.4.

Validation 2. Engine model presented in Section 3.3, fractal combustion model presented in Section 3.4.4 and $K-k$ turbulence model presented in Section 3.5.2. The references are taken from the measurements on a 2 liters engine whose main characteristics are presented in Table 3.5.

Displacement: 1998 cm3
Bore x Stroke: 82.7x93 mm
Number of cylinders: 4
Number of valves: 16
Volumetric ratio: 9.3:1
Max Rev: 6000 rpm
Min Rev: 1000 rpm

Table 3.4: Model validation 1. Engine Test Characteristics.

3.6.3.1 Model validation 1: comparison with the *global approach*

Figure 3.24 shows $\Psi(t)$ for a simulation when the chosen distance to have the walls influence is set to $l_i(t)/2$ with $l_i(t) = 0.05\sqrt[3]{V(t)}$ according to [Bozza et al., 2007]. The test was performed at $N = 5250\,rpm$, IMEP $= 11.4\,bar$. At the beginning of combustion, $\Psi(t) = 1$ because all the flame surface is propagating freely across the chamber. This means that the flame surface is not influenced by the walls ($\Xi(t)$ is weighted by $\Psi(t) = 1$). Once the flame starts to get close to the walls, $\Psi(t)$ decreases because part of flame has already touched the walls, thus decreasing the burning rate. In the figure, $\Psi(t)$ exhibits a saw tooth behavior: at each computation step, $\Psi(t)$ is interpolated depending on the current flame surface that reaches a distance $d_i(t) < l_i(t)/2$ from the cylinder walls. If the free flame surface spreading in the combustion chamber is smaller than the flame surface lost in the barrier (i.e. the cylinder head), it might happen that the flame surface used to compute the flame surface fraction $A_{f_{d_i}}$ (Equation (3.6.14)) at the current step is smaller than the fraction computed in the previous step, then $\Psi(t)$ decreases for the current computation.

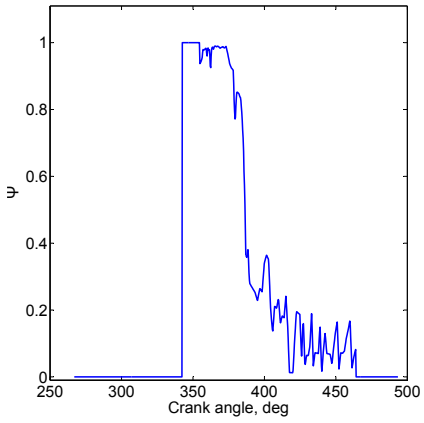

Figure 3.24: Evolution of Ψ during simulation.

The main results are shown in Figure 3.25, where the comparison of the simulations

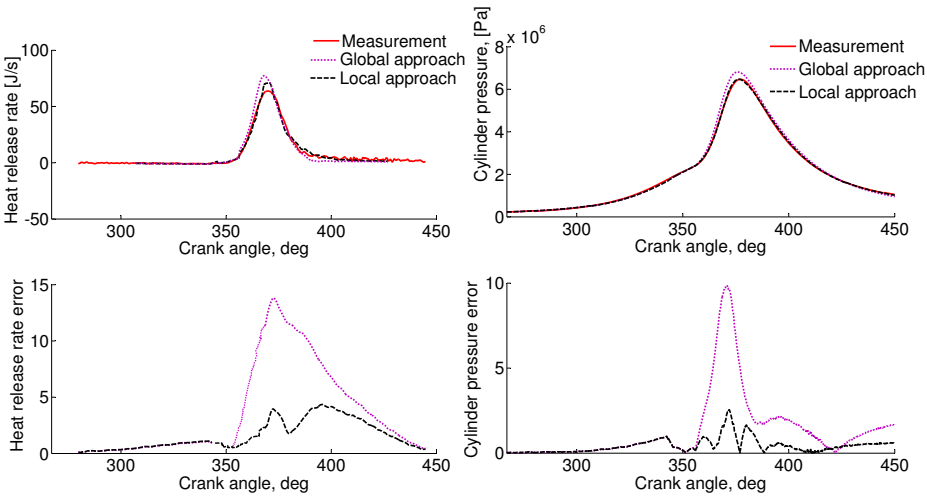

(a) Heat release rate (b) Cylinder Pressure

Figure 3.25: Heat release rate and cylinder pressure, comparison between the local approach and the global approach. IMEP = 11.4 bar, N = 5250 rpm.

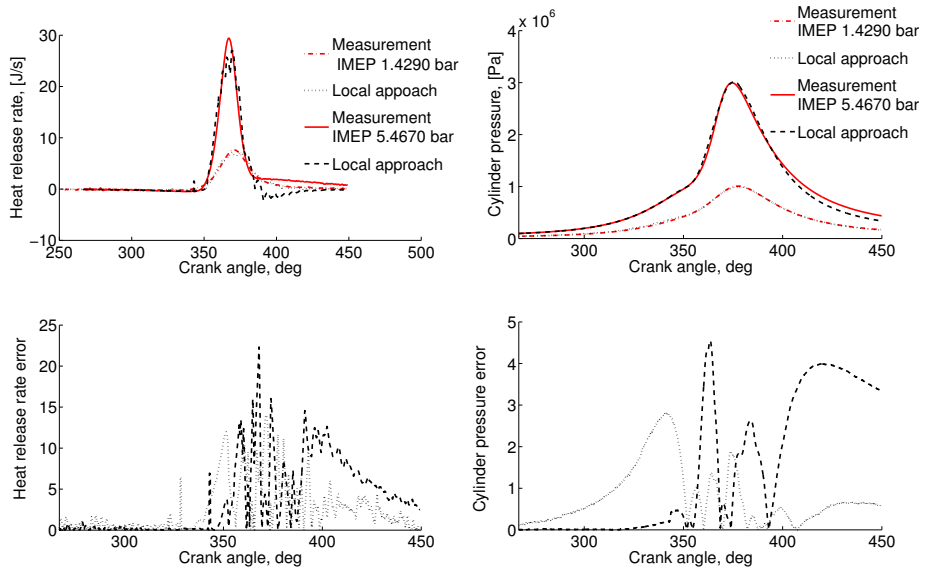

(a) Heat release rate (b) Cylinder Pressure

Figure 3.26: Heat release rate and cylinder pressure. N=1000rpm

when $\Psi(t)$ is included with respect to the *global approach* model are presented. The data to fit the model are the cylinder pressure (b tag in the figures) and the rate of energy released (a tag in the figures), the error is also depicted in the figures, which is computed as the relative difference between the curves with respect to the maximum of the reference in percentage. In the figures, the measurements are presented in solid lines and the model results before and after the inclusion of $\Psi(t)$ are in dotted and dashed

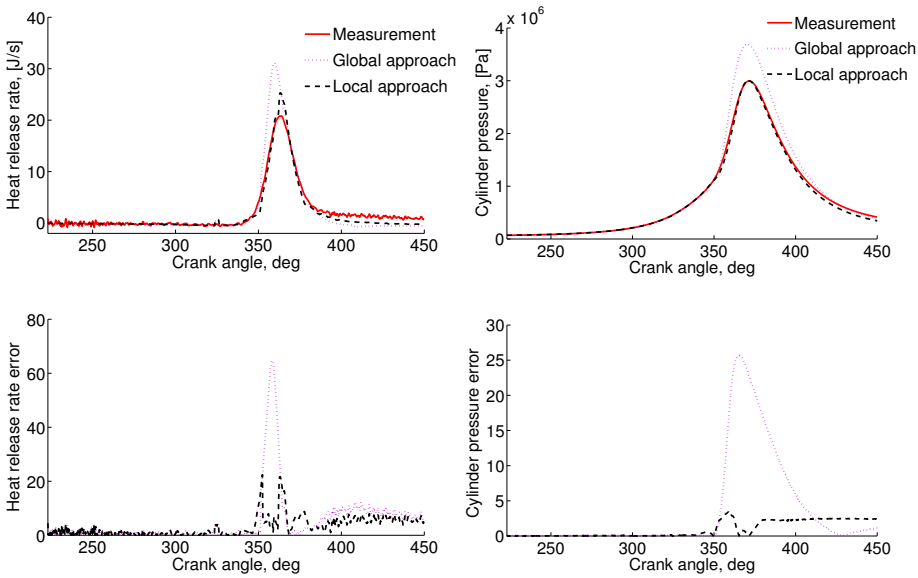

(a) Heat release rate (b) Cylinder Pressure

Figure 3.27: Heat release rate and cylinder pressure, comparison between the local approach and the global approach IMEP=4.723 bar, N=4400rpm.

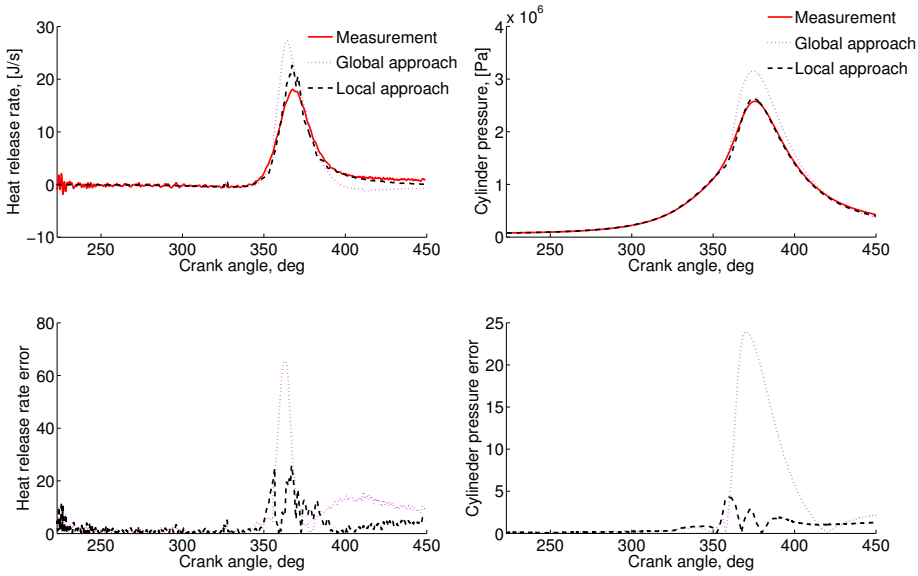

(a) Heat release rate (b) Cylinder Pressure

Figure 3.28: Heat release rate and cylinder pressure, comparison between the local approach and the global approach. IMEP=4.75 bar, N=4000rpm.

line, respectively.

In Figure 3.25b, the cylinder pressure has its maximum after the TDC, but before the cylinder charge is fully burned. It coincides with the moment when most of the

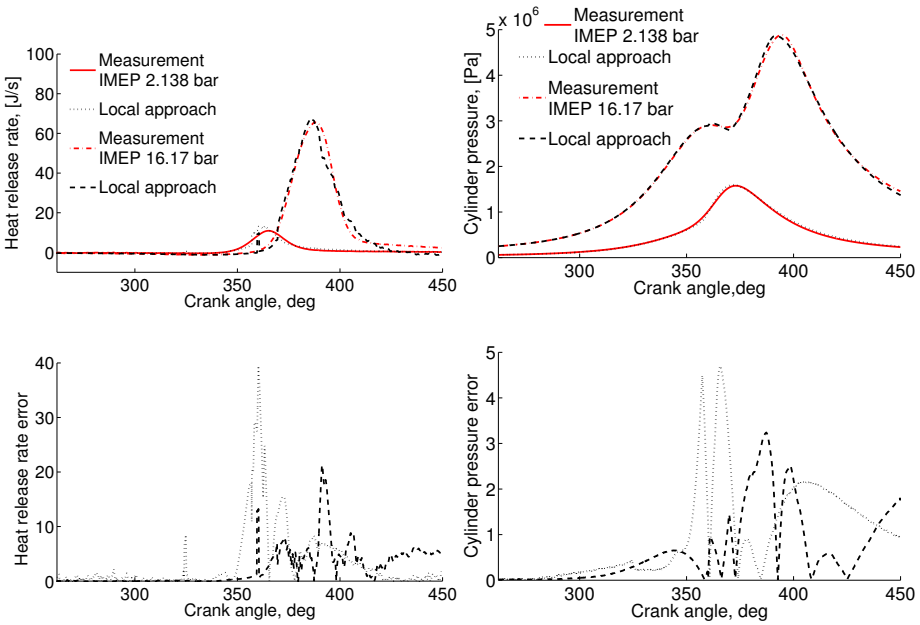

(a) Heat release rate (b) Cylinder Pressure

Figure 3.29: Heat release rate and cylinder pressure. N=1700rpm

flame reaches the cylinder walls [Heywood, 1988]. For this reason, when $\Psi(t)$ is not included in the system, the heat release rate shown in Figure 3.25a and the cylinder pressure in Figure 3.25b show an abrupt rise because the burning rate deceleration is not taken into account. Similarly, the cylinder pressure shows a bigger peak than expected when compared with the measurements. When $\Psi(t)$ is included, the heat release rate is reduced because of the deceleration on the burning rate. As a consequence the peak on the cylinder pressure is equally reduced. It shows that the introduction of a deceleration on the burning rate is required before the cylinder charge is fully burned.

Figure 3.26 shows an experience under low speed conditions ($N = 1000\ rpm$). In low load conditions, the cyclic variation of the engine tends to be greater than in high load operating conditions [Karim et al., 1988], this behavior alters the combustion process. To represent such behavior, an appropriate model of the cyclic variation might be included.

In [Steiner & Boulouchos, 1995], it is shown that while increasing engine speed, the characteristic wrinkling scale and the Kolmogorov scale decrease. Therefore, the time arrival of the flame surface to the wall becomes smaller, lowering the influence of the quenching phenomenon. Contrary, in low speed operating conditions, the quenching phenomena become more significant. In this thesis, even if the quench model is based on an integral scale computed with a geometrical aspect, it is also related to the wrinkling phenomena via the flame radius. For this reason, the function $\Psi(t)$ might be used in low speed as well as in high speed operating conditions. For the model proposed in this

thesis, a bigger integral scale in low operating conditions means a less steep slope on the extinction function presented earlier; giving a bigger deceleration of the burning rate, which would be the desired effect for low speed conditions. To be more coherent with the phenomena, a more accurate approximation of the integral scale taking into account the engine speed is recommended.

Further results are shown in figures 3.27, 3.28 and 3.29.

3.6.3.2 Model validation 2: spark plug position changes

To test the validity of the flame-wall interaction model with respect to changes in the combustion chamber geometry, two positions of the spark plug and two different spark plug types were tested. The flame surface geometry for the two positions of the spark plug and the two spark plug types were used to build the function $\Psi(t)$ for each case. The experiences described next were carried out and the obtained measurements were compared with the two zones engine model using the *local approach* for the flame-wall interaction. To calibrate the model, three parameters were adjusted: C_2 for the heat wall losses law (equation (3.3.7)), the coefficient c_r for the maximum wrinkling length (equation (3.4.12)) and a the mechanism to simulate the spark ignition that consists in a dirac of burned mass at the ignition time. A simplex search method was used to find the optimal solution for these parameters.

The new $K-k$ based turbulence model presented in 3.5.2 is used for the results presented in this section.

Experimental setup Experiments were carried out in a mono-cylinder SI engine characterized by a four-valve pent-roof chamber. Table 3.5 summarizes the main characteristics of the engine.

Bore x Stroke: 88x80 mm
Volumetric ratio: 9.5:1
Engine speed: 1998 rpm

Table 3.5: Model validation 2. Engine Test Characteristics

The engine was driven by an electric motor at a fixed engine speed and equipped with an optical encoder mounted on the main shaft, giving a 0.1 crank angle degree (CAD) as resolution. A conventional spark plug with an electrode space of $1\,mm$ as well as a projected tip spark plug were used. A timer card ensured the synchronization of the various trigger signals and the data acquisition systems. The engine sucks-in the air and a thermal mass flow-meter measure the mass flow. The iso-octane quantity was measured

by using a $0 - 8$ kg/h Brooks Quantim (QMBM) Coriolis mass flow meter. Before the intake pipe, the gases passed through a plenum volume, to avoid pressure oscillations inside the intake port. To provide a premixed air-fuel mixture inside the intake pipe, the liquid fuel was injected at inlet valve closure.

The cylinder pressure was recorded with a water-cooled AVL quartz pressure transducer connected to a charge amplifier at 0.1 CAD resolution. Before the experiments, the transducer was calibrated with a Keller high pressure hydraulic calibrator. The absolute cylinder pressure was deduced by equalizing the in-cylinder pressure at 20 CAD after inlet valve opening timing to the intake mean absolute pressure. Thus, 100 consecutive cycles of cylinder pressure data were acquired by a PC equipped with a National Instruments acquisition board.

The cylinder head is symmetric. Two spark plug positions were tested: centered in the cylinder head and shifted 14 mm from the cylinder head center. As well, two kinds of spark plug were exchanged for the tests, a standard spark plug and a projected tip electrode of 9.95 mm spark plug. Thus, for different engine operating conditions, two positions for the first spark plug and two positions for the second spark plug were used. Table 3.6 summarizes the four different validation choices.

Centered position	Standard spark plug type
	Projected spark plug type of 9.95 mm
Shifted position 14 mm	Standard spark plug type
	Projected spark plug type of 9.95 mm

Table 3.6: Spark plug changes validation

Several ignition times are investigated, for the centered position the variation goes from 25 CAD to 41 CAD before TDC and the lateral position the variation goes from 33 CAD to 47 CAD before TDC with a 2 CAD variation step between each explored operating point. The tests were performed at 2000 rpm.

Figure 3.30 shows the cylinder head where the two spark plug positions are indicated. The projected tip electrode spark plug is also shown.

Spark plug position changes results The model was tested with the procedure presented in Section 3.6.3.2. The tests were performed at 2000 rpm. At this speed, the quenching distance is relevant with respect to higher engine speeds [Steiner & Boulouchos, 1995]. Figures 3.31a and 3.31b show a resulting $\Psi(t)$ for two different experiences with the classic spark plug and the projected tip spark plug.

In the figures, $\Psi(t)$ decays fast at the beginning of the process and then rises again before the complete decay. This phenomenon is due to the fact that at the beginning, the early

(a) Test Engine (b) Projected tip spark plug

Figure 3.30: Experimental engine

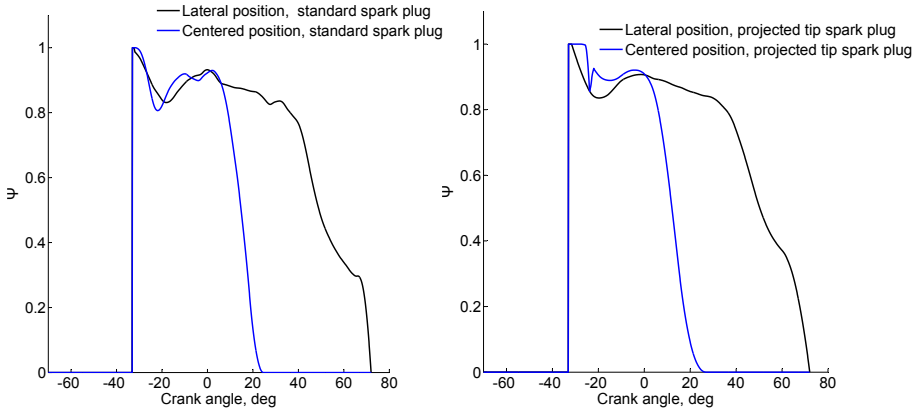

(a) $\Psi(t)$ (b) $\Psi(t)$

Figure 3.31: Evolution of $\Psi(t)$ during simulation for two positions of the spark plug.

flame reaches the cylinder head, resulting in a big portion of the existent flame touching the walls, which is taken into account in the $\Psi(t)$ function. This decrease is faster in the lateral position, because the flame reaches the cylinder head and a lateral portion of the cylinder, which is not the case in the centered position where the flame kernel touches symmetrically the head of the cylinder at the beginning of the process.

In Figure 3.31b, it is possible to see that for the centered position of the projected tip spark plug, the flame kernel propagates freely at the beginning of combustion ($\Psi(t) = 1$ for about 10 CAD) due to the fact that the flame is further from the cylinder head. After the rapid decrease during the beginning of combustion, $\Psi(t)$ shows a period of fast increase. This phase is due to the flame quenching and extinction when the flame reaches simultaneously the cylinder head and the side-wall of the cylinder, leading to a

smaller fraction of the flame surface interacting with the walls (Equation (3.6.14)). This phenomenon is accentuated for centered positions of the spark plug due to symmetry effects. To complete these results, in Figures 3.32a and 3.32b are presented two examples of the wrinkling coefficient $\Xi(t)$ and the corresponding factor $\Xi(t)\Psi(t)$ that multiplies the burning rate Equation (3.6.13), for different spark plug types and spark plug locations. As it can be seen in the figures, the function $\Psi(t)$ introduces a diminution in the wrinkling coefficient $\Xi(t)$ that results in a deceleration in the overall burning rate of the simulation. The effect of $\Psi(t)$ is introduced some degrees after the IT. In the figures: $IT = 33\ deg, \quad N = 2000$.

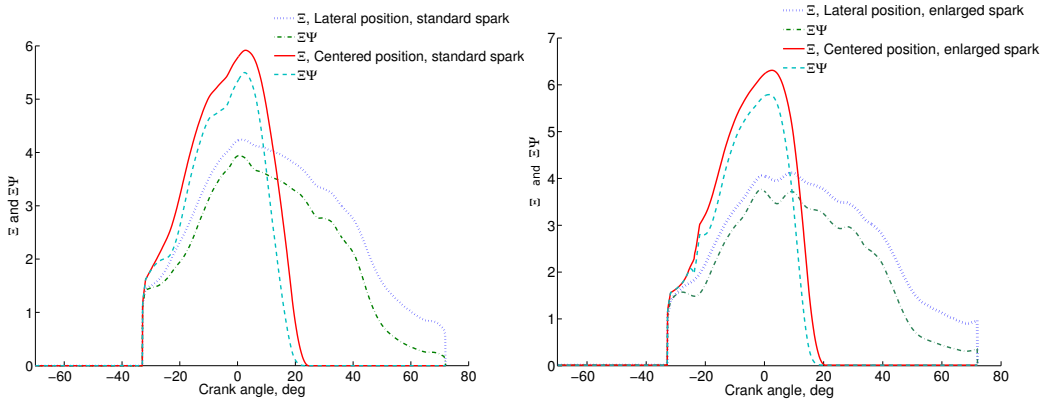

(a) $PMI = 4.62\ bar$ and $PMI = 5.19\ bar$ (b) $PMI = 4.64\ bar$ and $PMI = 5.09\ bar$

Figure 3.32: Evolution of $\Xi(t)\Psi(t)$ during simulation.

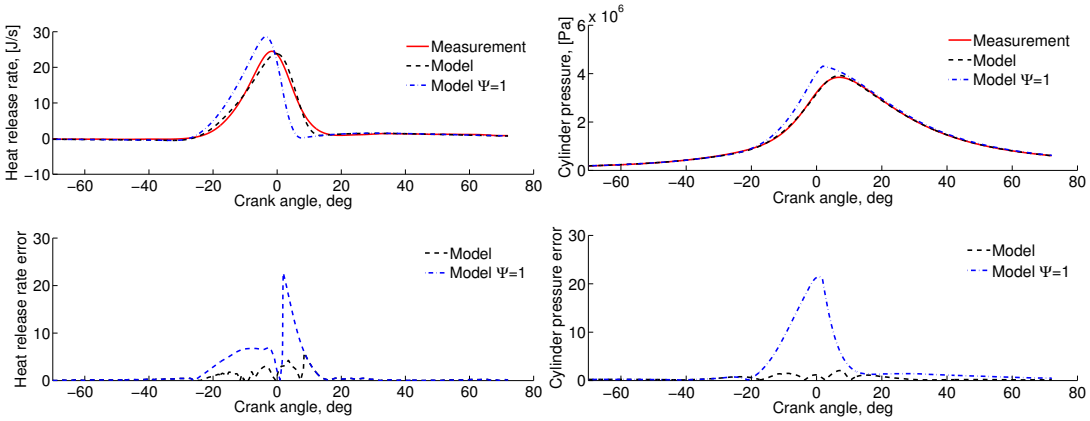

(a) Heat release rate (b) Cylinder Pressure

Figure 3.33: Heat release rate and cylinder pressure. Centered spark plug position. Standard spark plug type. IMEP=5.03 bar, Ignition Time=39 CAD before TDC.

To test the validity of the combustion model, it is compared with the pressure and the rate of energy released of the measurements. Different comparisons for many experiences

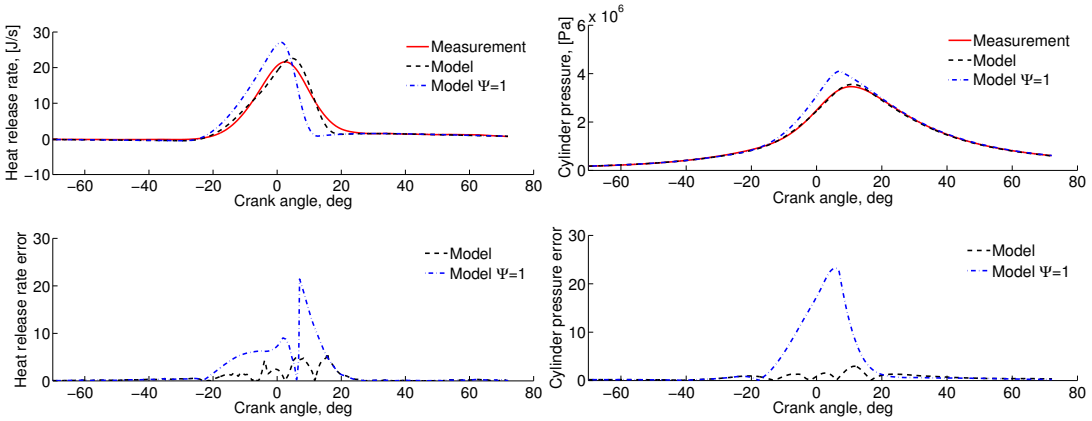

(a) Heat release rate (b) Cylinder Pressure

Figure 3.34: Heat release rate and cylinder pressure. Centered spark plug position. Standard spark plug type. IMEP=5.17 bar, Ignition Time=35 CAD before TDC.

are plotted in Figures 3.33 to 3.39. In the figures, the simulation of the two-zones model using the flame-wall interaction model are presented, as well, the simulations were performed without the flame-wall interaction scheme ($\Psi = 1$). As depicted, very satisfactory results were obtained. The errors on the heat release rate and the cylinder pressure are reduced approximately by a factor of 3 thanks to the proposed *local approach* with respect to the *global approach*. When including Ψ multiplying the burning rate, the simulations improve dramatically with respect to the simulations where there is no flame-wall interaction modeling.

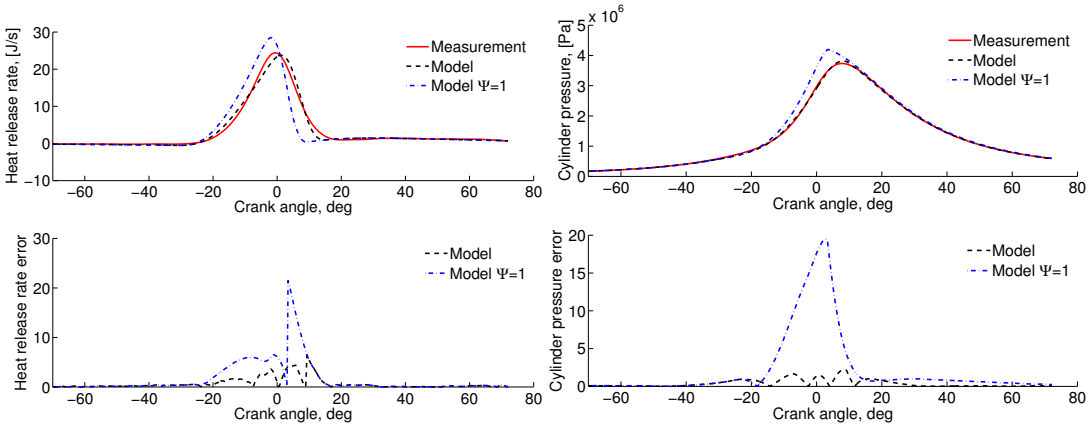

(a) Heat release rate (b) Cylinder Pressure

Figure 3.35: Heat release rate and cylinder pressure. Centered spark plug position. Projected tip spark plug type. IMEP=5 bar, Ignition Time=37 CAD before TDC.

Including $\Psi(t)$ in the engine model, provides a heat release rate reduction during the combustion process, modeling the deceleration on the burning rate due to the flame-wall

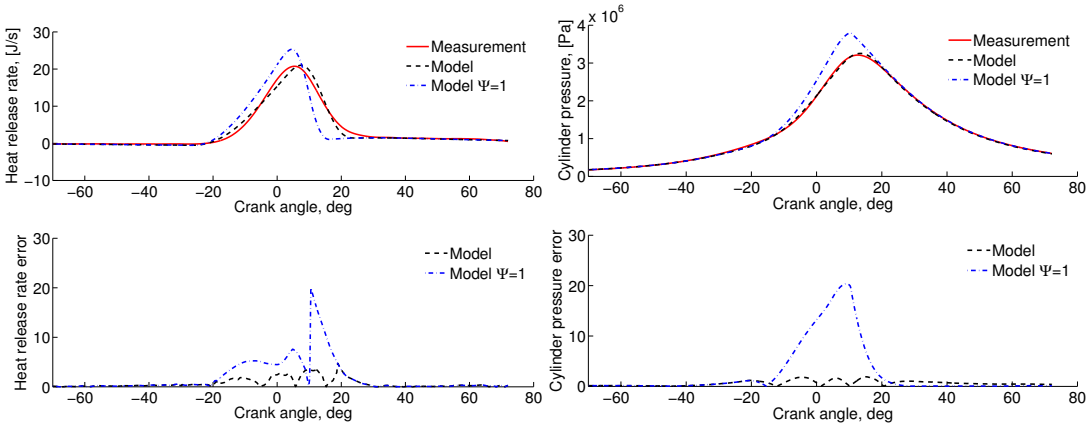

(a) Heat release rate (b) Cylinder Pressure

Figure 3.36: Heat release rate and cylinder pressure. Centered spark plug position. Projected tip spark plug type. IMEP=5 bar, Ignition Time=31 CAD before TDC.

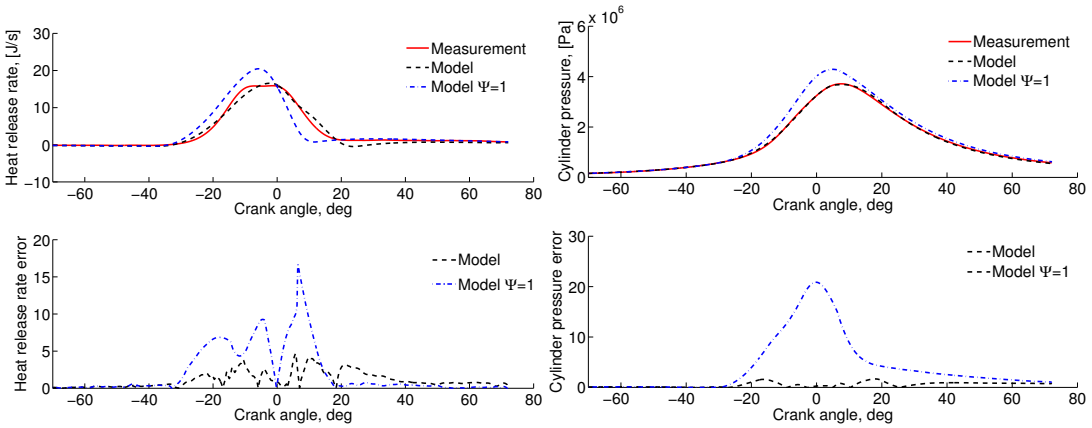

(a) Heat release rate (b) Cylinder Pressure

Figure 3.37: Heat release rate and cylinder pressure. Lateral spark plug position. Standard spark plug type. IMEP=4.92 bar, Ignition Time=45 CAD before TDC.

interaction. In the figures, the measurements are presented in solid lines and the model results are in dashed lines. The error is computed as the relative difference between the curves with respect to the maximum of the reference. The error is presented in percentage. The errors on heat release rate and cylinder pressure are below 5% during combustion and below 10% in the overall cycle. The mean errors in all cases remain below 3%. Table 3.7 summarizes the results depicted in the figures.

Those results are very satisfactory as there is an improvement with respect to the results when using a *global approach*, where the error was bigger than 15%. The presented results show that $\Psi(t)$ can represent the impact of the cylinder walls for a 0D combustion model. As $\Psi(t)$ is conceived as a dimensionless function multiplying the burning rate, it might

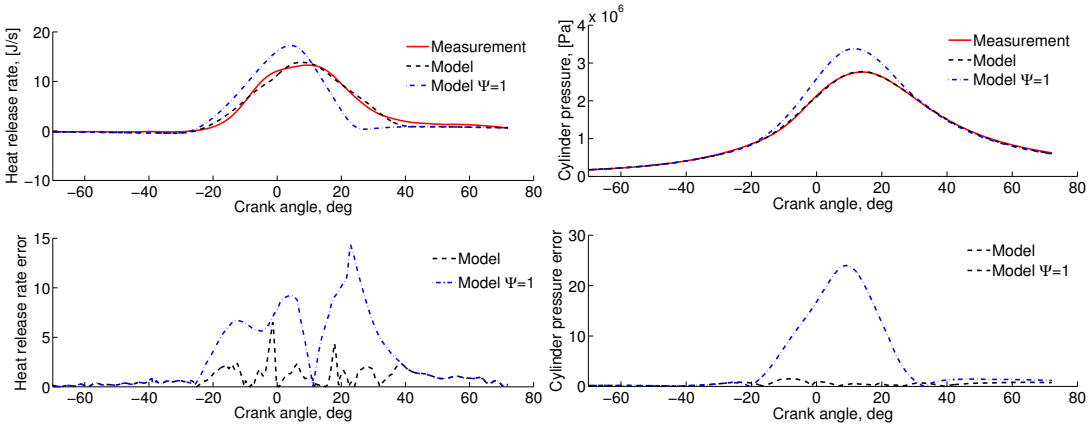

(a) Heat release rate (b) Cylinder Pressure

Figure 3.38: Heat release rate and cylinder pressure. Lateral spark plug position. Standard spark plug type. IMEP=4.98 bar, Ignition Time=39 CAD before TDC.

be used in many 0D combustion models.

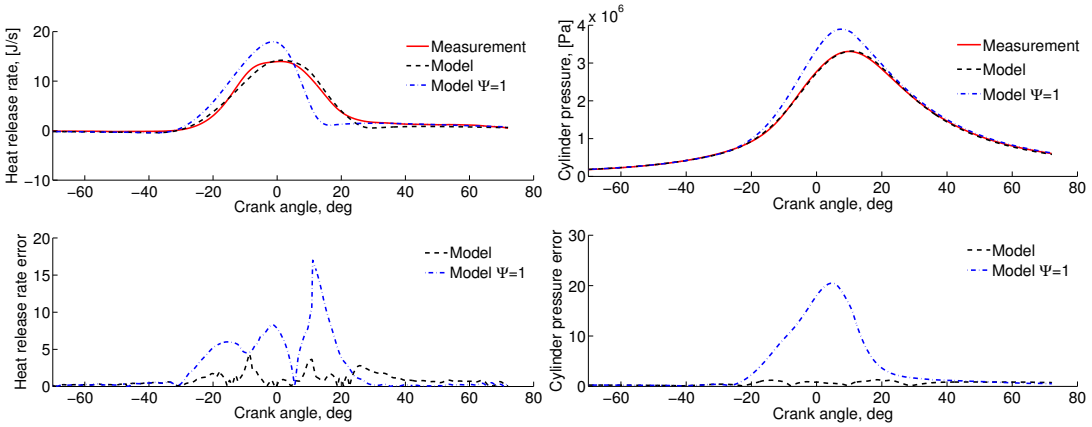

(a) Heat release rate (b) Cylinder Pressure

Figure 3.39: Heat release rate and cylinder pressure. Lateral spark plug position. Projected tip spark plug type. IMEP=4.87 bar, Ignition Time=47 CAD before TDC.

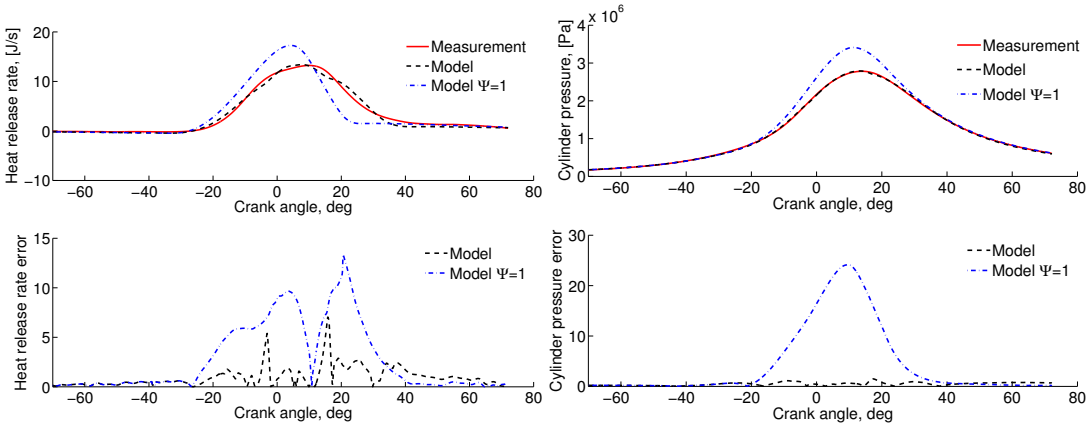

(a) Heat release rate (b) Cylinder Pressure

Figure 3.40: Heat release rate and cylinder pressure. Lateral spark plug position. Projected tip spark plug type. IMEP=4.9 bar, Ignition Time=39 CAD before TDC.

Figure	Spark plug type	Position	IMEP [bar]	IT [deg]	dQ mean error %	p mean error %
3.33	Standard	Centered	5.03	39	2.73	1.12
3.34	Standard	Centered	5.17	35	2.63	0.88
3.35	Projected	Centered	5	37	2.59	0.87
3.36	Projected	Centered	5	31	2.58	0.83
3.37	Standard	Lateral	4.92	45	3.25	0.74
3.38	Standard	Lateral	4.98	39	3.11	0.7
3.39	Projected	Lateral	4.87	47	3.4	0.84
3.40	Projected	Lateral	4.9	39	3.25	0.8

Table 3.7: Spark plug changes validation results summary. dQ is the heat release rate and p the cylinder pressure

3.7 Chapter Summary

The definition of a new model referred to as *local approach* that models the impact of the cylinder walls on the burning rate has been proposed. This new model takes into account the impact of the cylinder walls on the combustion process using the flame surface distribution with respect to the combustion chamber walls and the assumed linear decay during the flame-wall interaction. A well-defined geometric model of the combustion chamber has been designed in order to have more realistic results.

The model has been validated against experimental measurements. When the flame-wall interaction is not well taken into account, the energy release is usually overestimated at

the end of the combustion process, as well as the cylinder pressure. When the proposed flame-wall interaction model is included, very good results are obtained; the model improves dramatically with an enhanced fit to the measurements when compared to less accurate approximations, in terms of heat release rate and cylinder pressure estimation.

To determine the validity of the combustion model and the flame-wall interaction model in different conditions, an experimental setup was implemented where the combustion process was performed for two locations of the spark plug and two spark plug types. The model was validated by comparing simulated cylinder pressure and energy release rate with the experimental measurements. A good agreement between the implemented model and the experience was obtained.

The model has been validated against experimental measurements under low engine speed conditions, where the quench thickness is thicker than at high speed conditions, which leads to a major influence of the flame-wall interaction phenomenon on the combustion process.

The main objective of proposing this thermodynamical model is to contribute to the development of the engine control based design strategy to improve the engine performance and to meet the emissions and pollution normative. This engine might be used as reference model for the design of more simple modeling schemes to be used for control and observation purposes. This model might be used as reference to calibrate several engine parameters or more simpler combustion models (i.e parametric models) when there are not enough experimental measurements.

Chapter 4

Observers for enclosed mass estimation in the combustion chamber for a SI engine

The estimation of the total mass enclosed in the combustion chamber, that corresponds to the air plus the fuel and the recycled gases in the combustion chamber, after the inlet valve closure (IVC), is an interesting and challenging task for the engine modeling and control community. An accurate estimation of the cylinder enclosed mass allows a better control of the associated fuel injection and a better treatment of the pollutant residuals. Besides, among several objectives in Renault, it is the aim to:

- use as operating reference for the engine conditions the engine speed N and the enclosed mass in the combustion chamber (m_{IVC}), instead of the current references that are N and the fill-in parameters (Appendix A.2),
- being able to control the amount of mass in the combustion chamber after the IVC,
- and improve the engine calibration process knowing *a priori* the enclosed mass in the combustion chamber.

The introduction of sophisticated features such as variable valve timing (VVT), cam profile switching and variable geometry intake manifold in new production engines might result in the appearance of back flow inside the combustion chamber. This phenomenon combined with possible mass scavenging might induce a difference between the actual mass in the combustion chamber and the measurement provided by the mass flow meter in the intake manifold. Thus, the inclusion of these features require more advanced techniques to estimate the cylinder enclosed mass [Butt & Bhatti, 2008].

This thesis is focused on the modeling of a more physical description of the 0D engine modeling. In most of the engine models, the enclosed mass in the combustion chamber is assumed as known parameter equal to the measurement from the flow meter upstream the intake manifold. However, as it has been reported, this measurement contains inaccuracies due to the introduction of features as the VVT. Thus, an estimation strategy for the enclosed mass might be necessary to obtain realistic engine cycle simulations.

It is a common approach to estimate the enclosed mass in the combustion chamber using the variables in the engine air path (intake manifold pressure, exhaust manifold pressure, detailed valves profiles). However, since the cylinder pressure sensor might appear in future engines, it is evident that this sensor might give more precise information of the combustion process itself than the air path variables. The use of cylinder pressure measurements to estimate variables as the enclosed mass in the combustion chamber, the richness or the *knock*, among others, is presented as a promising method in the engine research. The two zones model proposed previously makes it possible to apprehend the basis of the 0D thermodynamical engine modeling in order to build a more simpler modeling scheme for the enclosed mass observers design.

The aim is to design an estimation strategy that uses the cylinder pressure measurement to estimate the enclosed mass in the combustion chamber of a SI engine (refer to Section 3.2 for the SI engine operation). The synthesis of two observers that use the cylinder pressure measurement during the compression and combustion strokes is proposed. The estimation principle relies on the assumption that it is possible to observe the cylinder temperature from an engine model that includes the wall losses. The enclosed mass is estimated with the cylinder pressure and the observed cylinder temperature. The estimated mass contains all the species in the combustion chamber and the air load can be computed by subtracting the residual mass from the total enclosed mass estimated. Several strategies such as the proposed in the Appendix A.2.1 might be used to compute the residual mass.

Chapter structure This chapter is introduced with a review of different strategies to compute the enclosed mass in the combustion chamber. Then, a 0D thermodynamical one zone model which has been validated against experimental measurements is proposed to be used for observers design. This model is based on the same physical principles than the engine model presented in Sections 3.3 and 3.4, but its dynamics is less complete with respect to the burning rate and the thermodynamical characteristics of the gases. Nevertheless, the one zone model represents well enough the physical processes regarding the engine thermodynamics and is appropriate for observer design.

A sliding mode observer for the wall losses estimation is presented later. This observer is derived from the 0D one zone thermodynamical engine model and its convergence and stability are proved. Based on these results, a reduced model for the heat wall losses

has been developed, such a model makes it possible to simplify the strong nonlinearities of Woschni's law presented in Equation (3.3.7). The enclosed mass observers are built using the 0D one zone engine model during the valves closure along with the heat wall losses reduced model.

The first observation strategy for the enclosed mass estimation is a high gain observer. This method is based on the fact that the system can be expressed in an additive triangular form. Thus the engine model is transformed into an equivalent system in additive triangular form, where the high gain observer is synthesized and the cylinder enclosed mass is computed. The second observation strategy is a parameter varying observer. In this strategy, a high gain observer is designed for a parameter varying polytopic model. The high gain strategy allows designing an observer that handles the uncertain part of the system, which is related to the observed state.

Remark 4.0.1. The sliding mode observer for the wall losses estimation was built with the aim to find a correlation between the engine wall losses and the cylinder temperature. This information together with the cylinder pressure would allow finding a static expression to estimate the enclosed masses. This strategy was not considered finally because the enclosed mass estimation results were deficient. Nevertheless, the synthesis of the sliding mode observer is an interesting result, which allows for a better understanding of the heat wall losses phenomenon.

Table 4.1 summarizes the observation strategies developed in this thesis, the application, the reference model used in each case and the range of validity of each strategy with respect to the engine cycle.

Sliding mode observer, Section 4.4	Heat wall losses estimation 0D reference one zone model Section 4.3 Computed during the whole engine cycle Valid during the valves closure.
High gain observer, Section 4.6	Enclosed mass estimation Reduced model in Section 4.5 Computed during the valves closure. Valid during the compression and combustion strokes.
LPV high gain observer, Section 4.7	Enclosed mass estimation Reduced model in Section 4.5 Computed during the valves closure. Valid during the compression stroke.

Table 4.1: Implemented observers, application and range of validity

The main contributions presented of this chapter are the principal subject of the following

publications:

- M. Rivas, E. Witrant, O. Sename and P. Higelin. Model Based High Gain Non Linear Observer for Enclosed Mass Estimation in a Spark Ignited Engine. IEEE American control conference, Montreal 2012.

- M. Rivas, O. Sename, E. Witrantl, P. Higelin and C. Caillol. Model Based High Gain Non Linear Observer for Enclosed Mass Estimation in a Spark Ignited Engine. IFAC ECOSM 2012, Rueil Malmaison.

- M. Rivas, O. Sename, E. Witrant, P. Higelin and C. Caillol. Energy Wall Losses Estimation of a Gasoline Engine Using a Sliding Mode Observer. SAE 2012-01-0674. 2012. SAE Technical Paper included in Modeling of SI and Diesel Engines, 2012.

4.1 Chapter nomenclature

All variables are in SI Metric Units.

Variables

A_w	Heat transfer wall area
h_c	Heat transfer coefficient for convective wall losses
H_p	Piston height
m	Total mass in the combustion chamber
p	Pressure
δQ_{th}	Wall losses
T	Temperature
U	Energy
V	Cylinder volume
ρ	LPV parameters
θ	Crank angle degree (rad)

Constant parameters

c_v	Specific heat at constant volume
k_0	Calibration constant
k_1	Calibration constant
N	Engine speed (rpm)
r	Specific gases constant
T_w	Wall temperature
ω	Engine speed (rad/s)

Acronyms

CAD	Crank angle degrees
EVC, EVO	Exhaust Valve Closure, Opening
IVC, IVO	Inlet Valve Closure, Opening
EVO_d, IVC_d	Exhaust Valve Closure delay, Inlet valve closure delay
IT	Ignition timing
$IMEP$	Mean effective pressure (bar)
LPV	Linear parameter varying

4.2 Enclosed mass in a SI engine: estimation strategies review

A large number of open loop techniques have been proposed recently to compute the total enclosed mass and/or the in-cylinder load. In those models, a balance between the total mass in the cylinder at the inlet valve closure (IVC), the back flow and the trapped mass at exhaust valve closure (EVC) are taken into account. Following the open loop strategy, iterative approaches that use the cylinder pressure measurement during the compression and combustion strokes have also been proposed. Alternatively, closed loop observer schemes have also been developed to estimate the engine load during the intake stroke, thus constraining the estimated variables with the online measurement. In this section, a review of some modeling techniques to estimate the enclosed mass in the combustion chamber and/or the in-cylinder load are described. Similarly to the contributions proposed in this thesis, these works are merged in projects related to the achievement of the severe emission regulations, because knowing precisely the air mass and the fuel mass that must be injected in the cylinder, allows for a better performance

of the post treatment stage.

4.2.1 Hart, Ziegler and Loffeld: Adaptive model for the cylinder air mass model

In this model proposed in [Hart et al., 1998], an adaptive Kalman filter is used to compute the temperature of the air mixed with the fuel T_{AF}, this variable together with the cylinder pressure during the compression stroke is used to define the air mass in the cylinder. The main hypothesis of this model is that the cylinder pressure is measured and that T_{AF} changes with the operating conditions but that it can be modeled as an adaptive parameter instead as a state.

The air mass m_{air} in the cylinder is modeled as a balance between the computed mass shortly after the IVC, the IGR masses m_{igr} and the injected fuel m_{fuel} as:

$$m_{air} = \overbrace{\frac{p_2 V_2}{R T_{AF}} \left(\frac{V_2}{V_1}\right)^{\gamma-1}}^{\text{mass after IVC}} - \frac{T_{RG}}{T_{AF}} m_{igr} - m_{fuel} \tag{4.2.1}$$

In the equation, the sub index 1 makes reference to the IVC moment (t_1) and the sub index 2 to any moment after the IVC during the compression stroke (t_2). p_2 is the cylinder pressure, V_2 is the cylinder volume, γ is the polytropic exponent and T_{RG} is the residual gas temperature. m_{igr} is computed with the model proposed in [Fox et al., 1993] and detailed in the appendix A.2.1, m_{fuel} is represented by a wetting model proposed in [Aquino, 1981]. The dynamics of the model is formulated as a first order Markovian noise process as:

$$\begin{aligned} \dot{x_1} &= \frac{V_2}{R T_{AF}} \left(\frac{V_2}{V_1}\right)^{\gamma-1} x_3 - \frac{T_{RG}}{T_{AF}} \dot{m}_{igr} - \dot{m}_{fuel} \\ \dot{x_2} &= x_3 \\ \dot{x_3} &= -x_3 + w(t) \end{aligned} \tag{4.2.2}$$

where $x_1 = m_{air}$ and $x_2 = p_2$ (the cylinder pressure at time t_2). The state x_3 represents the cylinder pressure for in-stationary working conditions. $w(t)$ is the measurement noise component. The model outputs are $y = [x_1, x_2]^T$.

This model represents a complete view of the problem, because it takes into account the valves overlap, the IGR and the fuel evaporation. Similarly to the contribution of this thesis, this works considers the hypothesis of the use of a combustion pressure sensor,

which has a very high potential as it is used more and more in engine modeling and control. Considering T_{AF} as an adaptive parameter allows T_{AF} changes to be taken into account, without considering it as a dynamical variable, which reduces the complexity of the physical model.

4.2.2 Mladek and Onder: Inducted air mass and residual gas fraction model

This model proposes an iterative algorithm to compute the air load in the combustion chamber. The algorithm is summarized in the flow chart in Figure 4.1, see [Mladek & Onder, 2000]. The main hypothesis of this model are that the cylinder pressure trace with respect to the crank angle is known and that there is a fixed and stoichiometric air-fuel ratio, thus the air load m_{air} can be computed as mass balance between the total mass m_{tot} and the IGR mass m_{igr}:

$$m_{air} = \frac{m_{tot} - m_{igr}}{1 + \frac{1}{LST}} \tag{4.2.3}$$

where LST is the stoichiometric air-fuel ratio. Thus, two main parameters remain to be estimated: m_{tot} and the IGR fraction X_{igr} to compute m_{igr}.

Two conditions are assumed to initiate the algorithm: the crank angle position at 50% burned mass fraction is known (CA50) and $X_{igr} = 10\%$ for the first iteration. The total mass is computed with this information, using the ideal gases law. With the total mass computed and the characteristics of the engine cycle at IVC (pressure and volume), the IGR gases temperature T_{igr}, the fresh gases temperature T_{FC} and the mixture gases temperature T_{mean} are computed from statical expressions deduced from the system energy mass balance. A first estimation of the X_{igr} is obtained through an energy mass balance. Using this new X_{igr}, the algorithm starts again until the difference between successive values of X_{igr} is less than 4%.

As the algorithm does not contain any dynamical equation, it does not need large computational resources to be performed, however, a lot of considerations and assumptions have been done regarding the stoichiometric air-ratio and the heat exchanges. As it is an open loop strategy, there is not any feedback to correct the errors that might arise from the reference during the mass computation.

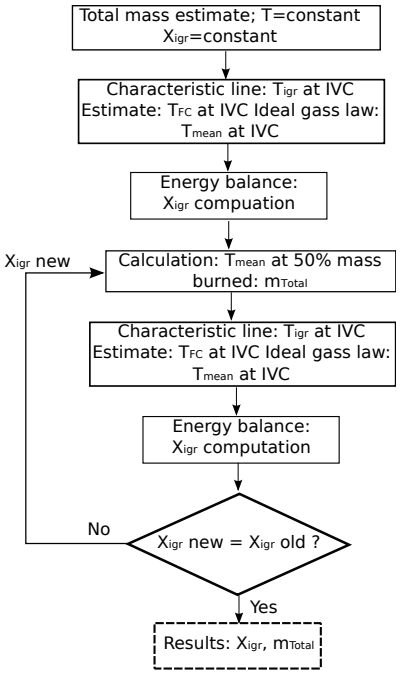

[Mladek & Onder, 2000]

Figure 4.1: Flow chart of the iterative process to compute the inducted air mass and the residual gas fraction.

4.2.3 Colin, Giansetti, Chamaillard and Higelin: In cylinder mass estimation model

This method is proposed in [Colin et al., 2007]. In this model an iterative algorithm during the compression stroke of the engine cycle is used to estimate the in-cylinder charge. The main hypothesis of this model are that the cylinder pressure with respect to the crank angle is known, the gases are considered ideal and the in-cylinder mass is considered constant as long as the valves are closed. The pressure during the compression stroke is considered as a polytropic phenomenon with a constant coefficient γ. The algorithm consists on fitting the cylinder pressure when the valves are closed before the combustion. Consequently, the first data point considered is located just after IVC and the last data point considered is located just before ignition.

The main idea of this model is to compute the residual mass fraction and recalculate the polytropic exponent γ iteratively. These two variables are used to obtain different physical variables which are used to compute the air mass m_{air}, the IGR mass fraction X_{igr} and the total mass in the cylinder m_{tot} .

In the algorithm, first the cylinder volume V is computed from the engine geometry, and the cylinder pressure p and the intake manifold pressure p_{int} are recorded. Using this information, X_{igr} is computed using an empirical correlation. The estimated cylinder

pressure is fitted assuming a polytropic transformation. The estimated cylinder pressure is extended from the beginning of the computation zone to the Bottom Dead Center (BDC) and a second offset compensation is computed with p_{int}. With this information, m_{tot} is computed using the ideal gas law. Finally, m_{air} at cycle n can be computed through a mass balance assuming that the residual gas fraction is known through the empirical correlation.

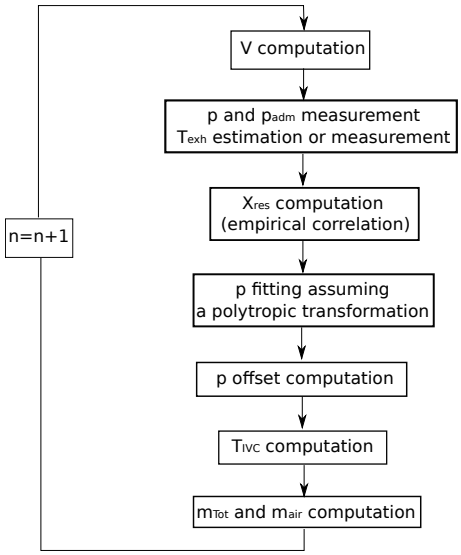

Figure 4.2: Flow chart of the iterative process in the approximation of Colin, Giansetti, Chamaillard and Higelin to compute the induced air mass and the enclosed mass in the combustion chamber

This algorithm presents an interesting method to compute the air load. The procedure followed is coherent as it is based on physical laws. However, it is conceived as an statical open loop strategy, and there is not any feedback to correct the errors that might arise during the algorithm computation, besides the fact that it takes many engine cycles to yield with a result.

4.2.4 Leroy, Alix, Chauvin, Duparchy and Le Berr: Modeling Fresh Air Load and Residual Gas Fraction on a Dual Independent Variable Valve Timing SI Engine

This method is proposed in [Leroy et al., 2008]. The proposed method consists in modeling the fresh air going through the intake valve of a gasoline engine equipped with VVT. The model is composed of three terms: a first term for the in-cylinder total mass m_{tot}, a second term for the gas mass that goes through both valves during the valve overlap (either backflow of burned gas, or scavenging of fresh air) $m_{overlap}$, and a last

term modeling the residual gas mass m_{res} staying in the cylinder from one cycle to the next. Thus, the air load that goes to the cylinder through the intake valve (IV) is:

$$m_{air}^{IV} = \alpha_1(N, p_{int})\rho_{int}V_{IVC} - \alpha_2(N, p_{int})\frac{OF}{N} - \alpha_3(N, p_{int})V_{EVC} \tag{4.2.4}$$

where α_1, α_2 and α_3 are look-up tables that depend on the engine speed N and the intake manifold pressure p_{int}. ρ_{int} is the density of the gases in the intake manifold, OF is the overlap factor detailed in Appendix A.2.1 and V_{EVV} is the cylinder volume at the exhaust valve closure (EVC).

The first term models the total mass trapped in the cylinder at IVC, thus from Equation (4.2.4), m_{tot} is:

$$m_{tot} = \alpha_1(N, p_{int})\rho_{int}V_{IVC} \tag{4.2.5}$$

The physical meaning of the second term of the model comes from the OF definition (appendix A.2.1) and Bernoulli's principle which is detailed in the appendix in Figure A.2 and Table A.1, thus:

$$m_{overlap} = \alpha_2(N, p_{int})\frac{OF}{N} \tag{4.2.6}$$

The third term represents the residual gases trapped in the cylinder at EVC:

$$m_{res} = \alpha_3(N, p_{int})V_{EVC} \tag{4.2.7}$$

Finally, the residual mass fraction is computed as:

$$X_{igr} = \frac{m_{res} + m_{overlap}}{m_{tot}} \tag{4.2.8}$$

This model presents a coherent methodology. However, the accuracy of the approximation and the results depend on the mentioned data maps for the α parameters, which might not be always available. Thus, this method does not provide a model that can be directly applied in other modeling schemes.

Different methods to estimate the enclosed mass in the combustion chamber have been proposed. Those methods might be categorized as open or closed loop depending on the use of an instantaneous feedback and/or on the use of the cylinder pressure variables or the air path variables. Such methods contain advanced physical and control theory, and show very promising results.

In this thesis, the aim is to propose an alternative approach for the enclosed mass estimation during the valves closure, using the cylinder pressure and a closed loop method. A $0D$ thermodynamical engine model is developed for control purposes. This model is based on the same physical principles than the 2 zones model presented in Chapter 3, but it only considers a single gas zone in the combustion chamber.

4.3 One zone thermodynamical model for observers design

In Chapter 3, a two zones thermodynamical model to represent the engine cycle was presented. The two zones thermodynamical model represents a detailed scheme of the engine cycle, including a detailed modeling of the combustion and the flame-wall interaction. Such model has a significant degree of complexity to be used directly for control and observation purposes. However, the two zones model serves as reference to design a more simple model for the enclosed mass estimation.

A 0D one zone engine model has been designed for the design of observers for the enclosed masses in the combustion chamber. This one zone engine model is based on the same physical principles than the two zones engine model presented in the previous chapter, but it considers only one gases zone, composed by all the species in the combustion chamber (unburned gases, burned gases and fuel) as a unique and whole mixture. Besides, the thermodynamical parameters of the gas, as the specific heat c_v and the perfect gases constant r are considered as constants. Finally, the main difference lies into the combustion modeling: a Vibe's law is used to model the burning rate due to the combustion process. With this considerations, the 0D one zone model has a less complete modeling scheme than the two zones model, but its dynamics is still representative of the physical phenomena during the engine cycle. This model has been validated against experimental measurements.

4.3.1 0D one zone thermodynamical engine model

In the one zone thermodynamical model, the combustion chamber is considered as a unique open system and a uniform in-cylinder pressure is assumed. The mass flow rate

in the cylinder is deduced from a balance equation corresponding to the mass transfer through the intake and the exhaust valves.

Similarly to the two zones combustion model presented in Chapter 3, the energy equation for the cylinder is inferred from the first principle of thermodynamics:

$$dU(t) = -\delta Q_{th}(t) - p(t)dV(t) + \Big(\sum_j h_j(t)dm_j(t)\Big) \tag{4.3.1}$$

where the subscript j denotes the energy getting into or out of the combustion chamber, $U(t)$ is the internal energy of the cylinder gas mixture, $\delta Q_{th}(t)$ expresses the heat transfer of the cylinder to the surroundings, $p(t)$ is the cylinder pressure, $V(t)$ is the cylinder volume occupied by the gases, $p(t)dV(t)$ corresponds to the work delivered on the piston, $\sum_j h_j(t)dm_j(t)$ is the total enthalpy flowing into or out of the cylinder and $h_j(t)$ is the specific enthalpy.

The total energy flowing into or out of the cylinder is the enthalpy flow from the breathing process and the combustion, given as:

$$\sum_j h_j(t)dm_j(t) = dm_{h_{int}}(t) - dm_{h_{exh}}(t) + dm_{h_{comb}}(t) \tag{4.3.2}$$

where

$$dm_{h_{int}}(t) = c_p T_{int}(t)dm_{int}(t,u), \quad dm_{exh}(t) = c_p T_{exh}(t)dm_{exh}(t,u),$$
$$dm_{h_{comb}}(t) = LHV\, dm_{comb}(t,u) \tag{4.3.3}$$

where $dm_{int}(t,u)$ and $dm_{exh}(t,u)$ are the mass flow going through the intake and the exhaust cylinder ports. The mass flow direction is defined as positive if it goes from the intake manifold to the cylinder (positive intake valve flow), and from the cylinder to the exhaust manifold (positive exhaust valve flow), otherwise the mass flow from the valves is negative. The system input is $u = [IVC_d, EVO_d, IT]$, the inputs IVC_d and EVO_d are the inlet valve variable delay and the exhaust valve variable delay respectively, those inputs intervene in the intake and exhaust mass flow. The input IT is the advance on the ignition timing and takes part on the definition of the burning rate $dm_{comb}(t,u)$. $T_{int}(t)$ and $T_{exh}(t)$ are the mass flow temperatures, which take the value of the volume temperature upstream of the flow direction:

- Intake valve flow: if the mass flow goes from the admission manifold to the cylinder (positive intake mass flow), then $T_{int}(t) = T_{col}$, where T_{col} is the intake manifold temperature, if the gas goes from the cylinder to the intake manifold (negative intake mass flow) $T_{int}(t) = T(t)$, where $T(t)$ is the cylinder temperature.

- Exhaust valve flow: if the mass flow goes from the cylinder to the exhaust manifold (positive exhaust mass flow), then $T_{exh}(t) = T(t)$, if the gas goes from the exhaust manifold to the cylinder (negative exhaust mass flow), $T_{exh}(t) = T_{ech}$, where T_{ech} is the exhaust manifold temperature.

c_p is the specific heat of the gas. The intake and outlet valves are modeled as restrictions between the intake manifold and the cylinder and between the exhaust manifold and the cylinder. The mass flow passing through the valves can be closely approximated by the air mass flow of a compressible fluid through a nozzle as presented in the appendix A.3 in Figure A.2 and Table A.1.

Remark 4.3.1. The inputs $u = [IVC_d, EVO_d, IT]$ are considered as a parameters since in this thesis, no control action is performed with these inputs. These inputs defines the inlet and exhaust valves opening and closing profiles which are fixed for the validation measurements.

Remark 4.3.2. Notice that Equation (4.3.1) is similar to Equation (3.3.1), but the subindex i related to the unburned gas or burned gas has been removed in (4.3.1) because there is only one gases zone.

Remark 4.3.3. Differently from the two zones model, in the one zone model the specific enthalpy $h_j(t)$ is not modeled since the enthalpy flow due to the breathing process is assumed as Equation (4.3.3).

The combustion enthalpy $dm_{h_{comb}}(t, u)$ is modeled as the burning rate multiplied by the lower heat value of the fuel LHV. For gasoline engines, LHV can be approximated to $4.15 \times 10^7 MJkg^{-1}$. $dm_{comb}(t, u)$ is the burning rate, commonly defined with a burned mass fraction curve, provided by the Vibe's law presented in Section 3.4.1 and rewritten here for practicality:

$$\begin{aligned} dm_{comb}(t,u) =& m_o a e^{-a\left(\frac{\theta(t)-\theta_0(u)}{\Delta_\theta}\right)^{(m_w+1)}} \\ & \times (m_w+1)\left(\frac{\theta(t)-\theta_0(u)}{\Delta_\theta}\right)^{m_w} \frac{2N\pi}{60\Delta_\theta} \end{aligned} \tag{4.3.4}$$

where N is the engine speed in rpm, m_o is the initial mass, θ_0 corresponds to the crank angle where the combustion begins and $u = IT$ is the ignition timing. a, m_w and Δ_θ are calibration parameters. The variable Δ_θ is included to calibrate the duration of burn. a and m_w are usually between 3 and 6 and Δ_θ varies from 60 to 110 degrees, being smaller for a retarded ignition timing and bigger for an advanced ignition timing.

The heat losses from the gases in the combustion chamber to the cylinder walls are given by Woschni's law as it was presented in Equation (3.3.5) and (3.3.7), which are rewritten here for a single zone scheme:

$$\delta Q_{th}(t) = h_c(t) A_w(t)(T(t) - T_w) \tag{4.3.5}$$

where T_w is the cylinder walls temperature which is considered as a constant. $A_w(t)$ is the wall transfer area:

$$A_w(t) = \frac{\pi}{2} d^2 + 4\frac{V(t)}{d} \tag{4.3.6}$$

where d is the constant cylinder bore. $h_c(t)$ is the heat transfer coefficient computed from Woschni's equation [Woschni, 1967]:

$$h_c(t) = \alpha_{th} d^{-0.2} p(t)^{0.8} T^{-0.53} \Big(C_1 V_p + C_2 \frac{V_{cyl} T_1}{p_1 V_1} (p(t) - p_0(t)) \Big) \tag{4.3.7}$$

The interest is to find the dynamical equations for the cylinder pressure $p(t)$ and the cylinder temperature $T(t)$. The integral of $dU(t)$ in Equation (4.3.1) can be written as:

$$U(t) = T(t) c_v m(t) \tag{4.3.8}$$

where $m(t)$ is the total mass of all the species in the cylinder and $T(t)$ corresponds to the temperature of the gases. Assuming that the specific heat constant c_v is constant, solving (4.3.8) for $T(t)$ and taking the time derivative:

$$dT(t) = \frac{1}{m(t) c_v} dU(t) - \frac{U(t)}{c_v(t) m(t)^2} dm(t) \tag{4.3.9}$$

where $dm(t) = dm_{int}(t) - dm_{exh}(t)$ is the mass balance through the cylinder ports. Solving (4.3.1) and (4.3.9) for $dT(t)$ it yields to:

$$\begin{aligned} dT(t) = \frac{1}{m(t) c_v} \Bigg(& - p(t) dV(t) - \delta Q_{th}(t) + dm_{h_{int}}(t) - dm_{h_{exh}}(t) + dm_{h_{comb}}(t) \\ & - T(t) c_v dm(t) \Bigg) \end{aligned} \tag{4.3.10}$$

The ideal gases law is defined as::

$$p(t)V(t) = rm(t)T(t) \tag{4.3.11}$$

thus, $m(t)$ can be replaced by $m(t) = \frac{p(t)V(t)}{rT(t)}$ and an ordinary differential equation is obtained for the system temperature dynamics as:

$$\begin{aligned} dT(t) = &- \frac{rdV(t)}{c_v V(t)}T(t) - \frac{r\delta Q_{th}(t)T(t)}{c_v V(t)p(t)} + \frac{rT(t)}{c_v V(t)p(t)}dm_{h_{int}}(t) \\ &- \frac{rT(t)}{c_v V(t)p(t)}dm_{h_{exh}}(t) + \frac{rT(t)}{c_v V(t)p(t)}dm_{h_{comb}}(t) - \frac{rT(t)^2}{p(t)V(t)}dm(t) \end{aligned} \tag{4.3.12}$$

To model $p(t)$, the ideal gases law is used. Taking the derivative of (4.3.11) and solving for $dp(t)$ leads to:

$$dp(t) = \frac{rT(t)dm(t)}{V(t)} + \frac{rm(t)dT(t)}{V(t)} - \frac{rT(t)m(t)dV(t)}{V(t)^2} \tag{4.3.13}$$

Finally, combining equations (4.3.12) and (4.3.13) and solving for $dp(t)$, the in-cylinder pressure dynamics is modeled as:

$$\begin{aligned} dp(t) = &\frac{r}{V(t)c_v}dm_{h_{int}}(t) - \frac{r}{V(t)c_v}dm_{h_{exh}}(t) - \left(\frac{r}{c_v} + 1\right)\frac{dV(t)}{V(t)}p(t) \\ &+ \frac{r}{V(t)c_v}dm_{h_{comb}}(t) - \frac{r}{V(t)c_v}\delta Q_{th}(t) \end{aligned} \tag{4.3.14}$$

Thus, a 0D one zone engine model is obtained, where the temperature $T(t)$ and the pressure $p(t)$ are the dynamical states. The one zone thermodynamical model is summarized as:

$$\begin{cases} \dot{x}(t) = f(x,u), \quad equations \quad (4.3.13) \quad and \quad (4.3.12) \\ x(t) = \begin{bmatrix} p(t) \\ T(t) \end{bmatrix} \\ y(t) = p(t) \\ u(t) = [IVC_d, EVO_d, IT] \end{cases} \tag{4.3.15}$$

4.3.2 0D one zone engine model evaluation

The 0D one zone engine model presented in the previous section is tested taking as reference the measurements of a 1.2 liters spark ignited engine, characterized by a four-valve chamber. The main characteristics of the engine are presented in Table 4.2. The data to fit the model is the cylinder pressure. The calibration parameters are those related to the Vibe's law in Equation (4.3.4): a, m_w and Δ_θ. The calibration constants where obtained using the derivative free simplex algorithm [Bixby, 1992].

The results shown in Figures 4.3a, 4.3b and 4.3c correspond to three different tests, where the cylinder pressure curves are normalized with respect to the IMEP.

Bore x Stroke: 72.2x73.1 mm
Volumetric ratio: 10.5:1
Engine speed: 1200 rpm up to 5000 rpm

Table 4.2: Engine test characteristics for the one zone model validation

The model accuracy is evaluated by computing the absolute value of the model IMEP and the measurement IMEP. This difference is presented in percentage with respect to the IMEP measurement. The model error with respect to the engine speed is depicted in Figure 4.3d. The 0D one zone model has less than 10% of error to represent the cylinder pressure using this criterion. Those results are accurate enough for the purpose of the mass estimation strategies proposed in this thesis. Indeed, the aim is not to provide an engine model or physical validation for combustion analysis, but to illustrate a closed loop methodology to estimate the wall losses when the valves are closed.

Differently from the two zone model presented in Chapter 3, the 0D one zone engine model designed here considers as constants the thermodynamical properties of the gas (parameters c_v, r and specific enthalpy). Besides it takes into account only one zone where all the species are contained and the burning rate is represented by a parametric combustion model, otherwise than the two zones model where a flamelet model is used for the burning rate. It means that the 0D one zone model cannot provide a detailed explanation of phenomena related to the cylinder wall interaction or the burning rate or the evolution of the combustion species (unburned gas, burned gas, fuel). For this reason, this model is only used for the purpose of proposing a mass observation strategy, and it is not possible to give any specification with respect to the evolution of the gases species separately.

In the next sections, the different observations strategies for the heat wall losses and the enclosed mass estimation are presented. Those strategies are based on the 0D one zone engine model presented here. Table 4.1 in the introduction of this chapter shows a summary of the observers that will be presented next.

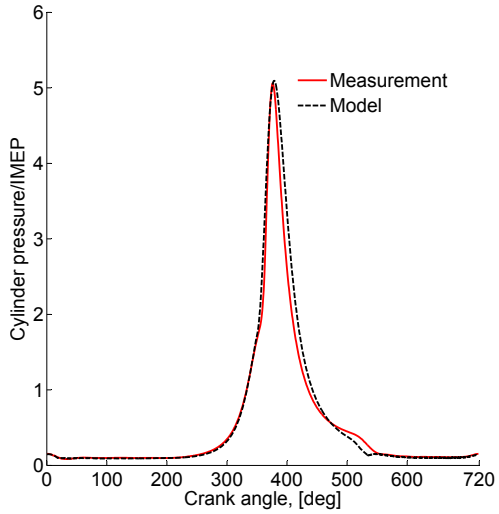

(a) Cylinder pressure. IMEP=10.68 bar, N=1200rpm.

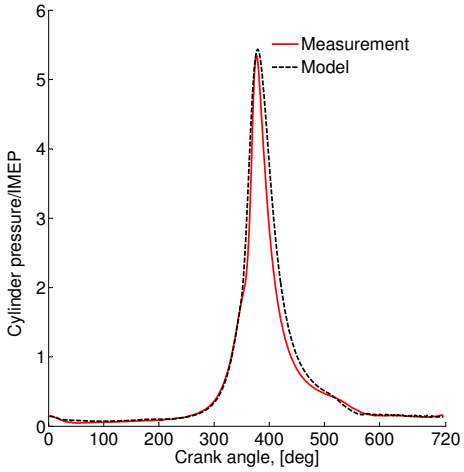

(b) Cylinder pressure. IMEP=13.38 bar, N=5500rpm.

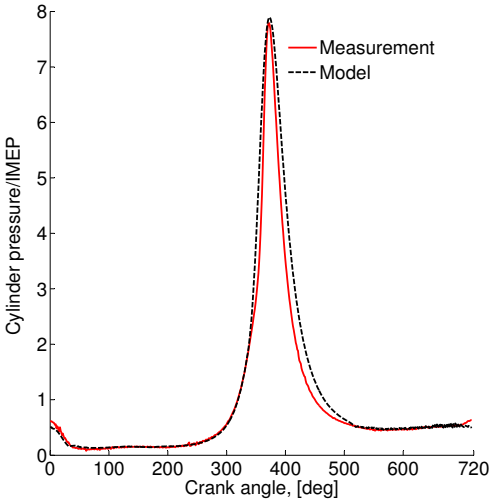

(c) Cylinder pressure. IMEP=2.09 bar, N=4000rpm.

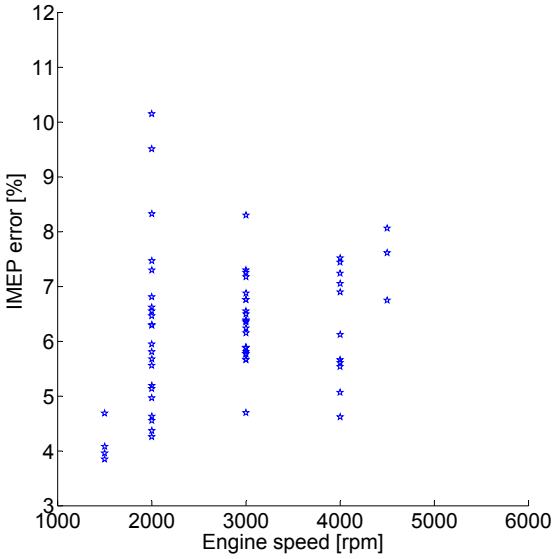

(d) IMEP error respect to the engine speed.

Figure 4.3: 0D one zone engine model evaluation

4.4 A sliding model observer for estimating the wall losses during the valves closure

In this section, the design of an sliding mode observer to estimate the heat wall losses during the compression and combustion strokes using the cylinder pressure measurement is

presented. The sliding mode observer is derived from the 0D one zone thermodynamical engine model presented before.

This observer is built to find a correlation between the engine wall losses and the cylinder temperature, which could provide a statical expression for estimating the enclosed masses. This mass estimation strategy was abandoned because the enclosed mass estimation results were deficient, but the sliding mode observer for the heat wall losses was kept as an interesting result, as it proved to be useful to compute the heat wall losses dynamics. Based on these results, a reduced model for the heat wall losses has been developed, which allows for simplifying the strong nonlinearities of Woschni's law (4.3.7) and build the enclosed mass observers.

The cylinder pressure dynamics depends on the energy balance in the combustion chamber. The enthalpy flow represents different physical phenomena depending on the crank angle position. Figure 4.4 depicts the evolution of the cylinder pressure depending on the crank angle, coupled with the intake and exhaust valves lift to illustrate the different engine strokes:

- The phase between the inlet valve opening (IVO) and the inlet valve closure (IVC) corresponds to the intake stroke,
- the phase between the exhaust valve opening (EVO) and the exhaust valve closure (EVC) corresponds to the exhaust stroke,
- the phase between the IVC and the ignition timing (IT) is the compression stroke, and
- the phase between the IT and the EVO is the combustion stroke.

As it was presented in Section 4.3, four main enthalpy flows are considered in the engine cycle: the enthalpy flow due to the energy supplied through the valves $dm_{h_{int/exh}}(t)$, the enthalpy flow supplied by the combustion $dm_{h_{comb}}(t)$ and the enthalpy flow due to the wall losses $\delta Q_{th}(t)$. The remaining energy component is the work delivered on the piston, which depends on the cylinder pressure. Table 4.3 explains how the enthalpy dynamics is taken into account depending on the engine stroke.

The goal is to build an observer for $\delta Q_{th}(t)$ using the 0D one zone engine model summarized in Equation (4.3.15). To do so, only the cylinder pressure dynamics in Equation (4.3.14) is used, and the notation is changed for $x_1(t) = p(t)$. The immersion transformation technique [Besancon, 2007] is used in order to obtain an extended state that is the sum $x_2(t) = dm_{h_{int}}(t) - dm_{h_{exh}}(t) - \delta Q_{th}(t)$, which includes all the enthalpy flow contributions except the combustion enthalpy and the work delivered on the piston. Thus, a transformed two states system is designed as follows:

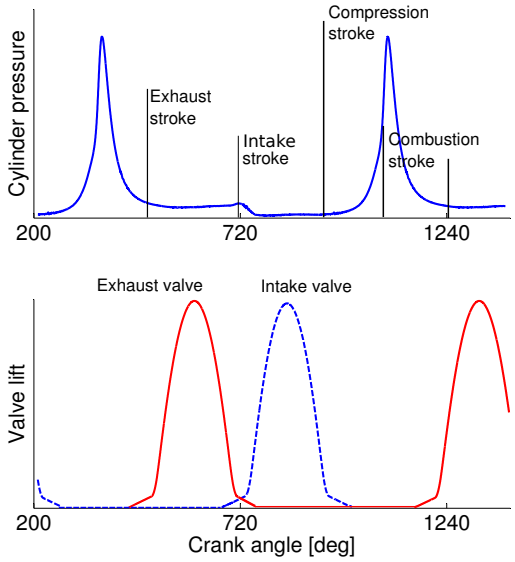

Figure 4.4: Engine cycles representation

	$dm_{h_{comb}}(t)$	$dm_{h_{int}}(t)$ and $dm_{h_{exh}}(t)$	$\delta Q_{th}(t))$
Intake	0	$\neq 0$	$\neq 0$
Exhaust	0	$\neq 0$	$\neq 0$
Compression	0	$= 0$	$\neq 0$
Combustion	$\neq 0$	$= 0$	$\neq 0$

Table 4.3: Engine strokes and enthalpy flows

$$\begin{aligned} \dot{x}_1(t) =& -\left(\frac{r}{c_v}+1\right)\frac{dV(t)}{V(t)}x_1(t) + \frac{r}{c_v V(t)}x_2(t) + \frac{r}{c_v V(t)}dm_{h_{comb}}(t) \\ \dot{x}_2(t) =& 0 \end{aligned} \tag{4.4.1}$$

In System (4.4.11), the pressure $x_1(t)$ is assumed to be a known measurement, the dynamics of $x_2(t)$ will be estimated through the sliding mode state observation technique, thus its dynamics is set to 0. The combustion enthalpy flow $dm_{h_{comb}}(t)$ is considered as a known measurable disturbance that varies in time. Under those assumptions, during the compression and combustion strokes the state $x_2(t)$ represents only the wall losses, as it is illustrated in Table 4.3.

4.4.1 Brief background on sliding mode observers

The complete development of the sliding model observer can be consulted in [Perruquetti, 2002]. Consider the class of system that writes as:

$$\begin{aligned} \dot{z} &= A_0 z + \phi(z,u) \\ y &= C_0 z \end{aligned} \tag{4.4.2}$$

where $z \in \mathbf{R}^n$, $A_0 \in \mathbf{R}^{n\times n}$, $\phi(z,u) : \mathbf{R}^n \to \mathbf{R}^n$ is a continuous function, globally Lipschitz in z. The matrices A_0 and C_0 are such that:

$$A_0 = \begin{bmatrix} 0 & 1 & 0 \\ 0 & ... & 1 \\ 0 & 0 & 0 \end{bmatrix}, \quad C_0 = \begin{bmatrix} 1 & 0... & 0 \end{bmatrix} \tag{4.4.3}$$

This particular form is referred to as the triangular additive form. When a system has this form, it is possible to define a step by step observation algorithm allowing the reconstruction of all the state with finite-time convergence, as the sliding mode observer.

The sliding mode observer is designed according to the following theorem:

Theorem 4.4.1. *If $\phi(z,u)$ is globally Lipschitz in z and u and such that $\partial\phi_i(z,u)/\partial z_j = 0$, for $j \geq i+1$, $1 \leq i,j \leq n$, then the system* (4.4.2) *admits an observer of the form [Perruquetti, 2002]:*

$$\begin{aligned} \dot{\hat{z}}_1 =& \hat{z}_2 + \phi_1(z_1,u) + \lambda_1 sign(z_1 - \hat{z}_1) \\ \dot{\hat{z}}_2 =& \hat{z}_3 + \phi_2(z_1,\tilde{z}_2,u) + \lambda_2 sign(\tilde{z}_2 - \hat{z}_2) \\ & . \\ & . \\ & . \\ \dot{\hat{z}}_n =& f(z_1,\tilde{z}_2..,\tilde{z}_n) + \lambda_n sign(\tilde{z}_n - \hat{z}_n) \end{aligned} \tag{4.4.4}$$

where $\hat{z}$ is the estimated state and $\tilde{z}$ is defined as:

$$\tilde{z}_i = \hat{z}_i + \lambda_{i-1} sign(z_{i-1} - \hat{z}_{i-1}) \tag{4.4.5}$$

and $\lambda_i \in \mathbf{R}$.

Sketch of proof To analyze the observer stability and give some knowledge of the λ_i parameters, the state space variable z_1 is analyzed first. Consider the sliding surfaces

$e_1 = z_1 - \hat{z}_1 \neq 0$, $e_2 = z_2 - \hat{z}_2 \neq 0$ and the Lyapunov function $V_1 = \frac{1}{2}e_1^2$. The condition $\dot{V}_1(z) < 0$ must be fulfilled to guarantee the stability of the observer and the convergence of e_1 to 0. The dynamics of e_1 is given by:

$$\dot{e}_1 = e_2 - \lambda_1 sign(e_1) \tag{4.4.6}$$

and

$$\dot{V} = e_1\dot{e}_1 = e_1(e_2 - \lambda_1 sign(e_1)) \tag{4.4.7}$$

which satisfies $\dot{V}_1 < 0$ when $\lambda_1 > |e_2|_{max}$. As the function $sign$ is used, and the Lyapunov function decreases, the convergence to the sliding surface $S = e_1$ in a finite time t_0 is obtained. Thus, for $\lambda_1 > |e_2|_{max}$, $\hat{z}_1$ converges to z_1 in finite time t_0 and $\hat{z}_1 = z_1$ remains for $t > t_0$.

Moreover, $\forall t > t_0$ such that $\dot{e}_1 = 0$, from Equation (4.4.6) it is verified that:

$$e_2 = \lambda_1 sign(e_1) \tag{4.4.8}$$

and considering $e_2 = \tilde{z}_2 - \hat{z}_2$, it yields to:

$$\tilde{z}_2 = \hat{z}_2 + \lambda_1 sign(e_1) \tag{4.4.9}$$

where $\tilde{z}_2 = z_2$ $\forall t > t_0$. (Equation (4.4.9) has the same form that Equation (4.4.5)).

The same procedure is followed for the states $z_2, ..., z_n$ and the stability is shown. The complete demonstration can be seen in [Perruquetti, 2002].

Remark 4.4.1. The time t_0 can be very short because it is natural to initiate $\hat{z}_1 = z_1$. The observer convergence is given from the convergence of the state 2.

♢

4.4.2 Sliding mode observer application

System (4.4.1) can be ordered to fit the triangular additive form as:

$$\dot{x}(t) = \begin{bmatrix} 0 & \frac{r}{c_v V(t)} \\ 0 & 0 \end{bmatrix} x(t) + \begin{bmatrix} -\left(\frac{r}{c_v}+1\right)\frac{dV(t)}{V(t)}x_1(t) + \frac{r}{c_v V(t)} dm_{h_{comb}}(t) \\ 0 \end{bmatrix} \tag{4.4.10}$$

However, the system (4.4.10), does not comply with the triangular form presented in Equation (4.4.2) since the first non-zero component in matrix A_0 is different from 1. It is possible to use an equivalent transformation through a dipheomorfism to obtain the same form. However, to avoid defining such a transformation, in this work the effect of this component is taken into account multiplying the observer gains by the scheduling parameter $r/(c_v V(t)) > 0$.

Thus, applying the sliding mode observer in Equation (4.4.4) for system (4.4.10) it yields to:

$$\begin{aligned} \dot{\hat{x}}_1(t) =& -\left(\frac{r}{c_v}+1\right)\frac{dV(t)}{V(t)}\hat{x}_1(t) + \frac{r}{c_v V(t)} dm_{h_{comb}}(t) \\ &+ \frac{r}{c_v V(t)}\hat{x}_2(t) + \frac{r}{c_v V(t)}\lambda_1 sign(x_1(t) - \hat{x}_1(t)) \\ \dot{\hat{x}}_2(t) =& \frac{r}{c_v V(t)}\lambda_2 sign(\tilde{x}_2(t) - \hat{x}_2(t)) \\ \tilde{x}_2(t) =& \hat{x}_2(t) + \frac{r}{c_v V(t)}\lambda_1 sign(x_1(t) - \hat{x}_1(t)) \end{aligned} \tag{4.4.11}$$

where λ_1 and λ_2 are the observer gains that have to be chosen to ensure the observer stability.

Remark 4.4.2. Note that the dynamics of the observed state $\dot{\hat{x}}_2 \neq 0$, even if $\dot{x}_2 = 0$, which implies that thanks to the sliding mode observer, the dynamics of the state x_2 can be rebuilt thought the observer.

The Lyapunov stability theorem [Khalil, 1996] is used to find λ_1 and λ_2 to ensure that the estimation error converges to 0.

Consider the Lyapunov function $V_1(t) = \frac{1}{2}e_1(t)^2$, and the estimation errors $e_1(t) = x_1(t) - \hat{x}_1(t)$ and $e_2 = x_2(t) - \hat{x}_2(t)$, thus $V_1(t)$ yields to:

$$\dot{V}_1(x(t)) = e_1(x(t))\dot{e}_1(x(t)) \tag{4.4.12}$$

$$\dot{V}_1(x(t)) = e_1(t)\Big(\frac{r}{c_v V(t)}e_2(t) - \frac{r}{c_v V(t)}\lambda_1 sign(e_1(t))\Big) \tag{4.4.13}$$

The condition $\dot{V}_1(x(t)) < 0$ must be full filled to ensure the observer stability in $x_1(t)$. Note that $r/(c_v V(t)) > 0$: keeping $\lambda_1 > |e_2|_{max}$ then ensures that $\dot{V}_1(x(t)) < 0$. The same procedure is applied to choose the parameter λ_2.

Consider the second Lyapunov function $V_2(t) = \frac{1}{2}e_2(t)^2$:

$$\dot{V}_2(x(t)) = -e_2(t)\frac{r}{c_v V(t)}\lambda_2 sign(e_2(t)) \tag{4.4.14}$$

The conditions $\dot{V}_2(x(t)) < 0$ must be fulfilled to ensure the observer stability in $x_2(t)$: keeping $\lambda_2 > 0$ ensures $\dot{V}_2(x(t)) < 0$ and the second state stability is ensured.

To ensure the convergence of the observer, the initial conditions $\hat{x}_{1_0}$ and $\hat{x}_{2_0}$ must belong to the region of attraction of the observer. The variable $x_1(t)$ is assumed to be measured, thus $\hat{x}_{1_0} = p_{IVC}$ that is the pressure measured at IVC.

$x_2(t)$ is unknown, hence the criterion $\lambda_1 > |e_2|_{max}$ is considered to choose $\hat{x}_{2_0}$. As it was proved, the stability of the sliding mode observer is guaranteed if $\lambda_1 > |e_2|_{max}$, thus if the condition $|x_{2_0} - \hat{x}_{2_0}| < \lambda_1$ is respected, the observer is able to recover the difference and estimate $x_2(t)$ accurately. This is an interesting fact, because when there is a large uncertainty on the initial condition of the unknown state, λ_1 can be chosen large enough to guaranty $|x_{2_0} - \hat{x}_{2_0}| < \lambda_1$ and the estimation error will converge to 0.

For the observer in Equation (4.4.11) the design parameter are as follows: $\lambda_1 = 10000$, $\lambda_2 = \lambda_1/10$ and $\hat{x}_{2_0} = -0.4J/s$. Those values were chosen taking into account the observer convergence conditions, the knowledge of the system and the reference model simulations.

When the enthalpy flow estimation is made over the whole engine cycle, the variable $x_2(t)$ represents different physical phenomena depending on the engine operating conditions, as it is presented in Table 4.3. The energy wall losses during the compression and combustion strokes are extracted from the enthalpy flow observation $\hat{x}_2(t)$, limiting the estimation to this specific cycle phase. During the compression and combustion strokes while the valves are closed, the energy sources are the enthalpy flow supplied by the combustion, the wall losses and the work delivered by the piston. The combustion enthalpy is assumed to be a known disturbance represented in the model by the Vibe's law. The work delivered by the piston, which depends on the cylinder pressure and the volume is also represented. To complete the energy sources during the compression and combustion strokes, $\hat{x}_2(t)$ must represent the heat transfer to the walls, thus $\hat{x}_2(t) = \delta\hat{Q}_{th}(t)$.

Figure 4.5 shows a scheme of the sliding mode observe implemented to estimate the heat wall losses.

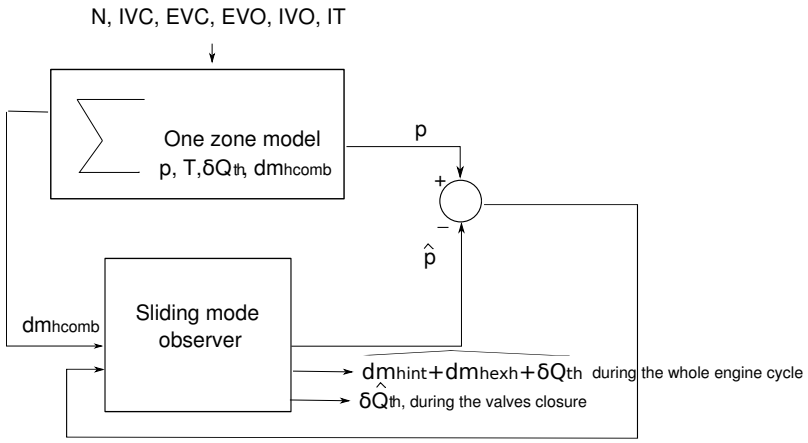

Figure 4.5: Model based sliding mode observer application scheme.

4.4.3 Observer results

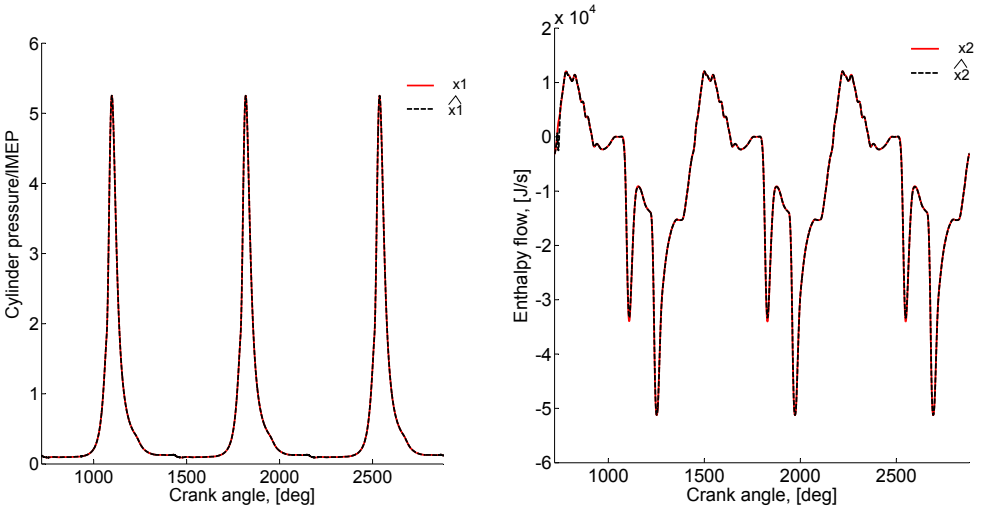

(a) Cylinder pressure estimation, $\hat{x}_1(t) = \hat{p}(t)$

(b) Enthalpy flow estimation, $\hat{x}_2(t)$: estimation of the sum of the enthalpy flows $dm_{h_{int}}(t) + dm_{h_{exh}}(t) + \delta Q_{th}(t)$

Figure 4.6: Cylinder pressure and heat flow estimation during 3 engine cycles. IMEP=10.68 bar, N=1200rpm.

Figures 4.6a and 4.6b show the observation results of the system in equations (4.4.11), validated against the model in equations (4.3.14) and (4.3.5). The solid lines represent the reference model and the dashed lines represent the observer results. The observer is efficient and effective in successive engine cycles to estimate $\hat{x}_1(t) = \hat{p}(t)$ and $\hat{x}_2(t)$ is the estimation of the enthalpy flows sum $dm_{h_{int}}(t) + dm_{h_{exh}}(t) + \delta Q_{th}(t)$.

Using the measured pressure $p(t) = x_1(t)$, the observer is able to estimate the second state $x_2(t)$, that corresponds to the sum of the enthalpy flows. During the valves closure,

the energy contributions come from the enthalpy due to the combustion $dm_{hcomb}(t)$ that is considered as a known disturbance represented in the model given by the Vibe's law, the work delivered on the piston that is represented by the term $-(\frac{r}{c_v}+1)\frac{dV(t)}{V(t)}x_1(t)$ and the heat wall losses $\delta Q_{th}(t)$, the enthalpy due to the valves flows $dm_{h_{int/exh}} = 0$. Thus during the valves closure, the variable $\hat{x}_2(t) = \delta\hat{Q}_{th}(t)$. This result is presented in Figure 4.7, which is a zoom of Figure 4.6 during the valves closure. Therefore, the enthalpy flow $\hat{x}_2(t)$ shown in Figure 4.7b corresponds to the heat wall losses $\delta\hat{Q}_{th}(t)$ during the valves closure and the effectiveness of the sliding mode strategy proposed in Equation (4.4.11) to obtain this variable is proved.

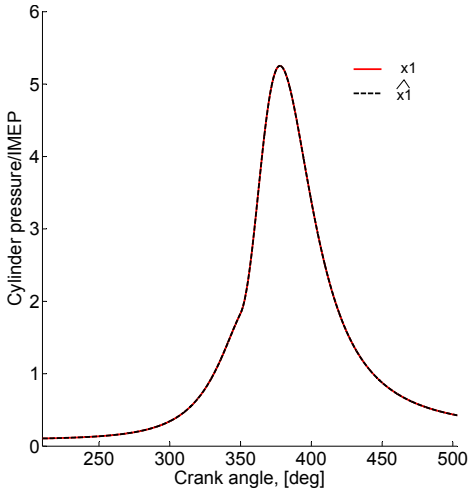

(a) Cylinder pressure estimation, $\hat{x}_1(t) = \hat{p}(t)$

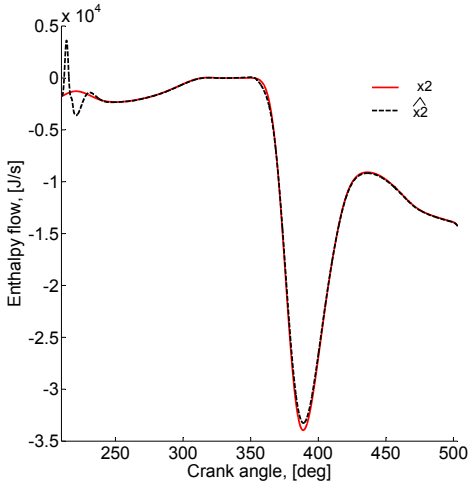

(b) Enthalpy flow estimation during compression and combustion strokes, $\hat{x}_2(t) = \delta\hat{Q}_{th}(t)$

Figure 4.7: Cylinder pressure estimation and heat flow estimation during the compression and combustion strokes while the valves are closed. IMEP=10.68 bar, N=1200rpm.

Figures 4.8a and 4.8b show the normalized observation error for variables $\hat{x}_1(t)$ and $\delta\hat{Q}_{th}(t)$ corresponding to the cylinder pressure and the enthalpy flow for the operating points data base. The results are satisfactory as the observation error of the cylinder pressure remains below 0.05% while the observation error of the enthalpy flow remains below 3%. Those results show that the sliding mode observer presented in Equation (4.4.11) is effective to estimate the enthalpy flow.

In order to illustrate the validity of observer, the accuracy evaluation has also been done using as virtual engine a simplified version of the two zones engine model presented in Chapter 3. To simplify the model, the parameters c_p, c_v and γ are considered as constants. The references are the cylinder pressure $p(t)$ and the heat wall losses in Equation (4.3.5). The results of this test are shown in Figure 4.9. A good agreement between the observation and the reference is obtained. Testing the observer in a model different from the one used for the synthesis illustrates the robustness of the sliding mode

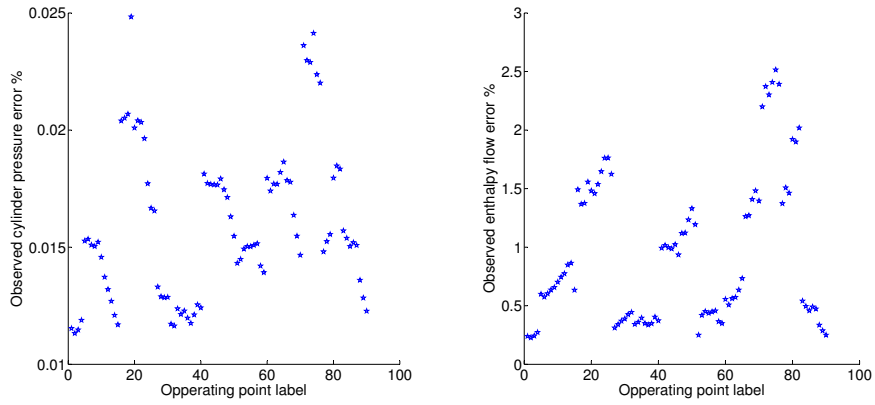

(a) Cylinder pressure estimation error (b) Enthalpy flow estimation error

Figure 4.8: Cylinder pressure and enthalpy flow observation errors for 90 operating points. IMEP=1-20 bar, N=1200-5500rpm

strategy and the possibility to adapt the observer in more complex systems.

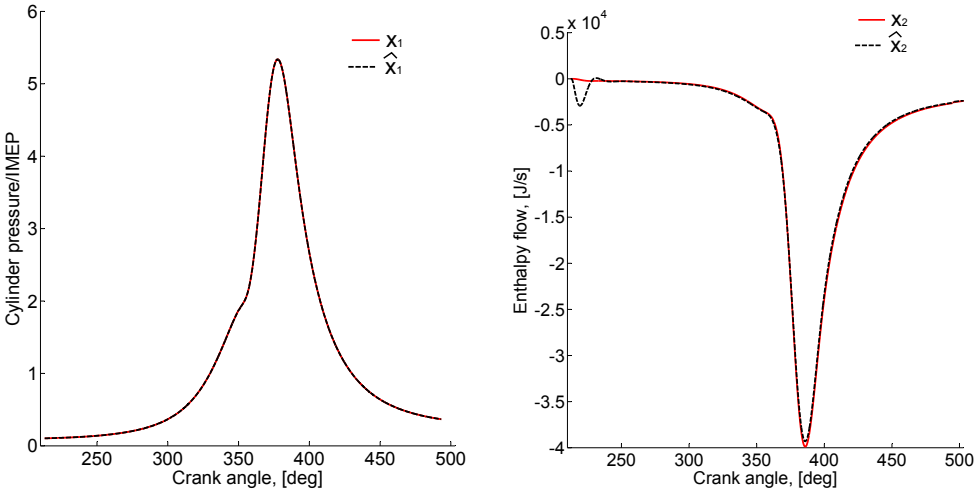

(a) Cylinder pressure estimation, $\hat{x}_1(t) = \hat{p}(t)$

(b) Enthalpy flow estimation during compression and combustion strokes, $\hat{x}_2(t) = \delta\hat{Q}_{th}(t)$

Figure 4.9: Validation two zones model: Cylinder pressure estimation and heat flow estimation during the compression and combustion strokes when the valves are closed using as virtual engine reference a two zones model. IMEP=10.68 bar, N=1200rpm.

4.5 One zone engine model reduction

During the valves closure, the unique energy components are the enthalpy due to the combustion $dm_{hcomb}(t)$, the wall losses $\delta Q_{th}(t)$ and the work delivered by the piston. The enthalpy due to the valves flows $dm_{h_{int/exh}}$ is zero. Thus from (4.3.12) and (4.3.14), and changing the notation by $x_1(t) = p(t)$ and $x_2(t) = T(t)$, the dynamics of the 0D one zone engine model during the valves closure is:

$$\begin{aligned} \dot{x}_1(t) &= -\left(\frac{r}{c_v}+1\right)\frac{dV(t)}{V(t)}x_1(t) - \frac{r}{c_v V}\delta Q_{th}(t) + \frac{r}{c_v V(t)}dm_{h_{comb}}(t) \\ \dot{x}_2(t) &= -\frac{rdV(t)}{c_v V(t)}x_2(t) - \frac{rx_2(t)}{c_v V(t)x_1(t)}\delta Q_{th}(t) + \frac{rx_2(t)}{c_v V(t)x_1(t)}dm_{h_{comb}}(t) \\ y(t) &= x_1(t), \quad u = IT, \quad x_1(t) = p(t), \quad x_2(t) = T(t) \end{aligned} \tag{4.5.1}$$

The wall losses $\delta Q_{th}(t)$ are first modeled using Woschni's approximation in Equation (4.3.7). Even if this approximation is widely used in 0D engine modeling, it contains strong nonlinearities that are difficult to handle from the observation point of view. For this reason, a reduced model of the wall losses for the compression and combustion strokes has been created. The proposed approximation keeps the convection principle from Equation (4.3.5) but replaces the convection coefficient $h_c(t)$ by a simpler structure:

$$h_c(t) = \omega x_1(t) \tag{4.5.2}$$

Similarly to Woschni's principle, the new $\delta Q_{th}(t)$ assumes that the convection coefficient is proportional to the engine speed and the cylinder pressure and two calibration parameters k_1 and k_0 are introduced. Thus, the engine wall losses are computed as:

$$\delta Q_{th}(t) = A_w(t)\omega x_1(t)(k_1 x_2(t) - k_0 T_w) \tag{4.5.3}$$

where $A_w(t)$ is the heat transfer area, modeled as in Equation (4.3.6). The wall losses model reduction is calibrated with respect to Woschni's approximation and a satisfactory result is obtained. The reduced model of the wall losses is also included in the 0D virtual engine model with good results. In Figure 4.10a, two examples for different operating conditions of the validation of the wall losses reduction model are presented. The relative error between equations (4.3.5) using expressions (4.3.7) and (4.5.3) is plotted in Figure 4.10b. The error was computed as the norm of the signals difference divided by the heat wall losses reference absolute maximum value $max(|\delta Q_{th}(t)|)$.

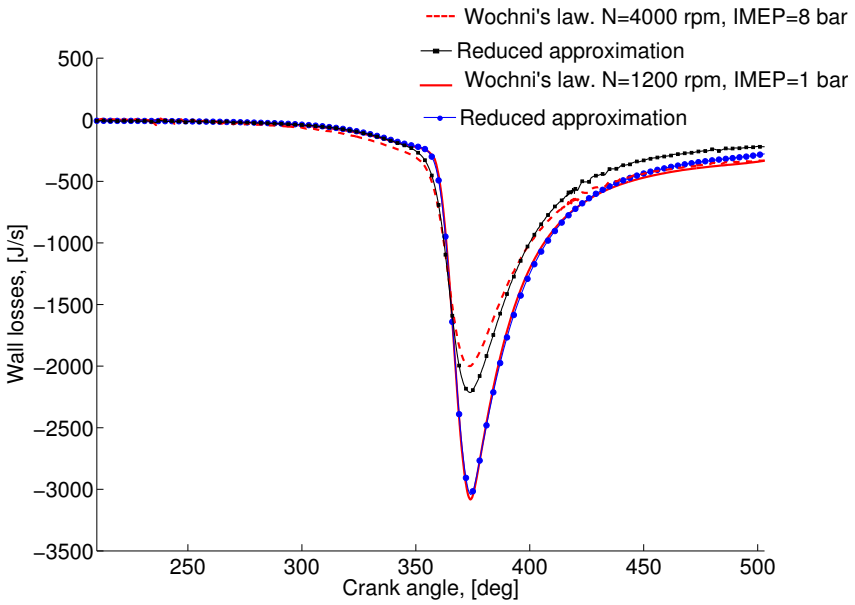

(a) Reduced model outputs

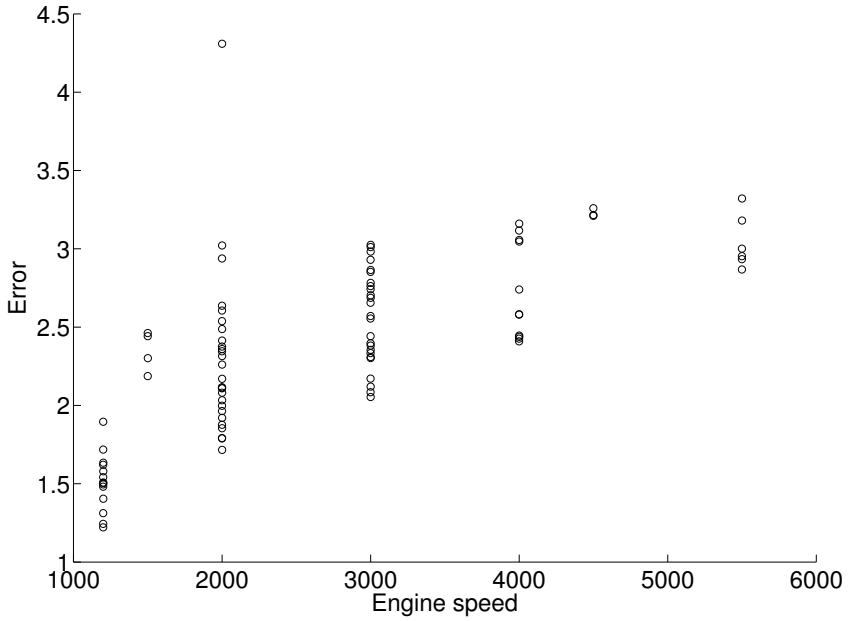

(b) Reduced model error

Figure 4.10: Reduced model results for the heat wall losses. Equations (4.3.5), (4.3.7) and (4.5.3)

Including the reduced model for the wall losses and denoting the system parameters as:

$$\begin{aligned} a_1(t) &= -\Big(\frac{r}{c_v}+1\Big)\frac{dV(t)}{V(t)}, \quad a_2(t) = -\frac{r}{c_v V(t)} \\ a_3(t) &= -\frac{r dV(t)}{c_v V(t)}, \quad a_4(t) = -\frac{r}{c_v V(t)} A_w(t)\omega \end{aligned} \tag{4.5.4}$$

the system (4.5.1) is written as:

$$\begin{aligned} \dot{x}_1(t) =& a_1(t)x_1(t) + a_4(t)x_1(t)(k_1 x_2(t) - k_0 T_w) - a_2 dm_{h_{comb}}(t) \\ \dot{x}_2(t) =& a_3 x_2(t) + a_4(t)x_2(t)(k_1 x_2(t) - k_0 T_w) - a_2(t)\frac{x_2(t)}{x_1(t)} dm_{h_{comb}}(t) \end{aligned} \tag{4.5.5}$$

The enclosed mass is then estimated using the ideal gas law as:

$$m(t) = \frac{x_1(t)V(t)}{r x_2(t)} \tag{4.5.6}$$

The cylinder pressure $x_1(t)$ is a known measurement but it is necessary to estimate the cylinder temperature $x_2(t)$ from Equation (4.5.5) to deduce the mass using Equation (4.5.6).

4.6 A high gain observer for estimating the enclosed mass in the combustion chamber

In this section, an estimation method for the total mass of all the species (fresh air, fuel and burned gases) enclosed in the combustion chamber during the compression and combustion strokes when the valves are closed, using the cylinder pressure measurement is presented. Differently from most of the mass estimation strategies, where the enclosed mass is computed from the air path measurements or with statical iterative models, this strategy uses the cylinder pressure dynamics to implement an observer. This strategy does not need many engine cycle computations to achieve the mass estimation.

A high gain nonlinear observer of the cylinder temperature during the valves closure is built and the enclosed mass is computed using the observed temperature and the cylinder pressure measurement with the ideal gases law. This approach has shown to be effective to handle strong nonlinearities of a combustion model. The reduced one zone engine model is used as a virtual engine to build the observer. The results of the observer are compared with the virtual engine model.

4.6.1 Brief background on high gain nonlinear observers

Consider a system that writes as:

$$\begin{aligned} \dot{x} &= A_0 x + \phi(x,u) \\ y &= C_0 x \end{aligned} \tag{4.6.1}$$

where $x \in \mathbf{R}^n$, $A_0 \in \mathbf{R}^{n\times n}$, $\phi(x,u) : \mathbf{R}^n \to \mathbf{R}^n$ is a continuous function, globally Lipschitz in x. The matrices A_0 and C_0 are such that:

$$A_0 = \begin{bmatrix} 0 & 1 & 0 \\ 0 & ... & 1 \\ 0 & 0 & 0 \end{bmatrix}, \quad C_0 = \begin{bmatrix} 1 & 0 & ...0 \end{bmatrix} \tag{4.6.2}$$

The nonlinear high gain observer is designed according to the following theorem.

Theorem 4.6.1. *[Besancon, 2007]. If $\phi(x,u)$ is globally Lipschitz in x and u where $||\phi(x_1,u) - \phi(x_2,u)|| < \delta||x_1 - x_2||$, $\delta \in \mathbf{R} > 0$, $x_1, x_2 \in D_x$ and such that $\partial\phi_i(x,u)/\partial x_j = 0$, for $j \geq i+1$, $1 \leq i,j \leq n$, then the system (4.6.1) admits an observer of the form:*

$$\dot{\hat{x}} = A_0\hat{x} + \phi(\hat{x},u) + \Lambda K_0(C_0\hat{x} - y) \tag{4.6.3}$$

where

$$\Lambda = \begin{bmatrix} \lambda_1 & 0 & 0 \\ 0 & ... & \\ 0 & 0 & \lambda_n \end{bmatrix} \in \mathbf{R}^{n\times n} \tag{4.6.4}$$

with K_0 such that $A_0 - K_0C_0$ is stable and $\lambda_1, ...\lambda_n$ are large enough.

The idea of this observer is to use the uniform observability to weight a gain based on the linear part, in order to make the linear dynamics of the observer error dominating the nonlinear one [Ljung, 1999]. The stability of the observer is analyzed next.

Stability Analysis To prove stability, the auxiliary variable $z = \Lambda^{-1}x$ is introduced and Λ is chosen as $\lambda_1 = \lambda, \quad \lambda_2 = \lambda^2, \quad \lambda_3 = \lambda^3, \quad ..., \lambda_n = \lambda^n$, the error $\epsilon = z - \hat{z}$ dynamics is:

$$\dot{\epsilon} = (\Lambda^{-1}A_0\Lambda - K_0C_0\Lambda)\epsilon + \Lambda^{-1}(\phi(z) - \phi(\hat{z})) \tag{4.6.5}$$

Considering the triangular structure of (4.6.2) and the fact that $C_0 = [\ 1 \quad 0 \quad ...0\ ]$, the error $\epsilon = z - \hat{z}$ dynamics is:

$$\dot{\epsilon} = \lambda(A_0 - K_0C_0)\epsilon + \Lambda^{-1}(\phi(z) - \phi(\hat{z})) \tag{4.6.6}$$

Given the Lyapunov function $V = \epsilon^T P\epsilon$, where P is symmetric and $P > 0$, the following stability condition must be satisfied to guarantee that the error ϵ converges to 0:

$$\lambda\epsilon^T\left[(A_0 - K_0C_0)^T P + P(A_0 - K_0C_0)\right]\epsilon + 2\epsilon^T P\Lambda^{-1}(\phi(z) - \phi(\hat{z})) < 0 \tag{4.6.7}$$

As it was stated in Theorem 4.6.1, the class of systems considered is restricted to those where $\phi(z)$ is Lipschitz, thus $\|\phi(z) - \phi(\hat{z})\| < \delta\|z - \hat{z}\|$ and condition (4.6.7) becomes:

$$\lambda\epsilon^T\left[(A_0 - K_0C_0)^T P + P(A_0 - K_0C_0)\right]\epsilon + 2\epsilon^T P\Lambda^{-1}\delta\epsilon < 0 \tag{4.6.8}$$

K_0 is chosen such that $A_0 - K_0C_0 < -\alpha_v||\epsilon||^2$, where α_v is a positive constant. Bounding the last term on the left of (4.6.8) by $\lambda^{-1}\delta\epsilon < \frac{\beta}{\lambda_{max}(P)}||\epsilon||^2$, ($\lambda_{max}$ denotes the maximum eigenvalue) where $\beta > 0$ is a tuning parameter, it yields:

$$\begin{aligned}\lambda\epsilon^T[(A_0 - K_0C_0)^T P + P(A_0 - K_0C_0)]\epsilon + 2\delta\epsilon^T P\Lambda^{-1}\epsilon \\ < -\lambda\alpha_v||\epsilon||^2 + \tfrac{\beta}{\lambda_{max}(P)}||\epsilon||^2\end{aligned} \tag{4.6.9}$$

for some constant values $\alpha_v > 0$ and β. Taking $\lambda > \frac{\beta}{\lambda_{max}(P)\alpha_v}$ is sufficient to guarantee (4.6.9).

4.6.2 High gain nonlinear observer application

In order to use a high gain nonlinear observer like (4.6.3) for system (4.5.5), the state space system must be transformed to fit the triangular additive form of system (4.6.1). An equivalent transformation is proposed to obtain this result.

Definition 4.6.1. *A system described by*

$$\dot{x} = f(x,u), \quad y = h(x) \tag{4.6.10}$$

for all $x \in \mathbf{R}^n$, $u \in \mathbf{R}^m$, $y \in \mathbf{R}^p$ *is said equivalent to the system:*

$$\dot{z} = F(z,u) \quad y = H(z) \tag{4.6.11}$$

if there exists a diffeomorphism $z = \Phi(x)$ *defined on* $\mathbf{R}^n$ *such that:*

$\forall u \in \mathbf{R}^m$, $\frac{\partial \Phi}{\partial x} f(x,u)|_{x=\Phi^{-1}(z)} = F(z,u)$ *and* $h \circ \Phi^{-1} = H$

System (4.6.10) *and system* (4.6.11) *are said to be equivalent by* $z = \Phi^{-1}$. *Then an observer for system* (4.6.11) *is an observer for system* (4.6.10)*[Perruquetti, 2002].*

Using this definition, the following equivalence transformation for system (4.5.5), which has been verified to fulfill the conditions in Definition 4.6.1 is performed:

$$z(t) = [x_1(t), a_4(t)k_1x_1(t)x_2(t)]^T \tag{4.6.12}$$

It implies the structured nonlinear dynamics:

$$\begin{bmatrix} \dot{z}_1(t) \\ \dot{z}_2(t) \end{bmatrix} = \begin{bmatrix} 0 & 1 \\ 0 & 0 \end{bmatrix} \begin{bmatrix} z_1(t) \\ z_2(t) \end{bmatrix} + \phi(z(t)) \tag{4.6.13}$$

where

$$\phi(z(t)) = \begin{bmatrix} (a_1(t) - a_4(t)k_0T_w)z_1(t) - a_2(t)dm_{h_{comb}}(t) \\ \left(\frac{\dot{a}_4(t)}{a_4(t)} + a_3(t) + a_1(t) - 2a_4(t)k_oT_w\right)z_2(t) + 2\frac{z_2(t)^2}{z_1(t)} - \\ 2a_2(t)dm_{h_{comb}}(t)\frac{z_2(t)^2}{z_1(t)} \end{bmatrix} \tag{4.6.14}$$

System (4.6.13) is in triangular additive form and it admits an observer of the form (4.6.3). It is consequently possible to design a high gain nonlinear observer to estimate $z_2(t)$ using the known measurement $z_1(t) = x_1(t) = p(t)$ as:

$$\dot{\hat{z}}(t) = A_0\hat{z}(t) + \phi(\hat{z}(t), u) + \begin{bmatrix} \lambda_1 & 0 \\ 0 & \lambda_2 \end{bmatrix} K_0(C_0\hat{z}(t) - z_1(t)) \tag{4.6.15}$$

The linear dynamics is assigned by the gain K_0, deduced from a Kalman filter [Naidu, 2003] to ensure the stability of $A_0 - K_0C_0$ as it is required for the high gain observer. The parameters are chosen as $\lambda_1 = 5000$ and $\lambda_2 = \lambda_1^2$ to guarantee the system convergence.

To recover the original state space variables of system (4.5.5), the inverse of the transformation (4.6.12) is performed and provides the physical states:

$$\hat{x}_1(t) = \hat{z}_1(t), \quad \hat{x}_2(t) = \frac{\hat{z}_2(t)}{a_4(t)k_1\hat{z}_1(t)} \tag{4.6.16}$$

Figure 4.11 shows a scheme of the high gain observer design.

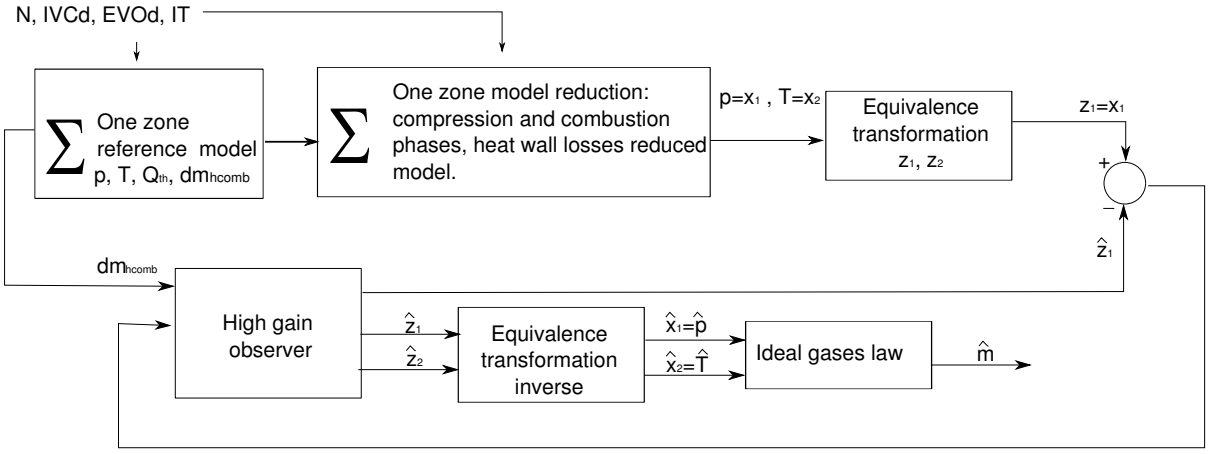

Figure 4.11: Model based high gain observer application scheme.

4.6.3 Simulation results

Using the perfect gas law in Equation (4.5.6), the enclosed mass is obtained as:

$$\hat{m}(t) = \frac{\hat{x}_1(t)V(t)}{r\hat{x}_2(t)} \tag{4.6.17}$$

Figures 4.12a, 4.12b and 4.12c show the virtual engine and estimation results for the operating conditions $N = 2000$ rpm and $IMEP = 10$ bar. Figures 4.12a and 4.12b

show the cylinder pressure and the temperature estimations, respectively, during the compression and combustion strokes (when the valves are closed). Figure 4.12c shows an augmented view of the mass estimation to better see the transitory stabilization. The second simulation case is shown in Figures 4.13a, 4.13b and 4.13c where the operating conditions are changed to $N = 4000$ rpm and $IMEP = 1.02$ bar.

The reference to validate the observer is the virtual engine model presented Section 4.3. The observer is enabled only during the valves closure. Such operating condition is enclosed between the vertical bars in the figures, which indicate the IVC event (left side bar) and the EVO event (right side bar). In the remaining parts of the engine cycle the observer is disabled and reset.

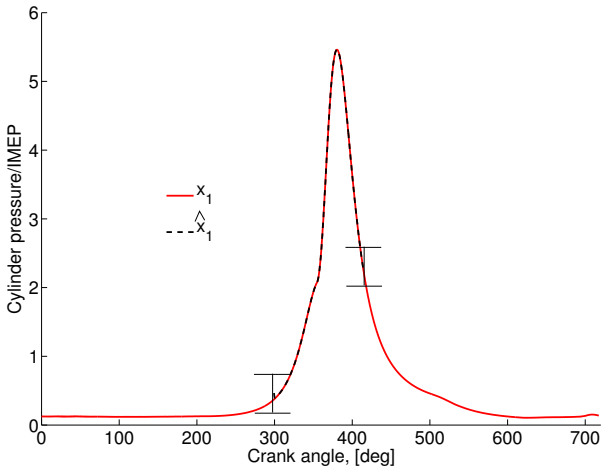

(a) Cylinder pressure

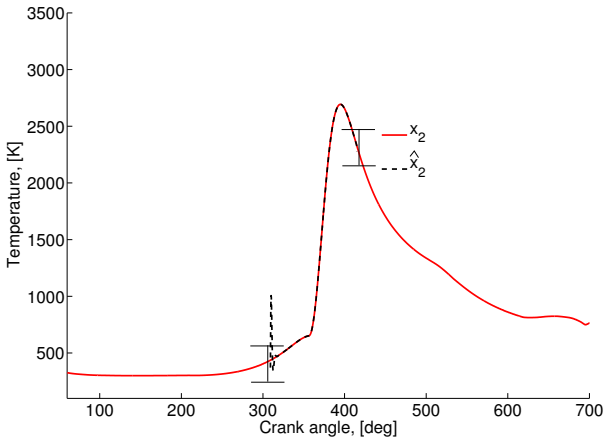

(b) Cylinder temperature

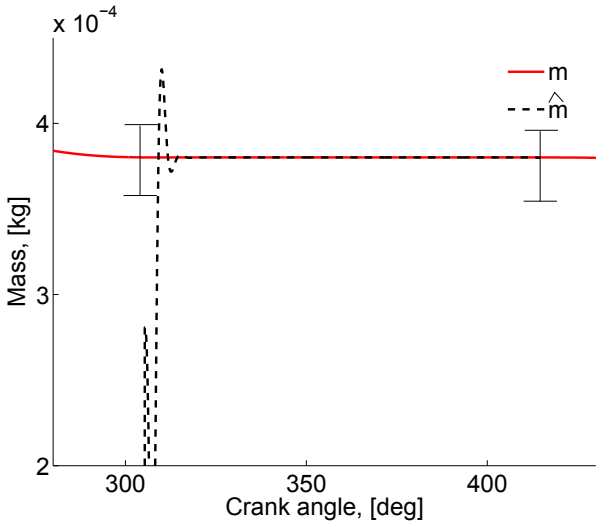

(c) Cylinder mass estimation

Figure 4.12: Case 1: $N = 2000$ rpm $IMEP = 10$ bar, $IT = 355$ CA.

The simulation shows satisfactory results of the enclosed mass estimation during the

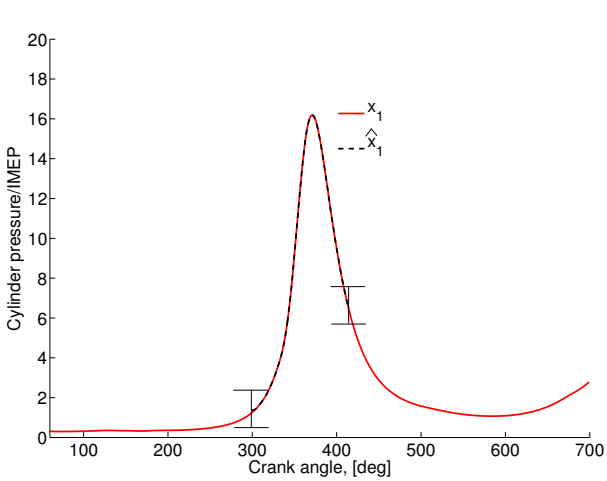

(a) Cylinder pressure

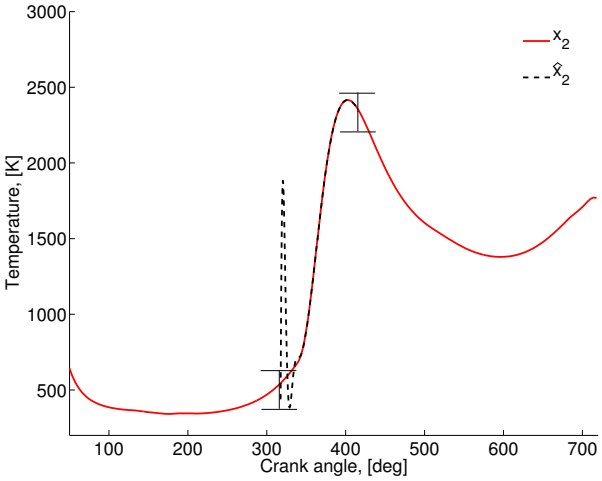

(b) Cylinder temperature

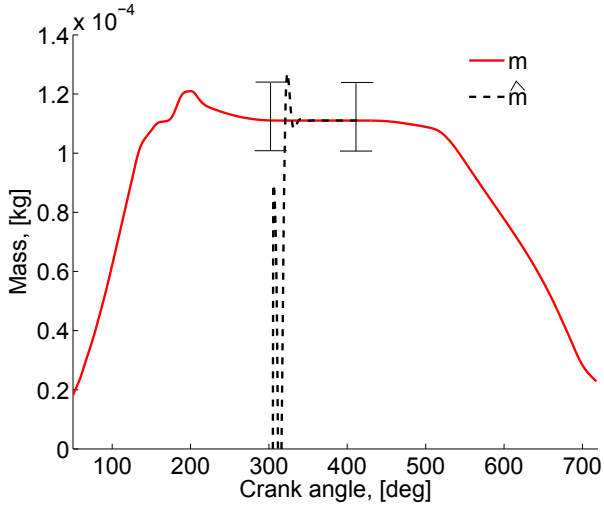

(c) Cylinder mass estimation

Figure 4.13: Case 2: $N = 4000$ rpm $IMEP = 1.02$ bar, $IT = 335$ CA.

compression and combustion strokes when the valves are closed. One engine cycle is enough for the observer convergence. The valves closure has a limited occurrence during the whole engine cycle, thus the time available for the mass estimation is limited. In this thesis, the interest is to compute the enclosed mass before the valves opening. Even if the transient behavior of the observation presents an elevated overestimation, the observation is stabilized soon enough before the engine valves opening. The mass estimation is achieved thus before the ignition timing in most operating conditions and the combustion modeling would not be necessary. It might not be the case at high engine speed conditions (4500 rpm up to 5500 rpm), where the compression stroke might be too short with respect to the observer settling time. Such condition is depicted in Figure 4.14, where the high gain observer results are tested for an operating condition where

the engine speed is $N = 5500\ rpm$. As it can be seen in the figure, the ignition arrives before the observer has converged, thus it is not possible to achieve an estimation only during the compression stroke.

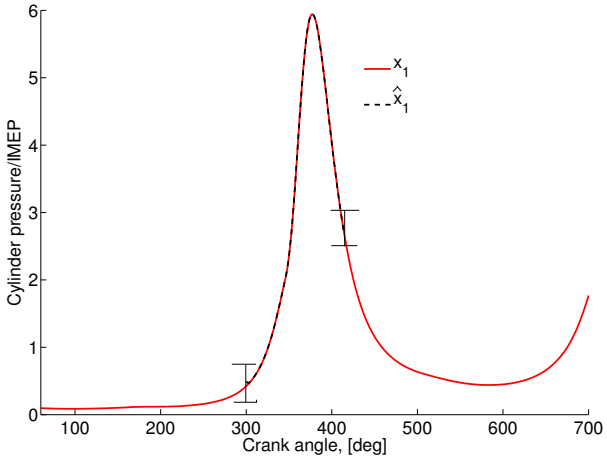

(a) Cylinder pressure

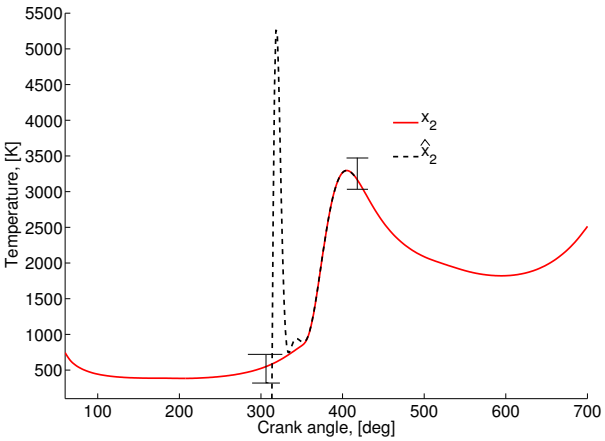

(b) Cylinder temperature

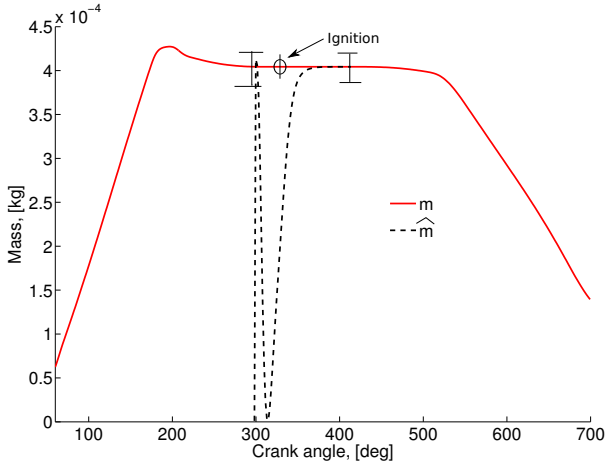

(c) Cylinder mass estimation

Figure 4.14: Case 3: $N = 5500$ rpm $IMEP = 12$ bar, $IT = 13.87$ CA.

For this reason, the estimation algorithm is computed during the compression and combustion strokes. The observer settling time to compute the enclosed mass is 3.1 ms. At 1200 rpm the valves closure lasts around 16 ms where the compression stroke lasts 6.5 ms for an $IT = 15\ CAD$ and an $IVC_d = 0\ CAD$, at 5500 rpm the valves closure lasts 3.5 ms, where the compression stroke lasts 1.4 ms for an $IT = 13.87\ CAD$ and an $IVC_d = 3\ CAD$.

Remark 4.6.1. Notice that if the IT is too advanced and/or the IVC is too delayed, it might shorten the compression stroke by some crank angle degrees.

A further validation is performed with respect to changes in the pressure reference $p(t)$.

Such result is depicted in Figure 4.15, where a perturbation in the pressure reference is introduced at 370 CAD. As it is depicted in the figure, the observer is able to recover the mass estimation in the presence of the perturbation. However, as the high gain technique is used, the observer performance contains an important overshoot. Besides, it is clear that the constraints reported before with respect to the settling time and duration of valves closure remain when a perturbation appears.

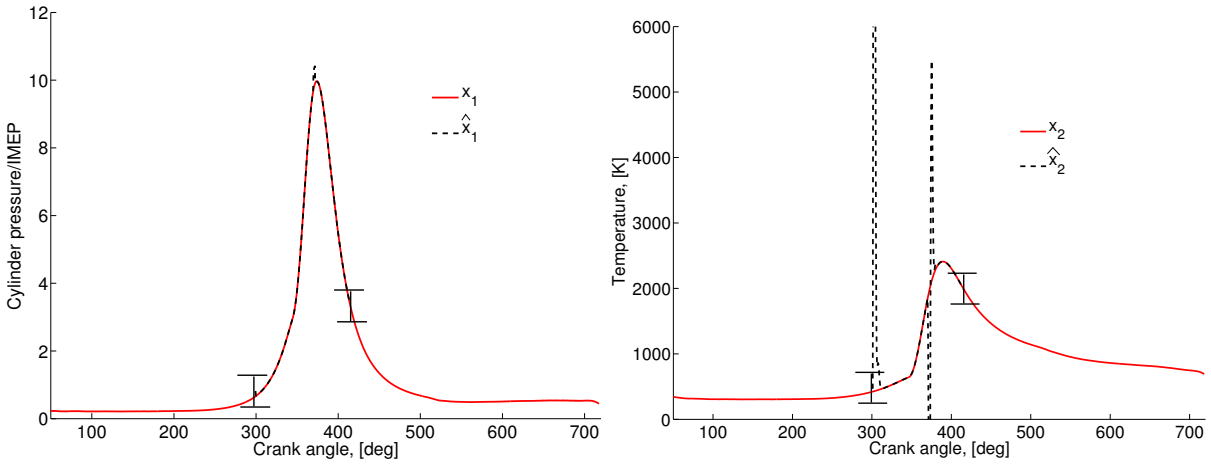

(a) Cylinder pressure

(b) Cylinder temperature

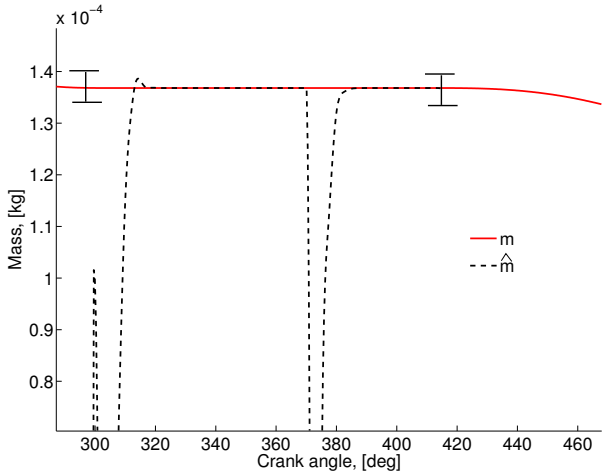

(c) Cylinder mass estimation

Figure 4.15: Case 4: $N = 1200$ rpm $IMEP = 2$ bar, $IT = 15$ CA.

With the aim to reduce the impact on the transitory to make the estimation less sensitive to the sampling time, an estimation strategy based on the linear parameter varying method is designed, only taking into account the combustion stroke, to avoid the use of a combustion model. Such strategy is presented in next section.

4.7 Some recent results on the synthesis of a parameter varying observer for the enclosed mass in a spark ignited engine

Linear parameter-varying (LPV) systems may be used as an intermediate model description in the process of synthesizing a controller for nonlinear models. The connection between the LPV system and the nonlinear model is kept, but in the synthesis step the LPV system is regarded as a linear differential inclusion, which in control theory is commonly used to express uncertainties. The result of the synthesis is an LPV controller and using the relation between the LPV system and the nonlinear system, the final nonlinear controller is obtained.

An autonomous LPV system is described by:

$$\dot{x}(t) = A(\rho(t))x(t), \quad x(t_0) = x_0 \tag{4.7.1}$$

where $x \in \mathbf{R}^n$ is the state vector, $A : \mathbf{R}^p \to \mathbf{R}^{n\times n}$, is the system matrix function and $\rho(t) \in \mathbf{R}^p$ is the parameter of the system. The parameter is not given a priori, but limited to a closed connected and bounded set $\Omega \in \mathbf{R}^p$.

Other possible trajectory of the parameter may be given by a state space dependence, $\rho(t) = \rho(x(t))$. This implies that LPV systems can represent nonlinear systems, i.e. trajectories of an LPV system can also be trajectories of a nonlinear system, as long as the parameter remains inside the bounding box.

The parameter dependence in an LPV system can have many forms. Some dependencies are of special importance when it comes to analysis and synthesis. For example, in this thesis the parameters $\rho(x(t))$ are assumed to be bounded in the convex set $[\underline{\rho_i}, \overline{\rho_i}]$ and $\rho_i \neq 0$, allowing the representation of the LPV system in a polytopic approach described by:

$$A(\rho(x(t))) = \sum_{i=1}^{M} \alpha_i(\rho(x(t)))A_i \tag{4.7.2}$$

where M is the number of vertexes of the polytope formed by the extreme values of the varying parameter $\rho(x(t))$ and the matrices $A_i \in \mathbf{R}^{n\times n}$. $\alpha_i(\rho(x(t))) \in \mathbf{R}$ is a scheduling function such that:

$$\sum_{i=1}^{M} \alpha_i(\rho_x) = 1 \tag{4.7.3}$$

A particular issue, whose solution has been explored with LPV approaches is the time-delay systems. In such systems, the time delay can be represented by a variation on the LPV parameters. Several approaches have been developed in order to deal with this problem. A relevant example of such a solution can be found in [Briat et al., 2011]. In this work, an algebraic approach is used to transform the time-delay system in a LPV static representation, where the conditions for stability and error convergence are given. The LPV systems with uncertain parameters can be seen as a particular case of a time-dely LPV system.

The challenge in using a linear parameter varying (LPV) polytopic model, for the enclosed mass estimation application of this thesis, is the fact that the observer varying parameters $\rho(x(t))$ depend on the estimated states and that nonlinear elements which also depends on the observed states, are added to the system, thus the observer contains uncertain elements $\rho(\hat{x}(t))$ and also perturbations.

Solutions to this class of problems have been explored in [Daafouz et al., 2008], [Maurice et al., 2010] and [Bara et al., 2010]. In those works, interesting strategies to relax the estimation error due to the uncertain parameters are proposed and the global asymptotic stability of the observers is ensured. However, for the application considered in this work, such strategies are not suitable as the global asymptotic stability criterion does not allow the complete elimination of the mismatch between the observation and the system states.

In order to cope with this problem, a high gain strategy is implemented in a parameter varying observer. Including a high gain strategy in a parameter varying observer improves the performance of the observer reducing the effect of uncertainties. It is important to notice that the design of a high gain parameter varying observer is an open problem. A related work can be found in [Gérard et al., 2010], where a high gain observer design is used to consider the level of disturbance attenuation of an LPV functional filter for bilinear systems with a disturbance attenuation specification. The observer gain is written as a function of the estimated state and the high gain observer is computed using Linear Matrix Inequalities (LMI) techniques. In this work, the high gain approach is used to ensure the stability of the filtering error and to optimize the disturbance attenuation.

In this section, a high gain observer for a parameter varying polytopic model is proposed to estimate the enclosed mass in the combustion chamber of a SI engine. The high gain strategy allows the design of an observer that handles the uncertain part of the system. The observer uses the cylinder pressure measurement during the compression stroke to estimate the enclosed mass. An engine compression model that is presented next is used to build the observer. The compression model is based on the reduced one zone model presented in Section 4.5.

4.7.1 Engine compression model

Only the compression stroke, after the inlet valve closure (IVC) is considered. During the compression stroke (while the valves are closed) no energy is transferred between the cylinder and the inlet and outlet ports. Besides, the cylinder enclosed mass remains constant. The engine model presented in Section 4.5 is used. Defining the cylinder pressure $p(t) = x_1(t)$ and the cylinder temperature $T(t) = x_2(t)$, the dynamics of the cylinder pressure and temperature during the compression stroke are given as:

$$\begin{aligned}\dot{x}_1(t) &= -\left(\frac{r}{c_v}+1\right)\frac{dV(t)}{V(t)}x_1(t) - \frac{r}{c_v V(t)}A_w(t)\omega x_1(t)(k_1 x_2(t) - k_0 T_w)\\ \dot{x}_2(t) &= -\frac{rdV(t)}{c_v V(t)}x_2(t) - \frac{r}{c_v V(t)}x_2(t)A_w(t)\omega(k_1 x_2(t) - k_0 T_w)\end{aligned} \tag{4.7.4}$$

Notice that this model is similar to the model presented in Equation (4.5.5) but the term corresponding to the combustion burning rate $dm_{h_{comb}}(t)$ has been set to 0.

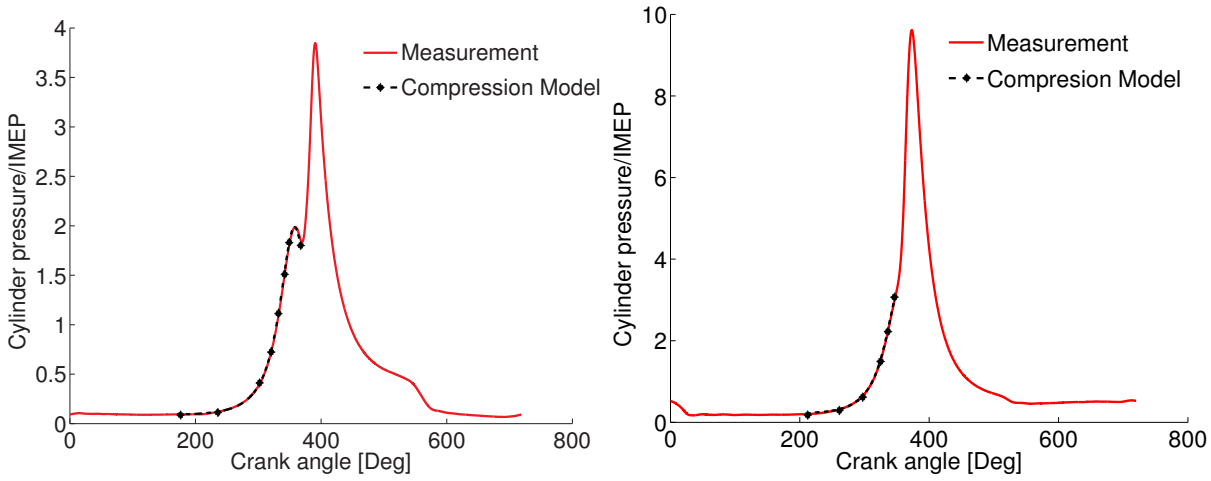

(a) Cylinder pressure. N=1500 rpm, IMEP=18 bar. (b) Cylinder pressure. N=1200 rpm, IMEP=2 bar.

Figure 4.16: Compression model validation

The compression model is tested by taking as a reference the measurements of a 1.2 liters engine. The engine characteristics are presented in Table 4.2. The data to fit the model is the cylinder pressure. A comparison between the measurements and the model is shown in Figures 4.16a and 4.16b. A good agreement between the measurements and the compression model is obtained, thus the model can be used as a virtual engine to build the observer. Notice that this validation is similar to the one presented in Section 4.3.2 but the results are plotted only during the compression stroke.

4.7.2 Parameter varying polytopic system representation

The model (4.7.4) can be written as the following LPV model:

$$\dot{x}(t) = A(\rho(x(t)))x(t) + \phi(x(t)), \quad y(t) = Cx(t) \tag{4.7.5}$$

where

$$x(t) = \begin{bmatrix} x_1(t) \\ x_2(t) \end{bmatrix}, \quad A(\rho(x(t))) = \begin{bmatrix} 0 & \frac{r}{c_v}\rho(x(t)) \\ 0 & 0 \end{bmatrix}, \quad C = \begin{bmatrix} 1 & 0 \end{bmatrix}, \tag{4.7.6}$$

$$\rho(x(t)) = -\frac{1}{V(t)}\omega A_w(t) k_1 x_1(t) \tag{4.7.7}$$

and

$$\phi(x(t)) = \begin{bmatrix} \Big(-\Big(\frac{r}{c_v}+1\Big)\frac{dV(t)}{V(t)} + \frac{r}{c_v V(t)}\omega A_w(t) k_0 T_w \Big) x_1(t) \\ \frac{r}{c_v}\Big(-\frac{dV(t)}{V(t)} - \frac{1}{V(t)}\omega A_w(t)(k_1 x_2(t) - k_0 T_w)\Big) x_2(t) \end{bmatrix} \tag{4.7.8}$$

From this part of the document, $\rho(x(t)) = \rho_x$ and $\rho(\hat{x}(t)) = \hat{\rho}_x$ to simplify the notation.

In this study, the parameter ρ_x is assumed to be bounded in the convex set $[\underline{\rho}, \overline{\rho}]$ and $\rho \neq 0$. It makes possible to represent the system (4.7.5) in a polytopic approach. Due to the fact that the system (4.7.6) is a quasi-LPV system since ρ_x depends on the state $x(t)$, the system state is assumed to belong to a bounded set $\Gamma \subset \mathbf{R}^n$, due to the nature of the involved physical variables. Under those conditions, the matrix $A(\rho_x)$ can be written in the form:

$$A(\rho_x) = \sum_{i=1}^{M} \alpha_i(\rho_x) A_i \tag{4.7.9}$$

where $M = 2$ is the number of vertexes of the polytope formed by the extremes of the varying parameter ρ_x. $\alpha_i(\rho_x) \in \mathbf{R}$ is a scheduling function such that $\sum_{i=1}^{M} \alpha_i(\rho_x) = 1$ and the matrices $A_i \in \mathbf{R}^{n\times n}$. $\phi(x(t))$ is a Lipschitz continuous function such that $||\phi(x_a) - \phi(x_b)|| < \delta||x_a - x_b||, \quad \delta > 0, \quad x_a, x_b \in \mathbf{D}_x$.

The state $x_2(t)$ is observed through the measurement of $x_1(t)$. It is assumed that the uncertainty in $x(t)$ is bounded by some constant $\Delta > 0 \in \mathbf{R}$, thus $||\rho_x - \hat{\rho}_x|| < \Delta$..

Remark 4.7.1. Note that system (4.7.6) is written in a state space form that allows the design of a high gain observer.

Remark 4.7.2. It is important to recall that system (4.7.6) is observable for all $\rho_x \neq 0$.

4.7.3 High gain observer for LPV systems

The high gain observer presented in Section 4.6.1 is extended to *LPV* systems using a polytopic representation. Given the system (4.7.5), an observer for the state $x(t)$ is proposed as:

$$\begin{aligned}\dot{\hat{x}}(t) =& A_0(\hat{\rho}_x)\hat{x}(t) + \Lambda L_0(\hat{\rho}_x)(y(t) - \hat{y}(t)) + \phi(\hat{x}(t)) \\ \hat{y}(t) =& C_0\hat{x}(t)\end{aligned} \tag{4.7.10}$$

where

$$A_0(\hat{\rho}_x) = \sum_{i=1}^{M} \alpha_i(\hat{\rho}_x)A_i \tag{4.7.11}$$

$$L_0(\hat{\rho}_x) = \sum_{i=1}^{M} \alpha_i(\hat{\rho}_x)L_i \tag{4.7.12}$$

and

$$\Lambda = \begin{bmatrix} \lambda & 0 & 0 \\ 0 & \lambda^2 & 0 \\ .... & & \\ 0 & 0 & \lambda^n \end{bmatrix} \tag{4.7.13}$$

where $\lambda \in \mathbf{R}$ and $\lambda > 1$. Notice that $\Lambda = \Lambda^T$.

The dynamics of the estimation error $e(t) = x(t) - \hat{x}(t)$ is governed by:

$$\dot{e}(t) = \Big[A_0(\hat{\rho}_x) - \Lambda L_0(\hat{\rho}_x)C_0\Big]e(t) + \phi(x(t)) - \phi(\hat{x}(t)) + v_x(t) \tag{4.7.14}$$

where

$$v_x(t) = \Big[A_0(\rho_x) - A_0(\hat{\rho}_x)\Big]x(t) \tag{4.7.15}$$

is considered as a bilinear perturbation that is bounded in the $\mathcal{L}_2$ sense and $\phi(x(t))$ is a Lipschitz continuous function such that $||\phi(x_a(t)) - \phi(x_b(t))|| < \delta||x_a(t) - x_b(t)||, \quad \delta > 0, \quad x_a, x_b \in \mathbf{D}_x$.

The following theorem will ensure the existence of an observer in the framework of the quadratic stability:

Theorem 4.7.1. *Consider the quasi-LPV system* (4.7.5) *and assume that* $\phi(x(t))$ *is a Lipschitz continuous function such that* $||\phi(x_a(t)) - \phi(x_b(t))|| < \delta||x_a(t) - x_b(t)||, \quad \delta > 0, \quad x_a, x_b \in \mathbf{D}_x$. *If there exists the state feedback* $L_0(\hat{\rho}_x)$, *the matrices* $P = P^T$ *such that* $P > 0$ *and* Λ *defined in Equation* (4.7.13), *such that the following inequality is satisfied for all* $\rho_x \in [\underline{\rho}, \overline{\rho}]$*:*

$$\begin{bmatrix} \Big[A_0(\hat{\rho}_x) - \Lambda L_0(\hat{\rho}_x)C_0\Big]^T P + P\Big[A_0(\hat{\rho}_x) - \Lambda L_0(\hat{\rho}_x)C_0\Big] & P \\ +2\delta P + I & \\ P & -\gamma^2 I \end{bmatrix} < 0 \tag{4.7.16}$$

for some constant $\gamma > 0$, *then* (4.7.10) *is an observer for the system* (4.7.5) *and the estimation error is asymptotically stable and satisfies* $||e(t)||_2 < \Lambda\gamma||v_x(t)||_2$.

Proof: To prove the stability, the auxiliary variable $z(t) = \Lambda^{-1}x(t)$ is introduced and the error dynamics $\epsilon(t) = z(t) - \hat{z}(t)$ is considered:

$$\begin{aligned} \dot{\epsilon}(t) = \quad & \Lambda^{-1}\Big[A_0(\hat{\rho}_x) - \Lambda L_0(\hat{\rho}_x)C_0\Big]\Lambda\epsilon(t) + \\ & \Lambda^{-1}\Big(\phi(x(t)) - \phi(\hat{x}(t))\Big) + \Lambda^{-1}v_x(t) \end{aligned} \tag{4.7.17}$$

Choosing the Lyapunov function $V(t) = \epsilon(t)^T P\epsilon(t)$ where $P = P^T > 0$, the following inequality must be satisfied in order to ensure the observer stability:

$$\dot{V}(t) = \dot{\epsilon}(t)^T P\epsilon(t) + \epsilon(t)^T P\dot{\epsilon}(t) < 0 \tag{4.7.18}$$

which yields to:

$$\dot{V}(t) = \epsilon(t)^T \Big[\Big(\Lambda A_0(\hat{\rho}_x)^T \Lambda^{-1} - \Lambda C_0^T L_0(\hat{\rho}_x)^T \Big) P \tag{4.7.19}$$
$$+P\Big(\Lambda^{-1} A_0(\hat{\rho}_x)\Lambda - L_0(\hat{\rho}_x) C_0 \Lambda\Big)\Big]\epsilon(t) + \Big(\phi(x(t)) - \phi(\hat{x}(t))\Big)^T \Lambda^{-1} P\epsilon(t) +$$
$$\epsilon(t)^T P\Lambda^{-1}\Big(\phi(x(t)) - \phi(\hat{x}(t))\Big) + v_x(t)^T \Lambda^{-1} P\epsilon(t) + \epsilon(t)^T P\Lambda^{-1} v_x(t) < 0$$

Considering the structure of Λ (Equation (4.7.13)) and the fact that $A_0(\hat{\rho}_x)$ is triangular and $C_0 = [\ 1 \quad .. \quad 0\ ]$, a simple calculation yields to:

$$\Lambda A_0(\hat{\rho}_x)^T \Lambda^{-1} - \Lambda C_0^T L_0(\hat{\rho}_x)^T = \lambda \Big[A_0(\hat{\rho}_x) - L_0(\hat{\rho}_x) C_0 \Big]^T \tag{4.7.20}$$

Replacing this result in (4.7.19) and taking into account that $\phi(x(t))$ satisfies $||\phi(x(t)) - \phi(\hat{x}(t))|| < \delta ||x(t) - \hat{x}(t)||$, the following inequality must be verified to ensure the error $\epsilon(t)$ converges to 0:

$$\lambda \epsilon(t)^T \Big[\Big(A_0(\hat{\rho}_x) - L_0(\hat{\rho}_x) C_0 \Big)^T P + P\Big(A_0(\hat{\rho}_x) - L_0(\hat{\rho}_x) C_0 \Big) \Big] \epsilon(t)$$
$$+2\delta \epsilon(t)^T P \epsilon(t) + v_x(t)^T P \Lambda^{-1} \epsilon(t) + \epsilon(t)^T \Lambda^{-1} P v_x(t) < 0 \tag{4.7.21}$$

Considering that $v_x(t)$ is $\mathcal{L}_2$ bounded, the application of the Bounded Real Lemma leads to the inequality:

$$\begin{bmatrix} G & \Lambda^{-1} P \\ \Lambda^{-1} P & -\gamma^2 I \end{bmatrix} < 0 \tag{4.7.22}$$

where

$$G = \ \lambda \Big[\Big(A_0(\hat{\rho}_x) - L_0(\hat{\rho}_x) C_0 \Big)^T P + P\Big(A_0(\hat{\rho}_x) - L_0(\hat{\rho}_x) C_0 \Big) \Big]$$
$$+2\delta P + I \tag{4.7.23}$$

therefore it is verified that $||\epsilon(t)||_2 < \gamma ||v_x(t)||_2$ for all $\rho_x \in [\underline{\rho}, \overline{\rho}]$. Since $\epsilon(t) = \Lambda^{-1} e(t)$, (4.7.23) becomes $||e(t)||_2 < \Lambda\gamma ||v_x(t)||_2$ and Theorem 4.7.1 is proved.

Remark 4.7.3. Notice that Inequality (4.7.22) is not a linear matrix inequality (LMI) because there is a nonlinear relation between the state feedback $L_0(\hat{\rho}_x)$ and the parameter Λ.

4.8 High gain nonlinear observer for LPV systems application

According to Theorem 4.7.1, for the observer in Equation (4.7.10), Inequality (4.7.16) must be accomplished to guarantee the observer stability. However, as there is a nonlinear relation between the parameter Λ and the gain $L_0(\hat{\rho}_x)$, it is not possible to use an LMI solver to obtain the observer feedback. Nevertheless, it has also been proved that if Inequality (4.7.21) is accomplished, Theorem 4.7.1 is satisfied. Thus, using this result, the procedure to obtain Λ and $L_0(\hat{\rho}_x)$ can be solved finding a feedback $L_0(\hat{\rho}_x)$ such that:

$$\Big(A_0(\hat{\rho}_x) - L_0(\hat{\rho}_x)C_0\Big)^T P + P\Big(A_0(\hat{\rho}_x) - L_0(\hat{\rho}_x)C_0\Big) < 0 \tag{4.8.1}$$

and a parameter λ large enough, such that (4.7.21) is accomplished similarly as it has been done for the classical high gain observation strategy presented before in Section 4.6.1.

In this thesis, to compute $L_0(\hat{\rho}_x)$ as (4.7.12), L_i are deduced from the dual solution of the quadratic stability of an uncertain plant developed in [Olalla et al., 2009] and [Feron et al., 1992], where a framework for robust linear quadratic regulators (LQRs) control for a convex model of power converters, taking into account uncertainty in the parameters is presented.

In this work, the LQR control problem with uncertain parameters is solved by using an LMI. In this thesis, the dual representation of the such controller is used. Thus, the solution to solve the state feedback K for the LQR problem is stated in the following theorem:

Theorem 4.8.1. *Consider the system:*

$$\begin{aligned} \dot{x}(t) =& Ax(t) + Bu(t) \\ y(t) =& Cx(t) \end{aligned} \tag{4.8.2}$$

where $A \in \mathbf{R}^{n\times n}$ and $B \in \mathbf{R}^{n\times p}$ contain uncertainties, $u(t) \in \mathbf{R}^p$ is the system input and $C \in \mathbf{R}^{q\times n}$ where q is the number of the system outputs. Given the symmetric matrix $P > 0 \in \mathbf{R}^{n\times n}$, the matrices Y and X and the parameter matrices $W > 0$ and $V = V^T > 0$, the optimal feedback gain K that guarantees that the system (4.8.2) is quadratically stable can be found by minimizing the following expression:

$$min(trace(X) + trace(VP)) \tag{4.8.3}$$

subject to the following linear matrix inequalities:

$$AP + PA^T + BY + Y^T B^T + I < 0, \quad \begin{bmatrix} X & W^{1/2}Y \\ Y^T W^{1/2} & P \end{bmatrix} < 0 \tag{4.8.4}$$

Once this minimization under constraints is solved, the controller can be recovered by $K = YP^{-1}$.

Remark 4.8.1. The polytopic application of this theorem consists on replacing the constraints involving matrices A and B by M constraints corresponding to the vertexes of the polytope formed by A_i and B_i, with matrices X_i and Y_i.

To obtain the observer gain $L_0(\hat{\rho}_x)$, the dual solution of the LQR problem in Theorem 4.8.1 for the polytopic case (remark 4.8.1) is used to compute L_i, which yields to the following proposition:

Proposition 4.8.2. *Consider the observer* (4.7.10). *Given the symmetric matrix* $P > 0 \in \mathbf{R}^{n\times n}$, *the matrices* Y_i *and* X_i *and the parameter matrices* W *and* $V = V^T > 0$, *such that the following expression is minimized:*

$$min(trace(X_i) + trace(VP)) \tag{4.8.5}$$

subject to the linear matrices inequalities:

$$A_i^T P + PA_i + C_0^T Y_i + Y_i^T C_0 + I < 0 \tag{4.8.6}$$

$$\begin{bmatrix} X_i & W^{1/2}Y_i \\ Y_i^T W^{1/2} & P \end{bmatrix} < 0 \tag{4.8.7}$$

for $i = 1, 2$, *the matrices* $L_i = Y_i P^{-1}$ *guarantee that* $\Big(A_0(\hat{\rho}_x) - L_0(\hat{\rho}_x)C_0\Big)^T P + P\Big(A_0(\hat{\rho}_x) - L_0(\hat{\rho}_x)C_0\Big) < 0$ *for all* $\rho_x \in [\underline{\rho}, \overline{\rho}]$.

This theorem satisfies Inequality (4.8.1). The parameters W and V are chosen as:

$$W = 0.05, \quad V = \begin{bmatrix} 1 & 0 \\ 0 & 1 \end{bmatrix} \tag{4.8.8}$$

To complete the observer design, the parameters in the matrix Λ have to be chosen large enough to guarantee the estimation error to converge to 0. In this thesis, $\lambda = 150$, thus:

$$\Lambda = \begin{bmatrix} 150 & 0 \\ 0 & 150^2 \end{bmatrix} \tag{4.8.9}$$

thus, $L_0(\hat{\rho}_x)$ and Λ have been designed such that Theorem 4.7.1 is satisfied.

Remark 4.8.2. Notice that observing (4.7.5)-(4.7.8) implies the estimates:

$$\hat{\rho}_x = -\frac{1}{V(t)}\omega A_w(t) k_1 \hat{x}_1(t) \tag{4.8.10}$$

and

$$\phi(\hat{x}(t)) = \begin{bmatrix} \Big(-\Big(\frac{r}{c_v}+1\Big)\frac{dV(t)}{V(t)} + \frac{r}{c_v V(t)}\omega A_w(t) k_0 T_w \Big)\hat{x}_1(t) \\ \frac{r}{c_v}\Big(-\frac{dV(t)}{V(t)} - \frac{1}{V(t)}\omega A_w(t)(k_1\hat{x}_2(t) - k_0 T_w)\Big)\hat{x}_2(t) \end{bmatrix} \tag{4.8.11}$$

However, since $y(t) = x_1(t)$ is a measured signal, $\hat{\rho}_x$ may indeed be replaced by:

$$\hat{\rho}_x = -\frac{1}{V(t)}\omega A_w(t) k_1 \hat{y}(t) \tag{4.8.12}$$

Remark 4.8.3. If the perturbation $v_x = 0$, Inequality (4.7.21) yields:

$$\begin{aligned} \lambda\epsilon(t)^T\Big[\Big(A_0(\hat{\rho}_x) - L_0(\hat{\rho}_x)C_0\Big)^T P + P\Big(A_0(\hat{\rho}_x) - L_0(\hat{\rho}_x)\Big)C_0)\Big]\epsilon(t) \\ +2\delta\epsilon(t)^T P\epsilon(t) < 0 \end{aligned} \tag{4.8.13}$$

As it has been shown in Proposition 4.8.2, it is possible to find a feedback such that Inequality (4.8.1) is accomplished, moreover, the dual solution of Theorem 4.8.1 guarantees the quadratic stability of an observer using such a feedback, thus the first term on Inequality (4.8.13) satisfies:

$$\lambda\epsilon(t)^T\Big[\Big(A_0(\hat{\rho}_x) - L_0(\hat{\rho}_x)C_0\Big)^T P + P\Big(A_0(\hat{\rho}_x) - L_0(\hat{\rho}_x)\Big)C_0)\Big]\epsilon(t) < -\lambda\alpha||\epsilon(t)||^2 \tag{4.8.14}$$

for some constant values $\alpha > 0$. Using this result in Inequality (4.8.14) and bounding the second term in the inequality, it yields to:

$$\lambda\epsilon(t)^T\Big[\Big(A_0(\hat{\rho}_x) - L_0(\hat{\rho}_x)C_0\Big)^T P + P\Big(A_0(\hat{\rho}_x) - L_0(\hat{\rho}_x)\Big)C_0)\Big]\epsilon(t) + 2\delta\epsilon(t)^T P\epsilon(t) < -\lambda\alpha||\epsilon(t)||^2 + \beta||\epsilon(t)||^2 \tag{4.8.15}$$

for some constant $\beta > 0$. Thus a bound value for λ can be obtained as $\lambda > \frac{\beta}{\alpha}$ that ensures the exponential stability of $\epsilon(t)$.

Remark 4.8.4. A restriction of this synthesis is the fact that the LQR dual adaptation to obtain the gains L_i has brought two more calibration parameters besides the values of Λ. Such parameters are the matrices V and W, present in the synthesis of the dual solution of Theorem 4.8.1, presented as the Proposition 4.8.2.

In order to summarize the procedure followed to use the LPV high gain observer to estimate the enclosed mass in the combustion chamber, Figure 4.17 depicts a scheme of the LPV high gain observer implementation.

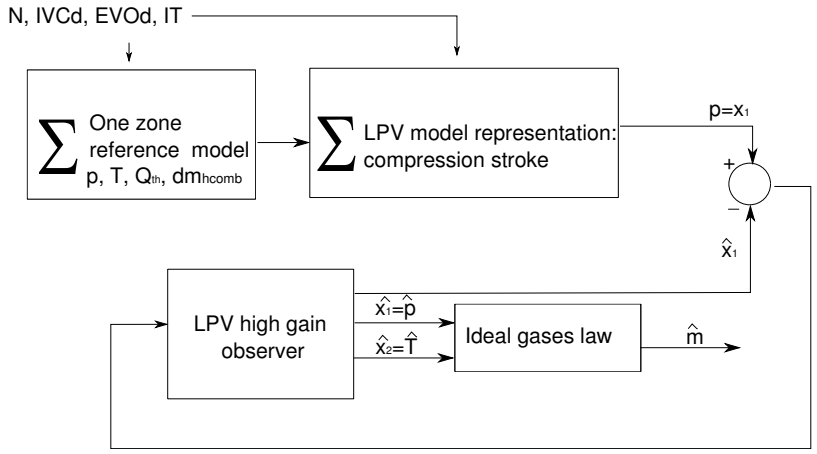

Figure 4.17: Model based LPV high gain observer application scheme.

4.8.1 Simulation results

Using the observed states $\hat{x}_1(t)$ and $\hat{x}_2(t)$, the enclosed mass in the cylinder is computed using the ideal gas law (4.5.6):

$$\hat{m}(t) = \frac{\hat{x}_1(t)V(t)}{r\hat{x}_2(t)} \tag{4.8.16}$$

Figures 4.18a and 4.18b show the cylinder pressure and temperature estimations during the compression stroke when the valves are closed and Figure 4.18c shows the result of the mass estimation, the operating conditions are $N = 4000$ rpm and $IMEP = 8$ bar. The second simulation case is shown in Figures 4.19a, 4.19b and 4.19c, where the operating conditions are changed to $N = 1200$ rpm and $IMEP = 2$ bar.

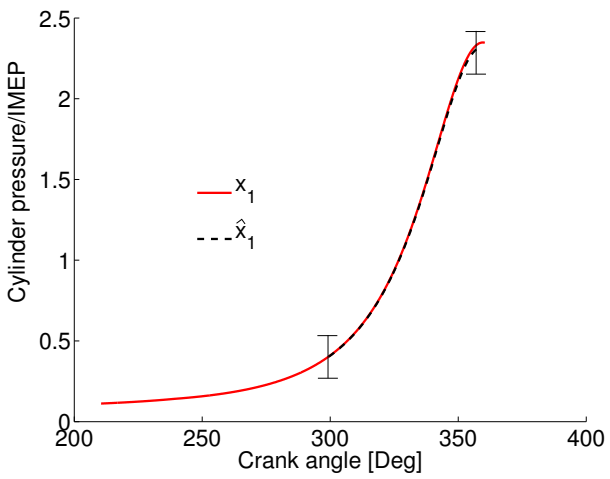

(a) Cylinder pressure

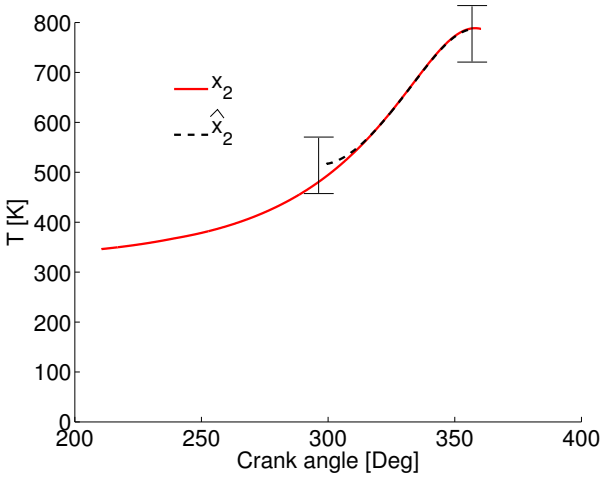

(b) Cylinder temperature

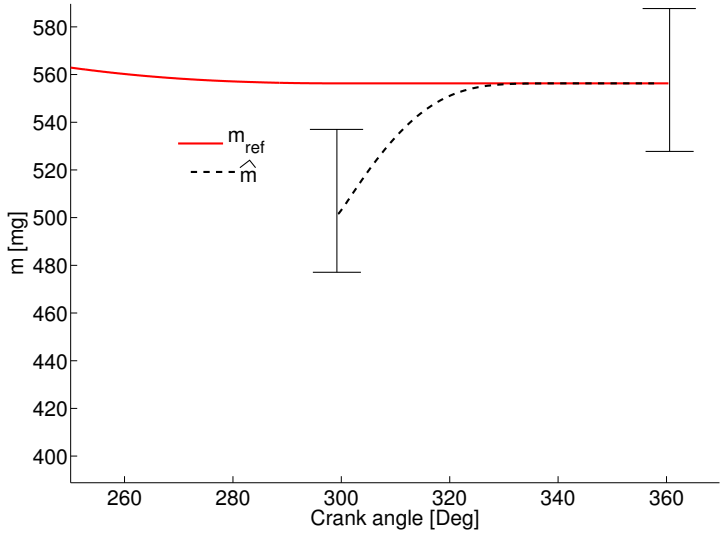

(c) Cylinder mass estimation

Figure 4.18: LPV observer. Case 1: N=4000 rpm IMEP=8 bar, IT=2.25 CAD

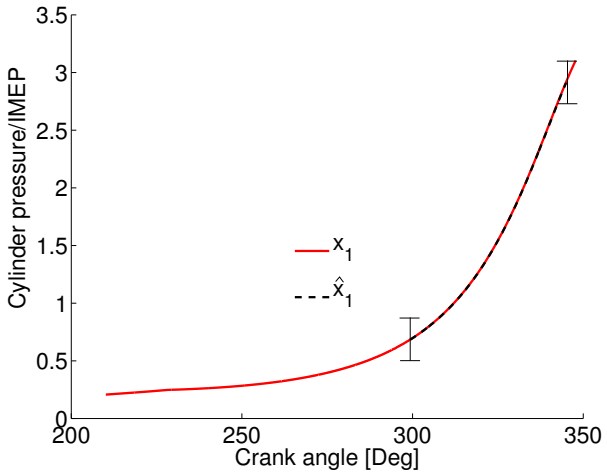

(a) Cylinder pressure

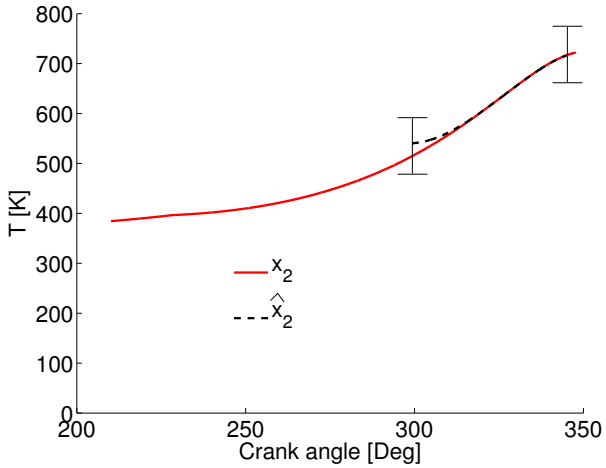

(b) Cylinder temperature

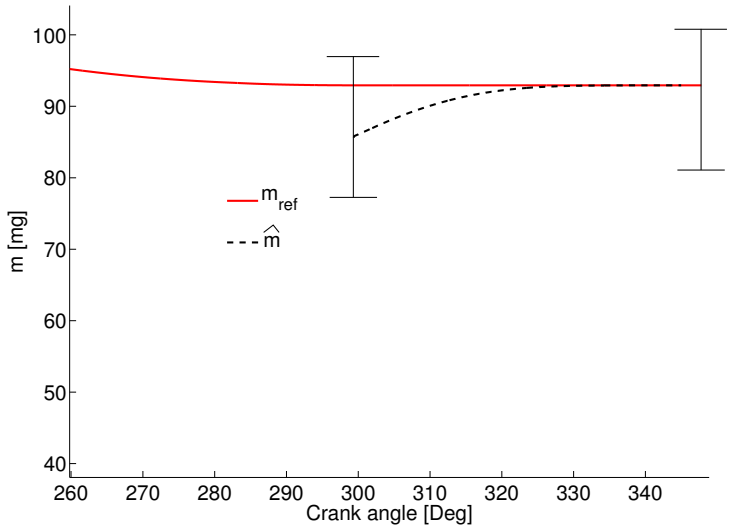

(c) Cylinder mass estimation

Figure 4.19: LPV observer. Case 2: N=1200 rpm IMEP= 2 bar, IT=15 CAD

The vertical bars in the figures represent the interval where the observer is valid: the observer is enabled only during the compression (valves closed), in the remaining parts of the cycle the observer is disabled and reset. One engine cycle is enough to accurately observe the variables of interest $\hat{x}_1(t)$ and $\hat{x}_2(t)$.

The compression stroke might be short in comparison with the whole engine cycle, limiting the available time for the estimation. In this thesis, the interest is to compute the enclosed mass before the ignition. The observer settling time to compute the enclosed mass is 1.7 ms. At 1200 rpm the compression stroke lasts 6.5 ms for an $IT = 15\ CAD$, at 5500 rpm the compression stroke lasts 1.4 ms for an $IT = 13\ CAD$ and at 4500 rpm, the compression stroke lasts around 2.1 ms. It shows that even if the initial error is

important when the observer is initialized, the estimated mass converges soon enough before the ignition timing for an engine speed $N < 4500\ rpm$, always that the compression stroke lasts more than 1.7 ms. For engine speeds above 4500 rpm, the convergence of the observer before the ignition timing is not ensured. An example of such limitation is shown in Figure 4.20, where a test at an engine speed of 5500 rpm is presented. Only the enclosed mass estimation is plotted. As the engine speed is high, the duration of the compression is short: 1.4 ms. Thus, the observer has not converged when the combustion starts, and the mass estimation cannot be achieved.

Remark 4.8.5. Notice that if the IT is too advanced and/or the IVC is too delayed, it might shorten the compression stroke by some crank angle degrees.

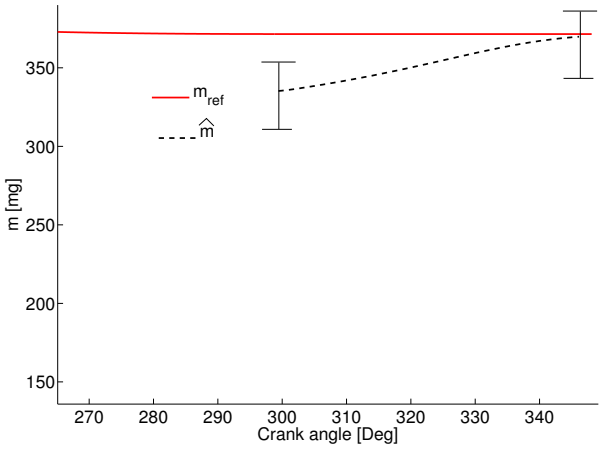

Figure 4.20: LPV observer mass estimation. Case 3: N=5500 rpm IMEP= 12 bar, IT=13.875

Comparing the results of the LPV high gain observer with the simulations obtained in the last section for the classical nonlinear high gain observer application, there is a slight improvement in the observer settling time: 1.3 ms for the LPV high gain observer and 3.1 ms for the nonlinear high gain observer. This reduction on the observer settling time makes it possible to estimate the enclosed mass at higher engine speeds, avoiding modeling the combustion process. However, at engine speeds bigger than 4500 rpm, the compression stroke might still be too short to achieve the mass estimation.

As it is shown in equations (4.8.12) and (4.8.11), the observer depends on uncertain parameters as it depends on the estimated states. It has been proved with Theorem 4.7.1 that the LPV high gain observer is able to cope with such uncertainties. A further validation is performed with respect to changes in the pressure reference $p(t)$. Changes in the pressure reference introduce perturbations in the parameter $\rho(t)$. Such result is depicted in Figure 4.21, where a perturbation in the pressure reference is introduced at 320 CAD. As it is depicted in the figure, the observer is able to recover the mass estimation in the presence of the perturbation. However, as the high gain technique is

used, the observer performance contains an important overshoot. Besides, it is clear that the constraints reported before with respect to the duration of the compression stroke remain when a perturbation appears.

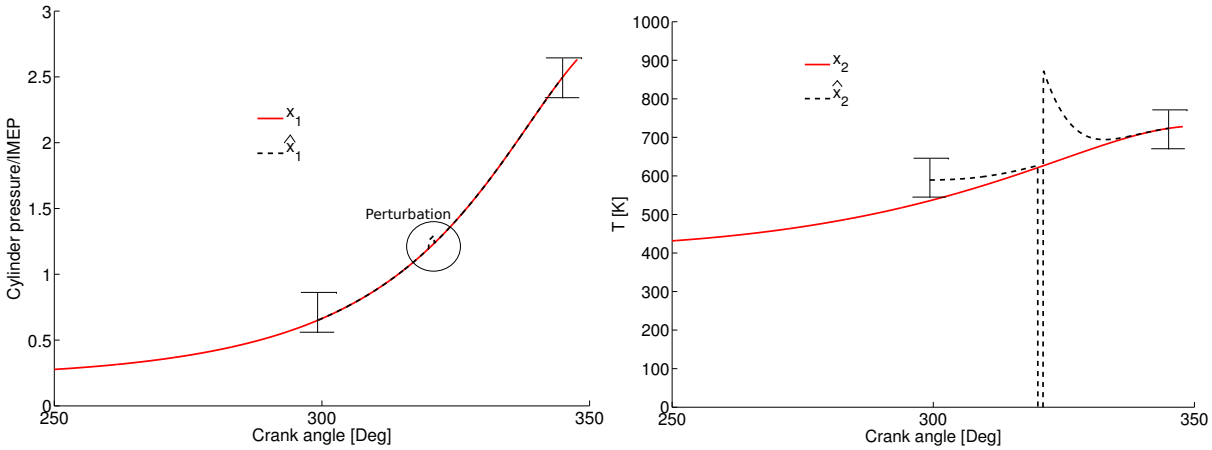

(a) Cylinder pressure

(b) Cylinder temperature

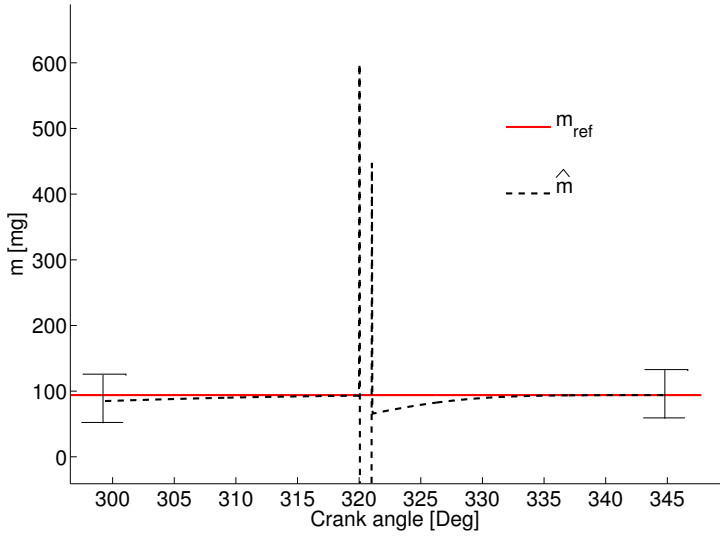

(c) Cylinder mass estimation

Figure 4.21: LPV observer. Case 4: N=1200 rpm IMEP= 2 bar, IT=15 CAD. Perturbation at 320 CAD.

Tests with respect to changes in the initial pressure condition of the observer $\hat{x}_{1_0}$ have been also studied and the result is presented in Figure 4.22a. It gives a robustness proof with respect to changes in the parameter $\hat{\rho}_x$ and also in the nonlinearities $\phi(\hat{x}(t))$, which depend on the state $\hat{x}_1$. As it can be seen, the observer presents an abrupt beginning, however, in spite of the uncertainty added to the initial condition, the observer is established soon enough before the ignition timing. Besides, the $\mathcal{L}_2$ norm of the function $v_x(t)$ has been computed for a normal variation of 50% in $\hat{x}_{1_0}$. 1000 samples

tests were performed. The result is presented in Figure 4.22b as an histogram. It is observed that in spite of the variation in $\hat{x}_{1_0}$ which introduces uncertainty in the parameter $\hat{\rho}_x$, the $\mathcal{L}_2$ norm of $v_x(t)$ is always bounded. It is important to said that in this application, $x_1(t)$ is assume to be measured, thus $\hat{x}_1(t)$ could be considered equal to x_1, in which case $v_x(t) = 0$. However, it is important to keep the assumption that it might be uncertainty in $v_x(t)$ in order to prove that a high gain strategy is suitable to vanish the effect of perturbations due to unknown parameters.

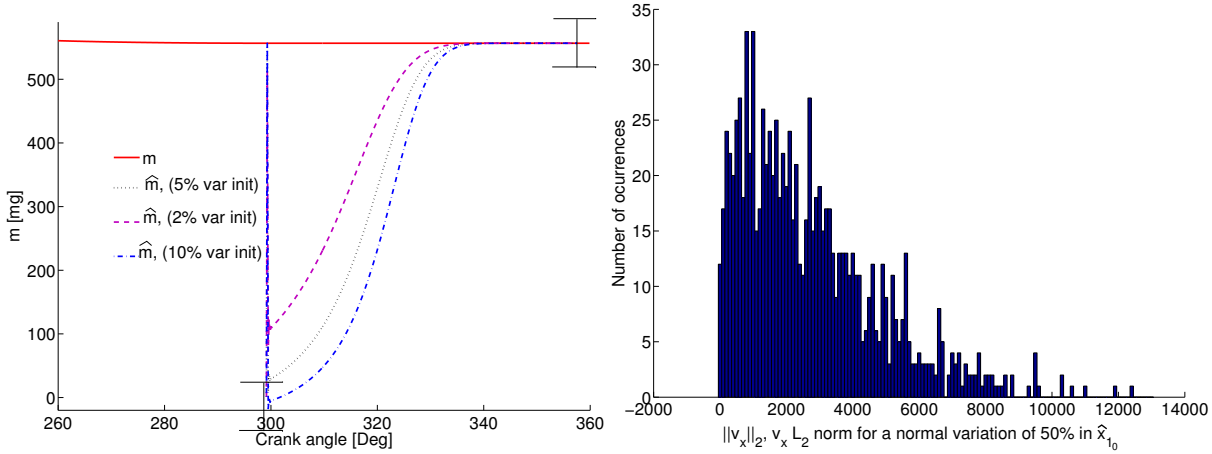

(a) Cylinder mass estimation for changes in the initial condition $\hat{x}_{1_0}$

(b) Histogram of a normal variation in the initial condition $\hat{x}_{1_0}$ of 50% with respect to its nominal value for 1000 samples.

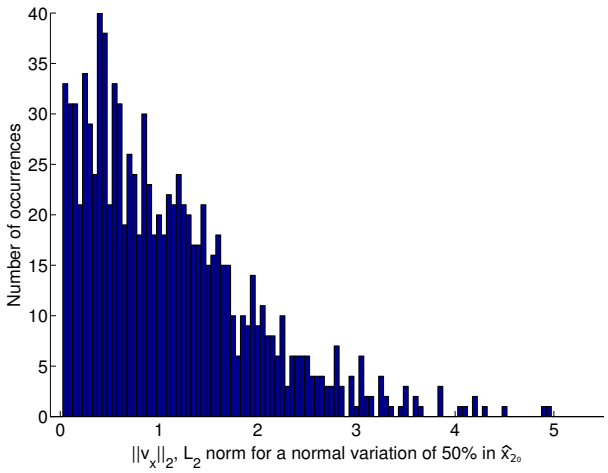

(c) Histogram of a normal variation in the initial condition $\hat{x}_{2_0}$ of 50% with respect to its nominal value for 1000 samples.

Figure 4.22: LPV observer, robustness and Montecarlo test with respect to changes in the initial conditions $\hat{x}_{1_0}$ and in $\hat{x}_{2_0}$, which implies changes in the parameter $\hat{\rho}_x$, in $v_x(t)$ and in $\phi(\hat{x}(t))$. Case 5: N=4000 rpm IMEP=8 bar, IT=2.25 CAD,

A final validation was performed with respect to changes in the modeling parameters k_1 and k_0 separately. A normal variation with a standard deviation of 10% was analyzed and a test with 1000 samples. The mass estimation error was computed in each case. Figures 4.23 shows the distribution of the error in both tests. From the figures it is concluded that for variations of maximum 10% in the parameter k_1 from its nominal value, the observation error remains below 10%. For similar variations in the parameter k_0, the observation error remains below 3%. Besides, the observer remains stable in spite of such variations.

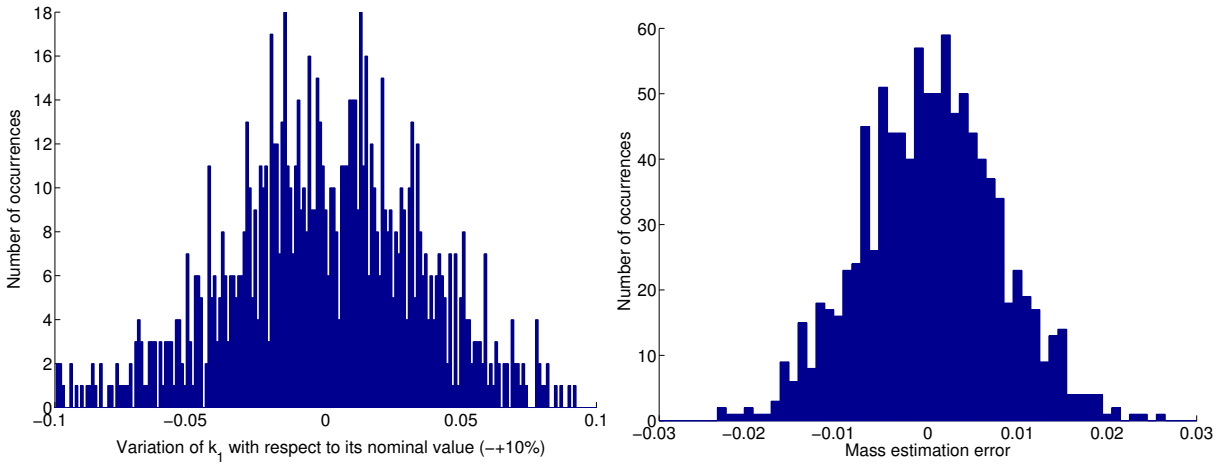

(a) Histogram of the variation in the initial modeling parameter $k_1 = \bar{k}_1 \pm \Delta\bar{k}_1$.

(b) Histogram of the variation in the initial modeling parameter $k_0 = \bar{k}_0 \pm \Delta\bar{k}_0$.

Figure 4.23: LPV observer. Histogram of the variation in the initial modeling parameters $k_{1,0}$. A normal deviation of $\pm 10\%$ for 1000 samples are tested.

The presence of noise has been also studied. Figure 4.24 shows a simulation where a noise signal have been added to the pressure reference. As it can be seen, the observer does not reject the noise. As the high gain technique is used, the observer gain is big and thus the noise is presented in the output. However, it is also noticed that such noise can be filtered with good results. For the case of this thesis, the cylinder pressure reference is pre-filtered, thus this issue does not affect the observer synthesis.

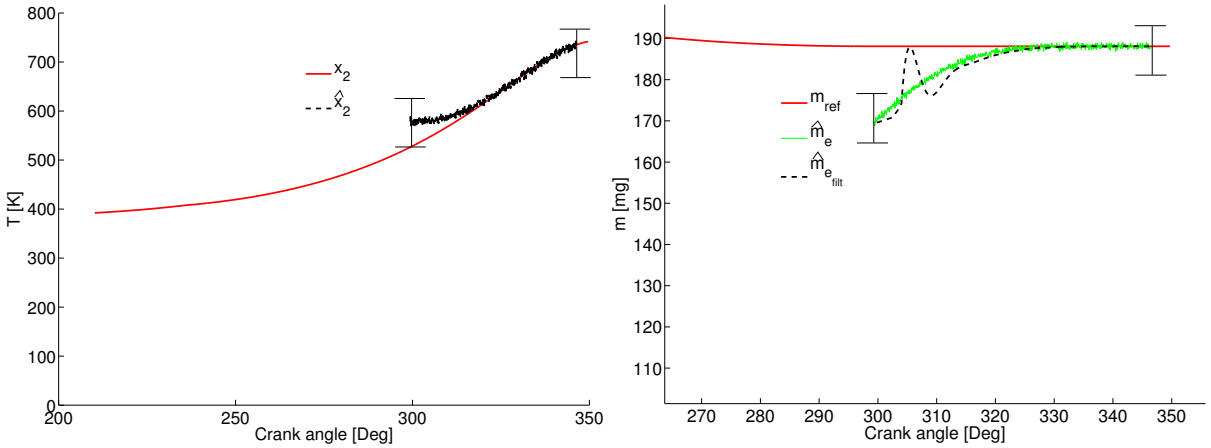

(a) Cylinder temperature

(b) Cylinder mass estimation

Figure 4.24: LPV observer. Case 6: N=2000 rpm IMEP= 6 bar, IT=13.5 CAD. Noise added to the reference $p(t)$.

4.9 Chapter Summary

A new methodology to estimate the cylinder enclosed mass during the combustion and/or compression strokes when the engine valves are closed has been proposed. The proposed strategy uses a one zone thermodynamical model where the states are the cylinder pressure $p(t)$ and the cylinder temperature $T(t)$. The cylinder pressure is measured and the temperature is observed. The enclosed mass is computed using the observed temperature and the cylinder pressure measurement, using the ideal gases law.

According to the one zone thermodynamical engine model presented in Section 4.3, during the combustion and compression strokes three phenomena are modeled as flow enthalpy: the work delivered by the piston, the wall losses and the heat from the burning rate. The burning rate is computed using a Vibe's law and the work delivered by the piston is modeled as an adiabatic compression process, the only remaining components to observe the temperature are the heat wall losses, which have been reduced with a simpler model in order to simplify the estimation design procedure.

Two observation strategies, which are valid only during the valves closure have been implemented: a high gain nonlinear observer enabled during the compression and combustion strokes and a high gain observer for parameter varying systems with uncertain parameters enabled only during the compression stroke, motivated by the fact that the enclosed mass remains constant after the IVC and that the compression stroke might be long enough to achieve convergence, which makes possible to avoid the use of a combustion model.

The classical high gain nonlinear observer presented in Section 4.6 is designed thanks

to an equivalent transformation, which makes possible to obtain a triangular form of the compression and combustion model, where the high gain observer is applied. This method has shown to be effective to compute the enclosed masses in the combustion chamber. It is an advantageous strategy as it allows for handling the strong nonlinearities of the engine model during the valves closure. The valves closure is short when compared to the whole engine cycle. However, the observer converges soon enough before the engine valves opening. The mass estimation is achieved before the ignition timing in most operating conditions and the combustion modeling would not be necessary. However, it might not be the case at high engine speed conditions (4500 rpm up to 5500 rpm), where the compression stroke might be too short with respect to the observer settling time. For this reason, the estimation algorithm is computed during the compression and combustion strokes.

The high gain observer for varying parameters presented in Section 4.7 is designed thanks to a polytopic representation of the compression model which yields on a system in triangular form where the high gain observation theory can be applied. The main contribution of this thesis with respect to this issue is to include a high gain strategy in a parameter varying observer for structured nonlinear systems, in order to cope with the system uncertainties. This estimation strategy has shown to be effective to estimate the cylinder enclosed mass during the compression stroke when the engine valves are closed. Including a high gain strategy in a parameter varying observer has shown good results, improving the performance of the observer, vanishing the effect of the uncertainties due to the observer dependency to the unknown states. Similar remarks with respect to the observer performance at high engine speeds mentioned for the high gain observer apply also for the high gain observer for parameter varying systems. This observer has shown to reduce the settling time with respect to the nonlinear high gain observer, which makes possible to estimate the enclosed mass at higher engine speeds avoiding to model the combustion process. However, at engine speeds bigger than 4500 rpm, the compression stroke might still be too short to achieve the mass estimation.

Chapter 5

Common rail injection system controller using input-state linearization and optimal control strategy with integral action

The common rail injection system controller has been designed with the aim to complete the SI engine modeling presented in previous chapters introducing a synthesis for the injection control, which is a crucial parameter in the combustion process. The aim is to synthesize a common rail control scheme for gasoline engines, which is based on the same physical principles of a diesel engine common rail system currently used in Renault. In the framework of this thesis, only the experimental characteristics and the model for the diesel common rail injection system are available, thus all the developments related to this issue have been designed for the diesel engine type. However, the common rail injection system for gasoline engines has a very similar architecture, thus the theory developed here for diesel engines can be applied to the SI gasoline case. This common rail application intends to be adapted to the common rail architecture and control scheme currently used in Renault.

The common rail system has been developed to reduce noise, exhaust emissions and fuel consumption while increasing the engine performance. The goal of a common rail injection system is to control the injection advance, duration and pressure, individually cylinder by cylinder, in order to manage accurately the combustion depending on the engine operating conditions. In a common rail system the fuel injection is performed at high pressure in each cylinder without passing through a pre-chamber as in the case of indirect injection. The injection control allows the regulation of the injection in small quantities, helping to decrease the pollutant emissions and also increasing the engine performance.

In the common rail systems, a high-pressure pump allows storing fuel in a distribution pipe at high pressure: from 300 $bars$ up to 1600 $bars$ in diesel engines, and from 20 bar up to 200 bar in gasoline engines. All the fuel injectors in the engine are supplied from this common distribution pipe referred as to the rail. A complete description of a common rail system is found in [Guerrassi & Dupraz, 1998], where the common rail system of Lucas Diesel Systems (currently property of Delphy Automotive Systems) is presented. Such architecture is the most spread in passenger cars.

In a common rail system, the main request is the error minimization between the rail pressure p_{rail} and a pressure reference p_{ref}. Several strategies have been proposed to control the common rail system, such strategies cover a large classification of control methods and modeling.

It is an usual practice in the industry to use a simple proportional-integrative-derivative (PID) controller for the common rail system. A main problem of the this technique is the difficult that finding the PID parameters for the whole operating range requires on an expensive calibration process. The PID gains are composed of several look-up tables containing several PID combinations for the different operating conditions. Besides, the PID does not guarantee the robustness and stability of the common rail system. With the aim to contribute to the common rail control development and to provide a common rail controller adapted to the current needs of the gasoline and diesel engines used in Renault, in this thesis two control strategies are implemented to control the p_{rail}: an optimal linear quadratic regulator LQR with integral action and an optimal LQR tracking (feedforward) with integral action strategy. Both strategies are merged in the model based control method. The proposed control strategies are compared to a proportional integral PI controller with pre-positioning system, which is currently used in Renault.

Remark 5.0.1. This common rail controller proposed in this thesis has been submitted internally in Renault for a patenting process.

Chapter structure This chapter is introduced with a basic explanation of the functionality of the common rail injection system, where the main aspects as the system architecture and operating mode are presented. A review of some common rail pressure system is presented with a brief explanation of the control strategy proposed in each case.

A 0D model of the common rail system is designed based on experimental data map and is presented in Section 5.4. The common rail model contains strong nonlinearities which might be hard to handle from the control point of view. In order to overcome this constraint, an input-state linearization method is applied in the common rail model. This procedure yields with a system virtual input v, which depends on the actual system input u. The optimal LQR strategies are applied to this system to obtain the virtual input v

that regulates p_{rail} to p_{ref}. The inverse transformation of the input state linearization is the performed to recover the input u.

The controllers are designed for the current $K9$ diesel engines used in Renault. To calibrate the engine, several data maps are used to reproduce the pressure reference and the operating conditions. Thus, for a given mean break effective pressure (IMEP) and an engine speed N, there is a p_{ref} expected in the rail in order to maintain the right performance of the common rail system. This same method is used in the car ECU for the common rail control. The pressure reference p_{ref} obtained through those data maps is used to validate the control strategies proposed in this thesis.

5.1 Chapter nomenclature

Unless it is specified, all variables are in SI Metric Units.

Variables

I_{imv}	Inlet metering valve (IMV) control electric current
m_{inj}	Injected fuel mass
p_{rail}	Rail pressure, $[bar]$
p_{ref}	Rail pressure reference
v	Virtual control input
T_{inj}	Injection timing

Constant parameters

N	Engine speed $[rpm]$
V_{rail}	Rail volume
β_f	Fuel compressibility factor
Γ_{rail}	Constant for unit conversion
κ_l	Leakage coefficient

5.2 Common rail injection system

A common rail system is usually composed by five principal elements arranged in two main circuits: a low pressure (LP) circuit ($4 - 10$ *bar*) and a high pressure (HP) circuit ($300 - 1600$ *bar*) for diesel engines ($20 - 200$ *bar* for gasoline engines). Those elements are the HP pump, the rail, the LP pump, the injectors and the inlet metering valve (IMV). Figure 5.1 presents the common rail system scheme used in this thesis. In the next paragraphs, each element in the scheme is briefly detailed.

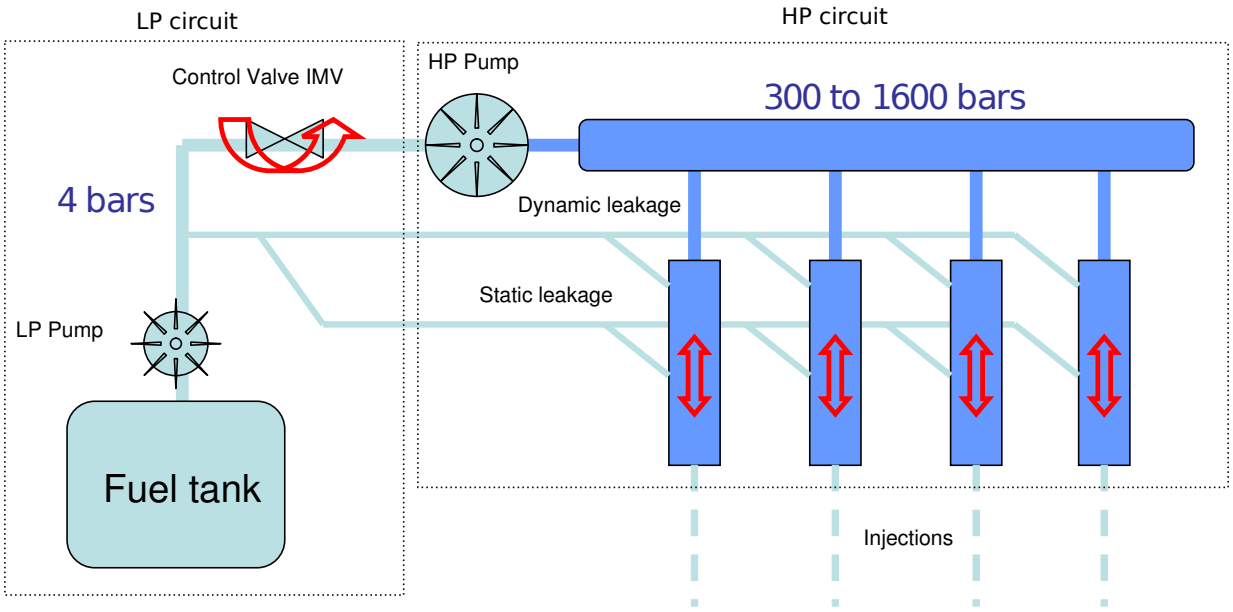

Figure 5.1: Scheme of the common rail system.

High pressure (HP) pump The HP pump boosts the fuel from the LP circuit to the HP circuit. The functionality of the HP pump depends on the pump type, a positive displacement pump is typically used in the common rail applications.

A positive displacement pump is composed principally by an expanding cavity on a suction side and a decreasing cavity on a discharge side [*Doe Fundamentals Handbook*, 1993]. Figure 5.2 shows a scheme of a positive displacement pump. The flow circulates into the pump as the cavity on the suction side expands and the flow goes out by the discharge side as the cavity collapses. The volume is constant at each cycle of operation. The HP pump follows a cycle of four steps to accomplish the boosting process:

- Vacuum. When the pressure in the cavity is lower than the pressure in the LP circuit, the pump admission opens and the cavity is filled with fuel.
- Compression. The volume of the pump cavity lowers causing an elevation of the flow pressure in the cavity,

- Repel. When the pressure in the pump cavity is bigger than the pressure in the rail, the pump opens the discharge side and the fuel flows to the HP circuit.
- Pressure loss. When the discharge side of the pump closes, the volume in the pump cavity increases, which lowers the pressure until it is lower than the LP circuit pressure and the cycle starts again.

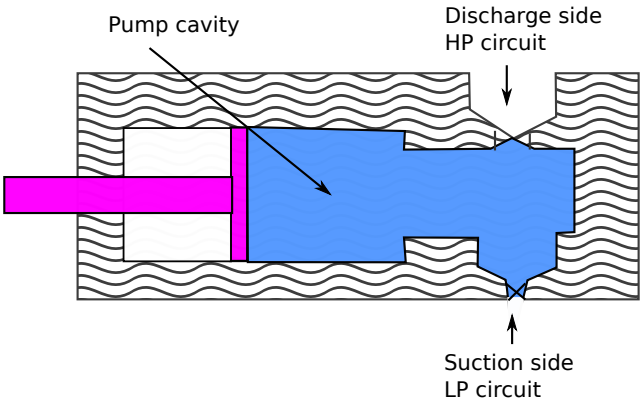

Figure 5.2: Scheme of the positive displacement pump.

The HP pump is not controllable as its speed is set by the engine speed N: pump speed $N_p = \frac{N}{2}$; thus to regulate the amount of fuel entering the pump and therefore the rail pressure, the control inlet metering valve (IMV) is installed. The fuel flow passing through the IMV is the variable that controls the pressure in the rail.

Inlet Metering Valve IMV The IMV regulates the amount of fuel that goes to the HP pump, that is the fuel entering into the rail. The IMV is directly connected to the HP pump. In common rail systems, the IMV is usually an electromechanical device controlled by an electric current I_{imv}. The IMV is usually a solenoid valve.

A solenoid valve is controlled by an electric current through a solenoid, which is switched on or off. A solenoid valve is composed by two main elements: the solenoid and the valve. The solenoid converts the electrical energy into mechanical energy which opens or closes the valve mechanically.

Rail The rail is a distribution pipe where the fuel is stocked before the injection. It can be of different forms such as cylindrical or spherical. It is usually characterized by its size and geometry. The rail communicates with each injector. The rail pressure reference p_{ref} is mapped with respect to several parameters, where the most relevant are the engine speed N and the torque demand. The rail pressure demand varies typically from 230 *bar* up to 1600 *bar* with a tolerance of 1% for diesel engines. The control of the rail pressure is of great importance since a bad tracking of the pressure reference usually leads to bad engine performance.

Low pressure (LP) pump The LP pump sucks-in the fuel from the fuel tank to set a higher pressure upstream the control IMV. It controls the fuel flow towards the HP pump to ensure the proper operation conditions of it.

Injectors The injectors provide the amount of fuel required per cycle to the engine depending on the injection timing, which is set depending on the operating conditions as well as on the rail pressure p_{rail}. Most of the injectors used in the common rail system are designed as a nozzle assembly made up of a needle-valve, a spring and a body. Figure 5.3 shows a scheme of a typical fuel injector. The fuel is delivered to the injector from the rail and then it passes through a drilling in the nozzle body, to a chamber where the needle-valve seats in the nozzle assembly. As the fuel pressure in the injector gallery rises, it acts on the tapered shoulder of the needle valve, increasing the pressure until it overcomes the force from a spring, and lifts the needle valve from its seat. The highly pressurized fuel enters the engine at a high velocity, in an atomized spray. As soon as delivery from the pump stops, the pressure under the needle tapered-shoulder drops, and the spring force pushes the needle down on the seat, cutting off the fuel supply to the engine.

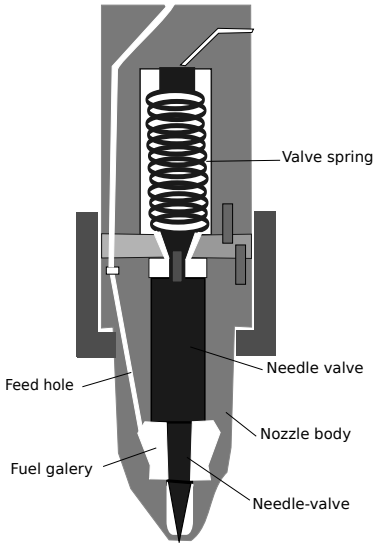

Figure 5.3: Scheme of the fuel injector of the common rail system.

Two different leakages are associated to the injectors; *static leakage* and *dynamic leakage*, which are recirculated upstream the control valve. The static leakage is used to overcome functioning failures and/or to regulate the rail during the slow driving, it guarantees a minimum rail pressure p_{rail} when the flow through the IMV is too low to drive the HP pump. The dynamic leakage is there to guaranty the functioning of the injector needle. Those leakages are found in the $K9$ common rail injection system and are modeled through statical data maps, which do not depend on the system control inputs.

In Figure 5.1 is also depicted the fuel tank where is stocked the fuel of the engine.

The problem to face in the common rail system is to ensure the appropriate rail pressure p_{rail} to have the accurate amount of fuel injected into the engine in all the operating conditions. The pressure that ensures such performance is given by a pressure reference p_{ref}. In order to treat this issue, different kind of control laws acting on the IMV can be designed. In the next section, several common rail injection system that have been proposed are presented, to illustrate the state of art of this issue.

5.3 Common rail injection control strategies review

The first prototype of a common rail system was developed in the late 1960s, but it is until 1990 that Robert Bosh GmbH acquired the design of the common rail system and in 1997 the first passenger cars equipped with a common rail system appeared: an Alfa Romeo 156 2.4 uniJet Turbo Diesel (JTD) and later in the same year a Mercedes-Benz C 220 Common Rail Direct Injection CDI. After these cars, the common rail injection system use has spread for the diesel passenger cars and nowadays, it has started to be used in gasoline engines.

The Proportional-Integrator-Derivative (PID) control method has been the most common way to operate the common rail system, but in recent years some alternative strategies have been explored in order to achieve the more and more restricting control requirements.

5.3.1 Gauthier, Sename, Dugard and Meissonnier: An LFT approach to H_∞ Control for diesel engine common rail system

A very representative and one of the most complete controllers for the common rail system is presented by Gauthier in PhD thesis and in several publications: [Gauthier, 2007], [Gauthier et al., 2006], [Gauthier et al., 2007*b*], [Gauthier et al., 2007*a*] and [Gauthier et al., 2007*c*]. In these works, the common rail system has a similar architecture than the one exposed in the previous section, but an additional a High Pressure Valve (HPV) connected upstream the rail is introduced. This valve has as purpose to drive the common rail system when the fuel flow through the HP pump is too low to control the pressure in the rail. When introducing the HPV, the system has two operating modes: single input single output (SISO) and multiple input single output (MISO). When the HPV is closed the rail pressure is controlled by the IMV, by the contrary, under certain conditions, the rail pressure is driven for both, the IMV and the HPV valve.

From a nonlinear model, the common rail system is represented in a LPV form using the

Linear Fractional Transformation (LFT) and the goal is to synthesize an LPV control law taking into account the varying parameters of the system. The LFT structure is detailed in [Gauthier et al., 2006] and [Gauthier et al., 2007*b*]. To give an example of Gauthier's approach, Figure 5.4 shows the architecture of the common rail LFT representation to build the controller of the IMV valve. In the figure, the different system parameters are presented by the various Δ_i. P_{dmnd} and F_{dmnd} are the pressure and torque references. $K(s)$ is the H_∞ controller for the IMV, which is driven by the control input U_{imv}. The variables W_1 and W_2 are performance criteria. The H_∞ strategy detailed in [Gauthier et al., 2007*a*] and [Gauthier et al., 2007*c*] is used as a control approach, two controllers are designed, one in continuous time and one in discrete time.

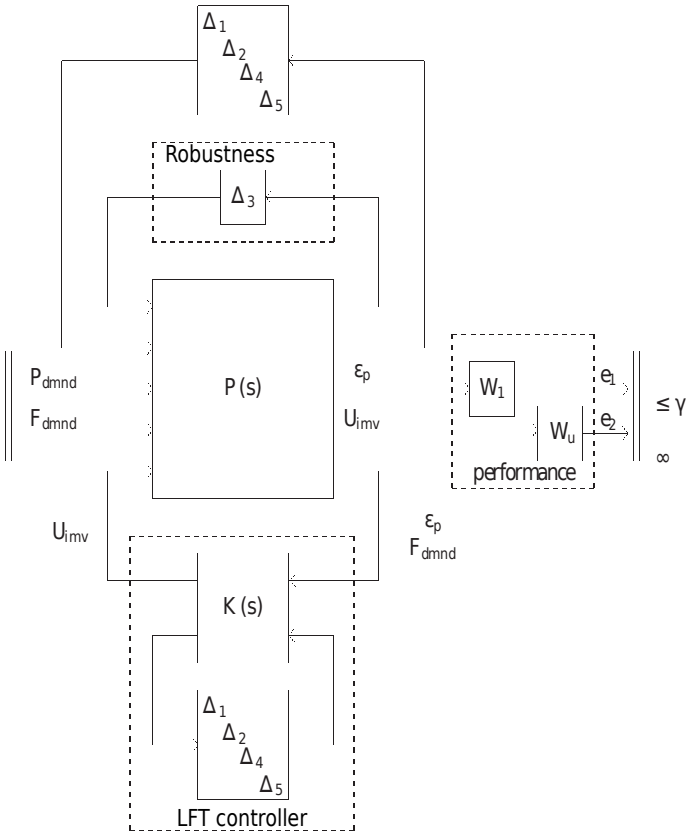

Figure 5.4: LFT Robust representation of the common rail system.
[Gauthier, 2007]

Remark 5.3.1. Even if the H_∞ controller proposed by Gauthier is a very complete strategy for the common rail problem, this method has not be considered in Renault because the intention is to keep the current common rail model and only introduce a more stable controller. Besides, it has been required to look for a strategy to improve the calibration process.

5.3.2 An and Shao: Common Rail Pressure Control Based on Neuron Adaptive PID

In [An & Shao, 2008], a diesel engine common rail pressure controller based on a neuronal adaptive PID has been proposed. A typical common rail structure similar to the one exposed in the previous section is used. The main content discussed in this paper is how to control the IMV effectively so that it can ensure the required pressure in the common rail when there are slightly pressure fluctuations. When the PID is used, as there is a limit in the output breadth, the system usually accumulates too much error because of the integral effect, resulting in oscillations of the controller. A single neuron self-learning and self-adapting system combined with the traditional PID controller is designed to improve the speed of the rail pressure controller, thus decreasing the oscillations and fluctuations. Figure 5.5 shows the architecture of the single neuron adaptive PID proposed by [An & Shao, 2008]. In the figure, p_{ref} is the pressure reference, $x_{1,2,3}$ are respectively the proportional, integrative and derivative parameters of the PID controller. The learning rule provides the weights $w_{1,2,3}$ which are the adaptive neuron self-learning parameters and the plant is the common rail system. $f(u)$ is a conversion function to transform the output of the PID to the common rail system u_{imv}.

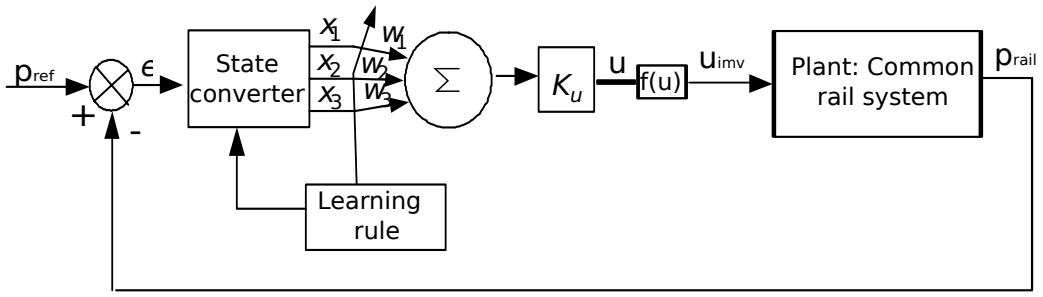

Figure 5.5: Single neuron adaptive PID scheme.
[An & Shao, 2008]

5.3.3 Chatlatanagulchai and Yaovaja: Gain-scheduling integrator-augmented sliding mode common rail control

In the work of [Chatlatanagulchai & Yaovaja, 2010] a gain-scheduling integrator-augmented sliding mode controller for a diesel engine is designed. Two advantages are mentioned in this work: the order reduction property and the robustness against plant uncertainty and disturbances. The sliding-mode controller uses a fast-switching control law to bring the error trajectory to the sliding surface and maintain it there. The sliding surface dynamics is independent of the plant model and the disturbances, which makes

the control law robust. Two sliding surfaces $s = [s_1, s_2]$ are designed, which depend on the rail pressure p_s and the reference pressure p_{ds}:

$$s_1 = a_0 e_0 + a_1 e_1 + e_2, \quad s_2 = 0 \tag{5.3.1}$$

where a_1 is an adjusting parameter, $e_1 = p_s - p_{ds}$, $e_2 = \dot{p}_s - \dot{p}_{ds}$ and $e_0 = \int e_1 dt$ is added to obtain zero steady state error. A candidate Lyapunov function is verified and a control law u_s is designed according to this criterion:

$$u_s = -k\frac{2}{\pi} arctan(s/\epsilon) \tag{5.3.2}$$

where ϵ is calibration a small number. The parameters a_0, a_1, k and ϵ are design parameters which are selected to give the best transient behavior. To adjust these parameters, the system is calibrated with respect to experimental measurements.

5.3.4 Balluchi, Bicchi, Mazzi, Sangiovanni-Vincentelli and Serra: Hybrid modelling and control of the common rail system

In the work of [Balluchi et al., 2007], the common rail fuel injection system for diesel engines under development at Magneti Marelli Powertrain is presented. This work has an important complexity as it considers the hybrid character of the common rail system due to the fluctuations on the rail pressure. Such fluctuations arise because of to the slow time-varying frequency of the HP pump cycles and the fast sampling frequency of the IMV. Such hybrid interactions in the plant and time domain heterogeneity might be due to:

- the discontinuous fuel flows of the HP pump and the injectors, whose frequencies are time-varying being proportional to the engine speed N, and
- the fixed sampling frequencies of the sensor pressure reading and the IMV valve actuation.

In this work, an adaptive algorithm is devised for on-line compensation of IMV uncertainties and a hybrid multi-rate controller is developed to handle the delay and the hybrid interactions in the plant. An hybrid model of the common rail system is developed and validated with respect to experimental measurements. The proposed solution is a hybrid

multi-rate controller consisting on two regulators, as shown in Figure 5.6. In the figure, the CM pressure controller is event-based and is synchronous with the HP pump fuel intake phases. It is executed at each ram top dead center (TDC) event, there are three rams in the HP pump hybrid model (do not confuse with the engine TDC).

k is the counter of ram TDC events. The CM pressure controller defines the desired fuel mass needed to control the rail pressure error to zero. A PI control with anti-windup and feedforward terms is used for this purpose.

The decimator converts the high frequency pressure error to the time varying HP pump frequency. The IMV controller runs at 200 Hz, l is the counter of the 200 Hz trigger that activates the controller.

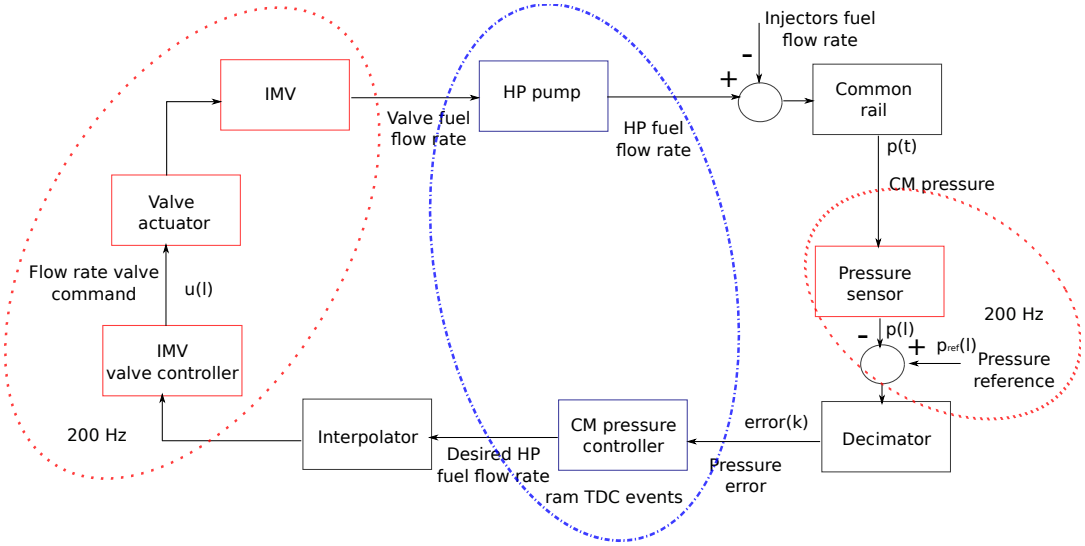

Figure 5.6: Hybrid multi-rate controller.
[Balluchi et al., 2007]

5.3.5 di Gaetaai, Montanaroa, Fiengob, Palladinob and Giglioa: A model-based gain scheduling approach for the common-rail system control for a GDI engine

In the work of [di Gaetaai et al., 2012], a gain scheduling pressure controller for gasoline direct injection (GDI) engine is designed to stabilize the mean fuel pressure into the rail and to track the demanded pressure trajectory. A simple control-oriented model which describes the pressure dynamics as a linear parameter-varying system, where the coefficient of the dynamics matrix and output matrix varies as a function of the engine speed N is used to describe the mean pressure dynamics in the rail.

The main idea of this work is to adapt the integral gain of a feedback controller and

a feedforward action, with respect to the HP pump battery voltage and pump speed, according to a model matching approach. This procedure yields the closed-loop dynamics of an LTI model independently from the scheduling variables.

Since the common rail model depends on the HP pump speed and battery voltage, a gain scheduling control algorithm varying the duty cycle (δ) of the pressure regulation electrovalve is proposed, in order to compensate the HP pump parameters variations. Figure 5.7 shows the controller proposed in this work which mainly comprises:

- a feedforward control action δ_{ff} designed as the steady-state control action needed to keep the mean value pressure at a demanded set point in the nominal case independently from the operating condition,

- a feedback control action δ_{fb} based on the difference between p_{ref} and p_{rail}, which is provided by the integral controller. This feedback provides a control action around the steady state error independently from the HP pump speed and battery voltage.

V_p and N_p are the HP pump battery voltage and speed, whose measurements are obtained by means of moving average filters (Filter blocks in Figure 5.7) based on the crank-angle domain, in order to reduce measurement noise and their high-frequency components.

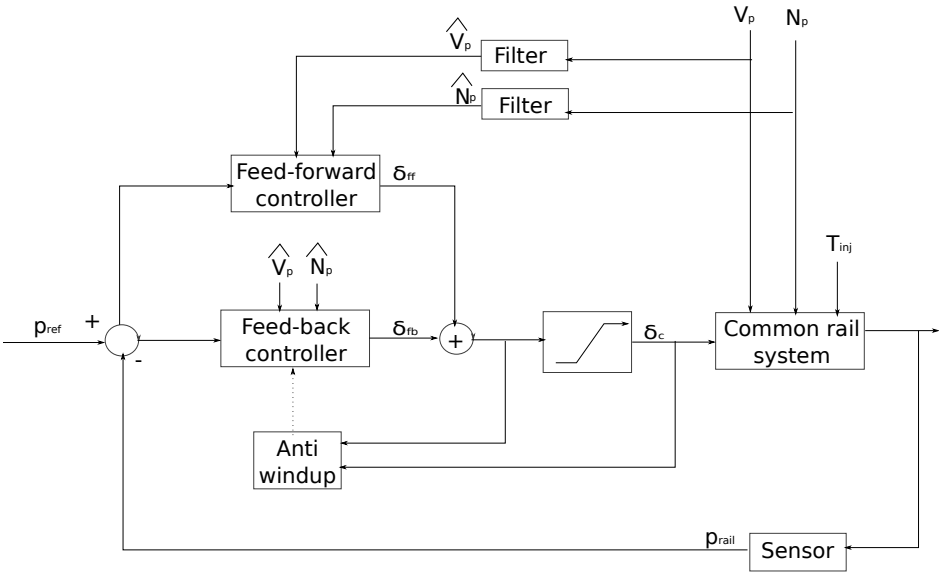

Figure 5.7: Gain scheduling pressure controlle.
[di Gaetaai et al., 2012]

As it has been presented, different methods to control the common rail system have been proposed. Many of these methods contain advanced control theory and very promising results. In this thesis, the aim is to propose a common rail controller that can be used in a SI gasoline engine. However, only the experimental data and architecture of a diesel common rail injection system is available. Such architecture belongs to the K9 Renault engine, which was launched in the Clio and Kangoo 1.5 l diesel cars in 2001. This engine is equipped by a common rail system designed by Delphi Automotive Systems. However, this common rail system is still driven by a traditional proportional-integrative PI controller which needs of a complex adjusting process in order to yield with the PI gains, besides the fact that there are no guaranties with respect to the system stability and optimality.

Two controllers based on the Linear Quadratic Regulator LQR scheme are designed, with the aim of proposing an optimal and stable strategy for the common rail system which can be used in the current $K9$ applications and that can be transposed to the SI gasoline engines. These controllers are designed using a 0D injection common rail model, which is built with the maps provided by the Department of Control and Calibration (Département de Côntrole et Mise au Point DCMAP) in Renault. Both of the proposed strategies can be implemented for the common rail injection system of gasoline engines.

5.4 0D injection common rail model

In order to design and test the control laws proposed in this thesis, a reduced 0D common rail injection model based on the architecture shown in Figure 5.1 is proposed. The model has one state that is p_{rail} and one control input that is the IMV control electric current I_{imv}. Next, the basic equations developed for the injection system are presented.

The dynamics of the rail pressure is given by:

$$\frac{dp_{rail}(t)}{dt} = \Gamma_{rail}\frac{\beta_f}{V_{rail}}(dm_{q_{pump}}(t) - dm_{l_{dyna}}(t) - dm_{l_{stat}}(t) - dm_{q_{inj}}(t)) \qquad (5.4.1)$$

Where $p_{rail}(t)$ is the rail pressure in bar, β_f is the is the fuel compressibility coefficient in Pa, V_{rail} is the rail volume in m^3, Γ_{rail} is a unit conversion constant, $dm_{q_{pump}}(t)$ is the volumetric flow of the HP pump, $dm_{l_{dyna}}(t)$ is the volumetric flow of the dynamic leakage, $dm_{l_{stat}}(t)$ is the volumetric flow of the static leakage and $dm_{q_{inj}}(t)$ is the volumetric injected fuel flow. All the volumetric flows are in m^3/s.

The dynamics of $p_{rail}(t)$ has a simple physical structure, but each volumetric flow is a function of different parameters, the system input and the system state. Equations (5.4.2) to (5.4.6) show the dependencies of each variable:

$$dm_{q_{pump}}(t) = f_{q_{pump}}(N, p_{rail}(t), I_{imv}(t)) \tag{5.4.2}$$

$$dm_{l_{dyna}}(t) = f_{l_{dyna}}(N, p_{rail}(t), T_{inj}(t), \kappa_l) \tag{5.4.3}$$

$$dm_{l_{stat}}(t) = f_{l_{stat}}(N, p_{rail}(t), T_{inj}(t), \kappa_l) \tag{5.4.4}$$

$$dm_{q_{inj}}(t) = f_{q_{inj}}(N, p_{rail}(t), T_{inj}(t), \kappa_l) \tag{5.4.5}$$

$$T_{inj}(t) = f_{T_{inj}}(p_{rail}(t), m_{inj}) \tag{5.4.6}$$

where $T_{inj}(t)$ is the injection timing, m_{inj} is the fuel mass to be injected per cycle, N is the engine speed and κ_l is a leakage coefficient. All the functions are data maps, there are no analytic expressions available for this functions in this reduced model. Figure 5.8 shows an example of the data map $f_{q_{pump}}(N, p_{rail}(t), I_{imv}(t))$, where the HP pump mass flow map with respect to p_{rail} for an engine speed of 2000 rpm in presented.

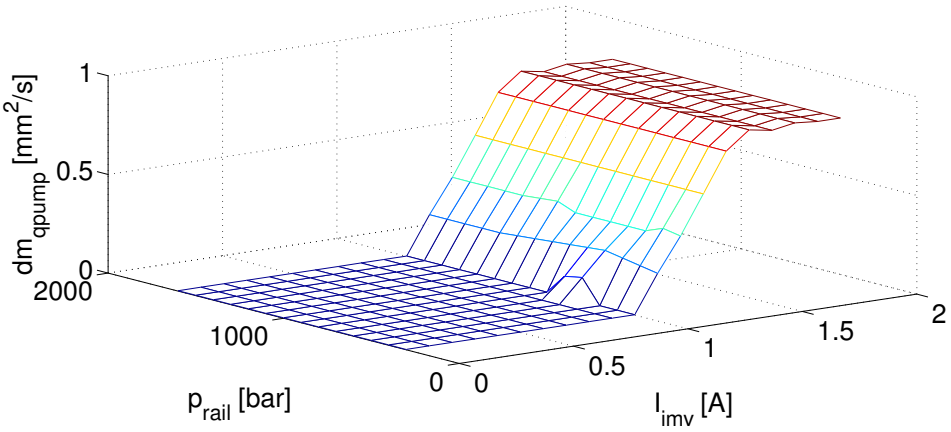

Figure 5.8: $f_{q_{pump}}(N, p_{rail}(t), I_{imv}(t))$. HP pump mass flow with respect to the $p_{rail}(t)$ and the $I_{imv}(t)$ for $N = 2000$ rpm.

Including expressions (5.4.2) up to (5.4.6) in (5.4.1), the p_{rail} dynamics is described as:

$$\frac{dp_{rail}(t)}{dt} = \Gamma_{rail}\frac{\beta_f}{V_{rail}}\Big(f_{q_{pump}}(N, p_{rail}(t), I_{imv}(t)) - f_{l_{dyna}}(N, p_{rail}(t), T_{inj}(t), \kappa_l) - f_{l_{stat}}(N, p_{rail}(t), T_{inj}(t), \kappa_l) - f_{q_{inj}}(N, p_{rail}(t), T_{inj}(t), \kappa_l)\Big) \quad (5.4.7)$$

As it can be seen in Equation (5.4.7), the system ends up being nonlinear and hard to handle from a control point of view as no analytical expression are available for the volumetric mass flow. Table 5.1 summarizes the common rail injection system model.

State space variable	$p_{rail}(t)$
Parameters	$N[rpm]$, T_{inj}, κ_l, m_{inj}
Inputs	$u = f_{q_{pump}}(N, p_{rail}(t), I_{imv}(t))$ (driven by the I_{imv})

Table 5.1: Common rail injection system model summary.

5.5 Rail pressure control

Because of the inherent complexity and nonlinear character of system (5.4.7), the control synthesis is not easy and may be involved. In this thesis, a transformation of the nonlinear system into a virtual linear system is used, allowing the design of a linear control strategy that ensures stability and optimal performances of the common rail injection system in the whole operating range.

Indeed an input-state linearization is used to cancel out the nonlinearities of the system dynamics which results in a virtual linear controllable system. Then, two optimal control approaches with integral action are developed to ensure the stability and optimality of the controller in all operating conditions. The virtual controller is then transformed to obtain the actual control input.

5.5.1 Fundamentals on Input-State Linearization

Definition 5.5.1. *[Khalil, 1996] A nonlinear system:*

$$\dot{x} = f(x) + G(x)u \quad (5.5.1)$$

where $f : D_x \to \mathbf{R}^n$ and $G : D \to \mathbf{R}^{n\times p}$ are sufficiently smooth on a domain $D_x \subset \mathbf{R}^n$, is said to be input-state linearizable if there exists a diffeomorphism $T : D_x \to \mathbf{R}^n$ such

that $D_z = T(D_x)$ contains the origin and the change of variables $z = T(x)$ transforms the system (5.5.1) *into the form*

$$\dot{z} = Az + B\beta^{-1}(x)(u - \alpha(x)) \tag{5.5.2}$$

where $A \in \mathbf{R}^{n\times n}$, $B \in \mathbf{R}^{n\times p}$, and such that the pair (A, B) is controllable, and the functions $\alpha(x) : \mathbf{R}^n \to \mathbf{R}^p$ and $\beta(x) : \mathbf{R}^n \to \mathbf{R}^{p\times p}$ are defined in a domain $D_x \subset \mathbf{R}^n$ that contains the origin. The matrix $\beta(x)$ is assumed to be non-singular for every $x \in D_x$. Notice that β^{-1} denotes the inverse of the matrix $\beta(x)$ for every x, and not the inverse map of the function $\beta(x)$.

The basic idea behind using the input-state linearization is to find a control input u such that the system nonlinearities are compensated, resulting in a controllable linear system.

One can assume that for the system (5.5.2) there exists the state feedback:

$$u = \alpha(x) + \beta(x)v \tag{5.5.3}$$

to obtain the consolidated linear system:

$$\dot{x} = Ax + Bv \tag{5.5.4}$$

As it can be seen in Equation (5.5.4), the final system has the form of a classic linear system.

Remark 5.5.1. If the system does not comply with the form presented in Equation (5.5.2), it does not mean that the input-state linearization cannot be performed. It is important to recall that the state model of a system is not unique. It depends on the choice of the state variables. Even if the state equation does not have the structure (5.5.2) for one choice of state variables, it might do so for another choice.

5.5.2 Common rail model transformation

As seen in section 5.2, the dynamics of $p_{rail}(t)$ is controlled varying the mass flow through the IMV, thus the system input is defined as:

$$u(t) = dm_{q_{pump}}(t) = f_{q_{pump}}(N, p_{rail}(t), I_{imv}(t)) \tag{5.5.5}$$

One can define the function $\alpha(p_{rail}(t))$ such that:

$$\begin{aligned}\alpha(p_{rail}(t)) = \quad & f_{l_{dyna}}(N, p_{rail}(t), T_{inj}(t), \kappa_l) + f_{l_{stat}}(N, p_{rail}(t), T_{inj}(t), \kappa_l) \\ & + f_{q_{inj}}(N, p_{rail}(t), T_{inj}(t), \kappa_l)\end{aligned} \tag{5.5.6}$$

and using the following equivalences, which match the components of Equation (5.5.2):

$$z(t) = p_{rail}(t), \quad B = \Gamma_{rail}\frac{\beta_f}{V_{rail}} \quad \beta(x) = 1, \quad A = 0 \tag{5.5.7}$$

the system (5.4.7) becomes:

$$\frac{dp_{rail}(t)}{dt} = \quad \Gamma_{rail}\frac{\beta_f}{V_{rail}}\Big(u(t) - \alpha(p_{rail}(t))\Big) \tag{5.5.8}$$

which presents the same form specified in Definition 5.5.1 in Equation (5.5.2).

Thus, according to Equation (5.5.3), the system state feedback is:

$$u(t) = \alpha(p_{rail}(t)) + v(t) \tag{5.5.9}$$

and the transformed linear system is:

$$\frac{dp_{rail}(t)}{dt} = \Gamma_{rail}\frac{\beta_f}{V_{rail}}v(t) \tag{5.5.10}$$

where $v(t)$ is the system virtual input. In this thesis it is assumed that the fuel compressibility coefficient β_f is constant, which is an approximation as this parameter might vary depending on the rail pressure. Under this assumption, the system (5.5.10) is linear. If the variation of the coefficient β_f is taken into account, the system can be represented in linear parameter varying LPV form and a convenient control strategy can be applied as presented in [Gauthier, 2007].

The common rail system is controlled with the mass flow passing through the HP pump $dm_{pump}(t)$ (Equation (5.5.5)). Indeed, the mass flow itself cannot be set directly and the HP pump is actually controlled through the IMV control electric current $I_{imv}(t)$. To obtain an analytical expression for $I_{imv}(t)$ it can be assumed the existence of the function $f^{-1}_{q_{pump}}(N, p_{rail}(t), dm_{pump}(t))$ such that:

$$I_{imv}(t) = f^{-1}_{q_{pump}}(N, p_{rail}(t), dm_{q_{pump}}(t)) \tag{5.5.11}$$

From equations (5.5.6) and (5.5.9), the virtual input $v(t)$ is:

$$\begin{aligned} v(t) = \quad & dm_{pump}(t) - f_{l_{dyna}}(N, p_{rail}(t), T_{inj}(t), \kappa_l) \\ & - f_{l_{stat}}(N, p_{rail}(t), T_{inj}(t), \kappa_l) - f_{q_{inj}}(N, p_{rail}(t), T_{inj}(t), \kappa_l) \end{aligned} \tag{5.5.12}$$

thus, using Equation (5.5.12) and after some arrangements, a relation between the virtual control input $v(t)$ and the system actual input $I_{imv}(t)$ is obtained as:

$$\begin{aligned} I_{imv}(t) = \quad & f^{-1}_{q_{pump}}\Big(N, p_{rail}(t), v(t) + f_{l_{dyna}}(N, p_{rail}(t), T_{inj}(t), \kappa_l) \\ & + f_{l_{stat}}(N, p_{rail}(t), T_{inj}(t), \kappa_l) + f_{q_{inj}}(N, p_{rail}(t), T_{inj}(t), \kappa_l)\Big) \end{aligned} \tag{5.5.13}$$

The common rail control presented here lies on the assumption that the computation $f^{-1}_{q_{pump}}(N, p_{rail}(t), dm_{pump}(t))$ can be performed. However, from Figure 5.8 it is clear that there are regions in the map of $f_{q_{pump}}(N, p_{rail}(t), I_{imv}(t))$ where the function is non-invertible.

Nevertheless, it is worth noticing that the non-invertible regions of the map correspond to uncontrollable operating conditions: for changes in the control input $I_{imv}(t)$ the mass flow $dm_{qpump}(t)$ remains constant, meaning that the system HP pump - IMV is saturated. Thus, the region where the map is not controllable can be removed from the system, as it does not contribute to the control action.

Figure 5.9 shows the data map of the function $f_{q_{pump}}(N, p_{rail}(t), I_{imv}(t))$ with respect to $p_{rail}(t)$ and $I_{imv}(t)$ for four engine speeds in the invertible region. The maps inversion $f^{-1}_{q_{pump}}(N, p_{rail}(t), dm_{pump}(t))$ can be performed on this region to obtain $I_{imv}(t)$ as in Equation (5.5.13).

Thanks to the input-state linearization performed on system (5.4.7), the linear system (5.5.10) is designed and different linear control strategies can be used to find $v(t)$ to control $p_{rail}(t)$. The actual system input $I_{imv}(t)$ can be obtained from the virtual input $v(t)$ through the transformation (5.5.13). In this thesis, two optimal Linear Quadratic Regulator (LQR) control approaches are developed. Both are designed using integral action in order to cancel the effects of the model error in the steady state response.

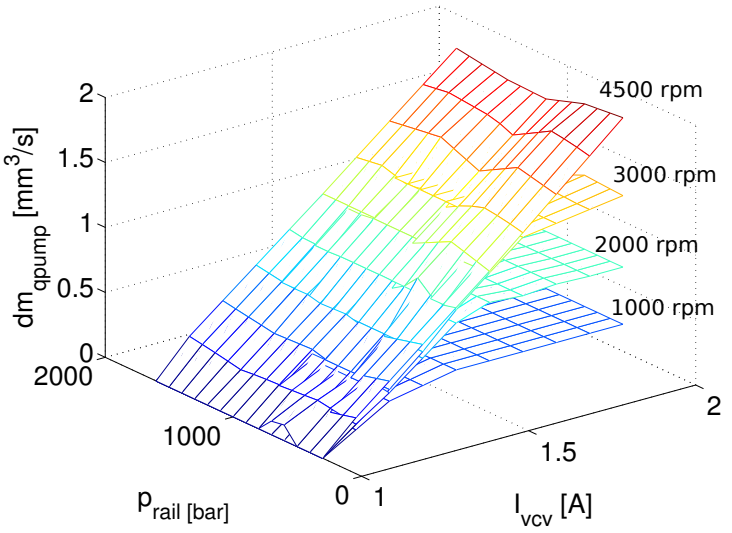

Figure 5.9: $dm_{pump}(t)$ with respect to p_{rail} and I_{imv} in the map invertible region.

5.5.3 Linear Quadratic Regulator (LQR)

In control theory, an optimal control problem attempts to find a controller that provides the best possible performance with respect to some given measurement of performance. The performance is represented by a cost function, defined to keep the energy expended by the control action itself limited. In this thesis, the common rail control problem is that the rail pressure p_{rail} follows a pressure reference p_{ref} as a tracking.

Two LQR controllers are studied in this thesis: an LQR tracking controller (feedforward) with integral action and an LQR with integral action. In the LQR tracking controller, the signal reference is considered as an exogenous input of the system, referred to as a feedforward, which is included in the LQR controller to obtain an instantaneous change on the controller when there is a change in the reference. This component differences the LQR tracking with integral action problem from the LQR with integral action problem, where the controller follows the changes in the reference only from the integral of the error between the output and the reference. The LQR tracking controller with integral action will be referred to as the LQR tracking and the LQR controller with integral action will be referred to as the LQR.

Linear Quadratic Regulator (LQR) tracking controller The aim solving an LQR tracking problem is to follow a time-dependent reference signal $r(t)$. The signal reference is an exogenous input of the system, referred to as a feedforward. A detailed development strategy can be seen in [Kwakernaak & Sivan, 1972] and [Mikles & Fikar, 2007].

Given the MIMO state space system:

$$\begin{aligned} \dot{x} &= Ax + Bu \\ y &= Cx \end{aligned} \tag{5.5.14}$$

where $x \in \mathbf{R}^n$ is the state vector, $u \in \mathbf{R}^p$ is the system input and the matrices $A \in \mathbf{R}^{n\times n}$, $B \in \mathbf{R}^{n\times p}$ and $C \in \mathbf{R}^{q\times n}$. A new state x_e is defined and an extended state space system is obtained as:

$$\dot{x_e} \quad = \quad A_e x_e + B_e u + \Omega_e r, \quad x_e = \begin{bmatrix} x \\ e \end{bmatrix} \tag{5.5.15}$$

where $A_e = \begin{bmatrix} A & 0 \\ -C & 0 \end{bmatrix}$, $B_e = \begin{bmatrix} B \\ 0 \end{bmatrix}$ and $\Omega_e = \begin{bmatrix} 0 \\ 1 \end{bmatrix}$.

The term $\Omega_e r$ is the feedforward term. A cost function is defined as the functional:

$$J(x_e, u) = \frac{1}{2}\int (x_e^T Q x_e + u^T R u)dt \tag{5.5.16}$$

where the Q and R are weighting parameters such that $Q = Q^T > 0, \quad Q \in \mathbf{R}^{n\times n}$ and $R = R^T > 0$, R of a convenient size.

Theorem 5.5.1. *Given the matrices $A \in \mathbf{R}^{n\times n}$, $B \in \mathbf{R}^{n\times p}$ and $C \in \mathbf{R}^{q\times n}$, and a matrix $P = P^T \in \mathbf{R}^{n\times n}$, such that:*

$$PA + A^T P - PBR^{-1}B^T P + Q = 0 \tag{5.5.17}$$

If (A, B) is controllable then (5.5.17) *has a unique positive definite symmetric solution P.* (5.5.17) *is referred as to Control Algebraic Riccati Equation CARE.*

Using Theorem 5.5.1, the solution to the linear static full state feedback problem of finding u that minimizes $J(x, u)$ yields to:

$$\begin{aligned} u &= -Kx_e + K_r r \\ K = R^{-1}B_e^T P, &\quad K_r = R^{-1}B_e^T \left(A_e^T - PB_e R^{-1}B_e^T\right)^{-1} P\Omega_e \end{aligned} \tag{5.5.18}$$

and the closed loop dynamics can be written as:

$$\dot{x}_e = (A_e - B_e K)\, x_e + K_r r, \quad x_e(0) = x_{e_0} \tag{5.5.19}$$

$$u = -R^{-1} B_e^T \lambda, \quad \lambda = P x_e - \delta \tag{5.5.20}$$

$$\delta = -\left(P B_e R^{-1} B_e^T - A_e^T \right)^{-1} P \Omega_e r \tag{5.5.21}$$

guarantees the stability of (5.5.15) subject to the optimality condition $J(x_e, u)$.

Remark 5.5.2. δ is an auxiliary variable introduced to solve the LQR problem for the extended state space system (5.5.15):

Proof The Euler-Lagrange equation is the solution where a given functional is stationary and it is used to solve the optimization problem of solving the functional $F = (x_e^T Q x_e + u^T R u)$ subject to the system (5.5.15). Thus, the Lagrange multiplier $\lambda(.)$ is introduced together with the Hamiltonian $H = F + \lambda^T \dot{x_e}$ and the next Euler-Lagrange conditions must be fulfilled:

$$\frac{\partial H}{\partial u} = 0, \quad \frac{\partial^2 H}{\partial^2 u} = cte, \quad \frac{\partial H}{\partial x} + \dot{\lambda}^T = 0 \tag{5.5.22}$$

Choosing

$$u = -R^{-1} B_e \lambda, \quad R > 0 \tag{5.5.23}$$

guarantees the first two conditions in Equation (5.5.22). The third condition of the Euler-Lagrange equations yields to:

$$Q x_e + A_e^T \lambda + \dot{\lambda} = 0 \tag{5.5.24}$$

(A_e, B_e) is assumed to be controllable. Choosing the Lagrange multiplier $\lambda(t) = P x_e - \delta$ such that $P = P^T \in \mathbf{R}^{n \times n}$ and solving the third condition of the Euler-Lagrange equations (5.5.22) yields to:

$$\left(\dot{P} + PA_e + A_e^T P - PB_e R^{-1} B_e^T P + Q\right) x_e + (PB_e R^{-1} B_e^T - A_e^T)\delta \quad (5.5.25)$$
$$+P\Omega_e r - \dot{\delta} = 0$$

As the goal is to analyze the optimal trajectory of u in an infinite time interval, the derivatives in Equation (5.5.25) can be set to zero. Thus, a solution of Equation (5.5.25) is:

$$PA_e + A_e^T P - PB_e R^{-1} B_e^T P + Q = 0 \quad (5.5.26)$$

and

$$(PB_e R^{-1} B_e^T - A_e^T)\delta + P\Omega_e r = 0 \quad (5.5.27)$$

Equation (5.5.26) is the CARE mentioned in Theorem 5.5.1, thus P can be solved from this definition, δ in Equation (5.5.27) is solved as:

$$\delta = (PB_e R^{-1} B_e^T - A_e^T)^{-1} P\Omega_e r \quad (5.5.28)$$

Using equations (5.5.26) and (5.5.28), the feedback controller (5.5.23) is:

$$u = -R^{-1} B_e (Px_e - \delta) \quad (5.5.29)$$
$$K = R^{-1} B_e^T P, \quad K_r = R^{-1} B_e^T \left(A_e^T - PB_e R^{-1} B_e^T\right)^{-1} P\Omega_e$$

resulting on the same conditions in Equation (5.5.20).

Linear Quadratic Regulator (LQR) The LQR regulator is a more general case than the LQR tracking presented previously, thus the feedforward term is not used. Only the main equations to solve the LQR problem are presented. A detailed development of the LQR strategy can be seen in [Kwakernaak & Sivan, 1972] and [Mikles & Fikar, 2007].

Given a MIMO system:

$$\dot{x} = Ax + Bu, \quad y = Cx \quad (5.5.30)$$

where the matrices $A \in \mathbf{R}^{n\times n}$ and $B \in \mathbf{R}^{n\times p}$ and the system input $u \in \mathbf{R}^p$; and a functional

$$J(x,u) = \frac{1}{2}\int (x^T Q x + u^T R u)dt \tag{5.5.31}$$

where the Q and R are weighting parameters such that $Q = Q^T > 0, \quad Q \in \mathbf{R}^{n\times n}$ and $R = R^T > 0$, R of a convenient size.

The aim is to compute the control u that minimizes $J(x,u)$ subject to the state space system (5.5.30).

If (A,B) is controllable, choosing a matrix $P = P^T \in \mathbf{R}^{n\times n}$, such that CARE defined in (5.5.17) holds, then the solution to the linear static full state feedback problem of finding u that minimizes $J(x,u)$ using P for (5.5.30) yields to:

$$u = -R^{-1}B^T P x = -Kx, \quad K = R^{-1}B^T P \tag{5.5.32}$$

and the closed loop dynamics:

$$\dot{x} = (A - BK)x, \quad x(0) = x_0 \tag{5.5.33}$$

guarantees the stability of (5.5.30) subject to the optimality condition $J(x,u)$. The proof of this result is the same than the proof presented previously for the tracking problem, changing the Lagrange multiplier by $\lambda = Px$ and the Hamiltonian by $H = F + \lambda^T \dot{x}$ where $F = x^T Q x + u^T R u$.

5.5.4 LQR controllers application

In this thesis, the interest is to find the minimum time for the state p_{rail} to reach the pressure reference p_{ref}, using a control strategy designed to optimize the engine performance in all operating conditions, according to the specifications in Table 5.2.

Both LQR controllers presented in Section 5.5.3 are implemented for the common rail system control. The main difference on both controllers lies on the feedforward:

- In the LQR tracking, the pressure reference p_{ref} is considered as an exogenous input for the system, referred to as the feedforward. Thus, the controller follows the changes in the reference tracking the trajectory of the error and of the reference itself, yielding on *instantaneous* changes on the controller for changes in the reference.

zero steady-state error	$p_{rail}(\infty) = p_{ref}$
overshoot	$< 5\%$
$p_{rail_{max}}$	1600 bar
settling time	< 1 s
$p_{rail} - p_{ref}$ tolerance	± 25 bar during transitory (after the rise time) ± 8 bar stable

Table 5.2: Dynamics specifications for the common rail system controller.

- In the LQR, the feedback is the error between the pressure reference and the rail pressure $p_{rail} - p_{ref}$, thus the controller follows the changes in the reference only tracking the trajectory of the error.

LQR tracking with integral action In this approach, the interest is to find the minimum time for the state p_{rail} to track a reference signal p_{ref} using the minimum amount of energy. The LQR tracking controller presented previously is applied.

Given the common rail system (5.5.10), the new state $e(t) = \int(p_{ref}(t) - p_{rail}(t))$ is defined. The goal of this term is to add an integral action to the controller to obtain zero steady state error. Including the new state, the extended state space system is:

$$\dot{x_e}(t) = A_e x_e(t) + B_e v(t) + \Omega_e p_{ref}(t), \quad x_e = \begin{bmatrix} p_{rail}(t) \\ e(t) \end{bmatrix} \tag{5.5.34}$$

where $A_e = \begin{bmatrix} 0 & 0 \\ -1 & 0 \end{bmatrix}$, $B_e = \begin{bmatrix} \Gamma_{rail}\frac{\beta_f}{V_{rail}} \\ 0 \end{bmatrix}$ and $\Omega_e = \begin{bmatrix} 0 \\ 1 \end{bmatrix}$

The cost function to minimize is:

$$J(t) = \frac{1}{2}\int (x_e(t)^T Q x_e(t) + R v(t)^2) dt \tag{5.5.35}$$

Q and R are chosen such that the weight is on the extended state $e(t)$ in order to minimize the error between p_{rail} and p_{ref} taking care on finding a minimal $v(t)$, but also taking into account that the weight for $v(t)$ has to be enough to give a non-negligible feedforward gain, such that the feedforward term has an important effect on the controller. Thus matrices Q and R are chosen as:

$$Q = \begin{bmatrix} 10000 & 0 \\ 0 & 25 \times 10^3 \end{bmatrix}, \quad R = 10 \tag{5.5.36}$$

The problem of finding a feedback controller $v(t)$ for system (5.5.34) subject to the cost function (5.5.35) was solved in Section 5.5.3 and has the solution:

$$v(t) = -Kx_e(t) - K_r p_{ref}(t) \tag{5.5.37}$$
$$K := \begin{bmatrix} K_p & K_i \end{bmatrix}^T = R^{-1}B_e^T P, \quad K_r = R^{-1}B_e^T \left(A_e^T - PB_e R^{-1}B_e^T\right)^{-1} P\Omega_e$$

The virtual controller $v(t)$ is the control input for system (5.5.10), thus the transformation in Equation (5.5.11) is performed to obtain I_{imv} that is used in the common rail system control input $u(t) = f_{q_{pump}}(N, p_{rail}(t), I_{imv}(t))$.

The controller architecture is displayed in figure 5.10. In the figure, two main elements are distinguished. Enclosed in dotted lines the LQR tracking which gives the virtual input $v(t)$. This input is transformed through the input-state linearization block into the input $u(t) = f_{q_{pump}}(N, p_{rail}(t), I_{imv}(t))$, which is used to obtain actual system input I_{imv}. The feedforward term is observed as an exogenous input in the system, controlled by the gain K_r.

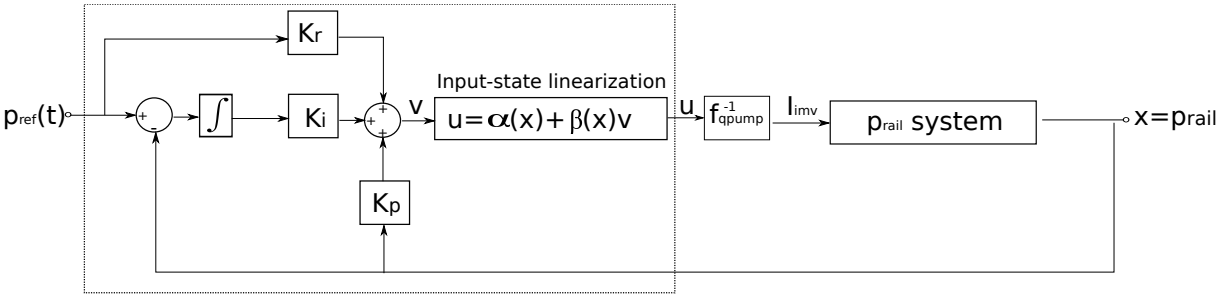

Figure 5.10: Optimal tracking control with integral action.

LQR with integral action The interest is to find the minimum time for the state $p_{rail}(t)$ to reach the pressure reference $p_{ref}(t)$ using the minimum amount of energy. The new state $e(t) = \int (p_{ref}(t) - p_{rail}(t))$ is defined. The goal of this term is to add an integral action to the controller to obtain zero steady state error. As well the pressure reference p_{ref} is introduced as an input. Given the system (5.5.10) and the new state $e(t)$, the extended state space system is:

$$\dot{x}_e(t) = A_e x_e(t) + B_e v_e(t), \quad x_e(t) = \begin{bmatrix} p_{rail}(t) \\ e(t) \end{bmatrix}, \tag{5.5.38}$$
$$v_e(t) = \begin{bmatrix} v(t) \\ p_{ref}(t) \end{bmatrix}$$

where $A_e = \begin{bmatrix} 0 & 0 \\ -1 & 0 \end{bmatrix}$ and $B_e = \begin{bmatrix} \Gamma_{rail}\frac{\beta_f}{V_{rail}} & 0 \\ 0 & 1 \end{bmatrix}$ and $v(t)$ the virtual input (5.5.12).

The cost function to minimize is:

$$J(t) = \int \frac{1}{2}(x_e(t)^T Q x_e(t) + v_e(t)^T R v_e(t)) \tag{5.5.39}$$

The matrix Q is chosen such that the weight is on the extended state $e(t)$, in order to minimize the error between p_{rail} and p_{ref} using the minimum $v(t)$, thus:

$$Q = \begin{bmatrix} 0.1 & 0 \\ 0 & 10 \end{bmatrix} \tag{5.5.40}$$

Remark 5.5.3. In theory, a feedforward term exists as long as the parameter R multiplies the input $p_{ref}(t)$. However, the aim with this controller is to avoid a feedforward term, thus R is chosen such that the weight of p_{ref} in $v_e(t)$ is large enough so that the feedback gain of the input $p_{ref}(t)$ in the controller is almost 0 and can be neglected:

$$R = \begin{bmatrix} 1 \times 10^{-3} & 0 \\ 0 & 1000 \end{bmatrix} \tag{5.5.41}$$

The problem of finding a feedback controller for (5.5.38) subject to the cost function (5.5.39) was presented before in Section 5.5.3 and has the solution:

$$v(t) = -R^{-1}B_e^T P x_e(t) = -K x_e(t), \quad K = R^{-1}B_e^T P \tag{5.5.42}$$

The gain $K = \begin{bmatrix} K_p & K_i \end{bmatrix}^T$ is obtained and the control input $v(t)$ is defined similarly to (5.5.42). The virtual controller $v(t)$ is the control input for system (5.5.10), thus

the transformation in Equation (5.5.11) is performed to obtain I_{imv} that is used in the common rail system control input $u(t) = f_{q_{pump}}(N, p_{rail}(t), I_{imv}(t))$.

The controller architecture is displayed in figure 5.11. In the figure, two main elements are distinguished. Enclosed in dotted lines the LQR controller with integral action which gives the virtual input $v(t)$. This input is transformed through the input-state linearization block into the input $u(t) = f_{q_{pump}}(N, p_{rail}(t), I_{imv}(t))$, which is used to obtain the actual system input I_{imv}.

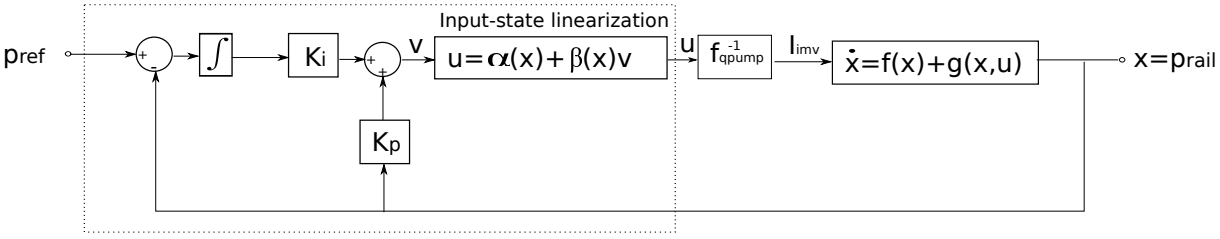

Figure 5.11: LQR controller with integral action.

Remark 5.5.4. Note that the difference between the LQR tracking controller and the LQR can be distinguished clearly from Figures 5.10 and 5.11. In the case of the LQR tracking controller (Figure 5.10), there is an additional term K_r in the feedback, which is the feedforward term that is added directly to the controller $v(t)$.

The common rail controller results are presented next. A comparison between both LQR controllers and a PI is performed in order to analyze the differences between the three different strategies.

5.5.5 LQR controller results

Using the model presented in 5.4, the common rail injection system is simulated, with the two developed LQR controllers and a traditional PI, in order to compare their responses and to establish the benefits achieved with each strategy.

The common rail pressure reference $p_{ref}(t)$ is obtained with a data map, where the inputs are the torque demand represented by the $IMEP$ cylinder pressure and the engine speed N. Phases of acceleration followed by phases of deceleration are tested. The engine speed is varied from 700 rpm up to 4000 rpm and $p_{ref}(t)$ varies from 250 bar up to 1600 bar. Figure 5.12 shows the simulation results. In the figure, $p_{rail}(t)$ and $p_{ref}(t)$ are plotted together with the error $\frac{|p_{rail}(t)-p_{ref}(t)|}{p_{ref_{max}}}$ and the acceleration and deceleration phases are also depicted:

- Phase 1. Acceleration from 9.4 s up to 33 s.

- Phase 2. Deceleration from 33 s up to 50 s. In this phase there is a strong deceleration, between 38 s up to 50 s the rail pressure is forced to its minimum value.
- Phase 3. Acceleration from 50 s up to 76 s. In this phase there is a strong acceleration, between 55 s up to 76 s the rail pressure is forced to its maximum value.
- Phase 4. Deceleration from 76 s up to 79 s.
- Phase 5. Acceleration plus stabilization from 79 s up to 106 s.
- Phase 6. Deceleration from 106 s up to 20 s.

From Figure 5.12 it is observed that all the controllers have a similar good tracking performance. Thanks to the integral action, all the controllers follow the reference with zero steady state error and the error in the three observers is lower than 10%. Besides the mean error in all the approaches remain lower than 0.5%:

- PI mean error= 0.26%
- LQR tracking with integral action error = 0.15%
- LQR with integral action = 0.20%.

The controller performance is now analyzed with respect to the control input. The control signal $I_{imv}(t)$ is shown in Figure 5.13. As illustrated, the control signal for the three controllers seems to be alike but some differences can be appreciated. There are some peaks where the control signal of the PI overpasses the other two control signals suggesting important differences in the transitory response. To give more details, Figure 5.14 shows a close up of Figure 5.13 in the peaks region. As it can be seen, the PI control signal is less smooth compared with the other two control approaches. This translates into more energy consumption, less robustness and a reduction on the actuator's lifetime.

To obtain a clearer appreciation of the responses, the step response of the controllers is shown in figure 5.15 together with the error. The results with respect to the controller requirements presented in Table 5.2 are presented in Table 5.3. The three approaches achieve an adequate response with similar characteristics. Small differences are presented between the three approaches. For instance, the LQR controller has a slower rise time for abrupt changes in $p_{ref}(t)$ than the other two controllers during the transitory, thus the maximum error with respect to the reference is bigger as depicted in 5.15b. This is due to the fact that the LQR controller has a smother response when compared to the other two methods. However, the mean error in this approach remains below 0.2% which

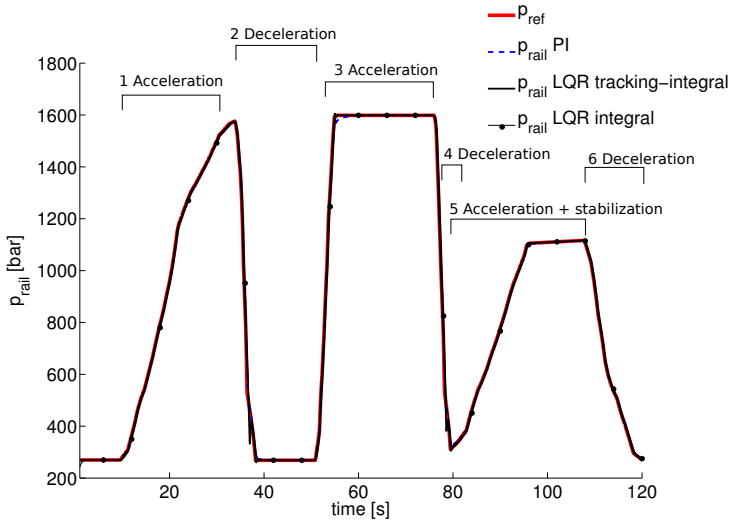

(a) $p_{rail}(t)$ as a function of time for all the control law.

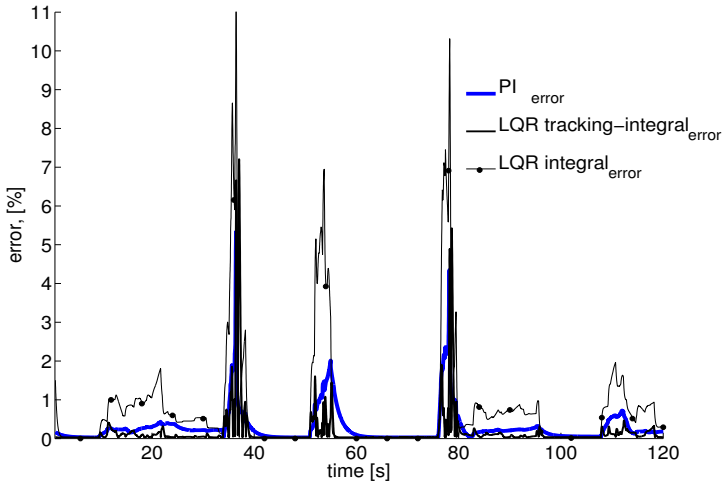

(b) $\frac{|p_{rail}(t)-p_{ref}(t)|}{p_{ref_{max}}}$ as a function of time for all the control law.

Figure 5.12: Simulation results for the common rail injection pressure controller.

corresponds to the same mean error range than the other two approaches. Besides, the settling time of the PI strategy is longer than the LQR strategies.

The LQR tracking controller has a faster response with respect to abrupt changes in the reference when compared to the LQR controller and the PI. However, the LQR tracking controller has a steeper response, which might produce overshoots in the pressure signal and saturation in the actuator.

Figure 5.16 shows the $I_{imv}(t)$ signal of the step response. As it is observed, the PI has the bigger current peak, followed by the LQR tracking controller. Differently, the LQR controller has a considerable smother input signal behavior with respect to the other two approaches.

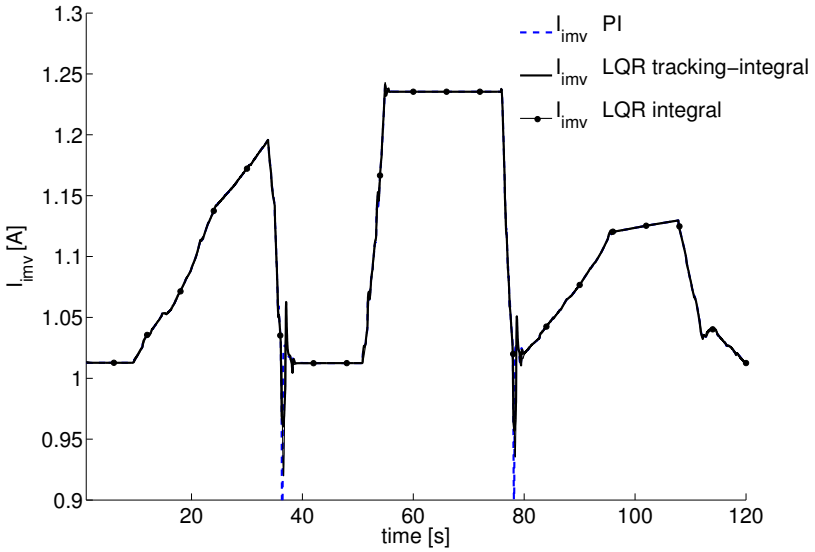

Figure 5.13: $I_{imv}(t)$ as a function of time for all the control laws.

	Overshoot	$p_{rail_{max}}$	Settling time	$p_{ref} - p_{rail}$ tolerance		mean error
Specification	$< 5\%$	1600 bar	$\leqslant 1$ s	Transitory (± 25 bar)	Stable (± 8 bar)	
LQR tracking	4%	1608 bar	1 s	40 bar	< 1 bar	0.11%
LQR	0	1600 bar	1 s	15 bar	< 1 bar	0.17%
PI	0	1600 bar	7 s	15 bar	8 bar	0.12%

Table 5.3: Common rail controller results.

The parameters Q and R can be adapted to an specific requirement if it is needed. For instance, if a faster response is required for the LQR tracking controller, decreasing the first element in the parameter matrix Q (Equation (5.5.36)) as:

$$Q = \begin{bmatrix} 10 & 0 \\ 0 & 25000 \end{bmatrix} \tag{5.5.43}$$

gives a slightly faster response as it is depicted in Figure 5.17a. This change of magnitude of the first element in the matrix Q decreases the weight of the signal pressure with respect to the cost function (5.5.35), thus the signal pressure has a bigger deviation, which results on a faster response but it also increases the overshoot up to 20%, which is out of the bounds of the controller requirement. However, this change decreases the peak magnitude of the IMV current $I_{imv}(t)$ from 1.38 A to 1.28 A as depicted in Figure 5.17b. Thus the parameters Q and R must be chosen as a trade-off between the system requirements and the controller response.

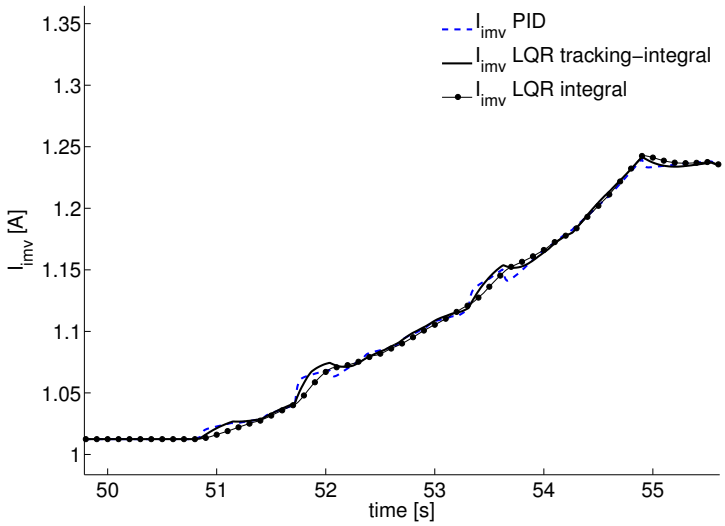

(a) $I_{imv}(t)$ as a function of time for all the control laws, zoom between 50 s to 55 s.

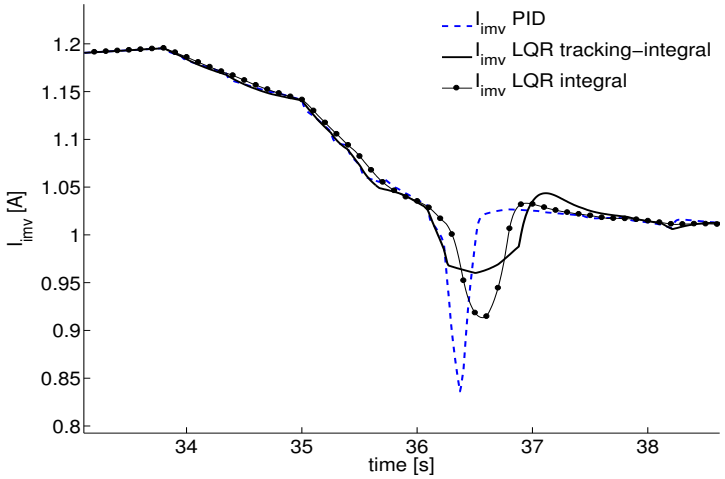

(b) $I_{imv}(t)$ as a function of time for all the control laws, zoom between 33 s to 38 s.

Figure 5.14: Simulation results for the IMV control current I_{imv}(t).

Until now, only slight differences have been remarked between the three different approaches, however, the most important remark with respect to the controllers is the fact that the PI controller calibration passes through an empirical process in order to find the PI gains, which are computed with experimental procedures and in many cases its representation is not unique, besides the fact that there are no guaranties with respect to stability or optimal behavior, thus the PI might not be reliable in some operating conditions. By the contrary, the LQR controllers are computing solving the CARE which guarantees the system stability, besides the fact that a cost function is defined in order to optimize different design criteria. A drawback of the LQR algorithm is that it still needs to specify the weighting factors Q and R and compare the results with the

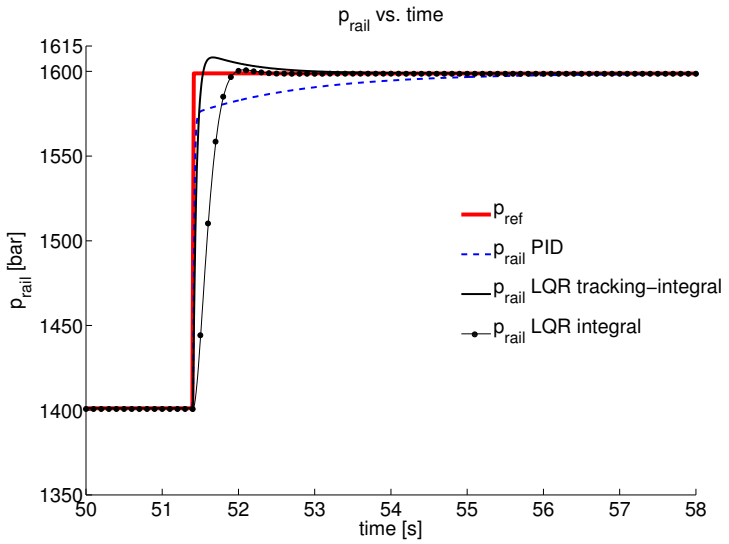

(a) Step response. $p_{rail}(t)$ as a function of time for all the control law.

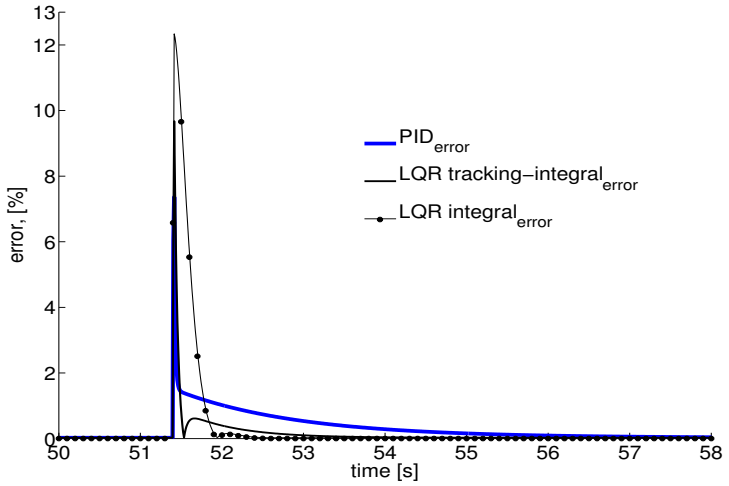

(b) Step response. $\frac{|p_{rail}(t)-p_{ref}(t)|}{p_{ref_{max}}}$ as a function of time for all the control law.

Figure 5.15: Step response for the common rail injection pressure controller.

specified design goals, so the controller synthesis needs a simulation process where the designer judges the produced *optimal* controller adjusting the weighting factors to get a controller more in line with the specified design goals. However, differently from the PI, those weighting factors are computed once and remain constants for all the operating range and do not compromise the controller stability.

A great advantage of the strategy proposed in this thesis is the fact that it has been conceived with the actual elements that are currently used in the car ECU for the common rail system. It means that this approach might be tested directly in the benchmark process without any additional consideration.

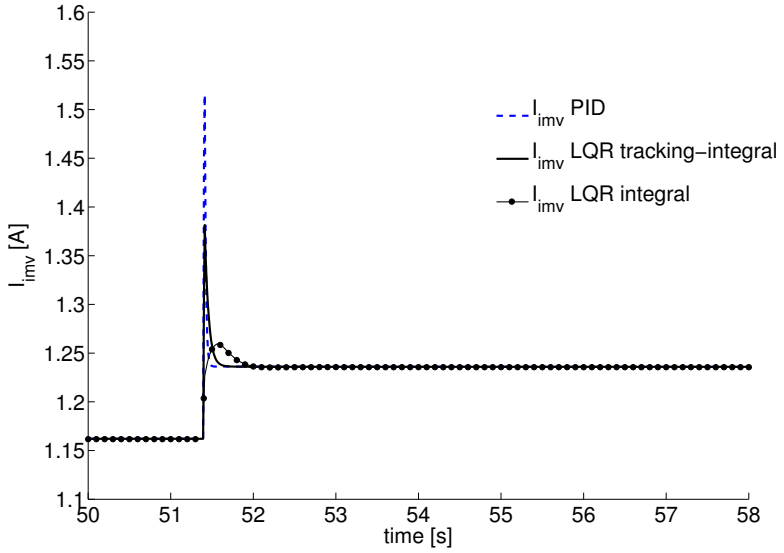

Figure 5.16: Step response. $I_{imv}(t)$ as a function of time.

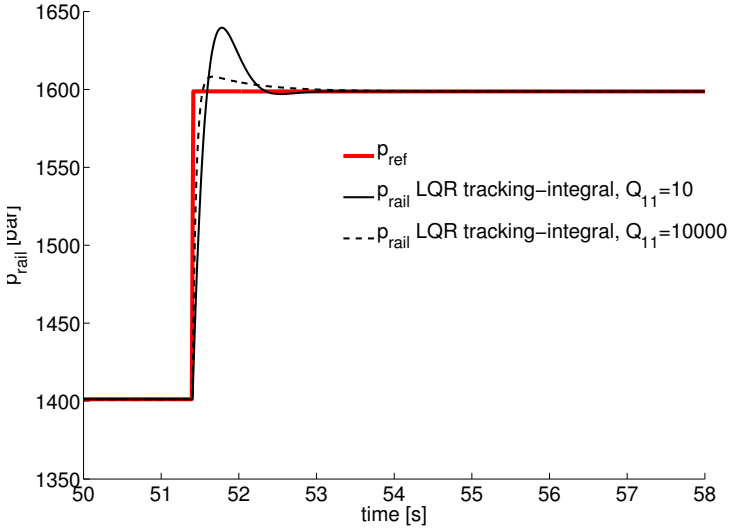

(a) Step response. $p_{rail}(t)$ as a function of time for the LQR tracking controller

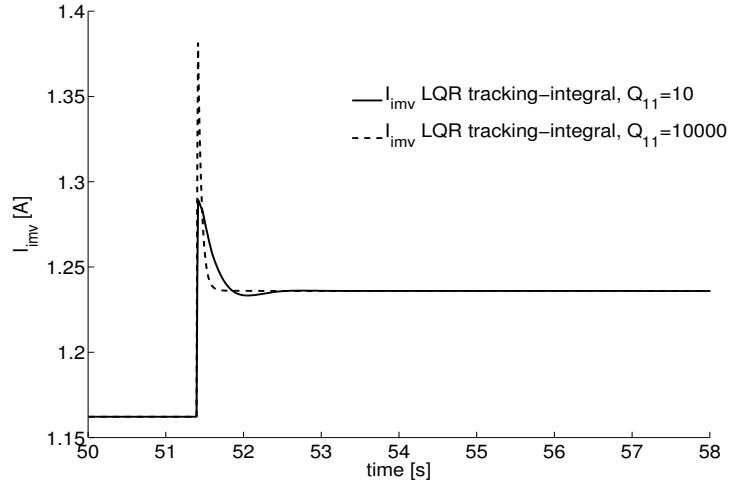

(b) Step response. $I_{imv}(t)$ as a function of time for the LQR tracking controller

Figure 5.17: Step response of the common rail injection pressure LQR tracking controller for two different Q parameters.

5.6 Chapter Summary

A common rail injection system model has been designed to develop a control strategy to track the rail pressure. The common rail system control device is the IMV which regulates the fuel flow going to the HP pump. The method consists on controlling the IMV current $I_{imv}(t)$ to regulate the IMV opening.

As the common rail model contains strong nonlinearities which are hard to handle from the control point of view, an input-state linearization strategy has been applied to obtain a virtual linear system, which is controlled by a virtual input $v(t)$. A linear control strategy is performed in the linear system and the virtual input is computed. The virtual input is used to recover the system actual input $I_{imv}(t)$. Using input-state linearization makes possible to cancel out the nonlinearities of the injection system and to have a linear controllable system which can be used to create linear control laws.

Two controllers are designed for the virtual linear system: an LQR controller with integral action and an LQR tracking controller with integral action. Both controllers have been compared to a traditional PI control method. The traditional PI control approach is simple to implement and effective but its stability and optimality on the whole operating range cannot be ensured. In terms of energy consumption and smoothness in the control signal, the response of the PI is poor; which might cause a reduction in the lifetime of the actuators and/or a loss of performance and stability under certain operating conditions.

When using the LQR approach, a unique control law has to be created for the whole operating range contrary to the PI strategy which usually needs of data maps of PI gains to be adjusted. A drawback of the LQR algorithm is that the weighting factors Q and R must be adjusted, so the controller synthesis needs a simulation process where the designer judges the produced *optimal* controller adjusting the weighting parameters. Differently from the PI, those weighting factors are computed once and remain constants for all the operating range and do not compromise the controller stability. Adjusting these parameters empirically is a common procedure. Besides, the controller adjusting is easier than the PI because only two parameters have to be changed to modify the response on the complete operating range, contrary to the PI controller, where the complete controller has to be re adjusted for changes in the operating conditions. As the proposed approach has to perform the input-state linearization, the CPU load might be bigger than in the current PI application.

The optimal control approaches developed in this thesis for the common rail injection system have a good performance, giving zero steady-state offset thanks to the integral action implemented and a smooth optimal control signal due to minimization of the cost functions defined.

Chapter 6

Conclusion and perspectives

In this thesis, different developments to enhance the 0D theromodynamical SI engine modeling and a model based control strategy for the diesel common rail injection systems, which can be transposed to gasoline engines have been proposed. These developments are an important contribution for the model-based control approach that Renault intends to implement to improve the engine performances and to meet the current regulation with respect to emissions and pollution. The main contributions of this thesis can be summarized as follows:

- A new model referred to as *local approach* that models the impact of the cylinder walls on the burning rate has been proposed. This new model takes into account the impact of the cylinder walls on the combustion process using the flame surface distribution with respect to the combustion chamber walls and the assumed linear decay of the burning rate during the flame-wall interaction. This model has been included in a two zones combustion model. It has been validated against experimental measurements. When the flame-wall interaction is not well taken into account, the energy release is usually overestimated at the end of the combustion process, as well as the cylinder pressure. When the proposed flame-wall interaction model is included, very good results are obtained; the model improves dramatically when compared to less accurate approximations (with an enhanced fit to the measurements), in terms of heat release rate and cylinder pressure estimation. The model has been also validated with respect to experimental measurements of experiences performed for two locations of the spark plug and two spark plug types, and a good agreement between the implemented model and the experience was obtained.

- A new method to estimate the cylinder enclosed mass during the combustion and/or compression strokes when the engine valves are closed has been proposed. A 0D one zone thermodynamical model is used where two state space variables are

defined: the cylinder pressure and the cylinder temperature. The cylinder pressure is assumed to be measured and the temperature is observed with two nonlinear strategies: a nonlinear high gain observer and an LPV with uncertain parameters high gain observer. The enclosed mass is computed using the observed temperature and the cylinder pressure measurement using the ideal gases law. The high gain nonlinear observer is conceived as a direct application of the high gain observer theory. In the LPV with uncertain parameters high gain observer, the contribution of this thesis is to include a high gain strategy in a parameter varying observer in order to cope with the mismatch between the estimated and the real parameters. Very promising results are obtained with the proposed mass estimation methods, which have shown to be effective to handle the strong nonlinearities of the system.

- A common rail injection model has been designed and a control strategy to regulate the rail pressure is proposed. The common rail system is controlled with the inlet metering valve IMV which regulates the fuel flow going to the high pressure pump HP. The control method consists in control the IMV control current $I_{imv}(t)$ to regulate the IMV opening. The common rail model contains strong nonlinearities, thus an input-state linearization strategy has been applied to obtain a virtual linear system, which is controlled by a virtual input $v(t)$. This allows a linear control strategy to be synthesized to compute the virtual input, which is used to recover the system actual input. Two controllers are designed for the virtual linear system: an LQR controller with integral action and an LQR tracking controller with integral action. The optimal control approaches developed in this thesis for the common rail injection system show good performances, giving zero steady-state offset thanks to the integral action and a smooth optimal control signal due to minimization of the cost functions defined.

Future work directions have been identified in order to improve and to generalize the methods developed in this thesis:

- When modeling the flame-wall interaction, the quenching distance is a critical modeling parameter. The quenching distance helps to define a boundary where the walls influence has more impact in the burning rate. In the *local approach* proposed in this thesis, the quenching distance criterion has been assumed to be the integral eddy length scale. However, the integral scale 0D models might not represent well enough the quenching distance than more complex modeling schemes. In order to improve the results of the flame-wall interaction modeling, a better representation of the quenching distance might be desired.

- In a 0D thermodynamical model, there exists the big challenge of modeling the enthalpy due to the heat wall losses and the enthalpy due to the combustion process. Indeed, in most of the models it is hard to decouple both enthalpies during the

calibration process because there are no experimental references of the enthalpy due to the heat wall losses and/or the burning rate enthalpy separately. The enclosed mass observers proposed in this thesis use the assumption that the enthalpy due to the combustion process is known, which might be an unrealistic approximation as the Vibe's law used to model the burning rate lacks of precision. An interesting challenge would be to have a more accurate model of the burning rate for a one zone engine model, and/or calibrate the heat wall losses model with actual enthalpy losses measurements to enhance the precision of the observers.

- The common rail control system used in Renault uses the static and dynamics leakages to guarantee the system performance when an abrupt loss of pressure is needed in the rail i.e in slow driving conditions. However, such leakages are considered as statical functions which do not have any control input. An interesting improvement for the common rail system would be the introduction of a method to actually control such leakages or the rail pressure regulation in such conditions. Indeed, a second control valve connected directly to the rail is a common improvement to regulate the rail pressure in slow driving. Including such a scheme would introduce another control input to the system.

Future work directions have been identified in a long term:

- Engine modeling strategies as the proposed in this thesis must be adapted to be used in real time applications. To do so, it is necessary to find a trade-off between the engine modeling complexity, the improvement achieved in the engine and the computational resources required. Besides, different modeling and estimation techniques, different from the proposed in this study might be tested in order to analyze possible improvements on the proposed strategy, in order to obtain faster estimations that can be used in real time.

- Nowadays, most of the modeling and control strategies of the physical phenomena in the combustion chamber are studied only theoretically or for benchmark processes. In a long term, these strategies are expected to be completely generalized in the benchmark, so it can be used more often than not in the engine calibration stage, reducing the development costs.

Bibliography

Adams, M., Cryan, S. & Mourelatou, A. [2009], 'Air emission inventory data in europe: new perspectives'.

Alharbi, Y. & Sick, V. [2010], 'Investigation of boundary layers in internal combustion engines using a hybrid algorithm of high speed micro-piv and ptv', *Exp Fluids* **49**.

Alizon, F. [2005], Transferts de chaleur convectifs dans la chambre de combustion des moteurs à combustion interne: Influence de l'aÃl'rodynamique interne, Technical report, PARIS VI.

An, S. & Shao, L. [2008], 'Diesel engine common rail pressure control based on neuron adaptive PID', *Cybernetic and Intelligent Systems* .

Angelberger, C., Poinsot, T. & Delhay, B. [1997], 'Improving near-wall combustion and wall heat transfer modeling in SI engine computation', *SAE technical papers series* (972881).

Aquino, C. [1981], 'Transient A/F control characteristics of the 5 liter central fuel injection engine', *SAE* .

Balluchi, A., Bicchi, A., Mazzi, E., Sangiovanni Vincentelli, A. & Serra, G. [2007], 'Hybrid modelling and control of the common rail injection system', *International Journal of Control* **80**(11), 1780–1795.

Bara, G., Daafouz, J., Kratz, F. & Ragot, J. [2010], 'Parameter dependent state observer design for affine LPV systems', *International journal of control* **74**(15).

Baratta, M., Catania, A., Spessa, E. & Vassallo, A. [2005], 'Development of an improved fractal model for the simulation of turbulent flame propagation in SI engines', *SAE* (2005-24-082).

Barba, C. & Burkhardt, C. [2000], 'A phenomenological combustion model for heat release rate prediction in hith-speed DI diesel engines with common rail injection', *SAE* .

Besancon, G. [2007], *Nonlinear Observer and Applications*, Springer.

Bixby, R. [1992], 'Implementing the simplex method: The initial basis', *ORSA Journal on Computing* (Vol 4 N0 3).

Blint, R. [1986], 'The relationship of the laminar flame width to flame speed', *Combustion science technology* **49**.

Blumberg, P., Lavoie, G. & Tabaczynski, R. [1980], 'Phenomenological models for reciprocating internal combustion engines', *Progress in Energy and Combustion Science* **5**(4), 313–326.

Bordet, N., Caillol, C., Higelin, P. & Talon, V. [2010], 'A physical 0D combustion model using tabulated chemistry with presumed probability density function approach for multi injection diesel engines', (2010-01-1493).

Bougrine, S., Richard, S. & Veynante, D. [2009], 'Modelling and simulation of the combustion ethanol blended fuels in a SI engine using a 0D coherent flame model', *SAE International* (2009-24-0016).

Boust, B., Sotton, J., Bellenoue, M. & Rivere, J. [2007], 'A novel physical approach for wall heat transfer in internal combustion engines', *SAE* (2007-24-0027).

Bozza, F., Gimelli, A., Merola, S. & Vaglieco, B. [2005], 'Validation of a fractal combusition model through flame imaging', *Modeling of SI and Diesel Engines 2005* (2005-01-1120).

Bozza, F., Gimelli, A., Strazzullo, L., Torella, E. & Cascone, C. [2007], 'Steady state and transient operation simulation of a downsized turbocharged SI engine', *Modeling of SI and Diesel Engines* (2007-01-0381).

Brecha, R. [2008], 'Emission scenarios in the face of fossil-fuel peaking', *Energy Policy* .

Briat, C., Sename, O. & Lafay, J. [2011], 'Design of LPV observers for LPV time-delay systems: an algebraic approach', *Journal of control* **9**(84), 1533–1542.

Bruneaux, G. [1996], 'Étude asymptotique, simulation numérique directe et modélisation de l'interaction flamme turbulente prémélangée-paroi', *PhD thesis, IFP et Ecole Centrale Paris* .

Butt, Q. & Bhatti, A. [2008], 'Estimation of gasoline engine parameters using high order sliding mode', *IEEE transactions on industrial electronics, Vol 55, pages 3891-3898* pp. 3891–3898.

Cavina, N., Siviero, C. & Suglia, R. [2004], 'Residual gas fraction estimation: Applicaton to a GDI engine with variable valve timing and EGR', *Si Engine Performance and Additives, Gasoline Engine Cold Start and Direct Injection* (2004-01-2943).

Charlette, F., Menevau, F. & Veynante, D. [2010], 'A power law flame wrinkling model for LES of premixed turbulent combustion', *Elsevier* .

Chase Jr, M., Davies, C., Jr, J. D., Frurip, D. & McDonald, R. [1986], *JANAF Thermochemical Tables*, 3rd edn, American Institute of Physics.

Chatlatanagulchai, W. & Yaovaja, K. [2010], 'Gain scheduling integrator augmented sliding mode control of common-rail pressure in diesel dual fuel engine', *SAE* (2010-01-1573).

Colin, G., Giansetti, P., Chamaillard, Y. & Higelin, P. [2007], 'In cylinder mass estimation using cylinder pressure', *SAE* (2007-24-0049).

Colin, O., Benkenida, A. & Angelberger, A. [2003], '3D modeling of mixing, ignition and combustion phenomena in highly stratified gasoline engine', *Oil and Gas Science and Technology* **58**, 47–62.

Daafouz, J., Bernoussou, J. & Geromel, J. [2008], 'On inexact LPV control design of continous time polytopic systems', *Transactions on automatic control* **53**(7).

di Gaetaai, A., Montanaroa, U., Fiengob, G., Palladinob, A. & Giglioa, V. [2012], 'A model-based gain scheduling approach for controlling the common-rail system for GDI engines', *International Journal of Control* **85**(4), 419âĂŞ436.

Doe Fundamentals Handbook [1993], *U.S. Department of Energy* **1-2**.

Ferguson, C. & Keck, J. [1977], 'On laminar flame quenching and its application to spark ignition engines', *Combustion and Flame* **28**.

Feron, E., Balakrishanan, V. & Boyd, S. [1992], 'Numerical methdos for $\mathbf{H}_2$ related problems', *Proceedings of the 1992 American Control Conference, Chicago* .

Foucher, F., Burnel, S. & Mounaim-Rousselle, C. [2002], 'Evaluation of burning rates in the vicinity of the piston in a spark ignition engine', *Procedings of the combusition institute* **29**, 751–757.

Foucher, F. & Mounaim-Rousselle, C. [2005], 'Fractal approach to the evaluation of burning rates in the vicinity of the piston in a spark-ignition engine', *Combustion and Flame* **143**, 323–332.

Fox, J., Cheng, W. & Heywood, J. [1993], 'A model for predicting residual gas fraction in spark-ignition engines', *SAE* (931025).

Gauthier, C. [2007], 'Commande multivariable de la pression d'injection dans un moteur diesel common rail', *Phd thesis, INP Grenoble* .

Gauthier, C., Sename, O., Dugard, L. & Meissonnier, G. [2006], 'An LFT approach to H_∞ control design for diesel engine common rail injection system', *Les Rencontres Scientifiques de l'IFP, Rueil Mailmaison* .

Gauthier, C., Sename, O., Dugard, L. & Meissonnier, G. [2007*a*], 'An H_∞ linear parameter-varying (lpv) controller for a diesel engine common rail injection system', *European Control Conference, ECC'07, Kos : Gréce (2007)* **62**, 513–522.

Gauthier, C., Sename, O., Dugard, L. & Meissonnier, G. [2007*b*], 'An LFT approach to H_∞ control design for diesel engine common rail injection system', *Oil and Gas Science and Technology* **62**, 513–522.

Gauthier, C., Sename, O., Dugard, L. & Meissonnier, G. [2007*c*], 'Some experimental results of a robust H_∞ linear parameter-varying (lpv) controller applies to a diesel engine common rail injection system', *IFAC Advances in Automotive Control* .

Gérard, B., Souley, H., Zasadzinski, M. & Darouach, M. [2010], 'H_∞ filter for bilinear systems using LPV approach', *IEEE Transactions on automatic control* **7**.

Guerrassi, N. & Dupraz, P. [1998], 'A common rail injection system for high speed direct injection diesel engines', *SAE Technical Papers* (980803).

Gulder, L. [1984], 'Correlations of laminar combustion data for alternative si engine fuels', *SAE* (841000).

Gulder, L., Smallwood, G., Wong, R., Snelling, D. & Smith, R. [2000], 'Flame front surface characteristics in turbulent premixed propane/air combustion', *Combustion and Flame* **120**, 407–416.

Han, A. & R.Reitz [1997], 'A temperature wall function formulation for variable-density turbulent flows with application to engine heat transfer modeling', *Int. J. Heat Mass Transfer* **40**.

Hart, M., Ziegler, M. & Loffeld, O. [1998], 'Adaptive estimation of cylinder air mass using the combustion pressure', *Electronic engine controls 1998: Diagnostics and Control* (980791).

Heywood, J. [1980], 'Engine combustion modeling - an overview', *Combustion Modeling in Reciprocating Engines* .

Heywood, J. [1988], *Internal Combustion Engine Fundamentals*, McGraw-Hill International Editions.

International Energy Agency [2011], *CO2 Emissions from fuel combustion highligths*, IEA.

Kang, K. & Baek, J. [1998], 'Turbulence characteristics of tumble ÌĎflow in a four-valve engine', *Experimental Thermal and Fluid Science* **18**, 1231–243.

Karim, G., Raine, R. & Jones, W. [1988], 'An examination of cyclic variations in a dual fuel engine', *SAE International Fall Fuels and Lubricants Meeting and Exhibition* (881661).

Keck, J. [1982], 'Turbulent flame structure and speed in spark-ignition engines', *Nineteenth Symposium (International) on Combustion, Cambridge* .

Khalil, H. [1996], *Nonlinear systems*, Prentice Hall.

Koehler, U. & Bargende, M. [2004], 'A model for a fast prediction of the in-cylinder residual gas mass', *SI Engine experiment and modeling* (2004-01-3053).

Krzyzanowski, M., Kuna-Dibbert, B. & Schneider, J. [2005], *Health effects of transport-related air pollution*, World Health Organization.

Kwakernaak, H. & Sivan, R. [1972], 'Linear optimal control systems', *John Wiley & Sons Inc* .

Lafossas, F., Colin, O., Berr, F. L. & Menegazzi, P. [2005], 'Application of a new 1D combustion model to gasoline transient engine operation', (2005-01-2107).

Lavoie, G., Heywood, J. & Keck, J. [1970], 'Experimental and theoretical study of nitric oxide formation in internal combustion engines', *Combustion Science and Technology* **1**(4), 313–326.

Leroy, T., Alix, G., Chauvin, J., Duarchy, A. & Berr, A. L. [2008], 'Modeling fresh air charge and residual gas fraction on dual independent variable valve timing si engine', *SAE Int.J.Engines* (2008-01-0983).

Ljung, L. [1999], *System identification, theory for the user (2nd Ed.)*, Prentice Hall.

Mattavi, J., Groff, E. & Lienesch, F. [1980], 'Engine improvements through combustion modelling', *Combustion Modeling in Reciprocating Engines* .

Maurice, W., Heemels, H., Daafouz, J. & Millerioux, G. [2010], 'Observer based control of discrete time LPV systems with uncertain parameters', *Transactions on automatic control* **55**(9).

Metghalchi, M. & Keck, J. [1982], 'Burning velocities of mixtures of air with methanol, isooctane, and indolene at high pressure and temperature', *Combustion and flame* **48**, 192–210.

Mikles, J. & Fikar, M. [2007], 'Process modeling, identification and control', *Springer* .

Mladek, M. & Onder, C. [2000], 'A model for the estimation of inducted air mass and the residual gas fraction using cylinder pressure measurement', *Modeling of SI Engines* (2000-01-0958).

Naidu, D. S. [2003], *Optimal Control Systems*, CRC Press.

Nishaiwaki, K. & Saijyo, K. [1999], 'Modeling of flame wall interaciton in SI engine combustion', *Proceedings of the 15 Internal Combusiton Engine Symposium* (9935158), 63–68.

Olalla, C., Leyva, R., El Aroudi, A. & Queinnec, I. [2009], 'Robust LQR control for PWM converters: an LMI approach', *IEEE Transactions on industrial electronics* **56**(7).

Perruquetti, W. [2002], *Sliding mode control in engineering*, Marcel Dekker,Inc.

Pierce, P., Ghandhi, J. & Martin, J. [1992], 'Near-wall velocity characteristics in valved and ported motored engines', *SAE* (920152).

Poinsot, T. & Veynante, D. [2001], *Theroetical and numerical combustion*, Edwards.

Poulos, S. & Heywood, J. [1983], 'The effect of chamber geometry on SI engine combustion', (830334).

Richard, S., Bougrine, S., Font, G., Lafossas, F. & Ber, F. L. [2009], 'On the reduction of a 3D CFD combustion model to build a physical 0D model for simulating heat release, knock and pollutants in si engines', *Oil and Gas Sciend and Technology* **64**, 223–242.

Richard, S., Colin, O., Vermorel, A., Benkenida, A., Angelberger, C. & Veynante, D. [2007], 'Towards large eddy simulation of combustion in spark ignition engines', *Sciences Direct* .

Senecal, P., Xin, J. & Reitz, R. [1996], 'Predictions of residual gas fraction in IC engines', *Modeling and Diagnostics in Diesel Engines,SAE* (962052).

Steiner, T. & Boulouchos, K. [1995], 'Near-wall unsteady premixed flame propagation in SI engines', *International Congress and Exposition SAE* (951001).

Summaries of EU legislation [2009], 'Regulation of the european parliament and of the council of 23 april 2009 setting emission performance standards for new passenger cars as part of the community's integrated approach to reduce co 2 emissions from light-duty vehicles', *OJ L 140 of 5.6.2009* (443).

Tennekes, H. & Lumley, J. [1985], *First course in turbulence*, The MIT press.

Vibe, I. [1956], 'Semi-empirical expression for combustion rate in engines', *Proceedings of Conference on piston engines, USSR Academy of Sciences* (Vol 4 N0 3), 186–191.

von Kármán, T. [1930], 'Mechanical similitude and turbulence', *Technical memorandums, National Advisory Committee for Aeronautics* **611**.

Weiss, M., Bonnel, P., Hummel, R., Manfredi, U., Colombo, R., Lanappe, G., Le Lijour, P. & Sculati, M. [2011], 'Analyzing on-road emissions of light-duty vehicles with portable emission measurement systems (pems)'.

Wilcox, D. [1993], *Turbulence modeling for CFD*, DCW Industries.

Woschni, G. [1967], 'A universally applicable equation for the instantaneus heat transfer coefficient in the interal combustion engine', *SAE* (670931).

Yoshiyama, S., Tomita, E., Zhang, Z. & Hamamoto, Y. [2001], 'Measurements and simulation of turbulent flame propagation in a spark ignition engine by using fractal burning model', *SAE* (2001-01-3603).

Zhao, X., Matthews, R. & Ellzey, E. [1994], 'Numerical simulations of combustion in SI engines: Comparison of the fractal flame model to the coherent flame model', *International Symposium COMODIA* .

Appendix A

Appendix

A.1 Variable Valve Timing (VVT) profiles in a SI engine

The variable valve timing (VVT) is a mechanism that allows alteration of the profile and the timing of the engine's valves lift. The VVT allows the lift, duration or timing (in various combinations) of the intake and/or exhaust valves to be changed while the engine is in operation.

The timing, duration and lift of these valve events have a significant impact on engine performance. In engines without VVT, the valves profiles are fixed, so performance at different loads and speeds is always a compromise between drivability (power and torque), fuel economy and emissions. An engine equipped with a variable valve timing does not have this constraint, allowing performance to be improved over the engine operating range.

Figure A.1 shows the intake and exhaust valves lift profile when including the VVT mechanism and when it is not included. Only the advance of the valves opening is altered in this example. In the figure:

- the phase between the inlet valve opening (IVO) and the inlet valve closure (IVC) corresponds the intake stroke,
- the phase between the exhaust valve opening (EVO) and the exhaust valve closure (EVC) corresponds to the exhaust stroke,
- the main events (IVO, IVC, EVO, EVC) are pointed and the event $IV = EV$ that is the moment where the intake valve and the exhaust valve have the same lift is also depicted.

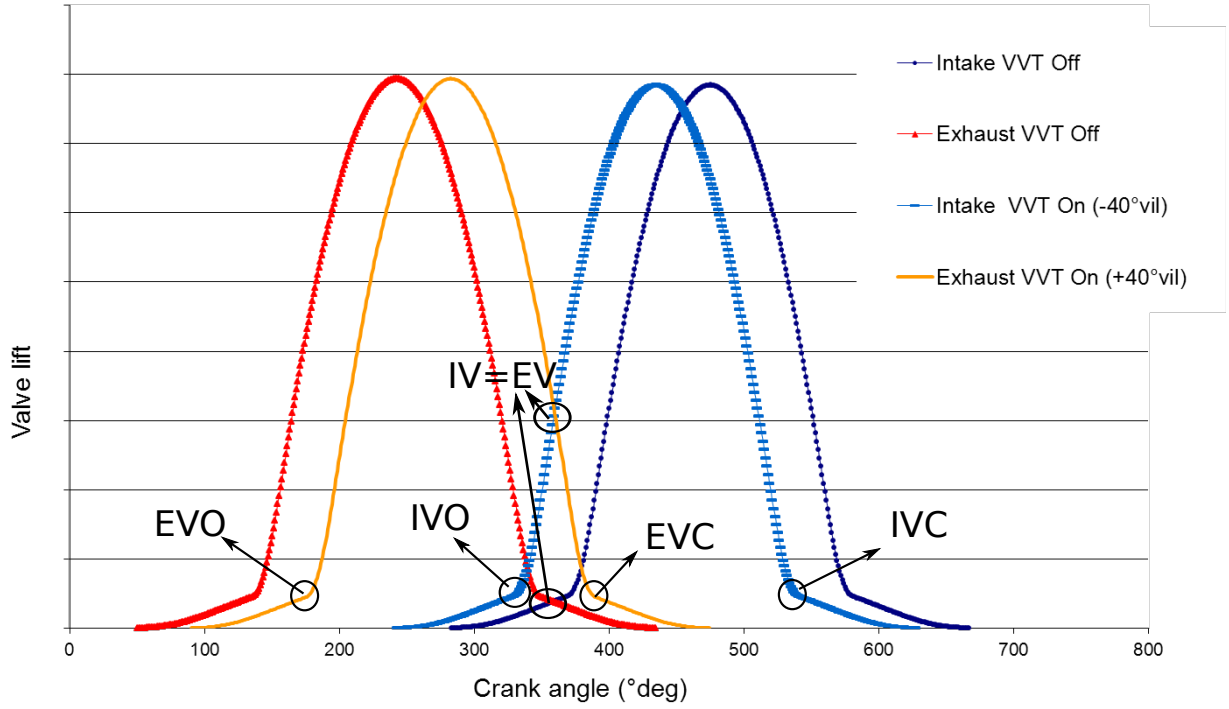

Figure A.1: VVT valves lift profiles.

The beginning of the cycle corresponds to the event where the piston moves vertically from the top dead center (TDC) to the bottom dead center (BDC) to fill-in the combustion chamber. The angle reference is given with respect to the crankshaft position. In the figure, the crank angle degree is out of phase 360 *deg*, taking as reference an engine cycle from 0 *deg* to 720 *deg*. Thus, the crankshaft position 360 *deg* corresponds to cycle beginning.

A.2 Fill in model

In the phenomenological engine models, the fill in model represents how is composed the mixture of gases in the intake manifold. The fill in model defines the gases origin (i.e. intake manifold, exhaust manifold) during the intake and combustion strokes. The fill in model can also differentiate the gases composition, which might be given in terms of burned gases and fresh gases proportion, or in more advanced strategies the chemical components can be distinguished. The exhaust gas recycled (EGR) and the internal gas recycled (IGR) topics are the main issues when modeling the fill in procedure.

In SI gasoline engines equipped with variable valve timing (VVT), there is a period

between the Inlet Valve Opening (IVO) and the Exhaust Valve Closure (EVC) when both valves are open called the overlap. During this period, there are gases dragged from the cylinder to the intake path (back flow); similarly, fresh gases might be as well dragged from the intake directly to the exhaust and from the exhaust to the intake (scavenging). All these phenomena produce differences in the composition of gases in the intake path and the cylinder. The EGR and IGR issues represent an important part of engine modeling because they define the composition (in terms of species or chemical components, or proportion, etc) of the gases in the combustion chamber and they help to define the amount of gases at IVC, which might vary from the flow meter measurement due to phenomena as the back flow and the scavenging.

The fill in strategy used in this thesis is presented first in this section, where the main issue to treat is the IGR. As the EGR is a device inserted in the engine and its characterization depends on the architecture of the engine path, in this thesis it is assumed that the EGR mass fraction is known from the air path modeling. Later a summary of different fill in models is also presented.

Fill in gases composition A common strategy for the fill in gases composition is to assume that they have the same stoichiometric proportion that the products of the combustion process. Thus the burned gas fraction X_b and the unburned gas fraction X_u in the EGR and the IGR can be approximated by:

$$\begin{aligned} X_b &= \frac{\phi\left(44n + 18\frac{m}{2} + 28\left(n + m\frac{m}{4}\right)\zeta\right)}{\phi\left(12n + m\right) + \left(n + \frac{m}{4}\left(32 + 28\zeta\right)\right)} \\ X_u &= \frac{\left(1-\phi\right)\left(n + \frac{m}{4}\right)\left(32 + 28\zeta\right)}{\phi\left(12n + m\right) + \left(n + \frac{m}{4}\left(32 + 28\zeta\right)\right)} \end{aligned} \tag{A.2.1}$$

where for a gasoline engine $n = 7.05$, $m = 163.5$ and $\zeta = \frac{m}{n}$.

Initial conditions at IVC The fill-in model also defines the initial state of the masses for cycle to cycle engine simulation. Thus, in a phenomenological engine model, the initial conditions of the gases in the combustion chamber at IVC are:

$$\begin{aligned} m_{b_0} &= m_{egr_b} + m_{igr_b} \\ m_{u_0} &= m_{egr_u} + m_{igr_u} + m_{air} \end{aligned} \tag{A.2.2}$$

where $m_{egr_{b,u}}$ are the burned and unburned EGR masses, $m_{igr_{b,u}}$ are the IGR burned and unburned masses and m_{air} is the admitted air. In order to define these variables, the

fill-in model is used. Next a summary of different fill-in models found in the literature for 0D engine modeling schemes are presented.

A.2.1 Fox IGR estimation model

In this thesis, the IGR model proposed in [Fox et al., 1993] is used, this model is based in the definition of the so known overlap factor. Figure A.1 shows a scheme of the VVT profiles during the engine cycle. The cycle is out of phase 360 deg (taking as reference the crank angle position), thus at 360 deg the piston is at TDC and moves vertically towards the BDC to fill-in the combustion chamber. Two profiles are shown: with VVT (on) and without VVT (off). Besides the overlap period, other important event to remark is when both valves have the same opening $IV = EV$.

In [Fox et al., 1993], the so known overlap factor OF is proposed:

$$OF = \frac{D_i A_i + D_e A_e}{V_{cyl}} \tag{A.2.3}$$

where

$$A_i = \int_{IVO}^{IV=EV} L_i(t) d\theta, \quad A_e = \int_{IV=EV}^{EVC} L_e(t) d\theta \tag{A.2.4}$$

where $L_e(t)$ and $L_i(t)$ are the exhaust and intake valves lifts, $D_{i,e}$ are the inlet and exhaust nozzle diameters and V_{cyl} is the cylinder geometric volume. The overlap factor is used to parametrize the amount of IGR .

According to [Fox et al., 1993], the IGR amount of gas is:

$$m_{igr} = \int_{IVO}^{EVC} \dot{m}_e(t) dt + m_{IVO} \tag{A.2.5}$$

where two main contributions are responsible of the presence of IGR: the first term in the right side of the equation which corresponds the gases coming from the exhaust port during the overlap period $m_e(t)$ and the second term which corresponds the trapped gases in the cylinder before the overlap period. Thus the residual gas mass fraction is also given by two components:

$$X_{igr} = C_1 \frac{p_{exh}}{p_{int}}^{\frac{\gamma+1}{2\gamma}} \frac{OF}{N} \sqrt{|p_{exh} - p_{int}|} + C_2 \frac{\phi \frac{p_{exh}}{p_{int}}^{\frac{1}{\gamma}}}{r_c} \tag{A.2.6}$$

where the first term in the right of the equation represents the gas mass fraction due to the overlap and the second term is the gas mass fraction of the gases trapped in the cylinder before the overlap. In the equation: p_{exh} is the pressure in the exhaust manifold, p_{int} is the pressure in the intake manifold, γ is the polytropic coefficient of the gases, N is the engine speed and r_c is the compression ratio. The constants C_1 and C_2 are used to calibrate the model to the working engine. In [Fox et al., 1993] these constants were fixed to 1.266 and 0.632 respectively.

A.2.2 Mass balance between the intake manifold and the cylinder

A model based in a simple mass balance between the intake manifold and the cylinder is presented here. This model does not take into account the VVT overlaps, under this assumption:

$$m_{air_a} = m_{air_c}, \quad m_{egr_a} = m_{egr_c}, \quad m = m_{int} + m_{igr_c} \tag{A.2.7}$$

where m_{air} is the air fresh mass, m_{int} is the mass filled-in from the intake manifold, m is the mass at IVC and the sub index a means the gases in the intake manifold and the sub index c means the gases in the cylinder.

The EGR fractin X_{egr_a} is assumed to be known. The mass from the intake manifold is:

$$m_{int} = m_{air} + m_{egr_a} \tag{A.2.8}$$

and

$$X_{egr_a} = \frac{m_{egr_a}}{m_{int}} \tag{A.2.9}$$

Using equations (A.2.8) and (A.2.10) and after some algebraic computations m_{egr_a} is:

$$m_{egr_a} = \frac{X_{egr_a}}{1 - X_{egr_a}} m_{air} \tag{A.2.10}$$

The IGR are only present inside the cylinder, then the subindex c is suppressed. The internal gases fraction is expressed as:

$$X_{igr} = \frac{m_{igr}}{m} \tag{A.2.11}$$

replacing m by the expression in Equation (A.2.7), the expression for the IGR gases is:

$$m_{igr} = \frac{X_{igr}}{1 - X_{igr}} \frac{1}{1 - X_{egr_a}} m_{air} \tag{A.2.12}$$

Inside the cylinder, the admitted gases are added to the IGR gases, then the EGR fraction inside the cylinder is:

$$X_{egr_c} = X_{egr_a} \left(1 - X_{igr}\right) \tag{A.2.13}$$

A.2.3 Senecal, Xin and Reitz. Residual gas fraction in IC engines

This model is taken from [Senecal et al., 1996]. It extends [Fox et al., 1993] work to the turbocharged engines case. When the turbocharger is included, it is possible to have flow going directly from the intake port to the exhaust because at some operating conditions, the pressure downstream the cylinder is smaller than the pressure on the intake path. Similarly to [Fox et al., 1993], the IGR is due to two main contributions: the gases coming from the exhaust port during the overlap period and the trapped gas in the cylinder before the overlap period:

$$X_{igr} = C_1 \left(\frac{RT_{int}}{p_{exh}}\right)^{1/2} \left(\frac{p_{exh}}{p_{int}}\right)^{\frac{\gamma+1}{2\gamma}} \frac{r_c - 1}{r_c} \frac{(1+\beta)^{\frac{\gamma-1}{2\gamma}}}{(1+\beta+\omega)^{1/2}} \sqrt{|p_{exh} - p_{int}|} \frac{OF}{N} \tag{A.2.14}$$

$$+ C_2 \frac{1}{r_c} \left(\frac{p_{exh}}{p_{int}}\right)^{1/\gamma} \frac{(1+\beta)^{\frac{\gamma-1}{\gamma}}}{1+\beta+\omega} (\phi^2 - 0.5295\phi + 0.5295) \tag{A.2.15}$$

$$\beta = \frac{\alpha m_{fuel} LHV}{m_{air} c_v r_c^{\gamma-1} T_{int}} \tag{A.2.16}$$

$$\omega = \frac{(1-\alpha) m_c LHV}{m_{air} c_p r_c^{\gamma-1} T_{int}} \tag{A.2.17}$$

α is the constant volume combustion fraction defined as:

$$\alpha = \frac{m_{f_{2,3}}}{m_{fuel}} \tag{A.2.18}$$

where $m_{f_{2,3}}$ is the mass of the burned fuel during the constant volume stage of the combustion process and m_f is the injected fuel. α is assumed to be equal to 1. LHV is the lower heat value of the fuel, R is the ideal gases constant, T_{int} is the gases temperature in the intake manifold, p_{int} and p_{exh} are the intake and exhaust pressures respectively, m_{air} is the fresh air from the admission manifold and m_{fuel} is the mass of the fuel. c_p and c_v are the specific heats of the gases.

The constants C_1 and C_2 are used to calibrate the model to the working engine. In [Senecal et al., 1996] they were fixed to 3.3089 and 2.2662 respectively. When $p_{exh} < p_{int}$ the sign of C_1 is inverted to model the back flow that goes from the inlet port to the exhaust port. The factor $(\phi^2 - 0.5295\phi + 0.5295)$ is added because a dependency on the charge richness has been noticed. Such factor might need calibration, as well as C_1 and C_2.

A.2.4 Cavina, Siveiro and Suglia residual mass fraction estimation

This model is taken from [Cavina et al., 2004]. It extends [Fox et al., 1993] and [Senecal et al., 1996] works which were presented just before, in order to obtain a white box model, which does not contain calibration constants. Similarly to [Fox et al., 1993] and [Senecal et al., 1996], the IGR is due to two main contributions: the gases coming from the exhaust port during the overlap period and the trapped gases in the cylinder before the overlap period. The main differences on this model is the fact that it does not consider the calibration values C_1 and C_2 as constants. These parameter are dependent on the X_{igr}, and in order to defined them, only values which might be available in the ECU are taken into account. As well, it takes into account the existence of EGR in the system.

$$X_{igr} = \sqrt{\frac{1}{C}\frac{\pi\sqrt{2}}{360}\frac{r_c - 1}{r_c}\frac{OF}{N}\sqrt{\frac{RT_{int}|p_{exh} - p_{int}|}{p_{exh}}}\left(\frac{p_{exh}}{p_{int}}\right)^{\frac{\gamma+1}{2\gamma}}} \tag{A.2.19}$$

$$+ \frac{1}{C}\frac{r_c - 1}{r_c}\phi\frac{V_{IVO}}{V_{cyl}}\left(\frac{p_{exh}}{p_{int}}\right)^{\frac{1}{\gamma}} \tag{A.2.20}$$

where V_{IVC} is the cylinder volume at IVC, V_{cyl} is the cylinder geometric volume, r_c is the engine geometrical compression ratio, c_v is the specific heat at constant volume of the gases and γ is the specific heat ratio and:

$$C = \left(1 + \frac{LHV}{c_v T_{int} \frac{m_{cyl}}{m_{fuel}} r_c^{\gamma+1}}\right)^{\frac{1}{\gamma}} \tag{A.2.21}$$

where m_{cyl} is the total enclosed mass in the combustion chamber. The fraction $\frac{m_{cyl}}{m_{fuel}}$ depends on X_{igr}:

$$\frac{m_{cyl}}{m_{fuel}} = 1 + \phi + \frac{X_{igr}}{1 - X_{igr}}\left(1 + \frac{\phi}{1 - X_{egr}}\right) + \frac{\phi X_{egr}}{1 - X_{egr}} \tag{A.2.22}$$

where ϕ is the air to fuel ratio.

A.2.5 Koehler and Bargende: In-cylinder residual mass model

This model is taken from [Koehler & Bargende, 2004]. The model goal is to obtain an universal formula to estimate the residual gas fraction in the cylinder. It is based on physical laws and provides an expression which is valid for VVT and turbocharged equipped engines.

This model takes into account the mass flow going through the inlet and exhaust valve. As the admitted flow is supposed to be known, it is enough to calculate the exhaust flow to find the balance between the two valves and find the IGR mass. The idea is to define the exhaust flow with the Bernoulli's laws, using the available data in the ECU.

The exhaust flow is divided in two main components: The exhaust mass flow which is caused by the volume change Δm_{RestV} and the second term Δm_{RestB} which results from the pressure difference between the exhaust port and the intake port. This model takes into account the valve lifts:

$$\Delta m_{RestV} = \rho \sum_{\theta=\theta_{IVO}}^{\theta_{EVC}} \left(\frac{dV}{d\theta} \frac{\alpha_{K_{exh}}^2}{\alpha_{K_{exh}}^2 + \alpha_{K_{int}}^2} \Delta\theta\right) \tag{A.2.23}$$

$$\Delta m_{RestB} = sign(p_{exh} - p_{int}) A_k \sqrt{2\rho |p_{exh} - p_{int}|} \frac{dt}{d\theta} \sum_{\theta=\theta_{IVO}}^{\theta_{EVC}} \left(\frac{\alpha_{K_{exh}} \alpha_{K_{int}}}{\sqrt{\alpha_{K_{exh}}^2 + \alpha_{K_{int}}^2}} \Delta\theta\right) \tag{A.2.24}$$

In the equations: θ is the crank angle, $\Delta\theta = \theta_{EVC} - \theta_{IVO}$ V and is the cylinder volume. The variables α_k are the discharge coefficients of the valves and $A_{eff} = A_k\alpha_k$ where A_k is the piston surface.

A.3 Two zones thermodynamic model

The thermodynamical model describes the energy balance inside the combustion chamber. This model is taken from [Bordet et al., 2010]. The aim of this section is to detail the procedure to obtain the gases temperature of the two zones model which was presented in Section 3.3. The nomenclature from Chapter 3 can be used for the equations presented in this section.

In this model, it is assumed that the cylinder volume is divided into two zones: the burned gases zone and the unburned gases zone. Each zone is defined by its mean thermodynamical properties and the specific heat and specific enthalpy of each gas component change according to the JANAF thermodynamic properties table [Chase Jr et al., 1986]. Both zones are assumed to have the same uniform in-cylinder pressure. Each zone is treated as a separated open system. The mass flow rate in each zone is deduced from a balance equation corresponding to mass transfer through intake and exhaust valves and the burning rate.

The energy equation for each zone is:

$$dU_i(t) = -p(t)dV_i(t) + \delta Q_{th_i}(t) + \left(\sum_j h_j(t)dm_j(t)\right)_i, \quad i = u, b \qquad (A.3.1)$$
$$j = int, \quad exh, \quad comb$$

The subindex i represents the zone, $i = b$ for burned gases or $i = u$ for unburned gases. The sub index j means intake ($j = int$), exhaust ($j = exh$) and combustion ($j = comb$), indicating the source of the energy: int, exh for the enthalpies coming from the gases passing through the intake and exhaust valves and $comb$ for the enthalpy from the combustion process. $U_i(t)$ is the internal energy of the cylinder gas mixture. $\delta Q_{th_i}(t)$ expresses the heat losses of the cylinder contents to the surroundings, $p(t)dV_i(t)$ corresponds to the piston work delivered, and $\left(\sum_j h_j(t)dm_j(t)\right)_i$ is the total energy flowing into or out of the zone i.

The left side of the equation A.3.1 can be written as:

$$dU_i(t) = u_i(t)dm_i(t) + m_i(t)\sum_j u_{i,j}(t)\frac{dY_{i,j}(t)}{dt} + m_i(t)C_{v_i}(t)dT_i(t) \qquad (A.3.2)$$

Where $u_{i,j}$ is the internal energy of the specie j in the zone i. Similarly $Y_{i,j}(t)$ corresponds to the mass fraction of the gases. $m_i(t)$ is the mass in the zone i.

It is known that:

$$u_i(t) = h_i(t) - p(t)V_i(t) = h_i(t) - r_i(t)T_i(t) \tag{A.3.3}$$

thus multiplying by $dm_i(t)$ it yields to:

$$u_i(t)dm_i(t) = h_i(t)dm_i(t) - p(t)V_i(t)dm_i(t) = h_i(t)dm_i(t) - r_i(t)T_i(t)dm_i(t) \tag{A.3.4}$$

Replacing A.3.4 in A.3.2 and making the difference between equations A.3.1 and A.3.2 :

$$\begin{aligned} m_i(t)c_{v_i}(t)dT_i(t) &= -p(t)dV_i(t) + \delta Q_{th_i}(t) + \textstyle\sum_j h_j(t)dm_j(t) - h_i(t)dm_i(t) \\ &\quad + r_i(t)T_i(t)dm_i(t) - m_i(t)\textstyle\sum_j u_{i,k}(t)\frac{dY_{i,j}(t)}{dt} \end{aligned} \tag{A.3.5}$$

This expression will be used later to calculate the gases temperature of each zone.

For a control volume enclosing the fuel/air mixture, the rate of change of the total mass $m(t)$ is equal to the sum of mass flowing into and out of the system:

$$dm(t) = \sum dm_i(t) \tag{A.3.6}$$

The intake and outlet valves are modeled as restrictions between the intake manifold or the exhaust manifold and the cylinder. The mass flow passing through the valves can be closely approximated by the air mass flow of a compressible fluid through a nozzle as depicted in Figure A.2. Table A.1 shows the equation of the mass flow passing through the restriction depending on the operating conditions.

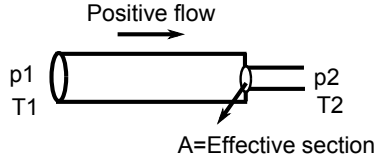

Figure A.2: Flow restriction

In Table A.1, $u = [IVC_d, EVO_d]$. The valves opening and closing effective sections are defined using as inputs the IVC_d and EVO_d.

$\mathbf{p_1 > p_2}$	$\mathbf{T_m = T_1}$
$(\gamma_i+1)^{\frac{\gamma_i}{\gamma_i-1}} > \frac{p_1}{p_2}$	$dm_i = A(t,u)p_1\sqrt{\frac{1}{r_iT_1}\left(\frac{2}{\gamma_i+1}\right)^{\frac{\gamma_i+1}{\gamma_i-1}}}$
$(\gamma_i+1)^{\frac{\gamma_i}{\gamma_i-1}} < \frac{p_1}{p_2}$	$dm_i = A(t,u)p_1 \times \sqrt{\frac{2}{rT_1}\left(\frac{\gamma_i}{\gamma_i-1}\right)\left(\left(\frac{p_2}{p_1}\right)^{\frac{2}{\gamma_i}} - \left(\frac{p_2}{p_1}\right)^{\frac{\gamma_i+1}{\gamma_i-1}}\right)}$
$\mathbf{p_1 < p_2}$	$\mathbf{T_m = T_2}$
$(\frac{\gamma_i+1}{2})^{\frac{\gamma_i}{\gamma_i-1}} > \frac{p_2}{p_1}$	$dm_i = -A(t,u)p_2\sqrt{\frac{1}{r_iT_2}\left(\frac{2}{\gamma_i+1}\right)^{\frac{\gamma_i+1}{\gamma_i-1}}}$
$(\frac{\gamma_i+1}{2})^{\frac{\gamma_i}{\gamma_i-1}} < \frac{p_2}{p_1}$	$dm_i = -A(t,u)p_2 \times \sqrt{\frac{2}{r_iT_2}\left(\frac{\gamma_i}{\gamma_i-1}\right)\left(\left(\frac{p_1}{p_2}\right)^{\frac{2}{\gamma_i}} - \left(\frac{p_1}{p_2}\right)^{\frac{\gamma_i+1}{\gamma_i-1}}\right)}$

Table A.1: Mass flow through the engine valves depending on the operating conditions

Remark A.3.1. The inputs IVC_d and EVO_d are considered as parameters since no control is performed with these inputs.

Performing an energy balance in each zone u, b and applying the equations presented previously, the thermodynamical characteristics of the gases in each zone can be obtained. An energy balance for the combustion chamber is also performed. All these procedures are presented in the next sections.

A.3.1 Unburned zone energy balance

The energy balance for the unburned gases zone is presented in the figure A.3. The energy sources for the unburned gases zone are the intake enthalpy, the exhaust enthalpy, and the enthalpy of the burning rate (combustion process).

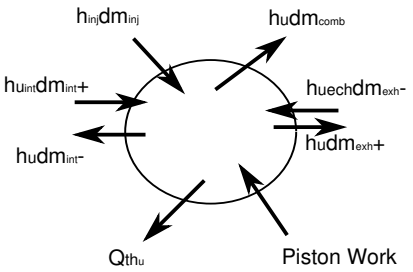

Figure A.3: Scheme of the unburned zone energy balance

In the following equations, the upper index + means the positive direction for the flow. For the valves flows, the mass flow direction is defined as positive if it goes from the intake manifold to the cylinder (positive intake valve flow), and from the cylinder to the exhaust manifold (positive exhaust valve flow), otherwise the mass flow from the valves is negative.

Taking into account the scheme in Figure A.3, the sum of the enthalpy flows in the unburned gases zone yields to:

$$\begin{aligned}\left(\sum_j h_j(t)dm_j(t)\right)_u = h_u(t)dm_u(t) = h_u(t)dm_{inj}(t) - h_u(t)dm_{comb}(t) \\ -h_u(t)dm_{u^+_{exh}}(t) + h_{u_{exh}}(t)dm_{u^-_{exh}}(t) + h_{u_{int}}(t)dm_{u^+_{int}}(t) - h_u(t)dm_{u^-_{int}}(t)\end{aligned} \quad (A.3.7)$$

and applying equation A.3.1 to the zone u and replacing the term $\left(\sum_j h_j(t)dm_j(t)\right)_i$ by (A.3.7) it yields to:

$$\begin{aligned}dU_u(t) = -p(t)dV_u(t) + \delta Q_{th_u}(t) + h_{inj}(t)dm_{inj}(t) - h_u(t)dm_{comb}(t) - \\ h_u(t)dm_{u^+_{exh}}(t) + h_{u_{exh}}(t)dm_{u^-_{exh}}(t) + h_{u_{int}}(t)dm_{u^+_{int}}(t) - h_u(t)dm_{u^-_{int}}(t)\end{aligned} \quad (A.3.8)$$

Replacing the precedent results in equation A.3.5 for the unburned gases zone:

$$\begin{aligned}m_u(t)c_{v,u}dT_u(t) = -p(t)dV_u(t) + \delta Q_{th,u}(t) + r_u(t)T_u(t)\dot{m}_u(t) \\ -m_u(t)\sum_j u_{u,j}(t)\tfrac{dY_{u,j}(t)}{dt} + dm_{inj}(t)(h_{inj}(t) - h_u(t)) \\ +dm_{u^-_{exh}}(t)(h_{u_{exh}}(t) - h_u(t)) + dm_{u^+_{int}}(t)(h_{u_{int}}(t) - h_u(t))\end{aligned} \quad (A.3.9)$$

From the perfect gases law:

$$p(t)V_u(t) = m_u(t)r_u(t)T_u(t) \quad (A.3.10)$$

and taking the time derivative:

$$\begin{aligned}p(t)dV_u(t) = r_u(t)T_u(t)dm_u(t) + m_u(t)T_u(t)dr_u(t) + m_u(t)r_u(t)dT_u(t) \\ -dp(t)V_u(t)\end{aligned} \quad (A.3.11)$$

Replacing A.3.11 in A.3.9:

$$\begin{aligned}m_u(t)c_{v,u}dT_u(t) + m_u(t)r_u(t)T_u(t) = -m_u(t)T_u(t)dr_u(t) + dp(t)V_u(t) \\ +\delta Q_{th,u}(t) - m_u(t)\sum_j u_{u,j}(t)\tfrac{dY_{u,j}(t)}{dt} + dm_{inj}(t)(h_{inj}(t)\end{aligned} \quad (A.3.12)$$

$$-h_u(t)) + dm_{u^-_{exh}}(t)(h_{u_{exh}}(t) - h_u(t)) + dm_{u^+_{int}}(t)(h_{u_{int}}(t) - h_u(t))$$

From the property $c_v + r = c_p$:

$$\begin{aligned} dT_u(t) = -\tfrac{1}{c_{p,u}}(t)T_u(t)dr_u(t) + \tfrac{V_u(t)}{m_u(t)c_{p,u}(t)}dp(t) + \tfrac{1}{m_u(t)c_{p,u}(t)}\delta Q_{th,u}(t) \\ -\tfrac{1}{c_{p,u}(t)}\textstyle\sum_j u_{u,j}(t)\tfrac{dY_{u,j}(t)}{dt} + \tfrac{1}{m_u(t)c_{p,u}(t)}dm_{inj}(t)(h_{inj}(t) - h_u(t)) \\ +\tfrac{1}{m_u(t)c_{p,u}(t)}dm_{u^-_{exh}}(t)(h_{u_{exh}}(t) - h_u(t)) + \tfrac{1}{m_u(t)c_{p,u}(t)}dm_{u^+_{int}}(t)(h_{u_{int}}(t) - h_u(t)) \end{aligned} \quad \text{(A.3.13)}$$

where

$$h_u(t) = f_h(T_u(t), m_u(t), m_{vap}(t)), \quad \text{(A.3.14)}$$

$$\begin{aligned} c_{p_u}(t) = f_{c_p}(T_u(t), m_u(t), m_{vap}(t)), \quad c_{v_u}(t) = f_{c_v}(T_u(t), m_u(t), m_{vap}(t)), \\ r_u(t) = f_r(m_u) \end{aligned} \quad \text{(A.3.15)}$$

are look up tables functions.

The heat wall losses δQ_{th_u} are computed as in Equation (3.3.5).

A.3.2 Burned zone energy balance

The energy balance for the burned gases zone is presented in the figure A.4.

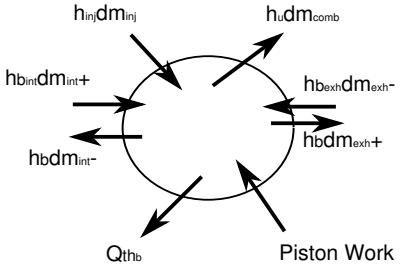

Figure A.4: Scheme of the burned zone energy balance

Taking into account the scheme in Figure A.4, the enthalpy flows sum for the burned gases zone yields to:

$$h_b(t)\dot{m}_b(t) \quad = h_b(t)dm_{comb}(t) - h_b(t)dm_{b^+_{exh}}(t) + h_{b_{exh}}(t)dm_{b^-_{exh}}(t)$$

$$+h_{b_{int}}(t)dm_{b^+_{int}}(t) - h_b(t)dm_{b^-_{int}}(t) \tag{A.3.16}$$

and applying equation A.3.1 to the zone b and replacing the term $\left(\sum_j h_j(t)dm_j(t)\right)_i$ by (A.3.16) it yields to:

$$\begin{aligned} dU_b(t) = \quad & -p(t)dV_b(t) + \delta Q_{th_b}(t) + h_u(t)dm_{comb}(t) - h_b(t)dm_{b^+_{exh}}(t) \\ & +h_{b_{exh}}(t)dm_{b^-_{exh}}(t) + h_{b_{int}}(t)dm_{b^+_{int}}(t) - h_b(t)dm_{^-_{int}}(t) \end{aligned} \tag{A.3.17}$$

For the burned gases $m_b(t)\sum_j u_{b,j}\frac{dY_{u,j}(t)}{dt} = 0$ because the load is assumed to be uniformly premixed. Replacing the precedent results in equation A.3.5 for the burned gases zone it yields to:

$$\begin{aligned} & m_b(t)c_{v,b}(t)dT_b(t) = -p(t)\tfrac{dV_b(t)}{dt} + \delta Q_{th,b}(t) + r_b(t)T_b(t)dm_b(t) \\ & +dm_{b_{comb}}(t)(h_u(t) - h_b(t)) + dm_{b^-_{exh}}(t)(h_{u_{exh}}(t) - h_u(t)) + dm_{b^+_{int}}(t)(h_{u_{int}}(t) - h_u(t)) \end{aligned} \tag{A.3.18}$$

From the perfect gases law:

$$p(t)V_b(t) = m_b(t)r_b(t)T_b(t) \tag{A.3.19}$$

and taking the time derivative:

$$p(t)dV_b(t) = r_b(t)T_b(t)dm_b(t) + m_b(t)r_b(t)dT_b(t) - dp(t)V_b(t) \tag{A.3.20}$$

Replacing A.3.20 in A.3.18:

$$\begin{aligned} & m_b(t)c_{v,b}(t)dT_b(t) + m_b(t)r_b(t)T_b(t) = dp(t)V_b(t) + \delta Q_{th,b}(t) \\ & +dm_{comb}(t)(h_u(t) - h_b(t)) + dm_{b^-_{exh}}(t)(h_{b_{exh}}(t) - h_b(t)) + dm_{b^+_{int}}(t)(h_{b_{int}}(t) - h_b(t)) \end{aligned} \tag{A.3.21}$$

From the property $c_v + r = c_p$:

$$dT_b(t) = \tfrac{V_b(t)}{m_b(t)c_{p,b}(t)}dp(t) + \tfrac{1}{m_b(t)c_{p,b}(t)}\delta Q_{th,b}(t) + \tag{A.3.22}$$

$$\frac{1}{m_b(t)c_{p,b}(t)}dm_{comb}(t)(h_u(t)-h_b(t))+\frac{1}{m_b(t)c_{p,b}(t)}dm_{b^-_{exh}}(t)(h_{b_{exh}}(t)-h_b(t))$$
$$+\frac{1}{m_b(t)c_{p,b}(t)}dm_{b^+_{int}}(t)(h_{b_{int}}(t)-h_b(t))$$

where

$$h_b(t)=f_h(T_b(t),m_u(t),m_{vap}(t)) \tag{A.3.23}$$

$$c_{p_b}=f_{c_p}(T_b,m_b,m_{vap}),\quad c_{v_b}=f_{c_v}(T_b,m_b,m_{vap}) \tag{A.3.24}$$
$$r_b=f_r(m)$$

are look up table functions.

The heat wall losses δQ_{th_b} are computed as in Equation (3.3.5).

A.3.3 Combustion chamber energy balance

The total internal energy in the combustion chamber is the sum between the burned and unburned zone internal energies:

$$U_{tot}(t)=U_u(t)+U_b(t) \tag{A.3.25}$$

Taking the time derivative:

$$dU_{tot}(t)=dU_u(t)+dU_b(t) \tag{A.3.26}$$

and applying A.3.1 to the combustion chamber it yields to:

$$dU_u(t)+dU_b(t)=-p(t)dV(t)+\delta Q_{th}(t)+\sum_j h_j(t)dm_j(t) \tag{A.3.27}$$

where the sub index $i=u,b$ has been suppressed in the left side of the equation because the combustion chamber is taken as a unique control volume. Using (A.3.2), the left side of the energy equation can be rewritten as:

$$dU_u(t) + dU_b(t) = u_u(t)dm_u + (t)m_u(t)\sum_j u_{u,j}(t)\frac{dY_{u,j}(t)}{dt} + m_u(t)c_{v,u}(t)dT_u(t) + u_b(t)dm_b(t) + m_b(t)c_{v,b}(t)dT_b(t) \quad \text{(A.3.28)}$$

Replacing A.3.13 in A.3.28 and using the fact that $c_{p_u}(t)/c_{v_u}(t) = \gamma_u(t)$, for the unburned gases zone it yields:

$$dU_u(t) = \left(1 - \frac{1}{\gamma_u(t)}\right) m_u(t)\sum_j u_{u,j}(t)\frac{dY_{u,j}(t)}{dt} + \frac{1}{\gamma_u(t)}V_u(t)dp(t) - \frac{1}{\gamma_u(t)}m_u(t)T_u(t)dr_u(t) + \frac{1}{\gamma_u(t)}\delta Q_{th,u}(t) + \frac{1}{\gamma_u(t)}dm_{inj}(t)(h_{inj}(t) - h_u(t)) + \frac{1}{\gamma_u(t)}dm_{u^-_{exh}}(t)(h_{u_{exh}}(t) - h_u(t)) + \frac{1}{\gamma_u(t)}dm_{u^+_{int}}(t)(h_{u_{int}}(t) - h_u(t)) + U_u(t)dm_u(t) \quad \text{(A.3.29)}$$

Replacing A.3.22 in A.3.28 and using the fact that $c_{p_b}/c_{v_b} = \gamma_b$, for the burned gases zone it yields:

$$dU_b(t) = \frac{1}{\gamma_b(t)}V_b(t)dp(t) + \frac{1}{\gamma_b(t)}\delta Q_{th,b}(t) + \frac{1}{\gamma_b(t)}dm_{comb}(h_u(t) - h_b(t)) + \frac{1}{\gamma_b(t)}dm_{b^+_{int}}(t)(h_{b_{int}}(t) - h_b(t)) + \frac{1}{\gamma_b(t)}dm_{b^-_{exh}}(t)(h_{b_{exh}}(t) - h_b(t)) + U_b(t)dm_b(t) \quad \text{(A.3.30)}$$

The mass balance for the combustion chamber is shown in figure A.5

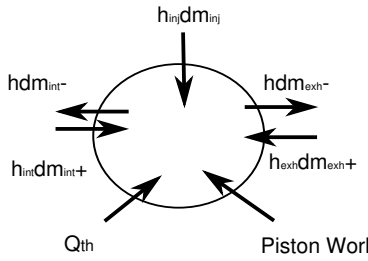

Figure A.5: Scheme of the cylinder mass balance

From the figure A.5, the energy balance for the cylinder is:

$$\sum_j h_j(t)dm_j(t) = h_{inj}(t)dm_{inj}(t) - dm_{u^-_{int}}(t)h_u(t) + dm_{b^-_{int}}(t)h_b(t) + h_{u_{int}}(t)dm_{u^+_{int}}(t) + h_{b_{int}}(t)dm_{b^+_{int}}(t) + h_{u_{exh}}(t)dm_{u^-_{exh}}(t) + h_{b_{exh}}(t)dm_{b^-_{exh}}(t) - h_u(t)dm_{u^+_{exh}}(t) + h_b(t)dm_{b^+_{exh}}(t) \quad \text{(A.3.31)}$$

Replacing A.3.29, A.3.30 and A.3.31 in A.3.27 and rearranging the expression to obtain $dp(t)$ it yields to:

$$\begin{aligned}\frac{dp(t)}{dt} = \quad & \frac{1}{\frac{V_u(t)}{\gamma_u(t)}+\frac{V_b(t)}{\gamma_b(t)}}\Bigg(- p(t)dV(t) + \left(1-\frac{1}{\gamma_u(t)}\right)\delta Q_{th_u}(t) + \left(1-\frac{1}{\gamma_b(t)}\right)\delta Q_{th_b}(t) \\ & - \left(1-\frac{1}{\gamma_u(t)}\right) m_u(t)\sum_j u_{u,j}(t)\frac{dY_{u,j}(t)}{dt} + \frac{1}{\gamma_u(t)} m_u(t)T_u(t)dr_u(t) \\ & + dm_{_{inj}}(t)\left(h_{inj}(t) - \frac{h_{inj}(t)-h_u(t)}{\gamma_u(t)}\right) + dm_{_{u^-_{exh}}}(t)\left(h_{u_{exh}}(t) - \frac{h_{u_{exh}}(t)-h_u(t)}{\gamma_u(t)}\right) \\ & + dm_{_{u^+_{int}}}(t)\left(h_{u_{int}}(t) - \frac{h_{u_{int}}(t)-h_u(t)}{\gamma_u(t)}\right) + dm_{_{b^+_{int}}}(t)\left(h_{b_{int}}(t) - \frac{h_{b_{int}}(t)-h_b(t)}{\gamma_b(t)}\right) \\ & + dm_{_{b^-_{exh}}}(t)\left(h_{b_{exh}}(t) - \frac{h_{b_{exh}}(t)-h_b(t)}{\gamma_b(t)}\right) - \frac{1}{\gamma_b(t)} dm_{_{comb}}(t)(h_u(t)-h_b(t)) \\ & - dm_{_{u^-_{int}}}(t)h_u(t) - dm_{_{u^+_{exh}}}(t)h_u(t) - dm_{_{b^-_{int}}}(t)h_b(t) - dm_{_{b^+_{exh}}}(t)h_b(t) \\ & - U_u(t)dm_u(t) - U_b(t)dm_b(t)\Bigg) \end{aligned} \tag{A.3.32}$$

Using the fact that $U(t)dm(t) = h(t)dm(t) - r(t)T(t)dm(t)$, the term $-U_u(t)dm_u(t) - U_b(t)dm_b(t)$ in equation A.3.32 can be replaced by:

$$\begin{aligned} U_u(t)dm_u(t) = \quad & h_u(t)(dm_{_{inj}}(t) + dm_{_{u^+_{int}}}(t) - dm_{_{u^-_{int}}}(t) - dm_{_{u^+_{exh}}}(t) \\ & + dm_{_{u^-_{exh}}})(t) - r_u(t)T_u(t)dm_u(t) \end{aligned} \tag{A.3.33}$$

$$\begin{aligned} U_b(t)dm_b(t) \quad & = h_b(t)(dm_{_{comb}}(t) + dm_{_{b^+_{int}}}(t) - dm_{_{b^-_{int}}}(t) - dm_{_{b^+_{exh}}}(t) \\ & + dm_{_{b^-_{exh}}}(t)) - r_b(t)T_b(t)dm_b(t) \end{aligned} \tag{A.3.34}$$

thus $dp(t)$ is:

$$\begin{aligned} dp(t) = \quad & \frac{1}{\frac{V_u(t)}{\gamma_u(t)}+\frac{V_b(t)}{\gamma_b(t)}}\Bigg(- p(t)dV(t) + \left(1-\frac{1}{\gamma_u(t)}\right)\delta Q_{th_u}(t) + \left(1-\frac{1}{\gamma_b(t)}\right)\delta Q_{th_b}(t) \\ & - \left(1-\frac{1}{\gamma_u(t)}\right) m_u(t)\sum_j u_{u,j}(t)\frac{dY_{u,j}(t)}{dt} + \frac{1}{\gamma_u(t)} m_u(t)T_u(t)dr_u(t) \\ & + r_u(t)T_u(t)dm_u(t) + r_b(t)T_b(t)dm_b(t) + dm_{inj}(t)\left(1-\frac{1}{\gamma_u(t)}\right)(h_{inj}(t) - h_u(t)) \\ & + dm_{_{u^-_{exh}}}(t)\left(1-\frac{1}{\gamma_u(t)}\right)(h_{u_{exh}}(t) - h_u(t)) + dm_{_{u^+_{int}}}(t)\left(1-\frac{1}{\gamma_u(t)}\right)(h_{u_{int}}(t) - h_u(t)) \\ & + dm_{_{b^+_{int}}}(t)\left(1-\frac{1}{\gamma_b(t)}\right)(h_{b_{int}}(t) - h_b(t)) + dm_{_{b^-_{exh}}}(t)\left(1-\frac{1}{\gamma_b(t)}\right)(h_{b_{exh}}(t) - h_b(t)) \\ & + \left(1-\frac{1}{\gamma_b(t)}\right) dm_{comb}(t)(h_u(t) - h_b(t))\Bigg) \end{aligned} \tag{A.3.35}$$

The rate of change due to the combustion process $dm_{comb}(t)$ can be represented by the combustion models presented in Section 3.4.

A.4 Geometric flame surface model

In order to create a geometric model of the flame surface A_l, the model of a simplified combustion chamber is developed first. In this model, two main parts are considered: the combustion chamber top and the cylindrical chamber body. The chamber top is modeled as a geometric cone taking into account the parameters depicted in Figure A.6.

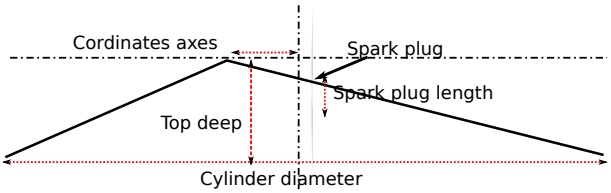

(a) Chamber top geometric parameters

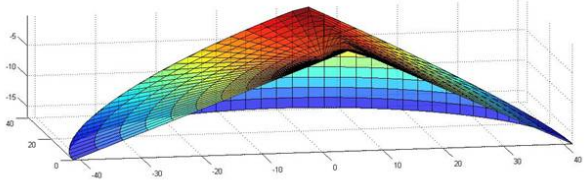

(b) Chamber top geometric scheme

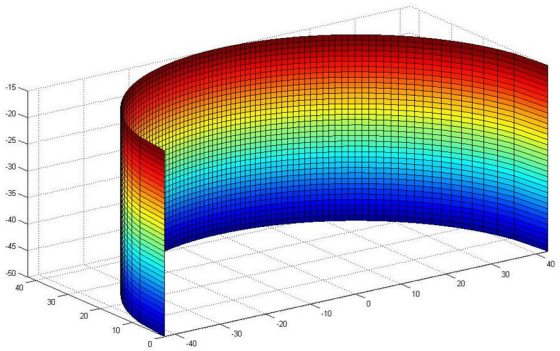

(c) Cylinder geometric scheme

Figure A.6: Geometric model of the combustion chamber top

A_l is designed as a semi sphere of radius R_f, centered in the spark plug position. A_l grows in the combustion chamber until it approaches the cylinder walls, the distance d_i from the flame surface to the combustion chamber is also mapped . Figure A.7 shows the combustion chamber with the flame surface inside.

First, the look up table $V_b/V = f_v(R_f, Hp)$ is designed, where V_b/V is the ratio between the burned gases volume and the combustion chamber volume, thus the magnitude varies between 0 up to 1 and H_p is the piston height. The look up table of V_b/V is inverted to obtain a map of the flame surface radius $R_f(t) = f_v^{-1}(V_b/V, H_p)$. Then, the look up table for A_l is defined as $A_l = f_A(R_f, H_p)$.

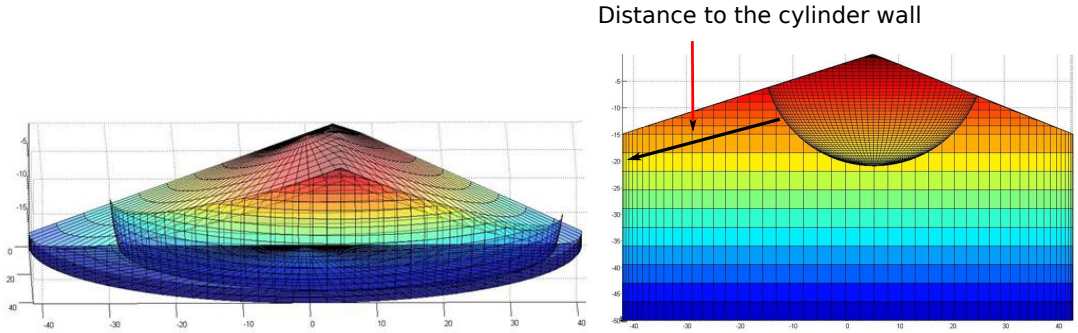

(a) Geometric flame surface inside the combustion chamber

(b) Mapping of the distance from the flame surface to the cylinder wall

Figure A.7: Geometric model of the flame surface inside the combustion chamber

Figure A.8 depicts the plot of R_f and A_l. In the figure the piston height goes from 0 up to the cylinder 90 mm, the flame radius is mapped for a maximum length of 120 mm.

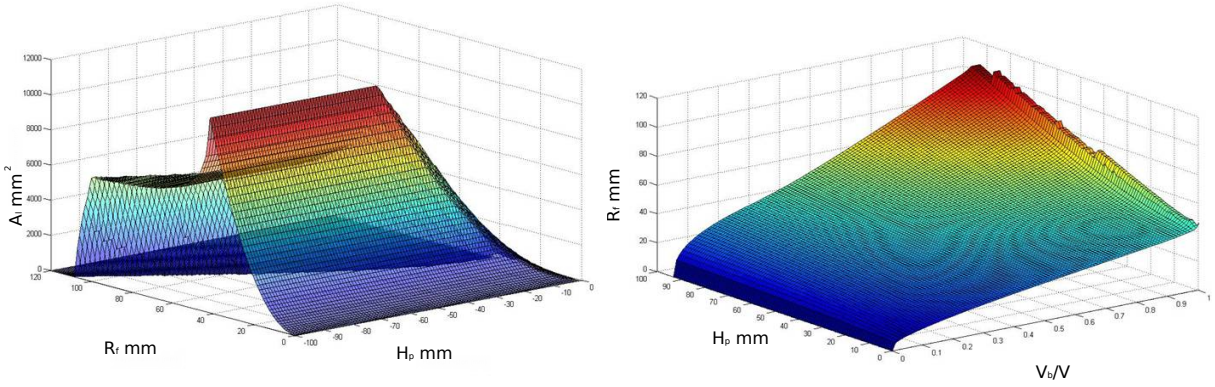

(a) A_l map plot

(b) R_f map plot

Figure A.8: Flame surface and flame radius maps plots

A.5 Reynolds stress tensor

The turbulence models in the engine modeling arise from the fluid dynamics theory. The most common turbulence models are based on the *Reynolds stress tensor* τ_{ij}, where the kinetic energy per unit volume of the turbulence fluctuations is assumed to be proportional to the trace of the *Reynolds stress tensor* equation [Wilcox, 1993]. The dynamics of τ_{ijk} is given the following equations (the time dependency of the variables is neglected for simplicity):

$$\frac{\partial \tau_{ij}}{\partial t} + \mathbf{U}_k \frac{\partial \tau_{ij}}{\partial x_k} = -\tau_{ik}\frac{\partial \mathbf{U}_j}{\partial x_k} - \tau_{ij}\frac{\partial \mathbf{U}_i}{\partial x_k} + \epsilon_{ij} - \pi_{ij} + \frac{\partial}{\partial x_k}\left(v\frac{\partial \tau_{ij}}{\partial x_k} + C_{ijk}\right) \tag{A.5.1}$$

$$\pi_{ij} = \overline{p\left(\frac{\partial u_i}{\partial x_j} + \frac{\partial u_j}{\partial x_i}\right)} \tag{A.5.2}$$

$$\epsilon_{ij} = \overline{2\mu\frac{\partial u_i}{\partial x_k}\frac{\partial u_j}{\partial x_k}} \tag{A.5.3}$$

$$C_{ijk} = \overline{\rho u_i u_j u_k} \tag{A.5.4}$$

where the sub-indexes i, j and k are the spatial coordinates. x indicates spatial derivative (i.e $\frac{\partial \tau_{ij}}{\partial x_k}$ is the spatial derivative of the tensor τ_{ij} with respect to the spatial coordinate k).

$\mathbf{u} = [u_i, u_j, u_k]$ is the fluid velocity vector, $\mathbf{U}$ is the mean fluid velocity, π_{ij} is the pressure strain correlation tensor, ϵ_{ij} is the dissipation rate and C_{ijk} is the turbulent transport tensor.

The Reynolds-stress tensor describes the random fluctuations of the various flow properties. According to Reynolds, all the quantities are expressed as sums of mean fluctuating parts. These equations are too complex for the purpose of this work, and will not be explained in details. They are exposed here in order to show the reference for the 0D turbulent energy model used in the qualitative analysis results and various dependencies in Chapter 3.